



OTTO VON GUERICKE  
UNIVERSITÄT  
MAGDEBURG

VST

FAKULTÄT FÜR VERFAHRENS-  
UND SYSTEMTECHNIK

# **Precipitation of barium sulfate in a semi-batch stirred tank reactor: Influence of feeding policy on particle size and morphology**

## **Dissertation**

zur Erlangung des akademischen Grades

## **Doktoringenieurin**

**(Dr.-Ing.)**

von Dipl.-Ing. Christiane Steyer (geb. Rudolph)

geb. am 04. Dezember 1972 in Stuttgart

genehmigt durch die Fakultät für Verfahrens- und Systemtechnik  
der Otto-von-Guericke-Universität Magdeburg

Promotionskommission:

apl. Prof. Dr. rer. nat. habil. Heike Lorenz (Vorsitz)

Prof. Dr.-Ing. habil. Kai Sundmacher (Gutachter)

Prof. Dr.-Ing. habil. Jürgen Tomas (Gutachter)

apl. Prof. Dr.-Ing. habil. Michael Mangold (Gutachter)

eingereicht am:

03. Februar 2012

Promotionskolloquium am:

27. September 2012



## **Danksagung**

Die vorliegende Dissertation ist das Ergebnis meiner Tätigkeit als wissenschaftliche Mitarbeiterin am Lehrstuhl für Systemverfahrenstechnik der Otto-von-Guericke-Universität Magdeburg unter der Leitung von Herrn Prof. Dr.-Ing. Sundmacher. Das Gelingen verdanke ich vielen Personen, denen ich an dieser Stelle meinen Dank aussprechen möchte.

An erster Stelle danke ich meinem Doktorvater Herrn Prof. Dr.-Ing. Sundmacher für die Möglichkeit, diese Arbeit unter seiner Führung fertig zu stellen. Dazu gehört auch die Bereitstellung des Arbeitsumfeldes mit den damit verknüpften arbeitsrelevanten Annehmlichkeiten, die aus den Mitteln des neuen Lehrstuhls und der engen Kooperation mit seiner MPI-Arbeitsgruppe einhergingen.

Herrn Prof. Dr.-Ing. Tomas möchte ich für die Übernahme des Promotionsgutachtens einschließlich seiner relevanten Anmerkungen danken.

Dafür danke ich ebenfalls Herrn apl. Prof. Dr.-Ing. Mangold, ebenso für den sehr angenehmen und ergebnisreichen wissenschaftlichen Austausch, der mich motiviert und fachlich weitergebracht hat.

Frau apl. Prof. Dr. rer. nat. Lorenz danke ich für ihren Vorsitz der Promotionskommission und für die immer bereitwillig gegebene fachliche Unterstützung.

Ganz besonders möchte ich Frau Evelin Felsch danken, die mit ihrem unermüdlichen Einsatz im Labor und am REM dafür gesorgt hat, dass diese Arbeit die gegebene Fülle an experimentellen Ergebnissen aufweisen kann.

Herrn Dr. rer. nat. Voigt danke ich für den hilfreichen fachlichen Austausch und die angenehme Zusammenarbeit.

Den Kollegen und Kolleginnen an der Uni und dem MPI danke ich für die Unterstützung in technischen Dingen und die angenehme Arbeitsatmosphäre einschließlich anregender Fachgespräche.

Meinen Eltern danke ich für ihre uneingeschränkte Unterstützung, die mir erst die Möglichkeit meiner beruflichen Entwicklung gegeben hat. Auch die vielen Zeiten der Kinderbetreuung sei erwähnt, vor allem von meiner Mutter, ohne welche die Arbeit jetzt noch nicht fertig wäre.

Meinem Mann danke ich für seine kompetente Hilfe bei Problemen mit nicht-konvergierender Numerik, seiner uneingeschränkten Bereitschaft, über ihn nicht betreffende fachliche Details zu diskutieren, und seiner Unterstützung und Motivation während der gesamten Zeit.



## Contents

Abstract.....	viii
Zusammenfassung .....	ix
1 Introduction and objective of this work.....	1
2 Theoretical background .....	7
2.1 Driving force of precipitation .....	7
2.2 Activity coefficient models.....	11
2.2.1 Extended Debye-Hückel approach .....	11
2.2.2 Bromley approach.....	13
2.2.3 Pitzer approach .....	15
2.3 Nucleation.....	19
2.3.1 Homogeneous nucleation.....	20
2.3.2 Heterogeneous nucleation.....	22
2.4 Growth .....	22
2.4.1 Molecular growth.....	23
2.4.2 Aggregational growth .....	26
2.4.3 Growth kinetics.....	27
2.5 Surface adsorption of ions .....	27
2.6 Agglomeration .....	29
2.7 Secondary processes .....	30
2.7.1 Ostwald Ripening .....	30
2.7.2 Recrystallization .....	31
2.8 Particle shape and dendritic growth.....	31
2.8.1 Equilibrium shape.....	31
2.8.2 Kinetically controlled shape .....	32
2.8.3 Dendritic growth.....	33
2.9 Characteristic length and shape factor .....	34
2.10 Mixing effects in a stirred tank reactor.....	36
2.11 Barium sulfate.....	39
2.11.1 Barium sulfate precipitation.....	41
2.11.2 Morphologies of barium sulfate precipitates .....	43
2.11.3 Influence of mixing and feeding policy on barium sulfate.....	45
2.11.4 Shape factors for precipitated barium sulfate .....	48
3 Experimental set-up and preliminary experimental investigations.....	50
3.1 Materials .....	50

3.2	Precipitation reactor and procedures .....	50
3.2.1	Reproducibility of experiments .....	52
3.3	Conditions of experimental series .....	55
3.4	Particle size measuring principles used .....	57
3.4.1	Extinction .....	57
3.4.2	Laser diffraction .....	58
3.5	Reference measurements with standard particles .....	59
3.6	X-ray spectrum (EDX analysis) of particles .....	60
3.7	X-ray powder diffractometry (XRD).....	60
3.8	Influence of KCl excess on particle morphology .....	62
4	Experimental results and discussion.....	65
4.1	Particle morphologies .....	65
4.1.1	High supersaturation.....	65
4.1.2	Low feed concentration .....	66
4.1.3	Higher feed concentration .....	71
4.2	Discussion of influences on morphologies.....	74
4.2.1	Influence of ion excess .....	74
4.2.2	Influence of feeding sequence .....	75
4.2.3	Influence of feed rate.....	76
4.2.4	Influencing particle morphology by feeding policy .....	79
4.3	Seeded precipitation .....	80
4.4	Particle sizes and size distributions .....	85
5	Population balance model for simulating the particle size distribution .....	100
5.1	General population balance equation (PBE) .....	101
5.2	Modelling of semi-batch BaSO <sub>4</sub> bulk precipitation .....	103
5.3	Two-compartment mixing model .....	105
5.4	Growth and nucleation kinetics .....	109
5.4.1	Supersaturation-dependent nucleation and growth kinetics .....	110
5.4.2	Supersaturation- and R-dependent nucleation and growth kinetics .....	111
6	Simulation results and discussion.....	114
6.1	Validation of supersaturation-dependent nucleation and growth kinetics.....	115
6.2	Validation of the supersaturation- and R-dependent kinetics.....	116
6.2.1	Application of Aoun et al.'s (1999) kinetics (ideal mixed batch).....	117
6.2.2	Application of R(t)-adapted kinetics to batch experiments.....	118
6.2.3	Application of R(t)-adapted kinetics to semi-batch experiments .....	121

6.3	Influence of the thermodynamic model .....	122
6.3.1	Simulation studies.....	122
6.3.2	Comparison with experimental results .....	125
6.4	Influence of kinetics.....	130
6.4.1	Shape factors.....	131
6.4.2	Sensitivity of nucleation and growth rates to R.....	136
6.5	Proposed kinetic model with $R$ - $S_a$ -dependent nucleation.....	139
7	Summary and conclusion.....	142
	List of symbols.....	145
	Greek symbols .....	147
	Subscripts.....	148
	Superscripts.....	149
	References.....	150
	Appendix A: Calculation of the mean activity coefficient .....	158
	A.1 Bromley model.....	159
	A.2 Pitzer model .....	161
	Appendix B: Values of supersaturation $S_a$ .....	165
	B.1 Theoretical maximum initial supersaturation $S_a$ of the experiments .....	165
	B.2 Different values of $S_a$ calculated with different methods.....	165
	Appendix C: Own Publications .....	170
	Appendix D: Lebenslauf.....	172

## **Abstract**

In this thesis, the precipitation of barium sulfate from barium chloride and potassium sulfate was investigated in a semi-batch stirred tank reactor with a single feed. The particle morphology and size distributions depending on feeding policy, i.e. feeding sequence and feed rate, as well as the level of supersaturation and barium to sulfate ion ratio were determined experimentally. The particle size distribution (PSD) was simulated using a one-dimensional population balance equation model. Although precipitation of barium sulfate is well studied in literature, an explicit investigation of the dependence of morphology on semi-batch feeding policy is still lacking. To monitor the particle morphologies scanning electron microscopy (SEM) images were taken. A strong dependency on the feeding sequence was observed, giving different particle morphologies at the same supersaturation level. Also the feed rate had a strong influence for otherwise the same experimental conditions, giving dendritic particle shapes for high feed rates, and cuboid shaped particles for lower feed rates. In all cases, particles grow with a characteristic morphology at specific experimental conditions defined by the supersaturation level, the ion ratio and the feeding policy. Not only the morphology, but also the active growth sites are dependent on the experimental conditions the particles were precipitated in. This is interesting if dealing with seed crystals that are usually assumed to be characterized by their size only. It is shown in this thesis that locations of active growth sites of the seed crystals depend on the supersaturation, ion ratio of reactants, and feed rate during precipitation. Therefore, the properties of the seed crystals influence the morphology and hence the size of the seeded precipitated particles. Experiments also show that excess of barium or sulfate ions in the crystallizer has a strong impact on the resulting PSDs. Theoretically, this effect is not well understood, as most kinetic models in literature are valid only for stoichiometric conditions. Thus, the influence of detailed, thermodynamically well formulated activity coefficient models on the PSDs in a one-dimensional population balance model for the semi-batch stirred tank reactor is investigated. The non-symmetry of these models with respect to excess of barium and sulfate ions is studied. It is found that the effect on the supersaturation is too weak to explain the experimental results by supersaturation dependent kinetics. It is concluded that for the conditions here it is not sufficient to use nucleation kinetics that depend on supersaturation only. Instead, the actual ratio of ions in the solution should be incorporated in the kinetic expression for the nucleation.



## **Zusammenfassung**

Es wurde die Fällung von Bariumsulfat aus Bariumchlorid und Kaliumsulfat in einem halbkontinuierlich betriebenen Rührkessel durchgeführt. Partikelmorphologien und Partikelgrößenverteilungen sowohl in Abhängigkeit von der Reihenfolge und Geschwindigkeit der Zudosierung, als auch von der Höhe der Übersättigung und dem Verhältnis Barium- / Sulfationen wurden experimentell untersucht. Die Partikelgrößenverteilungen wurden mit Hilfe eines eindimensionalen Populationsbilanzmodells simuliert.

Zur Analyse der Morphologien wurden Rasterelektronenmikroskop-Aufnahmen verwendet. Es wurde eine starke Abhängigkeit von der Dosierreihenfolge und der Dosiergeschwindigkeit der Reaktanden beobachtet. Für dasselbe Übersättigungsverhältnis stellten sich unterschiedliche Morphologien ein, je nachdem, ob Barium oder Sulfat im Überschuss vorlag. Bei schneller Zudosierung hatten die Partikel eine dendritische Form, wohingegen sich für langsames Dosieren kubische Partikel bildeten. In allen Fällen stellte sich eine für die entsprechenden experimentellen Bedingungen typische Partikelmorphologie ein, die reproduzierbar von der Übersättigung, dem Ionenverhältnis von Barium zu Sulfat und von der Dosierstrategie abhing. In dieser Arbeit wird ebenfalls gezeigt, dass das Muster der örtlichen Verteilung aktiver Wachstumsstellen vom Übersättigungsverhältnis, dem Ionenverhältnis der Reaktanden und der Dosiergeschwindigkeit abhängt. Die Eigenschaften der Saatkristalle beeinflussen daher die Morphologie und somit auch die Größe der resultierenden Partikel.

Die Partikelgrößenverteilung war unterschiedlich, je nachdem, ob während der Fällung Barium- oder Sulfationen im Überschuss im Rührkessel vorlagen. Es wurde hier daher der Einfluss eines detaillierten Modells zur Berechnung der thermodynamischen Triebkraft auf die Partikelgrößenverteilung untersucht. Die Triebkraft wird mit Hilfe der Aktivitätskoeffizienten zur Berechnung der Übersättigung dargestellt. Die bei den verwendeten Aktivitätskoeffizientenmodellen auftretende Asymmetrie in Bezug auf Barium- und Sulfationenüberschuss wurde ausgewertet. Der Einfluss dieser Asymmetrie auf die sich einstellende Partikelgrößenverteilung ist jedoch gering und kann die im Experiment beobachteten Ergebnisse daher nicht erklären. Es wurde gezeigt, dass neben der Übersättigung für die Nukleation Ansätze verwendet werden sollten, die auch das vorliegende Ionenverhältnis Barium / Sulfat in der Kinetik berücksichtigen.



## 1 Introduction and objective of this work

Precipitation of fine particles is an important production process in the chemical industries to obtain fine materials that are widely used, e.g. pharmaceuticals, catalysts, dyes and paint compounds. The product properties are strongly dependent on the properties of the particles, i.e. average size, size distribution, and morphology. Production of particles of defined size and shape requires fundamental knowledge and control methods for precipitation processes. Knowledge of the precipitation mechanisms such as nucleation, growth, and agglomeration during precipitation is also necessary. Influence of process parameters such as concentrations of reactants, supersaturation, fluid dynamics and mixing performance of the reaction device have to be determined to assure a product of well-defined properties. For this, laboratory experiments are still advised to determine the optimum operating conditions for industrial crystallizers. So far, the prediction of particle shape is extremely difficult and often not possible by mere theoretical considerations (Mersmann, 2001). There still exists a great demand in investigating resulting particle shapes in precipitation. The work deals with the precipitation of barium sulfate. The objective can be summarized in the listed three points which will be elaborated in the following:

1. To investigate the dependence of barium sulfate morphology on varying feed rates and feed sequences for a semi-batch operated stirred tank reactor at different supersaturation levels and ion ratios.
2. To show that seed crystals should not be classified in respect to their size only.
3. To investigate whether batch model kinetics from literature are sufficient to describe the observed different particle size distributions in semi-batch precipitation of barium sulfate if combined with a more sophisticated activity coefficient model approach for the driving force.

There were several experimental investigations of the precipitation phenomena and determination of nucleation and growth kinetics for barium sulfate (Angerhöfer (1994), Aoun et al. (1996, 1999), Chen et al. (1996), Gunn and Murthy (1972), Judat and Kind (2004), Kucher et al. (2006), Liu et al. (1976), Murthy (1994), Nielsen (1958, 1961, 1964), Taguchi et al. (1996), van Leeuwen (1998), Walton and Hlabse (1963), Wong et al. (2001)). Observations of non-trivial crystal forms for precipitation without additives indicate that the precipitation process can be quite complex. For some precipitation conditions, the particle shape is far from rhombohedral, which is the equilibrium form of barium sulfate (Hartmann and

Perdock (1955), Benton et al. (1993)). Instead, it is determined by growth kinetics (Nielsen, 1964).

The first aim of this work is to investigate how barium sulfate morphology depends on varying feed rates and feed sequences for a semi-batch operated stirred tank reactor at different supersaturation levels and ion ratios. To the knowledge of the author such knowledge is still missing, although precipitation of barium sulfate has been studied intensely in the literature. So far, most experimental work concentrated on the investigation of the influence of supersaturation and ion excess. Little attention was paid to the influence of the feeding time on particle morphology. Lower feed rate decreases the amount of reactant available per unit of time and thus decreases the supersaturation in comparison to quicker feeding of the same ion solution. For experiments in a stirred tank reactor, different feed rates for addition of the reactant were used by different authors without explicit consideration of the resulting supersaturation decrease. Hence, the possible influence of the feeding time on particle morphology was not considered. For their batch experiments, Aoun et al. (1999) for example mixed 10 l of each reactant in less than 3 seconds. Wong et al. (2001) added a feed of 135 ml to a tank volume of 7.5 l over a time span of 5 minutes. Some investigations were performed to observe particle forms in dependence on the feed rate for semi-batch single feed stirred tank reactors like the one used in this work, but a dedicated observation of its effect on particle morphology is lacking. Chen et al. (1996), and Phillips et al. (1999) varied the feeding time in a stirred single-feed semi-batch reactor, but these authors did not register the resulting particle form, i.e. they determined only the mean particle diameter. Judat (2003) varied the feed rate for his semi-batch Taylor-Couette reactor to some extent but only reported results on the influence on the mean particle diameter. The same is valid for Angerhöfer (1994), who used a batch stirred tank crystalliser to investigate the phenomena influencing the resulting crystal sizes. Bernard-Michel et al. (2002) varied the feed rate for their single feed strategy experiments, but their primary goal was not the identification of the dependence of particle form on process conditions. Li et al. (2007) made experiments with two different feed rates at fixed concentration conditions for their mixing chamber device, and observed multiple particle morphologies for the slower feed rate.

Concerning the feeding sequence, i.e. whether the barium- or the sulfate-containing salt solution was fed to the reactor, also only few experiments were carried out to investigate the influence on particle morphology. Wong et al. (2001) made

experiments for single-feed semi-batch precipitation using barium chloride with sodium sulfate and observed different particle morphologies for the two possible feeding sequences. Judat (2003) reported no influence on particle morphology for different feeding policies using a Taylor-Couette reactor for precipitation. Both authors observed smaller particle diameters for sulfate-containing feed. Aoun et al. (1999) observed no effect of the feeding strategy for their batch experiments.

Although there seems to be little influence of feeding sequence if the reactants are mixed rapidly, it is known that an excess of barium and sulfate ions have influence on the growth and nucleation kinetics. For the system barium chloride and potassium sulfate, Aoun et al. (1996) identified that both nucleation and crystal growth are changed (nucleation even significantly), and also differently, for ion excess of barium and sulfate. Although in a later paper, Aoun et al. softened this statement (Aoun et al., 1999), there are many references in the literature reporting different influences of barium or sulfate ion excess on the precipitation product. In general, the precipitated particles are smaller for barium excess (Schwarzer and Peukert (2002, 2004), Kucher et al. (2006), Wong et al. (2001)).

Not only the morphology, but also the active growth sites are dependent on the experimental conditions. This is important if dealing with seed crystals as they show different growth behaviour dependent on the conditions under which they were produced. Using seed crystals is usually seen as the way to produce well-defined particles, and also to study growth kinetics, since it is assumed that with seed crystals of one size the process can be started under reproducible conditions (Mersmann (2001), Liu et al. (1976), Tacuchi et al. (1996)). Hence, the second aim of this work is to show that seed crystals should not be classified in respect to their size only.

The third objective of this work is modelling and simulation of the precipitation process as mentioned above. Several kinetic models were presented in the literature for barium sulfate precipitation (Aoun et al. (1996, 1999), Nielsen (1958, 1961), Vicum et al. (2003), Angerhöfer (1994)). Aoun et al. (1999) give a summary of kinetic expressions from the literature including the experimental conditions and the mechanism and concentration ranges for growth and nucleation rates. A more recent list can also be found in the thesis of Petrova (2008). Most of the kinetic models were derived for batch operation and make no difference in driving force concerning barium or sulfate ion excess. For non-stoichiometric conditions, however,

experimental results are not predicted well by these models. Vicum et al. (2003) presumed the reason to be in the use of simplified thermodynamic models and were able to partly improve the fit of their experimental data by using the Pitzer model (Pitzer, 1973, 1991) for the calculation of the activity coefficients.

For modelling, the aim of this thesis is to investigate the influence of the activity coefficient model on the driving force if used with batch model kinetics from literature. Higher sophisticated models give non-symmetrical results in regard to the ion species in excess and thus different driving forces depending on the ion species' concentrations. It will be discussed whether such a sophisticated thermodynamic precipitation model is sufficient to describe different PSDs observed in the experiments for semi-batch precipitation of barium sulfate.

One model that includes an empirical approach to consider the non-symmetrical behavior of the  $\text{Ba}^{2+}$  -  $\text{SO}_4^{2-}$  -  $\text{Cl}^-$  -  $\text{K}^+$  - electrolyte solution with respect to different ion ratios was proposed by Aoun et al. (1996). There, the different influence of ion excess is considered empirically by fitted parameters to measured growth and nucleation rates for values of the ion ratio of barium to sulfate in the range from 0.1 to 10. It is derived for batch experiments and has to be modified to be able to be applied to semi-batch precipitation.

In Chapter 2, this thesis gives a summary of the theoretical background concerning precipitation in general and barium sulfate precipitation in detail, with a summary of the theory of the activity model approaches used. Three approaches are used for the calculation of the activity coefficient and the resulting supersaturation that will be used later to investigate the impact of the activity coefficient model on the simulated PSD results. The extended Debye-Hückel approach as used in Angerhöfer (1994) is symmetrical in regard to the barium and sulfate concentrations and is valid for ion strengths up to 0.1 mol/l. Bromley (1973) proposed a semi-empirical extension to the Debye-Hückel approach with interaction terms for differently charged ions in solution that is applicable up to an ion strength of 6 mol/l. Pitzer's approach (Pitzer, 1973, 1991) takes most short-range interionic forces like ion-pair interactions between like charged ions and ion-triplets into account. Both the Bromley and Pitzer models result in non-symmetrical activity coefficients with regard to barium and sulfate ion excess, respectively.

Chapter 3 summarises the materials used, the experimental set-up and procedures, as well as additional experiments that were performed to characterize the precipitated particles.

In Chapter 4 the experimental results are presented. Precipitation of barium sulfate is investigated concerning particle morphology and particle size distributions depending on feeding strategy, i.e. feeding sequence and feeding time in a semi-batch stirred tank reactor with one feed. The two possible feeding sequences for the semi-batch operation are applied. Morphologies resulting from seed crystal experiments are also investigated.

In Chapter 5, a one-dimensional population balance model to simulate the particle size distribution as a function of supersaturation, ion concentration and feed flow rate is derived and the nucleation and growth kinetics used are presented.

In Chapter 6, the results of the simulations of the measured particle size distributions using the one-dimensional population balance model from Chapter 5 are discussed. First, a symmetrical model with regard to supersaturation is used with the three different activity coefficient model approaches. Then, it is shown that nucleation kinetics are strongly dependent on barium and sulfate ion excess, respectively, and suggestions for a better kinetic model are made. For the symmetric model, nucleation and growth kinetics dependent on supersaturation were taken (parameters from Bałdyga et al. (1995), Vicum et al. (2003), Wei and Garside (1997) as specified later). This kinetic model is considered to be very suitable, as they cover the whole supersaturation range. They are distinguishing between homogeneous and heterogeneous nucleation and also between integration-limited and diffusion-limited growth via a two-step growth model as presented in Chapter 5. The kinetic model from Aoun et al. (1996) is also applied in a modified form to the non-stoichiometric semi-batch experiments as one possibility to account for the dependence of the PSD on the barium or sulfate ion excess.

Chapter 7 gives a summary and conclusion of the thesis.

In the Appendix, values for the supersaturation calculated with different methods are listed. A calculation example for both Bromley and Pitzer models is given, to make the application of these models more clear.



## 2 Theoretical background

In the following, the important micro- or sub-processes of precipitation (driving force, nucleation, growth, secondary processes like agglomeration and ripening, and surface adsorption of ions) will be discussed as well as the system barium sulfate and mixing effects in a stirred tank reactor.

This chapter summarizes all important sub-processes for this thesis connected to precipitation of barium sulfate in a stirred tank reactor. The theory presented focusses on the fundamentals needed for understanding of later discussed and applied content and equations. It might ignore some phenomena that can be important for other precipitation systems, e.g. breakage of crystals was assumed to be negligible in the present work, as it was done in other works concerning barium sulfate precipitation (Angerhöfer (1994), Judat (2003), Petrova (2008), Vicum (2005)). Therefore, the author kindly asks the reader to refer also to Atkins (1996), Dirksen und Ring (1991), Mersmann (2001), Söhnel and Garside (1992), and other literature references as mentioned in the following subchapters, for a more general and detailed summary on the subject of precipitation.

The formation of a solid substance in a liquid solution initiated by a chemical reaction is called precipitation. The mixing of reactants and subsequent chemical reaction leads to the formation of a soluble component. The composition of the multi-component mixture changes spontaneously by precipitation of the component from solute to solid phase. Mass transfer from one phase to the other takes place due to a thermodynamic driving force which results from the system not being in thermodynamic equilibrium. If a solution is supersaturated, the saturation concentration of the precipitating component in the liquid is lower than the actual concentration of this component for given pressure and temperature. Precipitation occurs until the equilibrium point for the given temperature and pressure is reached. By precipitation, amorphous or crystalline products can be formed. In this thesis, precipitation by ion reaction is considered.

### 2.1 Driving force of precipitation

Generally, the driving force is the difference of Gibbs free energy  $G^E$  of a system and its corresponding equilibrium state. For the characteristic driving force for mass transfer from solute to solid state the molar affinity was defined (Söhnel and Garside, 1992):

$$\Phi = \frac{\Delta G^E}{n_i} = \mu_i - \mu_i^* \quad (1)$$

The driving force can thus be described quantitatively by the difference of the chemical potentials of the precipitating component in the supersaturated liquid  $\mu_i$  and the formed solid in equilibrium state  $\mu_i^*$ .

For many precipitation reactions like the one investigated in this thesis, ions are present from the salts in liquid solution. The chemical potential of one component  $i$  that consists of  $\nu_+$  cations and  $\nu_-$  anions is calculated by

$$\mu_i = \mu_i^0 + \bar{R}T \ln a_{\pm,i}^\nu, \quad (2)$$

with  $\mu_i^0$  being the chemical potential of the pure component  $i$  at standard pressure and temperature,  $\bar{R}$  the universal gas constant,  $T$  the temperature in Kelvin,  $a_{\pm,i}$  the mean ionic activity of component  $i$  at given pressure, temperature and composition as calculated below, and  $\nu = \nu_+ + \nu_-$  the stoichiometric coefficients of the dissociated ions.

The activity describes the deviation from the ideal solution. It can be calculated using the mean ionic activity coefficient  $\gamma_{\pm}$  and the concentrations of the ions  $c_+$  and  $c_-$  (Mersmann (2001), Judat (2003)):

$$a_{\pm,i} = \gamma_{\pm} \left( \frac{c_+^{\nu_+} c_-^{\nu_-}}{c_{ges}^\nu} \right)^{1/\nu} \quad (3)$$

Models for the calculation of the ionic activity coefficients for ionic solutions will be presented in sections 2.2.1 to 2.2.3.

As dimensionless driving force one obtains (Judat, 2003):

$$\frac{\Phi_i}{\bar{R}T} = \frac{\mu_i - \mu_i^*}{\bar{R}T} = \nu \ln \left( \frac{a_{\pm,i}}{a_{\pm,i}^*} \right) = \nu \ln S_a, \quad (4)$$

with  $a_{\pm,i}$  being the mean ionic activity of the precipitating component in the supersaturated liquid and  $a_{\pm,i}^*$  the mean ionic activity of the solution in equilibrium with the solid phase. For the assumption of low ion concentrations, i.e. density of solvent is equal to the density of the solution,  $c_{ges}^\nu = c_{ges}^{*\nu}$  is assumed in Eq. (4).

$S_a = \frac{a_{\pm,i}}{a_{\pm,i}^*}$  is the activity based supersaturation ratio.

Other quantitative representations of the precipitation driving force are the relative supersaturation  $\sigma = S - 1$  or the absolute supersaturation, calculated e.g. by the difference in concentration of the precipitating component in the liquid phase and saturation concentration for the given state. Here, the activity based supersaturation ratio  $S_a$  will be used and will be addressed as supersaturation.

According to Ostwald und Freundlich the solubility depends on the size of the crystal. The activity of the dissolved substance in equilibrium with a crystal is a function of the crystal's characteristic length by the following relation also known as the Ostwald-Freundlich equation:

$$\ln \frac{a(L)}{a(\infty)} = \frac{2k_A \gamma_s M_s}{3k_V \nu \rho_s \bar{R} T \times L}, \quad (5)$$

with  $a(L)$  and  $a(\infty)$  being the activity of the dissolved substance in equilibrium with a crystal of characteristic length  $L$  and of infinite length (i.e. plane surface), respectively,  $\gamma_s$  the interfacial tension between crystal and solution,  $M_s$  the molar mass of the precipitated particles, and  $k_V$  and  $k_A$  the volume and surface shape factor of the crystal, respectively.

From Eq. (5) follows that the activity of a solution in equilibrium increases for decreasing particle size. This dependence only has a sensible impact for particles  $< 1 \mu\text{m}$ , though (Mersmann, 2001).

The concentration based ionic strength of a salt solution can be estimated by the concentration  $c_i$  and number of charges  $z_i$  of all present ion species  $i$  by (Atkins, 1996):

$$I_c = \frac{1}{2} \sum c_i z_i^2. \quad (6)$$

For the molality based ion strength  $I_m$  the concentrations in Eq. (6) have to be replaced by the molalities  $m_i$ :

$$I_m = \frac{1}{2} \sum m_i z_i^2. \quad (7)$$

With the assumption of the density of the solution being equal to the density of the solvent, which is a valid assumption for solutions of low concentrations as used in this work, the following relation holds:

$$I_m = \frac{I_c}{\rho_{H_2O}}. \quad (8)$$

In this thesis, barium sulfate precipitated by barium chloride and potassium sulfate was the used chemical substance. Barium sulfate behaves like a weak electrolyte forming ion pairs in solution which can become quite significant for higher concentrations (Monnin, 1999) following Eq. (9):



Thus, the ionic strength is less than the theoretical value and defined by the free ions in solution. The equilibrium between free ions and ion complexes is described by:

$$c_{BaSO_4(aq)} \rho_{H_2O} K_I = c_{Ba^{2+}} c_{SO_4^{2-}} \gamma_{\pm}^2 \quad (10)$$

with  $K_I$  being the equilibrium constant and  $\log(K_I) = -2.72$  (Monnin, 1999).

The thermodynamic solubility product is defined by (Mersmann, 2001):

$$K_a = a_+^{*v_+} a_-^{*v_-}. \quad (11)$$

The concentration based solubility product  $K_c$  at equilibrium can be calculated by:

$$K_c = \frac{K_a}{\gamma_{\pm}^{*v}}. \quad (12)$$

Barium sulfate is a salt that has a very low solubility. In this case,  $\gamma_{\pm}^*$  becomes close to 1 and  $K_c = K_a$  (Mersmann, 2001). A value for the solubility product  $K_c$  at 25 °C is  $1 \times 10^{-9.96}$  (for concentration in  $\text{mol}^2 \text{l}^{-2}$ , Söhnel and Garside, 1992). Taguchi et al. (1999) determined it experimentally to  $2.88 \times 10^{-10}$  for molalities in  $\text{mol}^2 \text{kg}^{-2}$ .

The supersaturation ratio for dissociated  $Ba^{2+}$  and  $SO_4^{2-}$  ions can be calculated from Eq. (13) (Mersmann, 2001):

$$S_a = \sqrt{\frac{a_{Ba^{2+}} \cdot a_{SO_4^{2-}}}{K_a}}. \quad (13)$$

Using activity coefficients, the supersaturation can be determined by

$$S_a = \sqrt{\frac{c_{Ba^{2+}} \gamma_{Ba^{2+}} \cdot c_{SO_4^{2-}} \gamma_{SO_4^{2-}}}{K_a}} = \sqrt{\frac{c_{Ba^{2+}} c_{SO_4^{2-}}}{K_a}} \cdot \gamma_{\pm}. \quad (14)$$

The ion excess of dissolved barium ions to sulfate ions is quantified by the concentration ratio  $R$ . It is defined as follows:

$$R = \frac{c_{Ba^{2+}}}{c_{SO_4^{2-}}}. \quad (15)$$

The free ion concentrations were taken for the calculation of supersaturation and ion ratio (Eq. (13) and (15)).

## 2.2 Activity coefficient models

The general form of most electrolyte solution models for calculating the activity coefficient consist of two terms (Vicum, 2003): The first accounts for long-range ion interactions between unlike charged ions, i.e. Coulombic attraction forces. The second term accounts for short range ion interactions. These are of increased importance for higher concentrations.

One simpler equation is the Debye-Hückel limiting law for solutions of ion strengths up to  $0.01 \text{ kmol/m}^3$ , taking into account the attractive Coulomb ion interactions only (Debye and Hückel, 1923):

$$\log \gamma_{\pm} = -A \cdot |z_{Ba^{2+}} z_{SO_4^{2-}}| \cdot \sqrt{I_c}, \quad (16)$$

with  $A$  being the Debye-Hückel constant and  $z_i$  the number of charges of ion species.

In the following, three activity coefficient models will be presented that differ in complexity with regard to interionic forces considered and symmetry for barium or sulfate excess, respectively. The first approach discussed is the extended Debye-Hückel model, which is the simplest model of the three, followed by the Bromley model and the Pitzer model.

### 2.2.1 Extended Debye-Hückel approach

For infinitely diluted solutions the difference due to Coulomb forces between the real behaviour of cations and anions compared to an ideal solution can be described by the Debye-Hückel limiting law which was extended for ion strengths up to  $0.1 \text{ kmol/m}^3$  as summarized in Angerhöfer (1994):

$$\log \gamma_{\pm} = -\frac{A \cdot |z_{Ba^{2+}} z_{SO_4^{2-}}| \cdot \sqrt{I_c}}{1 + B \cdot a \cdot \sqrt{I_c}}, \quad (17)$$

with  $|z_{Ba^{2+}} z_{SO_4^{2-}}| = 4$ ,  $I_c$  calculated by Eq.(6), and  $a$  being the smallest possible centre-to-centre distance between ions:

$$a = 4.5 \times 10^{-10} \text{ m} . \quad (18)$$

At a temperature of 25°C, the parameters A and B are calculated to (Angerhöfer, 1994):

$$A = 0.0163 \left[ \frac{\text{m}^3}{\text{mol}} \right]^{1/2} , \quad (19)$$

$$B = 1.0428 \times 10^8 \left[ \frac{\text{m}}{\text{mol}} \right]^{1/2} . \quad (20)$$

The extended Debye-Hückel approach is the simplest activity coefficient model of the three discussed here. It gives a "symmetrical" result regarding barium or sulfate excess and only considers long range interionic attraction forces between barium and sulfate ions. For implementation, the extended Debye-Hückel model is also used with considered reduction of free ion concentrations by complex formation (Eq. (10)). Figure 1 shows the difference in driving force for the total amount of barium and sulfate ions in the solution if the supersaturation is calculated with activity coefficients by the extended Debye-Hückel approach with and without complex formation of barium sulfate in solution. The influence of real effects on driving force can be seen by the difference of reached supersaturation values for the same concentration ratios, which differ for higher concentrations greatly. Figure 1 also shows the lines of constant supersaturation if calculated for  $\gamma_{\pm} = 1$ , i.e. ideal solution. It has been shown that the assumption of ideal solution, i.e. neglection of the activity coefficient for calculation of supersaturation is an inappropriate assumption if dealing with precipitation of barium sulfate (Öncül et al., 2005). The reason is the difference in driving force as visualised by Figure 1. It gets more significant for higher supersaturation.

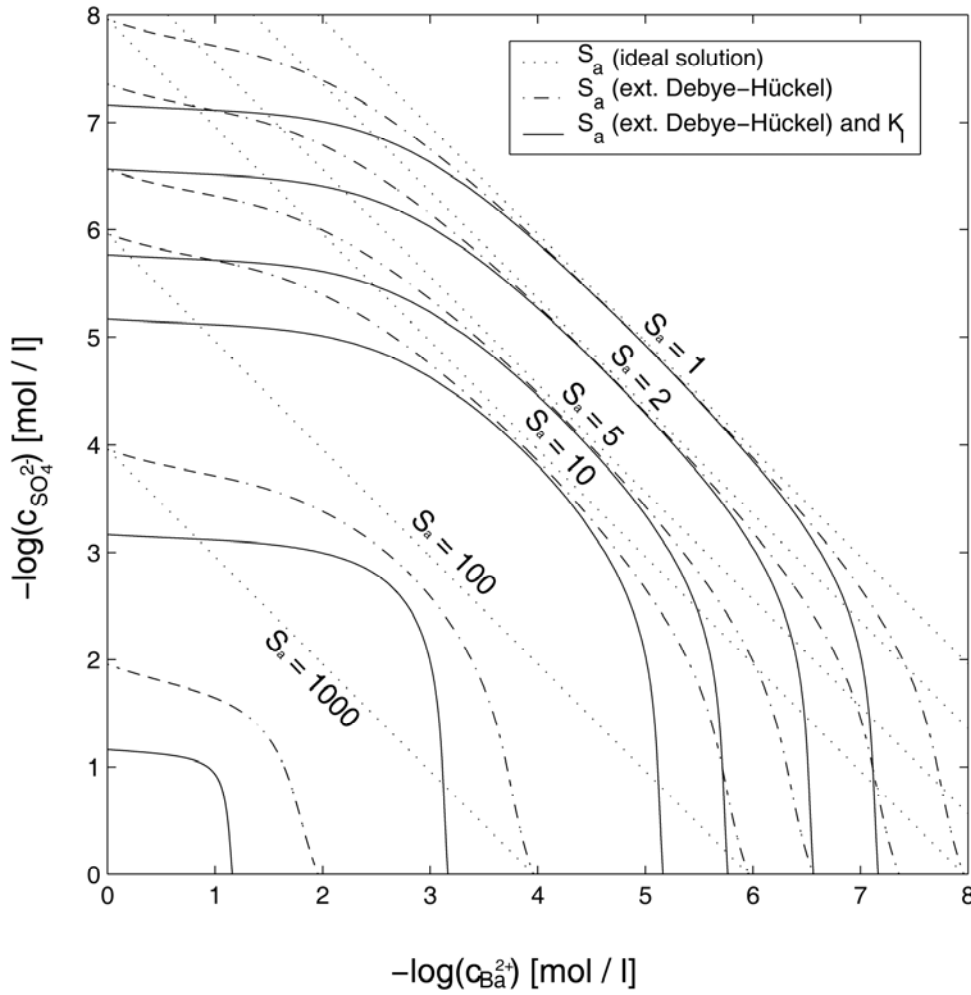


**Figure 1: Supersaturation diagram for  $\text{BaCl}_2$  and  $\text{K}_2\text{SO}_4$  in water at 25 °C, lines are for constant  $S_a$  (calculated by Eq. (14)). Dotted line: ideal solution ( $\gamma_{\text{Ba}^{2+}} = \gamma_{\text{SO}_4^{2-}} = 1$ ), dash-dotted line: calculated with extended Debye-Hückel approach (Eq. (17)), straight line: calculated with extended Debye-Hückel approach and considering only free ions in solution (Eq. (10)).**

### 2.2.2 Bromley approach

Bromley (1973) developed a multi-component version of the Debye-Hückel limiting law as a semi-empirical method for the calculation of the activity coefficients as a function of ionic strength up to 6 kmol/m<sup>3</sup>. It gives a non-symmetric activity coefficient with respect to barium or sulfate excess. Long range interionic forces between barium and sulfate ions and all counter ions present in solution are considered. Other repulsive ion interactions (between like-charged ions or ion-triplets) are not included:

$$\log \gamma_i^m = -A_m z_i^2 \frac{\sqrt{I_m}}{1 + \sqrt{I_m}} + F_i, \quad i = Ba^{2+}, SO_4^{2-}. \quad (21)$$

Luckas and Krissmann (2001) give a value of  $A_m = 0.5108 \left[ \frac{kg}{mol} \right]^{\frac{1}{2}}$  for water at 25 °C. In this work, for consistency reasons the same constant is used as in the extended Debye-Hückel model (Eq. (19)), giving:

$$A_m = A \sqrt{\rho_{H_2O}} = 0.5146 \left[ \frac{kg}{mol} \right]^{\frac{1}{2}}. \quad (22)$$

The mean activity coefficient of barium sulfate can be calculated from

$$\log \gamma_{\pm}^m = -A_m \left| z_{Ba^{2+}} z_{SO_4^{2-}} \right| \frac{\sqrt{I_m}}{1 + \sqrt{I_m}} + \frac{\left| z_{Ba^{2+}} z_{SO_4^{2-}} \right|}{\left| z_{Ba^{2+}} \right| + \left| z_{SO_4^{2-}} \right|} \left( \frac{F_{Ba^{2+}}}{\left| z_{Ba^{2+}} \right|} + \frac{F_{SO_4^{2-}}}{\left| z_{SO_4^{2-}} \right|} \right), \quad (23)$$

where the terms  $F_i$  represent the interactions between cations and anions.

For barium and sulfate ions, these can be calculated quantitatively as follows:

$$F_{SO_4^{2-}} = \sum_c B_{c,SO_4^{2-}}^* \bar{z}_{c,SO_4^{2-}}^{-2} m_c, \quad F_{Ba^{2+}} = \sum_a B_{Ba^{2+},a}^* \bar{z}_{Ba^{2+},a}^{-2} m_a, \quad (24)$$

with

$$\bar{z}_{ca} = \frac{1}{2} (|z_c| + |z_a|) \quad (25)$$

and

$$B_{ca}^* = \frac{(0.06 + 0.6B_{ca}) |z_c z_a|}{\left( 1 + \frac{1.5I_m}{|z_c z_a|} \right)^2} + B_{ca}, \quad (26)$$

where index  $c$  stands for the cations and index  $a$  for the anions in solution. For the ion solution of barium, sulfate, chloride, and potassium in water the interaction terms are as follows:

$$\begin{aligned} F_{Ba^{2+}} &= B_{Ba^{2+},SO_4^{2-}}^* \bar{z}_{Ba^{2+},SO_4^{2-}}^{-2} m_{SO_4^{2-}} + B_{Ba^{2+},Cl^-}^* \bar{z}_{Ba^{2+},Cl^-}^{-2} m_{Cl^-} \\ &= \frac{1}{\rho_{H_2O}} \left( B_{Ba^{2+},SO_4^{2-}}^* \bar{z}_{Ba^{2+},SO_4^{2-}}^{-2} c_{SO_4^{2-}} + B_{Ba^{2+},Cl^-}^* \bar{z}_{Ba^{2+},Cl^-}^{-2} c_{Cl^-} \right) \end{aligned} \quad (27)$$



$$\begin{aligned}
F_{SO_4^{2-}} &= B_{Ba^{2+}SO_4^{2-}}^* \bar{z}_{Ba^{2+}SO_4^{2-}}^{-2} m_{Ba^{2+}} + B_{K^+SO_4^{2-}}^* \bar{z}_{K^+SO_4^{2-}}^{-2} m_{K^+} \\
&= \frac{1}{\rho_{H_2O}} \left( B_{Ba^{2+}SO_4^{2-}}^* \bar{z}_{Ba^{2+}SO_4^{2-}}^{-2} c_{Ba^{2+}} + B_{K^+SO_4^{2-}}^* \bar{z}_{K^+SO_4^{2-}}^{-2} c_{K^+} \right)
\end{aligned} \quad (28)$$

For an example of the mean barium sulfate activity coefficient calculated with the Bromley model please refer to Appendix A.

### 2.2.3 Pitzer approach

By expansion of the Gibbs free energy using a virial series, Pitzer developed a widely used multi-component-electrolyte solution model for activity coefficients (Luckas and Krissmann (2001), Pitzer (1973)) which also results in non-symmetric activity coefficients with regard to barium or ion sulfate excess. In addition to the attractive Coulomb interactions, the model also includes repulsive interionic forces between like charged ions and ion-triplets:

$$\frac{G^E}{\tilde{m}_{LM} \bar{R}T} = f(I_m) + \sum_i \sum_j \lambda_{ij}(I_m) m_i m_j + \sum_i \sum_j \sum_k \mu_{ijk} m_i m_j m_k, \quad (29)$$

with  $m_i$  being the molality of component  $i$ . The first term represents an expanded Debye-Hückel term to account for the attractive forces. The other terms are for considering the repulsion. Binary pairs of species  $i$  and  $j$  are accounted by the parameters  $\lambda_{ij}(I_m)$ . Interactions between triplets of species  $i$ ,  $j$ , and  $k$  are represented by  $\mu_{ijk}$ . All contributions are related to the mass of the solvent,  $\tilde{m}_{LM}$ .

The parameters are calculated by:

$$\lambda_{ij}(I_m) = \begin{cases} B_{ij}^P(I_m) & \text{for } z_i z_j \neq |z_i z_j| \quad (\text{cation} - \text{anion}) \\ \Phi_{ij} & (c - c, a - a, \text{ion} - \text{molecule}, \text{molecule} - \text{molecule}) \end{cases} \quad (30)$$

with  $c$  for cation and  $a$  for anion,

$$\mu_{ijk} = \begin{cases} C_{ij} \sum_k m_k |z_k| & \text{for } z_i z_j \neq |z_i z_j| \\ \Psi_{ijk} & \text{otherwise} \end{cases} \quad (31)$$

The matrices of the interaction parameters  $B_{ij}^P$  and  $C_{ij}$  are symmetrical, i.e.

$$B_{ij}^P = B_{ji}^P, \quad C_{ij} = C_{ji}, \quad \text{and } B_{ii}^P = C_{ii} = 0.$$

For the functions  $f(I_m)$  and  $B_{ij}^P(I_m)$ , Pitzer identified the following correlation to fit best (Luckas and Krissmann, 2001):

$$f(I_m) = -A_\Theta(T) \frac{4I_m}{b} \ln(1 + b\sqrt{I_m}), \quad (32)$$

$$B_{ij}^P(I_m) = \beta_{ij}^{(0)} + \sum_{n=1}^q \frac{2\beta_{ij}^{(n)}}{\alpha_n^2 I_m} \left[ 1 - (1 + \alpha_n \sqrt{I_m}) \cdot \exp(-\alpha_n \sqrt{I_m}) \right], \quad (33)$$

with

$$A_\Theta = A_m \frac{\ln 10}{3}. \quad (34)$$

The parameters  $b$ ,  $q$  and  $\alpha_n$  were derived from data fitted to measured mean ion activity coefficients. For a non 2-2-electrolyte like  $\text{BaCl}_2$  and  $\text{K}_2\text{SO}_4$ , these parameters take the values:

$$b = 1.2; q = 1; \alpha_1 = 2.0. \quad (35)$$

The activity coefficients of the solute species in mixed electrolytes is defined by:

$$\ln \gamma_i^m = \frac{\partial \left( \frac{G^E}{RT} \right)}{\partial n_i} \quad (36)$$

The general equations give the activity coefficients of cation M and anion X (Pitzer, 1991):

$$\begin{aligned} \ln \gamma_M^m = & z_M^2 F + \sum_a m_a (2B_{Ma}^P + ZC_{Ma}) + \sum_c m_c \left( 2\Phi_{Mc} + \sum_a m_a \Psi_{Mca} \right) \\ & + \sum_a \sum_{<a'} m_a m_{a'} \Psi_{Maa'} + |z_M| \left[ \sum_c \sum_a m_c m_a C_{ca} + 2 \sum_n m_n \lambda_{nM} + \dots \right] \end{aligned} \quad (37)$$

$$\begin{aligned} \ln \gamma_X^m = & z_{\text{SO}_4^{2-}}^2 F + \sum_c m_c (2B_{cX}^P + ZC_{cX}) + \sum_a m_a \left( 2\Phi_{Xa} + \sum_c m_c \Psi_{cXa} \right) \\ & + \sum_c \sum_{<c'} m_c m_{c'} \Psi_{cc'X} + |z_X| \left[ \sum_c \sum_a m_c m_a C_{ca} + 2 \sum_n m_n \lambda_{nX} + \dots \right] \end{aligned} \quad (38)$$

with

$$F = f^\gamma + \sum_c \sum_a m_c m_a B_{ca}^{\prime P} + \sum_c \sum_{<c'} m_c m_{c'} \Phi'_{cc'} + \sum_a \sum_{<a'} m_a m_{a'} \Phi'_{aa'}, \quad (39)$$

with  $\Phi'$  being the ionic strength derivative of  $\Phi$ , and

$$Z = \sum_i m_i |z_i|, \quad (i = Ba^{2+}, SO_4^{2-}, K^+, Cl^-), \quad (40)$$

$$f^\gamma = -A_\Theta \left[ \frac{\sqrt{I_m}}{1 + b\sqrt{I_m}} + \frac{2}{b} \ln(1 + b\sqrt{I_m}) \right], \quad (41)$$

$$B_{ij}^{P'} = \frac{2\beta_{ij}^{(1)}}{\alpha_1^2 I_m^2} \left[ -1 + (1 + \alpha_1 \sqrt{I_m} + 0.5\alpha_1^2 I_m) \cdot \exp(-\alpha_1 \sqrt{I_m}) \right], \quad (42)$$

$$C_{ij} = \frac{C_{ij}^\ominus}{2\sqrt{|z_i z_j|}}. \quad (43)$$

In general, the mean activity coefficient can be obtained from:

$$\begin{aligned} \ln \gamma_\pm^m &= |z_M z_X| \cdot F \\ &+ (v_M/v) \sum_a m_a [2B_{Ma}^P + ZC_{Ma} + 2(v_M/v_X \Phi_{Xa})] \\ &+ (v_X/v) \sum_c m_c [2B_{cX}^P + ZC_{cX} + 2(v_M/v_X \Phi_{Mc})] \\ &+ \sum_c \sum_a m_c m_a v^{-1} [2v_M v_X C_{ca} + v_M \Psi_{Mca} + v_X \Psi_{caX}] \\ &+ \sum_c \sum_{c'} m_c m_{c'} (v_X/v) \Psi_{cc'X} + \sum_a \sum_{a'} m_a m_{a'} (v_M/v) \Psi_{Maa'} \\ &+ 2 \sum_n m_n (v_M \lambda_{nM} + v_X \lambda_{nX})/v \end{aligned} \quad (44)$$

where

$$v_M = \frac{m_M}{m_M + m_X}, \quad v_X = \frac{m_X}{m_M + m_X}, \quad (45)$$

$$v = v_X + v_M. \quad (46)$$

Eq. (44) is not to be used for weak electrolytes that form ion complexes. Instead, the mean activity coefficient has to be calculated by:

$$\gamma_\pm^m = \left[ (\gamma_{Ba^{2+}}^m)^{v_{Ba^{2+}}} (\gamma_{SO_4^{2-}}^m)^{v_{SO_4^{2-}}} \right]^{1/v_{Ba^{2+} + v_{SO_4^{2-}}}} \quad (47)$$

In practice, the interaction terms  $\Phi_{ij}$  and  $\Psi_{ijk}$  are often neglected (Luckas and Krissmann, 2001).

In this thesis, the barium sulfate was precipitated from barium chloride and potassium sulfate. Interactions between barium and sulfate ions in solution are considered by integrating the ion complex formation (Eq. (10)) into the model instead by interaction terms. For the calculation this means that all interaction terms

for these two ion species are set to zero. The consideration of complex formation is done by integrating the ion complex formation and therefore calculation of the free ion concentrations directly by Eq. (10) (Felmy et al. (1990), Monnin (1999)).

Thus, for the ion solution of barium, sulfate, chloride, and potassium in water the equations for the activity coefficients of barium, sulfate, and the mean activity coefficient are:

$$\begin{aligned} \ln \gamma_{Ba^{2+}}^m &= z_{Ba^{2+}}^2 F + m_{Cl^-} \left( 2B_{Ba^{2+}, Cl^-}^P + Z \cdot C_{Ba^{2+}, Cl^-} \right) \\ &+ \left| z_{Ba^{2+}} \right| \left( m_{K^+} m_{SO_4^{2-}} C_{K^+, SO_4^{2-}} + m_{K^+} m_{Cl^-} C_{K^+, Cl^-} + m_{Ba^{2+}} m_{Cl^-} C_{Ba^{2+}, Cl^-} \right) \end{aligned} \quad (48)$$

$$\begin{aligned} \ln \gamma_{SO_4^{2-}}^m &= z_{SO_4^{2-}}^2 F + m_{K^+} \left( 2B_{K^+, SO_4^{2-}}^P + Z \cdot C_{K^+, SO_4^{2-}} \right) \\ &+ \left| z_{SO_4^{2-}} \right| \left( m_{K^+} m_{SO_4^{2-}} C_{K^+, SO_4^{2-}} + m_{K^+} m_{Cl^-} C_{K^+, Cl^-} + m_{Ba^{2+}} m_{Cl^-} C_{Ba^{2+}, Cl^-} \right) \end{aligned} \quad (49)$$

$$\gamma_{\pm}^m = \sqrt{\gamma_{Ba^{2+}}^m \gamma_{SO_4^{2-}}^m}, \quad (50)$$

$$F = f^\gamma + m_{K^+} m_{SO_4^{2-}} B_{K^+, SO_4^{2-}}^{1P} + m_{K^+} m_{Cl^-} B_{K^+, Cl^-}^{1P} + m_{Ba^{2+}} m_{Cl^-} B_{Ba^{2+}, Cl^-}^{1P}, \quad (51)$$

$$Z = m_{Ba^{2+}} \left| z_{Ba^{2+}} \right| + m_{SO_4^{2-}} \left| z_{SO_4^{2-}} \right| + m_{K^+} \left| z_{K^+} \right| + m_{Cl^-} \left| z_{Cl^-} \right|, \quad (52)$$

$$B_{ij}^P = \beta_{ij}^{(0)} + \frac{2\beta_{ij}^{(1)}}{\alpha_1^2 I_m} \left[ 1 - \left( 1 + \alpha_1 \sqrt{I_m} \right) \cdot \exp\left( -\alpha_1 \sqrt{I_m} \right) \right], \quad (53)$$

with  $ij = (Ba^{2+}, Cl^-), (K^+, Cl^-), (K^+, SO_4^{2-})$  for Eq. (53) and also (42).

For an example of the mean barium sulfate activity coefficient calculated with the Pitzer model please refer to the Appendix A.

Figure 2 shows lines of constant supersaturation for the three activity coefficient models. The differences between the model predictions are most pronounced at high supersaturation and high ion excess. Especially one should note that the lines of constant supersaturation are no longer symmetric for the case of the Bromley or Pitzer model. For lower supersaturation and stoichiometric concentrations, all three models give similar results. In the figure, the ion complex formation (Eq. (10)) was considered for all three models.

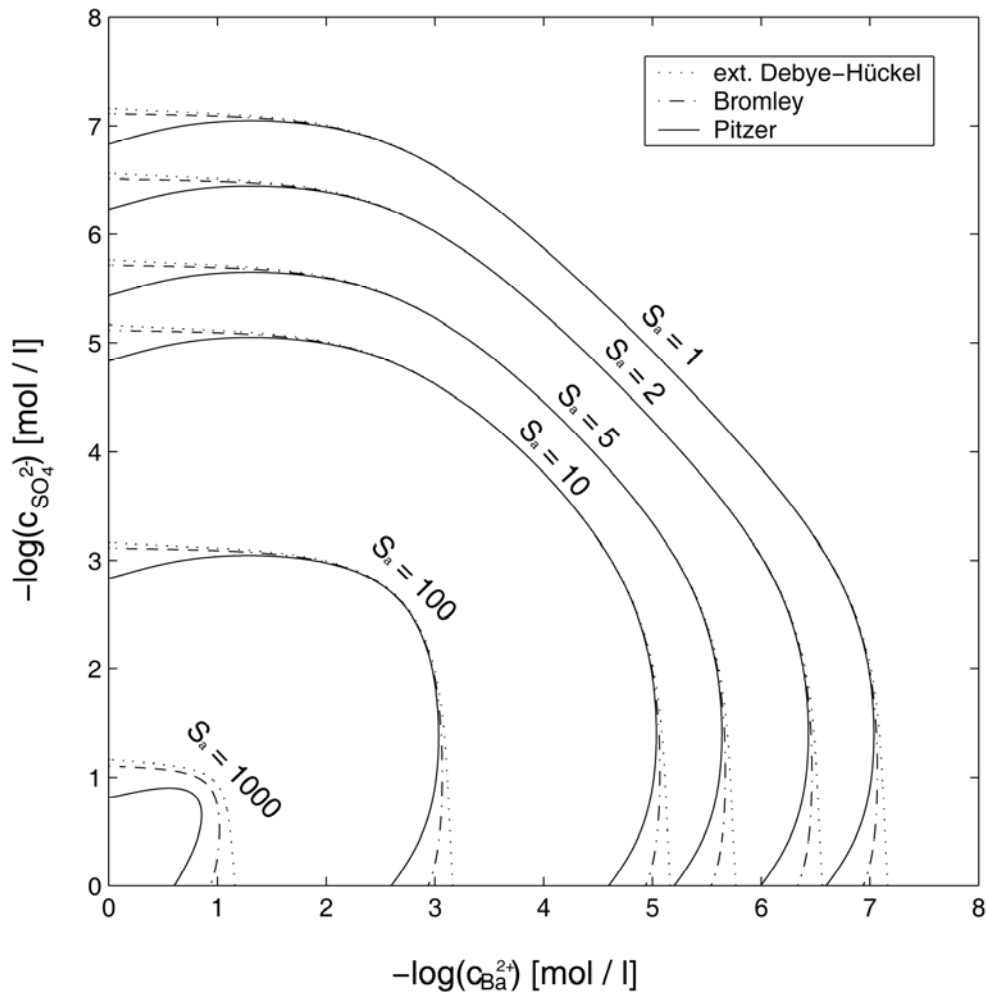


**Figure 2: Supersaturation diagram comparing the three activity coefficient models. Ion complex formation of barium and sulfate was considered for all models.**

### 2.3 Nucleation

Nucleation is the first step in the precipitation of a solute substance. Depending on the mechanisms of interface creation, the nucleation is divided into primary and secondary nucleation. Primary nucleation is the dominant nucleation mechanism for barium sulfate precipitation. Secondary nucleation is the creation of nuclei by breakage or attrition and is assumed to play a minor role here as it was done in other works concerning barium sulfate precipitation (Angerhöfer (1994), Judat (2003), Petrova (2008), Vicum (2005)).

Primary nucleation is subdivided further into homogeneous and heterogeneous nucleation. Homogeneous primary nucleation is the spontaneous formation of nuclei in the absence of other solids like seed crystals or impurities. Heterogeneous primary nucleation is called the nucleation on existing solids, often impurities (Mersmann,

2001). The two primary nucleation mechanisms will be discussed in more detail in the following.

### 2.3.1 Homogeneous nucleation

For precipitation, homogeneous nucleation is the dominant nucleation mechanism for very high supersaturation. Fast local fluctuations on the molecular length scale inside a homogeneous phase lead to the clustering of ions or molecules due to adhesive forces (Dirksen und Ring, 1991, Mersmann, 2001). The difference in total Gibbs free energy  $\Delta G^E$  of such a cluster consists of the energy  $\Delta G_V^E$  proportional to the volume of the newly created phase:

$$\Delta G_V^E = -V \frac{\rho_s}{M_s} \Phi, \quad (54)$$

with  $V$ ,  $\rho_s$ , and  $M_s$  being the volume, density, and mole mass of a cluster, respectively, and  $\Phi$  the molar affinity (Eq. (1)), as well as the energy  $\Delta G_A^E$  which is needed to create the new solid surface:

$$\Delta G_A^E = A\gamma_s, \quad (55)$$

with  $A$  being the surface of the cluster, and  $\gamma_s$  the interfacial tension.

$\Delta G_V^E$  is released by the formation of the new phase and therefore negative. It is proportional to the volume of the cluster and thus to  $L^3$  with  $L$  being the cluster size.  $\Delta G_A^E$  is added to the cluster and is therefore positive. It is proportional to the cluster surface and thus to  $L^2$ .

If plotted over the nuclei size, the total change of Gibbs free energy of nucleation

$$\Delta G^E = -V \frac{\rho_s}{M_s} \Phi + A\gamma_s \quad (56)$$

therefore goes through a maximum where

$$\frac{\partial \Delta G^E}{\partial L} = 0. \quad (57)$$

At this point, the total enthalpy does not change for removing or adding cluster units. It defines the smallest thermodynamically stable nucleus of size  $L^*$  which can be derived from the last two equations with the assumption of a spherical nucleus to:

$$L^* = \frac{2M_s\gamma_s}{\rho_s v \bar{R} T \ln S_a}. \quad (58)$$

The critical nucleus size  $L^*$  is dependent on the supersaturation conditions in the solution. For higher supersaturation the critical nuclei size decreases, i.e. smaller nuclei are stable than for lower supersaturation.

If one more unit is added to clusters of critical size  $L^*$ , the cluster becomes a thermodynamic stable nucleus. Nuclei of smaller size than  $L^*$  are instable and dissolve.

The number of nuclei growing bigger than the critical size  $L^*$  can be taken to calculate the rate of homogeneous nucleation  $r_N$  (Mersmann, 2001):

$$r_N = kn_c Z, \quad (59)$$

with  $k$  being the rate of stable nuclei formation,  $n_c$  being the number concentration of critical clusters, and  $Z$  the imbalance factor that relates the number of critical nuclei of the equilibrium state to the stationary state. The nucleation theory assumes that the clusters formed by stochastic collisions of ions or molecules can be described by a Boltzmann distribution. It is also assumed that the nucleating system consists of one component, and that the small clusters have bulk properties. For multicomponent systems, the approach has to be extended to consider the effect of the different components' diffusivities and integration into the solid phase on the nucleation rate (Mersmann, 2001).

In practice empirical approaches for the homogeneous nucleation rate proportional to the supersaturation like the following are often used (Judat, 2003):

$$r_N = k_n (S_a - 1)^m, \quad (60)$$

with  $k_n$  being the rate constant and  $m$  the kinetic exponential factor. Another empirical nucleation rate approach is used in this thesis (Eqs. (126) and (132), Vicum et al., 2003) of the form

$$r_N = k_n \exp\left(\frac{-A}{\ln^B S_a}\right), \quad (61)$$

with  $A, B$  being empirical rate constants.

Like most empiric laws, the approaches' area of application is highly dependent on the experimental conditions and system used for parameter fitting.

The delay time until the homogeneous nucleation conditions reach the steady state nucleation rate is called induction time. For high supersaturation, the "steady-state nucleation" is established rather quickly. For ionic solutions it is in the order of  $\mu\text{s}$  (Dirksen und Ring, 1991).

### 2.3.2 Heterogeneous nucleation

Solid particles are often present in reality, since it is impossible to completely purify a liquid from all impurities. Even in bidistilled water, solid matter with an approx. surface of  $2.5 \times 10^3 \text{ m}^2$  can be found in one cubic metre (Schubert and Mersmann, 1996). For heterogeneous nucleation the energy needed for nucleation is significantly reduced by the presence of solid impurities in the solution such that on their surface nuclei of the precipitate are formed. Also surface area of walls and baffles in the tank can lead to heterogeneous nucleation.

The free energy needed for nucleation is reduced if compared to the homogeneous nucleation rate (Mersmann, 2001):

$$\Delta G_{het}^E = f \Delta G_{hom}^E, \quad (62)$$

with  $f$  being a correction factor between 0 and 1. It depends on the contact angle between solution, nuclei and foreign particle. The contact angle is dependent on the interfacial tension between solution, nuclei and foreign particle (Judat, 2003). At a contact angle of  $180^\circ$ ,  $f$  is equal to one which means no wetting of the surface and therefore homogeneous nucleation behaviour. For  $f \rightarrow 0$ , i.e. contact angle going to  $0^\circ$ , nucleation work is zero.

The heterogeneous nucleation rate increases proportionally to the surface area of the foreign particles. For precipitation, it is the dominant nucleation mechanism at low supersaturation (Mersmann, 2001). A rate law can be derived similar to the one for homogeneous nucleation, additionally depending on the volumetric surface of the foreign particles, the adsorption constant, the contact angle, and the surface diffusion coefficient (Mersmann, 2001).

For heterogeneous nucleation kinetics, often the same empirical approach as for homogeneous nucleation is used, but both rate constant and exponential factor are significantly different for homogeneous and heterogeneous nucleation.

## 2.4 Growth

The growth of the particles is with the nucleation a primary process in precipitation (in relation to the secondary processes summarised in Chapter 2.7). The growth rate is dependent on the concentration of the dissolved precipitate and the total surface of the growing particles. The main effects are the motion of growth units to the particle surface and their integration into it.



Growth mechanisms can be molecular, or it can be by self-assembled aggregation with recrystallisation of small growth units (Dirksen und Ring (1991), Judat and Kind (2004)). The two growth mechanisms will be presented in the following.

#### 2.4.1 Molecular growth

Growth units in molecular growth are molecules, atoms or ions. In solution, growth units are ions surrounded by solvent ions or molecules in a coordination shell. The growth unit first diffuses from the supersaturated bulk liquid to the surface. Then it is adsorbed, diffuses along the surface until it either dissolves again, or gets finally integrated into the solid surface. This takes place at the energetically most preferable surface sites (Dirksen und Ring, 1991). Integration of a growth unit on a smooth surface is energetically less stable compared to the case where the ion has more than one bonding neighbour. Therefore, it preferably occurs on sites where the ions can be integrated more strongly into the crystal lattice, i.e. on step sites or, even more preferably, on kink sites where there are three neighbouring lattice ions, as shown in Figure 3. For adsorption and integration into the particle surface, the solvent molecules have to be released (Dirksen und Ring, 1991).

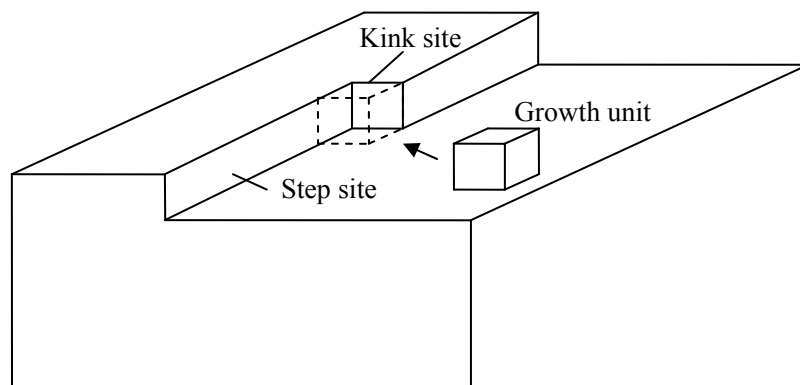


**Figure 3: Integration of a growth unit at a kink site.**

For the general growth model it is usually divided into the diffusion of growth units to the surface and the integration into it, with the supersaturation or  $\Delta c$  as the driving force (Mersmann, 2001). Depending on which of the subsequent growth steps diffusion or integration is slower and therefore rate determining, molecular growth can be either diffusion limited or integration limited. The total concentration difference  $\Delta c$  is divided into two gradients of the two growth steps, with  $c_{int}$  being the concentration at the interface between the diffusion layer and the adsorption

layer. The mass flux density  $\dot{m}$  to the crystal surface is therefore always determined by the two serial fluxes:

$$\dot{m} = k_D(c - c_{int}) = k_R(c_{int} - c^*)^r, \quad (63)$$

with  $k_D$  being the mass transport coefficient,  $k_R$  the integration rate, and  $r$  the integration order.

Instead of the mass flux density the crystal growth can be described by the overall growth rate  $G$ , defined as the change over time of a characteristic particle length  $L$ , as it will be used in this work:

$$G = \frac{dL}{dt}. \quad (64)$$

Figure 4 shows the idealized concentration gradient from the continuous solution to the crystal surface for the two limiting cases. For diffusion limitation,  $\Delta c \approx c - c_{int}$ . Growth is completely controlled by the transport of growth units to the surface. For integration limitation,  $\Delta c \approx c_{int} - c^*$ . Growth occurs at the energetically most favourable sites by surface nucleation or screw dislocation events, as will be discussed in the following subchapters.

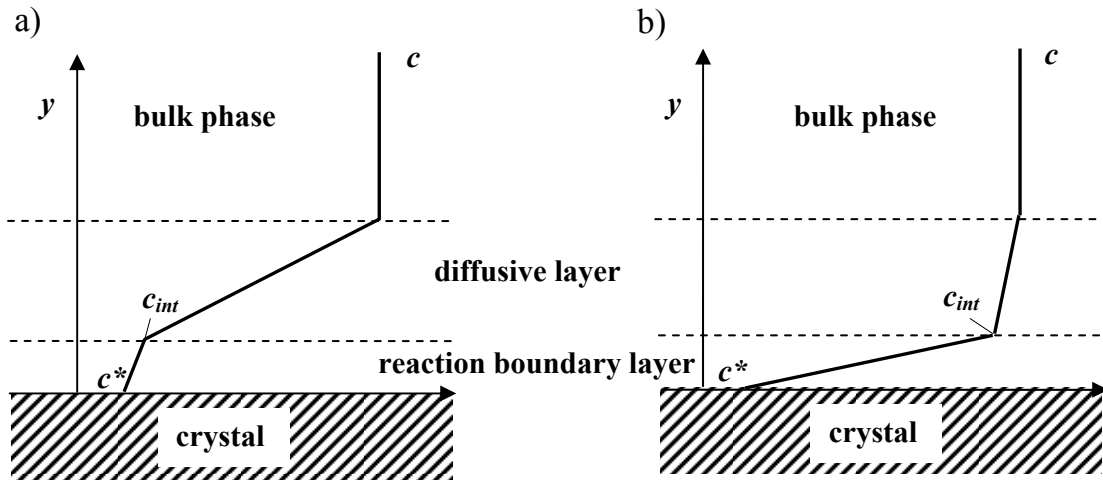
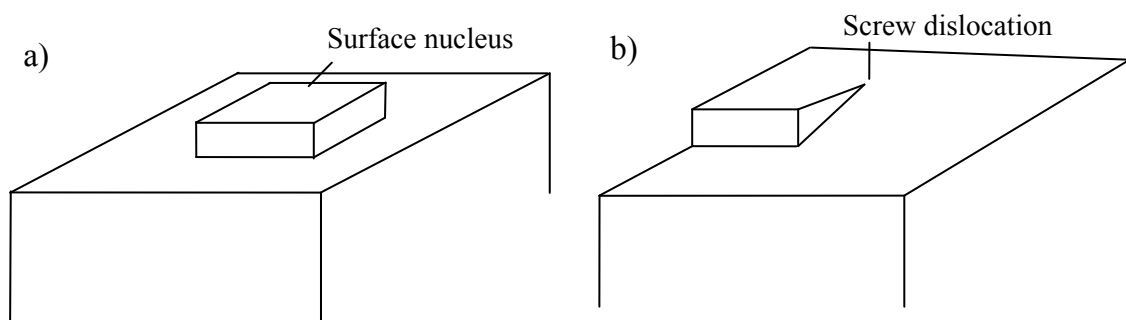


**Figure 4: Concentration differences for diffusion limited (a) or integration limited growth (b).**

#### *Growth by surface nucleation*

On a smooth surface the first growth site is created by surface nucleation, as shown in Figure 5a. This addition of the first atom to the surface is the rate-limiting step for growth on a smooth surface, while addition to this layer needs less energy and happens quickly in comparison. Depending on the average time needed for the

surface nucleation event to take place in comparison to the average time necessary to grow a two-dimensional layer over the whole surface, growth by surface nucleation can be mononuclear or polynuclear. For mononuclear growth, the surface nucleation time scale is less than the time needed for one surface nucleus to grow to a whole layer on the surface, as it is the case for low supersaturation. At higher supersaturations, the surface nucleation event happens faster and several surface nuclei grow at the same time, leading to polynuclear growth. The regime change from mononuclear to polynuclear growth is reached if the time between two surface nucleation events is approx. 60% of the time needed to complete the entire layer



(Dirksen und Ring, 1991).

**Figure 5: Growth sites for molecular growth. a) by surface nucleation; b) by screw dislocation.**

#### *Screw dislocation growth*

In reality, most surfaces are not ideally smooth but have dislocations where growth can occur. These dislocations serve as starting points for screw dislocation growth, where growth happens in a spiral pattern that operates as a continuous source of step and kink sites (Figure 5b). Screw dislocation occurs for all levels of supersaturation. It is the sole explanation of growing crystals if the supersaturation is too low for surface nucleation events.

#### *Diffusion limited growth*

The change from diffusion limited to integration limited growth can be considered as a continuous transition that happens in a certain supersaturation window. At low supersaturation, the only possible integration sites are imperfections such as screw dislocations. At increasing supersaturation, the energy needed for surface nucleation decreases. The formation of surface nuclei from adsorbed growth units creates new sources of integration sites. At further increasing supersaturation, the growth of a

whole layer from one surface nucleus is much slower than the new surface nucleation events. Numerous energetically favourable growth sites are formed that continuously roughen the surface. The polynuclear growth for higher supersaturation can become so fast that dendritic arms can be formed by new nuclei growing on an already existing nucleus on the particle surface (Dirksen and Ring (1991), Mersmann (2001), ref. also to Chapter 2.8).

The generation of higher number of integration sites at high supersaturation is one of the reasons why the growth rate increases exponentially with supersaturation. The rough surface provides enough favourable sites for approaching growth units, so that the growth rate at high supersaturation becomes limited by the diffusion of the growth units from the liquid bulk phase to the particle surface (Dirksen and Ring (1991), Mersmann (2001)).

#### *2.4.2 Aggregational growth*

In aggregation, primary particles are bonded by solid bridges to larger aggregates with smaller specific surface. If this phenomenon occurs, it has a significant influence on the resulting particle size distribution. Aggregation is enhanced by low surface potentials as the small growth units will minimize their specific surface area, which is equivalent to minimization of the Gibbs free energy (Dirksen and Ring, 1991). In aggregation, the growth units are larger than that of an atom, molecule or ion. For barium sulfate, self-assembled aggregation, i.e. aggregation in an “ordered manner” due to specific interaction of particle surfaces was described by Angerhöfer (1994). Judat and Kind (2004) also consider it as one explanation for their aggregation growth model. Judat and Kind (2004) formulated a growth model for barium sulfate by aggregation in a highly ordered manner of growth units at the initial growth stages of nano-scale size and formation of a crystal through recrystallisation. Based on this model, they explained the porous structure of their barium sulfate crystals. These sponge-like structures in precipitated barium sulfate were observed beforehand by Petres et al. (1969), who concluded that molecular growth cannot be the only growth mechanism in barium sulfate precipitation without giving proof. At high supersaturation, Judat and Kind assumed that growth through self-assembled aggregation might be dominant due to the high availability of supersaturated substance to grow crystalline bonds between the former primary particles. For lower supersaturation, molecular growth might play the main role. Since experiments with lower supersaturation are modelled in this thesis, aggregational growth is assumed to

play a minor role. It is not explicitly considered in the growth law kinetics but included into the empirical growth law used.

### 2.4.3 Growth kinetics

The growth rate generally can be described by the following approach:

$$G = k_g f(S_a) \quad (65)$$

with  $k_g$  being the proportionality constant and  $S_a$  the supersaturation (Judat, 2003).

For molecular growth, different growth laws for the growth models described above have been derived as summarised in Table 1. For mono- and polynuclear growth, the growth rate contains an exponential factor (Dirksen and Ring (1991), Mersmann (2001), Nielsen and Toft (1984), Walton (1967)): For screw dislocation growth, it is proportional to  $(S_a - 1)^2$ , and for diffusion controlled growth, the proportionality is linear.

**Table 1: The function  $f(S_a)$  for the different growth mechanisms (Dirksen and Ring (1991), Nielsen and Toft (1984))**

Growth mechanism	$f(S_a)$
mononuclear	$\exp(K_e / \ln S_a)$
polynuclear	$S_a^{7/6} (S_a - 1)^{2/3} (\ln S_a)^{1/6} \exp(K_e / \ln S_a)$
screw dislocation	$(S_a - 1)^2$
diffusion controlled	$(S_a - 1)$

The overall growth rate can be calculated by a combination of the different mechanisms. The two-step model combines the transport and integration growth mechanisms using a parabolic law for the integration step. If more than one component is needed for the crystal structure, each component has its own diffusive transport behaviour and an own flux equation that has to be related to the crystal stoichiometry for each component (Dirksen and Ring, 1991). In this thesis there are two substances ( $Ba^{2+}$  and  $SO_4^{2-}$ ). The two-step growth law is therefore:

$$G = k_r (S_{a,int} - 1)^2 = k_{D,Ba^{2+}} (c_{Ba^{2+}} - c_{Ba^{2+},int}) = k_{D,SO_4^{2-}} (c_{SO_4^{2-}} - c_{SO_4^{2-},int}). \quad (66)$$

## 2.5 Surface adsorption of ions

In an electrolyte solution, the surface of a colloid particle is electrically charged. There are three mechanisms due to which charging of the colloidal surface can occur (Mersmann, 2001):

1. Dissociation of ions and ion groups from the surface into the bulk electrolyte solution.
2. Adsorption of ions of the bulk electrolyte solution on the surface.
3. Crystal lattice defects, e.g. by replacement of lattice ions with ions of opposite charge.

Often the cations are dissociated from the surface and transferred to the bulk electrolyte solution, resulting in a negative surface charge of the particle (Shaw, 1999). Counter ions are attracted to the surface and an ion layer of higher concentrations of ions than in the bulk is formed around the particle surface, called the electrical double layer. The two kinds of ions that get adsorbed directly onto the crystal lattice can be assumed to be lattice ions and hydronium and hydroxide ions (Eble, 2000).

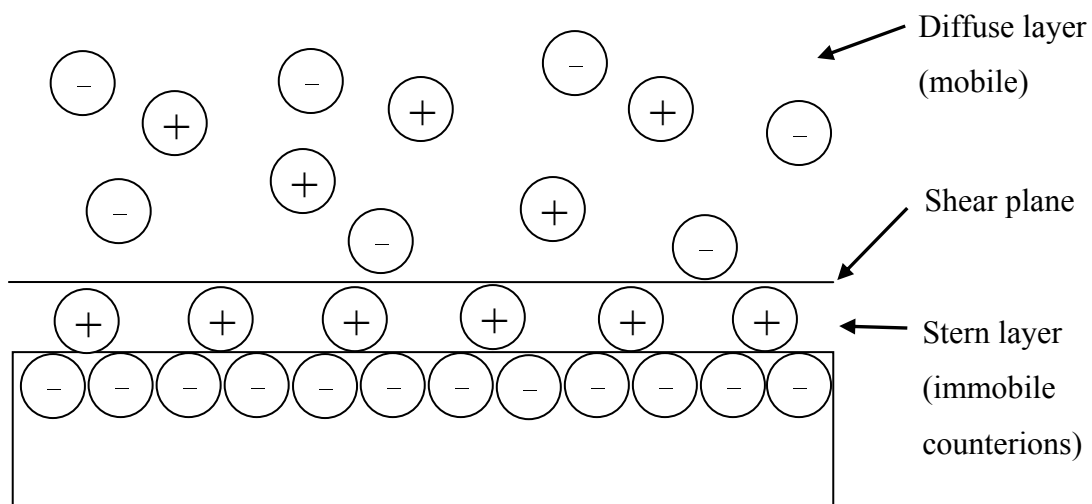


**Figure 6: Principle of the electrical double layer at the particle surface (from Myers, 1999).**

A more detailed model for the electrical double layer is shown in Figure 6 (Myers, 1999). Here, the double layer consists of two parallel layers of ions. The first is formed by ions that attach directly to the charged particle surface forming a fixed layer on the surface, the Stern plane. The second layer consists of free ions in the fluid under the influence of electrical attraction, forming the diffuse layer whose concentration decreases exponentially with distance from the particle surface to the bulk average concentration. The extent of the diffuse layer depends on the electrolyte concentration of the solution. Increasing the ion strength of the solution reduces the range of the repulsive forces of the charged surface.

If a charged particle and an electrolyte solution move relatively to each other, the diffuse ions of the electrical double layer up to approximately the Stern layer will move, the dividing line between moving ions and surface called the shear plane (Myers, 1999). The difference in potential from shear plane to bulk solution is called the  $\zeta$  (zeta) or electrokinetic potential. It can be determined by the movement of the mobile ions under the influence of tangential stress, e.g. by application of an electrical field to the suspension, and is a measure for the electrokinetic behaviour and also of the stability of the colloids in suspension. The surface charge of the particles formed by the double layer act as electrostatic repulsive force in the DLVO theory that describes the stability of particle suspensions by the two dominant acting forces, the attractive force being the Van der Waals forces between the particles (Mersmann, 2001).

For barium sulfate it is known that barium ions preferably adsorb on the barium sulfate particle surface, forming a positive charge (Buchanan and Heyman (1948), Eble (2000), Schwarzer and Peukert (2004)). The amount and charge of attached ions on the particle surface is dependent on supersaturation  $S_a$  and ion ratio  $R$ .

## 2.6 Agglomeration

Agglomeration in precipitation is the collision and following adherence of particles. The term is generally used for a non-permanent connection caused by particle-particle interaction forces like the Van der Waals force which can be separated by redispersion. Depending on the mechanism that influences the collision frequency, agglomeration is called perikinetic agglomeration which is mainly caused by diffusion of the particles by Brownian motion, and orthokinetic where the particles collide due to hydrodynamic motions caused by field forces such as convection or sedimentation (Mersmann, 2001).

The agglomeration rate is influenced by the colloid stability factor and also the number density of particles (Dirksen and Ring, 1991). The agglomeration kinetics can be described by the collision frequency of particles and the effectiveness of the collision, both determining the success of the agglomeration. The stability of the agglomerate is determined by the stress it is exposed to, and the reversibility and strength of the bonding forces (Eble, 2000).

In systems at high supersaturation with mainly homogeneous nucleation and high particle concentration the collision frequency increases. In this case, agglomeration

can be of high importance and significantly influence the particle size and size distributions.

For systems with particle concentrations less than  $10^7$  particles per ml, agglomeration generally plays a minor role. Secondary growth by agglomeration is therefore unlikely for precipitation with mainly heterogeneous nucleation mechanism (Walton, 1967).

In this thesis, agglomeration was only observed to happen in the higher supersaturation experiments (Chapter 4.1.1). For the experiments at lower supersaturation, agglomeration was not observed. This was also reported from other works dealing with barium sulfate precipitation (Angerhöfer (1994), Aoun et al. (1996), Bałdyga et al. (1995), Bałdyga and Orciuch (2001), Dirksen and Ring (1991), Kucher et al. (2006), Walton (1967)).

## 2.7 Secondary processes

Secondary processes happen after the supersaturation is depleted and the main precipitation mechanisms, mainly nucleation and growth, ceased. They are also called aging and their timescale is of magnitudes higher than for precipitation (Söhnel and Garside, 1992). The ones discussed here are Ostwald Ripening and recrystallization for particles that remain in the solution.

### 2.7.1 Ostwald Ripening

Ostwald ripening describes the growth of bigger particles on the expense of smaller ones in a colloid population in contact with the mother liquor (Mersmann (2001), Söhnel and Garside (1992)). Similar to the vapour pressure of liquid droplets, smaller particles have a higher solubility due to the higher surface curvature and dissolve, whereas bigger particles grow because of the now available dissolved product. The Ostwald-Freundlich equation (Eq. (5)) describes solubility's size-dependence for crystals of a characteristic length. The result is a shift to bigger particle sizes and also to narrower particle size distributions.

One reason for this is the system's attempt to minimize the Gibb's energy to reach the state of thermodynamic equilibrium. The total Gibb's free energy can be calculated by:

$$G = -ST + Vp + \sum \mu_j n_j + \gamma_s A. \quad (67)$$

with A being the total surface area of the solid phase.



For constant pressure, temperature, and composition, the Gibbs energy can only be reduced by reduction of the surface area. Thus, by dissolution of the smaller particles and the growth of the bigger ones, the system reduces the overall specific surface of the solid phase.

### 2.7.2 *Recrystallization*

To minimize the Gibbs free energy of the system, metastable crystals having a kinetically controlled morphology dissolve and recrystallize into more stable polymorphs (Mersmann (2001), Söhnle and Garside (1992)). This also includes the transformation of dendrites, platelets, and needles into energetically more favorable, more isomorphic crystals.

## 2.8 Particle shape and dendritic growth

Please note that throughout this work, the term “morphology” is used for the different metastable particle shapes of barium sulfate that are formed in the precipitation experiments especially under conditions of fast growth at high supersaturations.

The shape of a crystal can be influenced by different growth rates of crystal faces, some of which can be reduced by adsorbed impurities, solvent ions or other additives (Mersmann, 2001). There can be very great differences in growth rates for different faces. Fast-growing faces tend to disappear after some period of time. The largest faces of a crystal are in general the slowest growing. Crystal shapes can also be influenced by agglomeration, a phenomenon already discussed in Chapter 2.6.

Crystal shape can be either thermodynamically or kinetically controlled (Dirksen and Ring, 1991). It is therefore not only influenced by its internal structure, but also by the environment in which it grows (Cardew (1985), Mersmann (2001), Winn and Doherty (2000)). For crystals grown at very low supersaturation ratios, the thermodynamic control of a crystal shape is important. At increasing supersaturation, the shape of a crystal is kinetically driven forming metastable particle shapes. In all cases, each face always moves parallel to its original position (Mersmann, 2001).

### 2.8.1 *Equilibrium shape*

The shape of a crystal reveals the underlying atomic structure (Cardew, 1985). Gibbs formulated the theory that in its equilibrium shape the crystal's surface free energy will have its minimum value (Dirksen and Ring, 1991). By correlating the growth

rate of a crystal face to its surface energy, Wulff derived an explanation that considers the observation that the high surface energy surfaces have the smallest surface area (Dirksen and Ring (1991), Mersmann (2001)). He also stated that for a crystal of fixed weight, the lowest free energy of the crystal can only correspond to one shape. In his theory, the ratio of the distance from a face to the specific surface energies determines the equilibrium crystal shape, i.e. if the surface tension is low a face is developed to a higher degree. The high energy face disappears for some growth process, because it grows faster (Walton, 1967). Figure 7 shows a two-dimensional example of a crystal with different face growth rates. It can be seen how the crystal habit changes over time. For all intermediate shapes shown in Figure 7, the direction of the normals on the faces remain constant as well as the angles between the faces (Mersmann, 2001). The faces with the lowest growth rate determine the final crystal shape. In general, low-index faces grow slower than high-index faces. The three fundamental types of crystal habit can be explained by this growth behaviour, namely planar, isometric, and needlelike or prismatic (Mersmann, 2001).

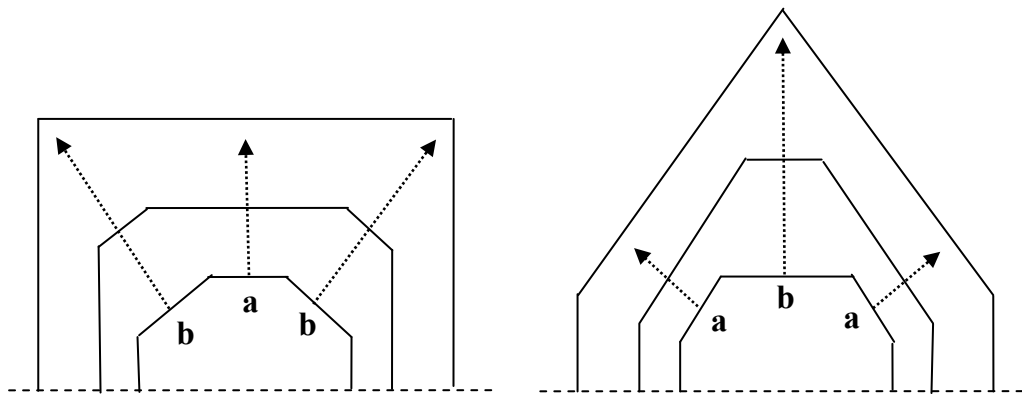


**Figure 7: Development of crystal habit over time for different face growth rates. a: slow-growing faces, b: fast-growing faces (Mersmann, 2001).**

### 2.8.2 Kinetically controlled shape

For increasing thermodynamic driving force, the shape of the precipitated particles is determined by kinetics and differs from the equilibrium habit. Metastable particle shapes are formed which can transform into more stable ones through aging (Eble, 2000; ref. also to Chapter 2.7.2).

The following reasons lead to the formation of kinetically controlled crystal shapes:

1. The face growth rates depend on supersaturation and ion concentrations and can change depending on it, resulting in different crystal shapes at different

supersaturation levels as different face growth rates get rate determining (Dirksen and Ring (1991), Walton (1967)).

2. Impurities, counter ions, and solvent molecules or ions adsorb on a crystal face and will stabilize that face, lowering the face's interfacial energy and thus reduce or block the growth of that face (Walton, 1967).
3. Inclusion of solvent ions, additives, or impurities upon growth can influence the crystal shape (Dirksen and Ring, 1991). For high growth rate the deviation from the equilibrium shape gets larger for higher concentrations of foreign substances in the solution.
4. The number of imperfections of the crystal lattice increases at higher supersaturations, i.e. number of kink sites increases where growth preferably occurs and excrescences can start to grow (ref. also to the following subchapter and Chapter 2.4).

Prediction of the kinetic shape is still difficult. With the existing models good results were achieved for the equilibrium shape of some substances, but the prediction of particle shapes for precipitation in solution are rather poor (Mersmann, 2001). This is because models for the equilibrium shape do not include the influence of the crystal's surroundings, thus their suitability for prediction of kinetically controlled shapes in precipitation is low (Winn and Doherty, 2000). There exist approaches to include the effect of the solution into the crystal shape modelling (Bisker-Leib and Doherty (2001), Borchert et al. (2009), Cardew (1985), Winn and Doherty (2000)). Still, modelling of kinetically driven crystal shapes is a very challenging and active research field.

### 2.8.3 *Dendritic growth*

Dendritic crystals are formed when supersaturation is still below the critical value for homogeneous nucleation but transport of growth units to the surface is rate determining (Phillips et al., 1999).

For diffusion-controlled growth, the concentration at the surface can be non-uniform. Since surface nucleation events depend strongly on supersaturation, the different concentrations will lead to different surface nucleation rates and growth rates along the particle surface. The surface gets rougher, and growth rates are now different on different parts of the surface. The corners of a face tend to grow faster than the middle probably due to the better availability of growth units from the bulk phase.

This leads to the edges growing faster, leading to the formation of dendrites (Dirksen and Ring (1991), Nielsen (1964)).

In addition to the integration sites formed by surface nucleation events, the higher growth rate due to higher supersaturation also leads to more imperfections in the crystal lattice on which new growth layers can start to grow with different orientation, leading not only to a rougher surface but also to the possible growth of star-like crystals (Angerhöfer (1994), Judat and Kind (2004)).

Adsorption of ions can also hinder certain dislocations from growing, whereas other sites grow overhangs, leading to dendritic arms growing out of the face (Judat and Kind, 2004).

## 2.9 Characteristic length and shape factor

For modelling a crystal population with a 1-D simulation model, i.e. a population balance system, the particle size distribution (PSD) is often used as the main product property. For a spherical particle, the size is the diameter. In case of an anisotropically grown crystal, no definite diameter is available and a characteristic length has to be defined.

One possibility is the use of the sphere equivalent diameter. The volume or surface of the particle is set in relation to the same volume or surface of a sphere, respectively. The volume equivalent spherical diameter is therefore:

$$x_V = \sqrt[3]{\frac{6}{\pi} V_P}, \quad (68)$$

and the surface equivalent spherical diameter

$$x_A = \sqrt{\frac{1}{\pi} A_P}, \quad (69)$$

with  $V_P$  and  $A_P$  being the particle volume and surface, respectively. The ratio of the equivalent diameters gives a possible definition for a shape factor:

$$k_{A,V} = \frac{x_A}{x_V}. \quad (70)$$

Another possibility is the use of a characteristic length of the particle, usually the longest axis, as the characteristic size  $L$ , and to relate it to the diameter  $d$  of a sphere of the same volume by the relation (Baldyga et al., 1995)

$$k_V L^3 = \frac{\pi}{6} d^3, \quad (71)$$

with  $k_V$  being the volume shape factor defined by the characteristic size of the particle by

$$k_V = \frac{V_P}{L^3}. \quad (72)$$

Analogous, the surface shape factor can be defined by the characteristic size  $L$  by

$$k_A = \frac{A_P}{L^2}. \quad (73)$$

The ratio  $\frac{k_A}{k_V}$  gives the overall shape factor.

From Eq. (71) follows for the characteristic size  $L$ :

$$L = \left( \frac{\pi}{6k_V} \right)^{1/3} d = \phi_V d, \quad (74)$$

with  $\phi_V$  being the sphericity of the particle as defined by this equation (Bałdyga et al., 1995).

The sphericity can also be defined by the ratio of the surface of a sphere of the same volume to the particle surface by (Mersmann, 2001):

$$\psi_V = \frac{(6k_V/\pi)^{2/3}}{k_A/\pi}. \quad (75)$$

Here, sphericity is close to one for isometric particles.

Other attempts to characterize particle shapes by other mathematical descriptors have been made as well (Pons et al., 1997).

For comparison of experimental and simulated results for PSDs and all information gained thereof (e.g. growth and nucleation rates) it is crucial to know which definition of shape factors and characteristic particle length was used. For precipitated particles of the same substance, differences in reported kinetic rates and values for shape factors can result of the use of different definitions for these factors. It is therefore of great importance to clearly specify the used definitions for characteristic length and shape factors for colloid populations. In this work, the volume shape factor will be used for calculations as defined by Eq. (72).

Table 2 gives some examples of shape factors and sphericity as defined by Eq. (72), (73), and (75) for common geometries (Mersmann, 2001) with the longest axis as characteristic size  $L$ .

**Table 2: Shape factors and sphericity as defined by Eq. (72), (73), and (75) (Mersmann, 2001)**

geometric shape	$k_V$	$k_A$	$\psi_V$
sphere	0.524	3.142	1.00
cube	1.000	6.000	0.81
plate $10 \times 10 \times 1$	0.100	2.4	0.43
octahedron	0.471	3.464	0.85

## 2.10 Mixing effects in a stirred tank reactor

For precipitation in this work, a stirred tank with single feed inlet was used. The mixing effects due to the flow field in the vessel define the local reactant concentrations and therefore the local supersaturations which influence the precipitation kinetics. A turbulent flow field is often aspired to chemical reactors since mass and heat transport are intensified greatly in comparison to laminar or bulk flow. The turbulent flow regime is consistent of a chaotic structure of different sized eddies (Judat, 2003). In a stirred vessel, mixing occurs on different length and time scales (van Leeuwen et al., 1996). The stirrer introduces kinematic energy on the macromixing scale by circulating the fluid, the time-scale expressed by the circulation time in the reactor. Turbulent mixing is most intense in the stirrer region where the mixing of the feed species with the bulk at the feed point by turbulent motion takes place. The energy is transferred by impulse cascades to smaller eddies. Segregated reactants are mixed in what is called mesomixing scale still larger than the Kolmogorov microscale (Vicun et al., 2003).

Micromixing describes the mixing on the scale of the smallest eddies at the transition to molecular diffusion. At a wave length  $k_K$  the energy will be dissipated into heat. The corresponding eddy size is called the Kolmogorov-eddy size  $\lambda_K$  (Judat, 2003). It can be calculated by the kinematic viscosity of the fluid and the turbulent energy dissipation rate  $\varepsilon$ :

$$\lambda_K = \left( \frac{\nu^3}{\varepsilon} \right)^{1/4}, \quad (76)$$

The Reynolds number gives a measure of the stirring intensity and is defined by

$$\text{Re} = \frac{N_{stirr} d^2}{\nu}, \quad (77)$$

with  $\nu$  being the fluid's kinematic viscosity,  $N_{stirr}$  the number of stirrer revolutions, and  $d$  the impeller diameter.

For  $\text{Re} > 10^4$ , the flow can be assumed to be turbulent. For operating a stirrer its power consumption is important. It is described by the power number  $P_N$  of the stirrer:

$$P_N = \frac{P}{\rho N_{stirr}^3 d^5}, \quad (78)$$

with  $\rho$  being the density of fluid and  $P$  the power consumption.

In the turbulent region for  $\text{Re} > 10^4$ ,  $P_N$  is nearly constant and can be approximated to four for a Rushton stirrer as it is used in this work.

The mixing times necessary for macro- and micromixing have a great influence on the product precipitated in a stirred reactor. For reaction, the reactants have to meet on a molecular level reached by micromixing. The characteristic time constant for micromixing can be estimated to (Bałdyga et al., 1995):

$$\tau_w = 12(\nu/\varepsilon)^{1/2}, \quad (79)$$

with  $\nu$  being the kinematic viscosity of the solvent and  $\varepsilon$  the local turbulent energy dissipation rate.  $\tau_w$  is of the order of tens of milliseconds (Taguchi et al., 1999). Eddies contributing most to the micromixing are created and destroyed with a frequency of  $\tau_w^{-1}$  and have a diameter of  $12\lambda_K$  (Judat, 2003).

The mean rate of energy dissipation can be estimated by (Bałdyga et al., 1995):

$$\bar{\varepsilon} = \frac{P_N N_{stirr}^3 d^5}{V}, \quad (80)$$

where  $V$  is the total stirred tank volume. For the local energy dissipation Bałdyga et al. (1995) divided the reactor into the impeller zone  $i$  being 5% of the reactor content with

$$\varepsilon_i = 15\bar{\varepsilon}, \quad (81)$$

and the bulk zone  $b$  with

$$\varepsilon_b = 0.25\bar{\varepsilon}. \quad (82)$$

The Schmidt number gives the ratio of diffusion of momentum expressed by the kinematic viscosity to the diffusion of mass in a fluid and is defined by:

$$Sc = \frac{\nu}{D_{AB}}, \quad (83)$$

with  $D_{AB}$  being the diffusion coefficient of the ion species in the fluid.

For  $Sc < 4000$ , time scale of diffusion is very small in comparison to the time scale of dissipation of microsized eddy layers, i.e. so-called engulfment is the rate determining step for micro-mixing (Bałdyga et al., 1995).

For macromixing, the characteristic time constant stands for the time that is needed to reach a final concentration field in the tank and can be taken to be equal to the circulation time in the reactor, expressed as tank volume over the circulation capacity (van Leeuwen, 1998):

$$\tau_c = \frac{V}{N_Q N_{stirr} d^3}, \quad (84)$$

with  $N_Q$  being the pumping number.

$\tau_c$  can be in the order of seconds (Taguchi et al., 1999).

The characteristic time for nucleation is in the order of  $10^{-10}$  s (Rauscher et al., 2005) and can be estimated by the inverse nucleation rate and an average crystal number concentration  $\bar{N}$  (Bałdyga et al., 1995):

$$\tau_N = \frac{\bar{N}}{r_N}. \quad (85)$$

The characteristic time constant for growth can be estimated by the following equation containing the growth rate (Bałdyga et al., 1995) and is in the order of tens of seconds (Rauscher et al., 2005):

$$\tau_G = \frac{M_s}{\rho_s G a} c_s, \quad (86)$$

where  $M_s$  is the molar mass and  $\rho_s$  the density of the particles,  $a$  the specific particle surface,  $G$  the growth rate, and  $c_s$  the concentration of solved precipitating substance.

Precipitation by ion reaction of scarcely soluble salts as discussed in this thesis happens very fast and is often assumed to be instantaneous. Comparing the characteristic time constant of the mixing and precipitation effects showed that for a precipitation reaction in a stirred tank reactor, the characteristic time for nucleation is



much smaller than for micromixing and growth, since  $\tau_N < \tau_w < \tau_G < \tau_c$  (Rauscher et al., 2005). The fast nucleation rate will lead to precipitation events occurring before the reactor content is completely mixed. This is the reason why ideal mixing cannot be assumed for precipitation in a stirred tank but concentration gradients are formed near the inlet point which influences the resulting particle size distribution. For bulk precipitation in a stirred tank reactor, mixing effects have therefore to be considered. In this work, a simple two-compartment mixing model was applied in the simulation model to account for the non-ideal mixing in the vessel as discussed in Chapter 5.3. In general, for semi-batch precipitation at high supersaturation in a stirred vessel with one feed near the impeller the mean particle diameter decreases for increasing higher number of stirrer revolutions which defines the power input (Mersmann, 2001). Söhnel and Garside (1992) summarize the general influence of feeding policy on a precipitation system as follows: For semi-batch precipitation the resulting crystals are usually larger than for batch precipitation of the same system. Usually, at lower concentrations the particles precipitated are larger than at high supersaturations. The influence of the feed rate is dependent on the particular system.

## 2.11 Barium sulfate

The crystal grid structure of barium sulfate is orthorhombic, one unit cell containing four barium and also four sulfate ions.

Figure 8 shows a unit cell with its cell dimensions. The large rhomb face was identified to be (001), with the side faces being (210) by many sources (Benton et al. (1993), Black et al. (1991), Dunn et al. (1999), Hartmann and Perdock (1955)). Takiyama (1959) analysed crystal shape of barium sulfate precipitates using an electron micro-diffraction method, but they arranged the particles to the orientation so that they grew along the (100) plane for the platelet crystals.

Barium sulfate only has one crystal modification. Nevertheless, in technical production different metastable particle shapes are formed due to the influence of the kinetics of the precipitation reaction, leading to different kinetically controlled particle forms by reasons already mentioned in Chapter 2.8. Theoretically, the crystals should transform into their thermodynamic most stable form by recrystallization. For barium sulfate this process is very slow, though. Even in geological findings there were metastable morphologies present (Archibald et al, 1997).

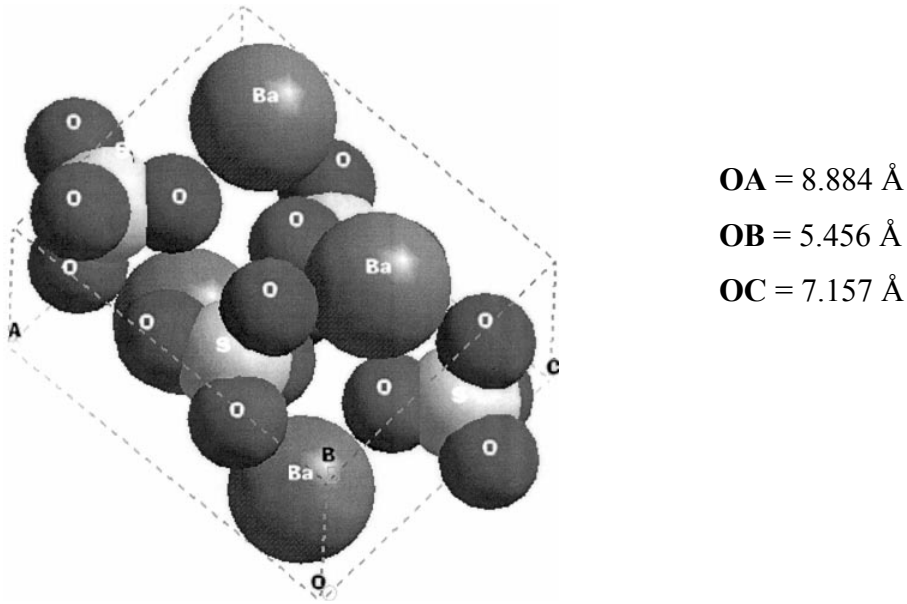


**Figure 8: Unit cell of barium sulfate and cell dimensions (from Dunn et al. (1999), also in Judat (2003)).**

Table 3 gives some data on barium sulfate.

**Table 3: Barium sulfate data at 25 °C (Atkins, 1996; D'Ans and Lax, 1998; Söhnel and Garside, 1992)**

Density	$\rho_p$	$4.48 \times 10^3$	[kg/m <sup>3</sup> ]
Molar mass	$M_C$	233.4	[kg/kmol]
Melting temperature	$T_{melt}$	1580	[°C]
Solubility product	$K_a$	$10^{-9.96}$	[mol <sup>2</sup> / l <sup>2</sup> ]
Reaction equilibrium for ion complex formation	$K_I$	$10^{-2.72}$	[mol / kg]
Refraction index	$R_I$	1.67	[-]
diffusion coefficient	$D_{AB}$	$1.67 \times 10^{-9}$	[m <sup>2</sup> / s]
Schmidt number, Eq. (83)	$Sc$	533	[-]
diffusion coefficient of Ba <sup>2+</sup> ions*	$D_{AB,Ba^{2+}}$	$8.46 \times 10^{-10}$	[m <sup>2</sup> / s]
diffusion coefficient of SO <sub>4</sub> <sup>2-</sup> ions <sup>†</sup>	$D_{AB,SO_4^{2-}}$	$1.1 \times 10^{-9}$	[m <sup>2</sup> / s]
Solubility of BaCl <sub>2</sub>	$c^*$	260	[g/kg]
Molar mass of BaCl <sub>2</sub>	$M_C$	208.24	[kg/kmol]
Solubility of K <sub>2</sub> SO <sub>4</sub>	$c^*$	100	[g/kg]
Molar mass of K <sub>2</sub> SO <sub>4</sub>	$M_C$	174.27	[kg/kmol]

<sup>†</sup>calculated from conductivity of ions at infinite dilution

Barium sulfate, also referred to as barite, is a widely used substance. In industry it is used as a filler and extender in plastics and paints, as well as in pharmaceuticals. In research it is widely used as model substance for precipitation problems. Barium sulfate was also often used as a model substance for investigations such as general precipitation phenomena, validation of particle population modelling approaches, fluid dynamic modelling, and production of nanoparticles (Adityawarman et al. (2008), Bałdyga and Orciuch (2001), Bałdyga et al. (1995), Fischer and Rhinehammer (1953), Jaworski and Nienow (2003), Marchisio et al. (2002), Niemann et al. (2006), Schwarzer et al. (2006), Schwarzer and Peukert (2002), Schwarzer and Peukert (2004), Vicum et al. (2003)).

### *2.11.1 Barium sulfate precipitation*

The dominating nucleation mechanism for barium sulfate precipitation can be homogeneous or heterogeneous depending on supersaturation. For low supersaturation, nucleation of barium sulfate is mainly heterogeneous, for high supersaturation, homogeneous nucleation has become so fast that it is the dominant mechanism. In between, a transition region with growing influence of homogeneous nucleation can be found. Different authors identified values for the supersaturation level for the dominant nucleation kinetics. Angerhöfer (1994) found a value of  $S_a = 250$  for the transition from heterogeneous to homogeneous nucleation in the system barium dihydroxide and sulfuric acid. Kucher et al. (2006) identified heterogeneous nucleation as dominant process for  $S_a < 550$  for the system barium chloride and sodium sulfate. For the same system, Nielsen (1961) reported homogeneous nucleation to be the dominant mechanism for  $S_a > 475$ . Schubert and Mersmann (1996) determined the transition to be at  $S_a = 200$ . Vicum et al. (2003) re-evaluated Nielsen's data and stated heterogeneous nucleation kinetics to be dominant below  $S_a = 280$ .

For growth of barium sulfate, as was mentioned in Chapter 2.8, at lower initial supersaturation the dominant mechanism is polynuclear surface nucleation, with an exponential growth law. It gives rhombic particles with smooth surfaces (Angerhöfer (1994), Nielsen (1958)). Nielsen (1958) concluded from his experimental data a direct transition to diffusion-controlled growth at  $S_a = 32$ . More recent research suggests a transition to an integration-controlled growth region, which would include growth on screw dislocations and by surface nucleation, with a parabolic growth law

(Angerhöfer (1994), Mersmann (2001), Walton (1967)). Angerhöfer (1994) observed a transition from polynuclear to integration-controlled growth at  $S_a = 18$ . Wong et al. (2001) used a value of  $S_a = 475$  at which growth becomes mainly diffusion-controlled.

Several kinetic growth models for barium sulfate precipitation were presented in the literature derived by precipitation experiments (Aoun et al. (1996, 1999), Nielsen (1958, 1961), Vicum et al. (2003), Angerhöfer (1994)).

Schubert and Mersmann (1996) derived an approach for heterogeneous growth based on statistical thermodynamic for systems where the number of foreign particles is large in comparison to the number of nuclei.

There also exist investigations of growth and dissolution behaviour of different faces, mainly the two lowest energy surfaces [001] and [210] of barium sulfate crystals in aqueous solution (Bosbach et al. (1998), Dunn et al. (1999)). Other research dealt with the influence of pH-value and additives during precipitation on barium sulfate particle size and shape (Bala et al. (2006), Hennessy and Graham (2002), Jones et al. (2002, 2004), Schulek (1954), van der Leeden and Rosmalen (1995), Wang et al. (2005, 2006), Yu et al. (2005)).

Precipitation kinetics are also influenced by excess of sulfate and barium ions. For non-stoichiometric feeding conditions of the reacting species, Aoun et al. (1996) identified different nucleation rates for the system barium chloride and potassium sulfate. Aoun et al. presented the model to draw attention to the fact that barium sulfate, albeit widely used in literature to validate mixing models, is not a trivial precipitation system and care has to be taken to chose appropriate kinetic laws for validation of theoretic models.

Agglomeration occurs in barium sulfate precipitation at high initial supersaturation levels when homogeneous nucleation dominates (Walton, 1967). For low supersaturation agglomeration was not observed by most authors (Angerhöfer (1994), Aoun et al. (1996), Bałdyga and Orciuch (2001), Kucher et al. (2006)). The dendrites observed are crystals growing from a single nucleus, not by agglomeration of smaller particles (Takiyama, 1959, and own X-ray diffraction (XRD) measurements, ref. Chapter 3.7). Agglomeration also gets hindered by an excess of barium ions, which preferably adsorb on the barium sulfate particle surface, forming a positive charge and leading to repulsive potentials between particles (Buchanan and Heyman (1948), Schwarzer and Peukert (2004)). The amount and charge of ions

attached to the particle surface is dependent on supersaturation  $S_a$  and ion ratio  $R$ . Thus, smaller particles are formed for  $R > 1$  in comparison to  $R < 1$  at the same supersaturation level (Kucher et al. (2006), Schwarzer and Peukert (2002)). Adsorbed ions also can change face growth rates and thus habit modifications, by changing the energy surface, blocking growth sites or hindering ion diffusion to the surface (Dirksen and Ring (1991), Walton (1967)). Song et al. (2003) observed rods and fibres in their precipitation on organic-aqueous interfaces, but only for  $R < 1$ . The particles remained small for barium ion excess. It can be assumed that the effect of barium ions attaching to the particle surface thus leading to repulsive forces and hindering agglomeration and growth of particles played a significant role in this result.

Li et al. (2007) classified the dominating nucleation and growth mechanisms for barium sulfate precipitation into four regions depending on supersaturation using their membrane dispersion mini-reactor. For supersaturation values calculated using Eq. (13), Li et al. identified a growth region at low supersaturation  $S_a < 86$ , a growth-controlled transition region for  $86 < S_a < 295$  which leads to a nucleation-controlled transition region, and a nucleation region at high supersaturation of  $S_a > 850$ .

### 2.11.2 Morphologies of barium sulfate precipitates

A summary of the observed barium sulfate morphologies, i.e. particle forms is given in this subchapter.

For all particle morphologies reported in literature, a general tendency concerning the dependence on supersaturation and on  $\text{Ba}^{2+}$  or  $\text{SO}_4^{2-}$  ion excess can be identified as described in the following.

At low supersaturation, thin plate formations and nearly rhombohedral forms with sharp edges and smooth surfaces were observed (Angerhöfer (1994), Benton et al. (1993), Dunn et al. (1999), Fischer and Rhinehammer (1953), Li et al. (2007), Nielsen (1964)). At medium supersaturation, structures are formed that have a plate as basis, with outgrowing excrescences. The particles have two favoured growth directions, and are thin in the third direction, with sharp edges (Angerhöfer (1994), Benton et al. (1993), Bernard-Michel et al. (2002), Judat und Kind (2004), Nielsen (1964), Wong et al. (2001)). At higher supersaturation, the edges get rounder, the surfaces rougher. Number and size of excrescences increase. Crystal forms observed are four-armed stars or rosettes (Aoun et al. (1999), Bernard-Michel et al. (2002), Judat and Kind (2004), Kucher et al. (2006)), stars and dendrites (Benton et al.

(1993), Dunn et al. (1999), Li et al. (2007), Nielsen (1964)), longish forms with two preferred growth directions and excrescences (Fischer and Rhinehammer, 1953). At very high supersaturation, small, nearly monodisperse crystals are observed that form more or less compact agglomerates (Judat and Kind (2004), Kucher et al. (2006), Li et al. (2007), Nielsen (1964)).

Barium sulfate dendrites have their main stems along the same axes as the platelet crystals, the active growth faces remaining the same for the different particle shapes for increasing supersaturation (Benton et al., 1993).

With an excess of  $\text{Ba}^{2+}$  - ions the particles tend to be smaller than with an equivalent excess of  $\text{SO}_4^{2-}$  ions (Buchanan (1949), Kucher et al. (2006), Fischer and Rhinehammer (1953), Schwarzer and Peukert (2002, 2004), Wong et al. (2001)). Agglomeration, if at all present, seems to be hindered for ion excess (Eble (2000), Judat (2003), Kucher et al. (2006), Schwarzer and Peukert (2002)). In general, excess of an ion species leads to a decrease of perfection of crystal surface, i.e. the surface becomes rougher, and has more excrescences or even dendritic forms (Fischer and Rhinehammer (1953), Kucher et al. (2006)).

Table 4 summarises roughly the main effects of initial supersaturation on batch precipitation of barium sulfate. The classification of Li et al. (2007) was chosen for characterising the according precipitation regions and the dominating mechanisms for nucleation rate, growth rate, the general crystal morphology, and whether agglomeration can be expected.

**Table 4: Rough classification of dominant precipitation mechanisms for barium sulfate depending on supersaturation.**

precipitation region*	$S_a^*$	dominant nucleation mechanism	dominant growth mechanism	agglomeration	morphology
growth	< 85	heterogeneous	integration controlled	no	cubes, platelets
transition	85 - 850	heterogeneous	diffusion controlled	no	dendrites
nucleation	> 850	homogeneous	diffusion controlled	yes	spherical (small)

\*Classification and  $S_a$  values from Li et al. (2007)

### 2.11.3 Influence of mixing and feeding policy on barium sulfate

For barium sulfate precipitation micromixing was observed to have an influence on particle size if the local supersaturation was high enough for homogeneous nucleation to occur. Judat (2003, also in Judat et al., 2004) explained this by the increase of nucleation rate for higher micromixing intensity. Growth being slower than the micromixing rate, more particles are formed that cannot grow as much as for the case of lower nucleation rate. Judat performed mixing experiments for higher supersaturation in a Taylor-Couette reactor with axial flow enabling independent adjustment of macro- and micromixing conditions. For micromixing he observed a strong influence on the particle size, but not on the morphology of the barium sulfate particles.

Judat (2003) also obtained smaller mean particles in case of sulfate feed. He explains it by the reported higher affinity of barium ions to attach on the particle surface (Eble, 2000). Judat did not observe an effect of the feeding sequence on the particle morphology. He also varied the feeding time in his Taylor-Couette reactor without observing any changes in mean particle size.

Smaller particles for higher mixing intensity were also observed by Schwarzer and Peukert (2002). They investigated the influence of mixing on precipitation of small particles at high supersaturations ( $S_a = 3400$ ). Experiments were performed in a T-mixer with the possibility to influence the mixing intensity by adjusting the flow rate.

Liu et al. (1976) determined growth and dissolution behaviour of barium sulfate using self produced seed crystals at medium supersaturation. Smaller particles formed during precipitation in highly stirred conditions. For the case of no stirring, the particles are bigger and form more dendrites. Liu et al. concluded, that due to increased frequency of ion encounters upon stirring the rate of nucleation is increased, leading to more and therefore smaller particles.

Li et al. (2007) made experiments in a custom membrane dispersion mini-reactor where the flow rate defined the grade of mixing in the experimental set-up. The investigated range of supersaturations was from very low to high ( $S_a$  between 40 and 1335). They made experiments with two different feed rates per concentration conditions and observed different morphologies coexisting for the lower feed rate. Since the feed rate determined the rate of mixing in Li et al.'s mixing chamber

device, one possible reason for this could be high fluctuations in local supersaturation due to little mixing.

For their batch precipitation system at lower supersaturations in a stirred vessel, Aoun et al. (1999) concluded that there is no influence of micromixing due to observations of no influence of stirrer speed on number concentration, mean size, and crystal morphology. They also detected no influence of the particle morphology on the feeding sequence.

Chen et al. (1996) performed stoichiometric experiments at medium supersaturation in a stirred tank with one feed for the system barium chloride and sodium sulfate, investigating the effect of number of stirrer revolutions, feed rate, and feed inlet point but did not determine the shape of their precipitated particles. The operating condition was semi-batch with barium chloride in the feed. They observed a dependence of stirrer speed on the mean particle diameter showing an “optimum” stirrer speed for the smallest particle mean diameter for fixed feed rate and supersaturation.

Chen et al. (1996) also reported different dependencies of the mean particle diameter for different feed rates depending on stirrer speed and three different feed point locations. With inlet points nearer to the impeller, lower stirrer speeds were necessary to obtain the observed smallest particles. They concluded that the feed location should be placed closely to the impeller in order to save energy. The results from Chen et al. also show that the conclusion whether feed location leads to an increase or a decrease of particle size is also dependent on stirrer speed. For the feed inlet point next to the impeller they also observed little influence of the feeding time on mean particle size.

The same dependence on stirrer speed as reported by Chen et al. (1996) was observed by Angerhöfer (1994) who used a stirred batch crystalliser with two feeds to investigate the influence of stirrer speed on resulting crystal sizes for different initial supersaturations, feed inlet points, and stirrer geometries. The precipitation system used was barium sulfate by barium hydroxide and sulfuric acid to exclude any influence of counter ions. He also varied the feed rate for some experiments. A clear influence of different feed rates on particle mean size for Angerhöfer’s results cannot be concluded due to scattering of the data.



Fitchett and Tarbell (1990) performed experiments in a continuously stirred tank reactor with mixed product removal (MSMPR) for medium and high supersaturations investigating the influence of power input (calculated as a sum of stirrer speed and power input by feed velocity), residence time, and feed concentration on mean particle size. They also took SEM pictures for characterisation of some particle morphologies. For high supersaturation, morphology was independent on stirrer speed. The measured particle mean size showed a maximum for increasing power input. This maximum was at lower power input values at lower feed concentrations.

Wong et al. (2001) investigated the mean particle size in dependence on the stirrer speed in a stirred tank reactor for non-stoichiometric semi-batch operation at low to medium supersaturations. They did not conclude any dependence on stirrer speed due to scatter in the results. Concerning the feeding sequence they observed larger crystal sizes for barium sulfate feed in comparison to sodium sulfate feed as reported above for other researchers.

Bernard-Michel et al. (2002) varied feed rate and inlet positions for feeding strategy experiments in a stirred tank reactor. They evaluated the shapes using a semi-automated picture analysis procedure defining particle properties for quantification.

Phillips et al. (1999) performed experiments for two feed inlet points (near the surface and near the impeller) in a single feed stirred tank reactor. Influence of stirrer speed was not very strong in all cases. For the feed inlet point at the surface, data scattered much more than for the inlet point at the impeller. They concluded from their experiments that the initial reactants' concentration has a higher effect on the crystal morphology than the feed inlet location.

Other research investigated the dependence of the mean particle diameter on the feed inlet points for stirred tank reactors with two feeds (Bałdyga et al. (1995), Wong et al. (2003)). Bałdyga et al. reported bigger particles with more platelets if the inlet points of feeds were located near the surface. Adding the reactants closer to the impeller lead to smaller, more star shaped particles.

#### 2.11.4 Shape factors for precipitated barium sulfate

Due to the different supersaturation levels and ion ratios present in batch and semi-batch precipitation, the growth habit of crystals can change over time as several stages of supersaturation are reached (Dirksen and Ring, 1991). Thus, for different stages of the experiments the shape factor of the product particles can also change. Vicum et al. (2003) assumed constant shape factors along isogrowth lines, but the transition from one to the other if calculating a dynamic experiment is not covered in that paper. In the literature, shape factors for batch precipitation are usually assumed to be a constant value, derived by evaluating the morphology of the product crystals (Bałdyga et al. (1995), Mersmann (2001), Pagliolico et al. (1999), Podczeczek (1997)). Experiments showed that also for semi-batch precipitation operation the initial concentrations, i.e. the initial local supersaturation dominates the morphology of the particle (van Leeuwen (1998), Liu et al. (1976), Wong et al. (2001)). It is therefore a justified assumption to use constant shape factors for the modelling of the semi-batch experiments as it will be done in this work.

Bałdyga and Podgórska determined shape factors for barium sulfate in dependence on different supersaturation assuming equi-dimensional growth, i.e.  $k_A = 6 k_V$  (Bałdyga et al. (1995), Podgórska (1993)), see Table 5.

These values were used by Bałdyga and his co-authors extensively (Bałdyga et al. (2005), Bałdyga and Orciuch (1997, 2001), Phillips et al. (1999), Vicum et al. (2003)). Bałdyga and Orciuch (1997, 2001) used the lowest and the highest reported shape factor to define the range of expected crystal shapes in their simulation. Vicum et al. (2003) assumed these values to be constant along iso-growth lines for their non-stoichiometric precipitation experiments as listed in Table 5.

**Table 5: Shape factors reported by Bałdyga and co-authors as referenced in the text.**

$k_A$ (Eq. (72))	$k_V$ (Eq. (73))	$\phi_V$ (Eq. (75))	particle shape	iso-growth rate G
8.17	1.362	0.727	well-formed rectangular	$\approx < 6.4$ nm/s
47.22	7.88	0.405	star-like “rose”	$\approx 20.0 - 64$ nm/s
348.0	58	0.208	dendritic	$\approx 640$ nm/s

Pagliolico et al. (1999) derived shape factors for barium sulfate crystals precipitated in a continuous Couette reactor as listed in Table 6.

**Table 6: Shape factors for crystal morphologies from Pagliolico et al. (1999)**

$k_A$ (Eq. (72))	$k_V$ (Eq. (73))	$\phi_V$ (Eq. (75))	particle shape
1.1	0.05	2.19	tabular (dendritic)
1.6	0.05-0.07	1.96-2.19	tabular (with pyramidal growth)
2.4	0.07-0.09	1.80-1.96	simple twin
5.8	0.3-0.4	1.09-1.20	rose

Marchisio et al. (2001) observed different barium sulfate particle morphologies in their experiments using a tubular reactor, but decided to use an average value for the shape factor for all their simulations (Table 7).

**Table 7: Average shape factor as used by Marchisio et al. (2001).**

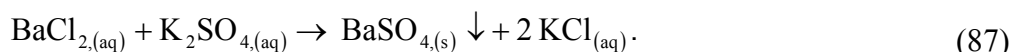
$k_A$ (Eq. (72))	$k_V$ (Eq. (73))	$\phi_V$ (Eq. (75))
30	5	0.333

Fitchett and Tarbell (1990) estimated the volume shape factor for their flat, dendritic particles precipitated in an MSMR reactor to be  $k_V = 0.06$ .

### 3 Experimental set-up and preliminary experimental investigations

#### 3.1 Materials

The reactants used were barium chloride (barium chloride-dihydrate for analysis, 99% purity, Merck KGaA, Darmstadt, Germany) and potassium sulfate (potassium sulfate for analysis, 99% purity, Merck KGaA, Darmstadt, Germany), all without any further purification or conditioning. Deionized water was used as solvent. The precipitation reaction follows Eq. (87):



#### 3.2 Precipitation reactor and procedures

To ensure reproducible experimental conditions, a standardized glass Rushton tank of 1 l maximum volume was used. The tank was continuously stirred by a standard six-blade Rushton turbine impeller and equipped with four equally distributed baffles. Figure 9 shows the experimental setup and Figure 10 together with Table 8 gives the tank and stirrer dimensions.

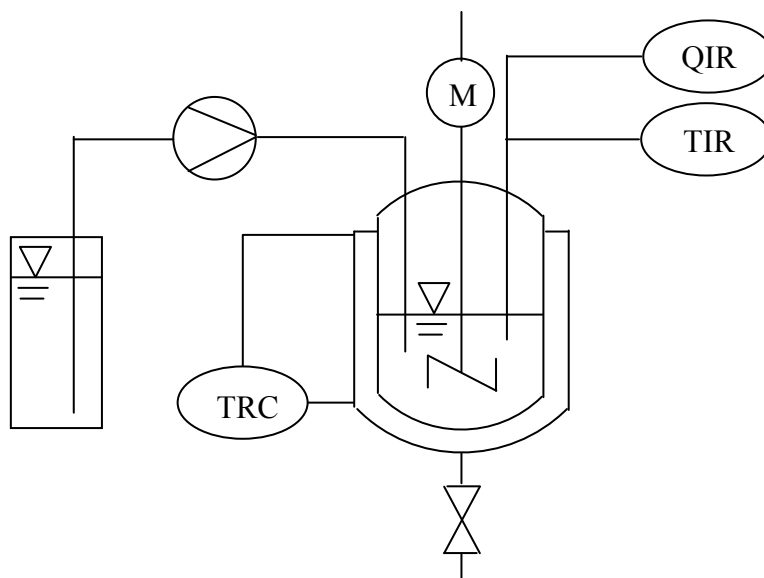


**Figure 9: Schematic experimental set-up.**

Temperature was kept constant at 25 °C via a thermal bath. The operating mode was single feed semi-batch. Feed location point for all experiments was 15 mm above and 10 mm besides the stirrer blades. The vessel was filled with one salt solution of 350 ml liquid volume. 350 ml of the other salt solution was pumped with a constant feed

rate into the stirred vessel. Both feeding sequences were carried out for all experiments. The flow regime in the vessel was turbulent at a number of stirrer revolutions of 800 rpm with a Reynolds number of about  $Re = 13,500$  if calculated by Eq. (77) using the stirrer properties of the experimental set-up (Figure 10) and a kinematic viscosity  $\nu = 8.9 \times 10^{-7} \text{ m}^2/\text{s}$  for the solvent (water). The stirrer tangential speed was therefore 1.2 m/s.

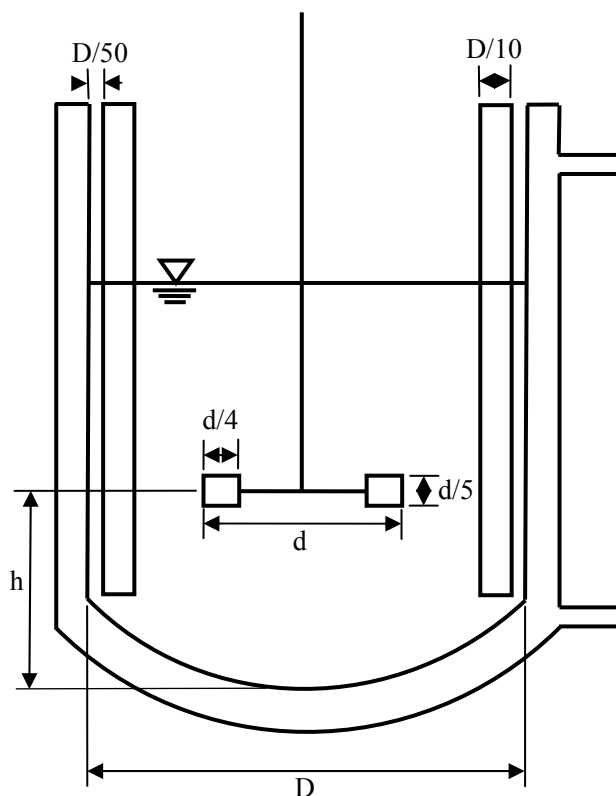


**Table 8: Tank and stirrer dimensions.**

<b>vessel</b>	D	10 cm
<b>baffles</b>	D/10	1 cm
	D/50	0.2 cm
<b>stirrer</b>	d	3 cm
	d/4	0.75 cm
	d/5	0.6 cm
	h/d	1.5

**Figure 10: Geometry and dimensions of the used standard Rushton tank.**

The experimental parameters investigated were the following:

1. Theoretical initial supersaturation, notated as  $S_a$  in tables, figures, and in the discussion of experiments. The values of  $S_a$  used throughout this work to characterize the experimental conditions are calculated by the initial educt concentrations if ideally mixed, applying the extended Debye-Hückel model with no reaction and no complex formation of ions as specified in Appendix B. Values were between  $S_a = 274$  and  $S_a = 1336$ .
2. Theoretical initial ion ratio, notated as  $R$  in tables, figures, and in the discussion of experiments. It was also calculated by the initial educt concentrations for the assumption of ideal mixing. The investigated range was from  $R = 0.1$  and  $R = 10$ .

3. Feeding sequence, i.e. the two cases for mixing the two salt solutions barium chloride and potassium sulfate in a single-feed stirred tank reactor with one in the feed and the other in the vessel. For characterization, the salt solution in the feed is specified in tables and figures.
4. Feed rate. The feed rate was varied between 0.4 ml/min and 80 ml/min for the semi-batch experiments. Batch experiments were realized using a dropping funnel, leading to an approximate feed rate of 600 ml/min.

For all experiments, samples were taken out of the well-mixed vessel near the stirrer via pipette and introduced with smallest possible delay into a laser scatter particle sizer (CILAS -Lasergranulometer 1180, Quantachrome GmbH & Co. KG, Odelzhausen, Germany), for determining the particle size distribution (PSD) of the precipitated particles (ref. Chapter 3.4.2). The mean diameter of particles in the vessel during the experiment was measured using an online probe (Aello 1400 In-Line Sensor Systems, GWT-TUD GmbH, dept. Aello, Dresden, Germany, ref. Chapter 3.4.1).

Directly after precipitation, the particles were examined via a light-optical microscope. For this, a small droplet of the product solution was placed directly onto the sample holder (Zeiss Axio Imager A1, Carl Zeiss AG, Germany). Pictures of particle morphologies were also gained using scanning electron microscopy (SEM, DSM 942, Carl Zeiss AG, Germany, and SEM, XL series, Philips (Figure 14 and Figure 17)). For the scanning electron microscopy (SEM) analysis, samples were washed and diluted two times with saturated barium sulfate solution (prepared from barium sulfate extra pure, Honeywell Riedel-de Haën, Seelze GmbH, Seelze, Germany) and shortly washed with deionised water before being brought onto the sample holder.

EDX analysis of X-ray spectra was performed for selected particle samples by high resolution scanning electron microscope (SEM, Philips, XL series; ref. Chapter 0). X-ray diffraction (XRD) analysis was made for some samples (X-Ray Diffraction System X'Pert Pro, PANalytical; ref. Chapter 3.7).

### *3.2.1 Reproducibility of experiments*

All precipitation experiments were carried out at least two times. Figure 11 shows the PSDs of different samples for the same experimental conditions chosen as an example to give an impression on the reproducibility of the experiments. The PSDs

for two samples taken from different vessel locations of the same run directly after the end of the feeding time (black and blue lines) are shown as measured by the CILAS device. The black line is not easy to spot, as it is nearly consistent with the green line, which shows data for the same run 1/2 hour after the feeding was over. Also included is the PSD at the end of the feeding time for a second run of the same experimental conditions (red line).

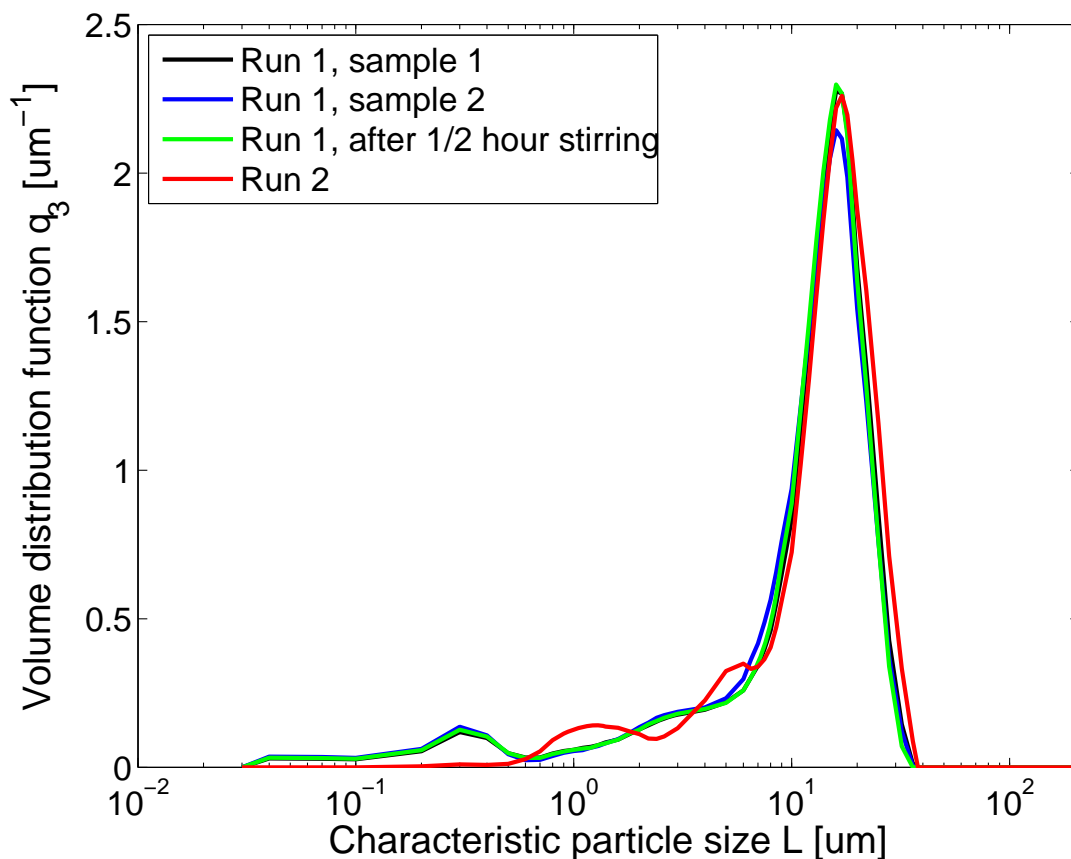


**Figure 11: Particle size distribution of different samples for the same experimental conditions ( $S_a = 527$ , low feed concentration, barium chloride feed, 5 ml/min feed rate, 800 rpm, 25 °C).**

It can be seen that the consistency for the same run between different samples is very high, thus sample drawing was obviously done in a reproducible way. Reproducibility between two different runs, each carried out with new sets of reactants and in an accordingly cleaned vessel also showed acceptable agreement. In general, the agreement was higher for potassium sulfate feed than for barium chloride feed. One explanation for this could be that for barium excess the particle growth is better „controlled“ due to the attaching barium ions which also lead to smaller particles, whereas for sulfate excess, growth on all crystal faces is less restricted, leading to bigger particles and a higher variety in sizes.

Overall, differences in mean diameters of up to 1  $\mu\text{m}$  from run to run were observed which is similar to those reported in literature (Angerhöfer, 1994). Also, no difference can be seen between the PSDs directly after the feeding time and after another half an hour of stirring in the vessel. This is also validated as shown in Figure 12 where the development of the mean particle diameter for half an hour after the end of the feeding time is shown for the same experiment as in Figure 11 as measured with the Aello device. No change in mean diameter can be detected.

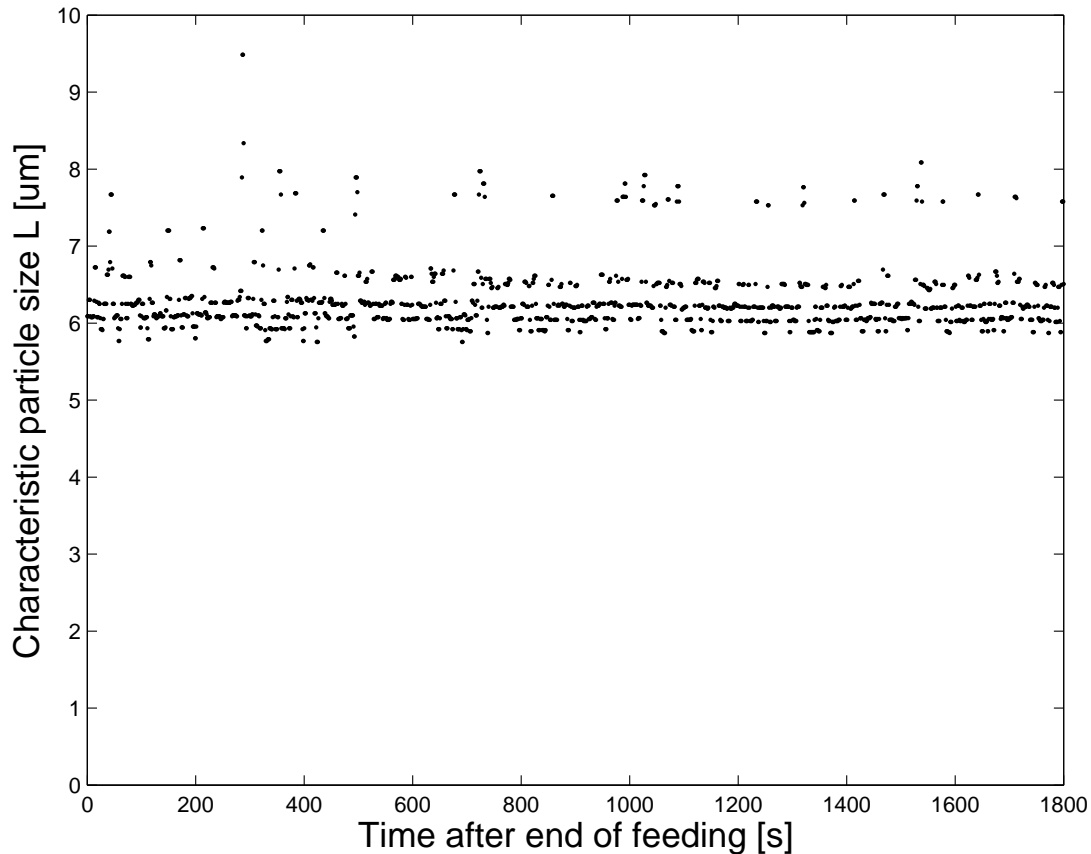


**Figure 12: Development of mean particle diameter after the end of the feeding time ( $S_a = 527$ , low feed concentration, barium chloride feed, 5 ml/min feed rate).**

Figure 13 shows the microscope pictures of particles of another experimental run at different retention times in the vessel. The suspension was constantly stirred during the whole run time. The first sample was taken directly after the end of the feeding time, the second 24 hours later. A third sample was taken after five days. For the last sample (Figure 13.3), more breakage due to the long stirring time seems to have taken place as more pieces of broken particles could be found. Also Oswald ripening might have taken place which lets the particles grow a bit further. Yet, the morphology of the particles did not change during the whole time. Due to this, together with the consistent PSDs as shown in Figure 11 (lines 1 and 3) the end of



the feeding time was defined to be the end of the precipitation reaction and then samples for particle characterisation were taken for all experiments discussed in Chapter 4.

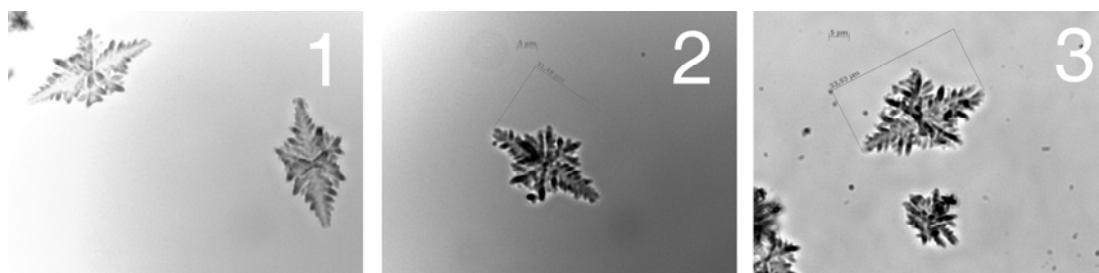


**Figure 13: Microscope particle pictures of the same precipitation experiment. Samples were taken 1: after the end of feeding time, 2: after 24 h of stirring, and 3: after 5 days of stirring. Experimental conditions:  $S_a = 527$  (lower feed concentration), barium chloride feed, 80 ml/min feed rate.**

SEM images were taken from one of the experimental runs for every experiment. The images included in this work were chosen to give a representative impression on the observed particle morphologies for every experiment.

In some experiments, a coexistence of flat and star-like crystals was observed as reported by Bernard-Michel et al. (2002). The star-like particles looked like several single flat ones grown from each other by surface nucleation events. In their experiments, Bernard-Michel et al. called them sand-roses. In this work, the sand-roses were a minority and the “arms” had the same morphologies as the single flat particles. It was therefore decided for this work to include SEM images of flat particles to study the morphology.

Also, for some experiments, differently sized particles were present. In this case, for the SEM images shown in this work the pictures showing the morphology best were chosen for the discussion.

### 3.3 Conditions of experimental series

One series of experiments for high supersaturation of  $S_a = 1336$  with varying feed rates was performed, using the parameters listed in Table 9. Table 10 and Table 11 contain the parameters of the experiments at lower supersaturations. The concentrations were chosen so that the amount of precipitated  $\text{BaSO}_4$  was the same for all of these experiments, but smaller than for the experiments at high supersaturation from Table 9.

**Table 9: Conditions of the precipitation experiments for high supersaturation ( $S_a = 1336$ , Chapter 4.1.1)**

concentration of reactant [mol/l]		feed rate [ml/min]	$S_a$ [-]	$R$ [-] ( $K_2SO_4$ and $BaCl_2$ feed)	
in vessel	in feed				
0.1	0.1	80	1336	1	
0.1	0.1	20	1336	1	
0.1	0.1	5	1336	1	
0.1	0.1	0.4	1336	1	

In Table 10, the concentration of the salt solution provided in the vessel was lower than or equal to the second reactant in the feed.

**Table 10: Precipitation experimental conditions at low feed concentration (Chapter 4.1.2)**

No.	concentration of reactant [mol/l]		feed rate [ml/min]	$S_a$ [-]	$R$ [-]	
	in vessel	in feed			$K_2SO_4$ feed	$BaCl_2$ feed
1	0.1	0.01	80	527	10	0.1
2	0.075	0.01	80	498	7.5	0.13
3	0.05	0.01	80	456	5	0.2
4	0.01	0.01	80	274	1	1
5	0.1	0.01	20	527	10	0.1
6	0.1	0.01	5	527	10	0.1
7	0.1	0.01	0.4	527	10	0.1
8	0.01	0.01	20	274	1	1
9	0.01	0.01	5	274	1	1
10	0.01	0.01	0.4	274	1	1
11	0.01	0.01	batch	274	1	1

These experiments can be divided into three series: the first series dealt with varying the amount of ion excess  $R$  by varying the concentrations (first four lines of Table 10), in the second and third series the feed rate was varied at fixed  $S_a = 527$  and  $S_a = 274$ , respectively. Batch operation was realised in the same experimental set-up as for the semi-batch operation by adding the feed at the highest possible feed rate. For this, a dropping funnel was used to enable reproducibility, leading to an approximate feed rate of 600 ml/min with a feeding time of 35 s. Stirring of the batch experiments

was then continued until a total time of 262.5 s to ensure constant conditions in the vessel before samples were taken. The resulting similar particle morphologies for the two feeding sequences as shown in Figure 20 give reason to the conclusion that batch conditions were basically fulfilled with the chosen set up.

In Table 11, the concentration of the reactant in the feed was higher than that of the salt solution provided in the vessel. The experiments therefore have the reversed conditions as the ones listed in Table 10 (for  $R$  not equal to one). The experiments in Table 11 were carried out only once to compare the particle morphologies. No particle size distributions were measured for these experiments.

For seeded precipitation (Chapter 4.3), experiments were performed in two stages. First the seed particles were precipitated in the reactor the same way as the experiments described above. A third of the well-mixed vessel content was taken, the seed crystals washed in saturated barium sulfate solution and used as seed crystals in another experiment with different conditions in the newly prepared reactor. To do this, the seed crystals were part of the salt solution already in the vessel, while the other salt solution was pumped into the reactor as feed in the semi-batch mode.

**Table 11: Precipitation experimental conditions at high feed concentration (Chapter 4.1.3)**

concentration of reactant [mol/l]		feed rate [ml/min]	$S_a$ [-]	$R$ [-]	
in vessel	in feed			$K_2SO_4$ feed	$BaCl_2$ feed
0.01	0.1	80	527	0.1	10
0.01	0.075	80	498	0.13	7.5
0.01	0.05	80	456	0.2	5
0.01	0.1	20	527	0.1	10
0.01	0.1	5	527	0.1	10
0.01	0.1	0.4	527	0.1	10

### 3.4 Particle size measuring principles used

#### 3.4.1 Extinction

Extinction is the attenuation of light when passing through material. Phenomena occurring are adsorption, scattering, diffraction, and reflection. This measuring principle is used by the Aello probe (Aello 1400 In-Line Sensor Systems, GWT-

TUD GmbH, dept. Aello, Dresden, Germany) to determine the mean particle diameter at a given time. It measures directly in the reaction vessel. The cone shaped probe has a trench where emitter and receiver of laser light of three different frequencies are adjusted on opposite sides. This part of the probe has to be covered with the fluid suspension, allowing a representative part of the fluid to flow through the measuring trench so that the laser light signals go through the sample.

The Aello device uses two different measuring principles for different particle size ranges:

1. Dynamic extinction: In addition to extinction, the fluctuation of the light intensity is measured. The particles have to be of a similar size range as the diameter of the measuring beam (1 - 500  $\mu\text{m}$ ). From the measured values for transmission and its standard deviation the size and the concentration of the particles in the suspension can be determined.
2. Spectral extinction: For this measuring principle the light attenuation of different wave lengths is used to determine particle sizes between 10 nm and 3  $\mu\text{m}$ . From the extinction of the different laser frequencies the size and the concentration of the nano particles in the suspension can be determined.

#### 3.4.2 *Laser diffraction*

For measuring the particle size distributions, a laser scatter particle sizer (CILAS - Lasergranulometer 1180, Quantachrome GmbH & Co. KG, Odelzhausen, Germany) is used which operates with laser diffraction. The measuring principle of laser diffraction is the fact that particles of different size scatter light differently. The scattered light is collected by photodetectors at different angles. The resulting light distribution is called the diffraction pattern. For a single sphere the diffraction pattern shows a typical ring structure. With light scattering theories from Mie and Fraunhofer the interaction of light with particles can be described mathematically and a resulting particle size distribution can be calculated for dilute suspensions. The particle concentration is assumed to be so low that scattered radiation is directly measured by the detector (i.e. single scattering) and not rescattered by other particles (i.e. multiple scattering).

The particle size detected by the laser particle sizer  $d_{43}$  was identified to be approximately the width of the particle for the case of a platelet shape (Marchisio et al. (2002), Pagliolico et al. (1999)) and the diameter of the crystal if the crystal is round (Marchisio et al., 2002).

For the PSD measurements done in this work, the same spherical shape factor was used for the evaluation of all experiments. This seems to be a useful approach if dealing with different (unknown) particle shapes and also to unify the measuring routine for all experiments.

To prevent agglomeration, usually ultrasound is applied to the particle suspension in the CILAS device either before or during measurement. But for this present work this was not done, as dendritic particles tend to be easily breakable. The well mixed sample from the vessel was introduced into the measuring circuit with the smallest possible delay where it got diluted strongly and pumped constantly. It was assumed that this was sufficient to prevent agglomeration and also sedimentation of particles during the measurements.

The volume-based particle frequency distribution histogram given by the CILAS experimental device is calculated out of the volume cumulative curve  $Q_3(L)$ . The equation used is derived for the normalized frequency distribution in a log-diagram due to the logarithmic scale of the volume cumulative curve  $Q_3(L)$ :

$$q_3(L_i) = \frac{Q_3(L_i) - Q_3(L_{i-1})}{\log\left(\frac{L_i}{L_{i-1}}\right)}. \quad (88)$$

with  $q_3$  being the volume-based particle frequency distribution.

### 3.5 Reference measurements with standard particles

In Chapter 4, the mean diameters measured by the two devices (Aello and CILAS) gave values up to ten times different in size (see Table 14). In general the mean diameters given by Aello were smaller than the ones calculated from the particle size distributions obtained with CILAS. To be able to make a general statement, standard spherical particles (Polystyrene) were measured with both devices. Standards used were from the company micro particles GmbH with the following specifications:

1. Particle standard: „1.998  $\mu\text{m} \pm 0.031 \mu\text{m}$ , SD = 0.042  $\mu\text{m}$ , PS-ST-L1186“,
2. Particle standard: „9.727  $\mu\text{m} \pm 0.108 \mu\text{m}$ , SD = 0.134  $\mu\text{m}$ , PS/Q-ST-L935“.

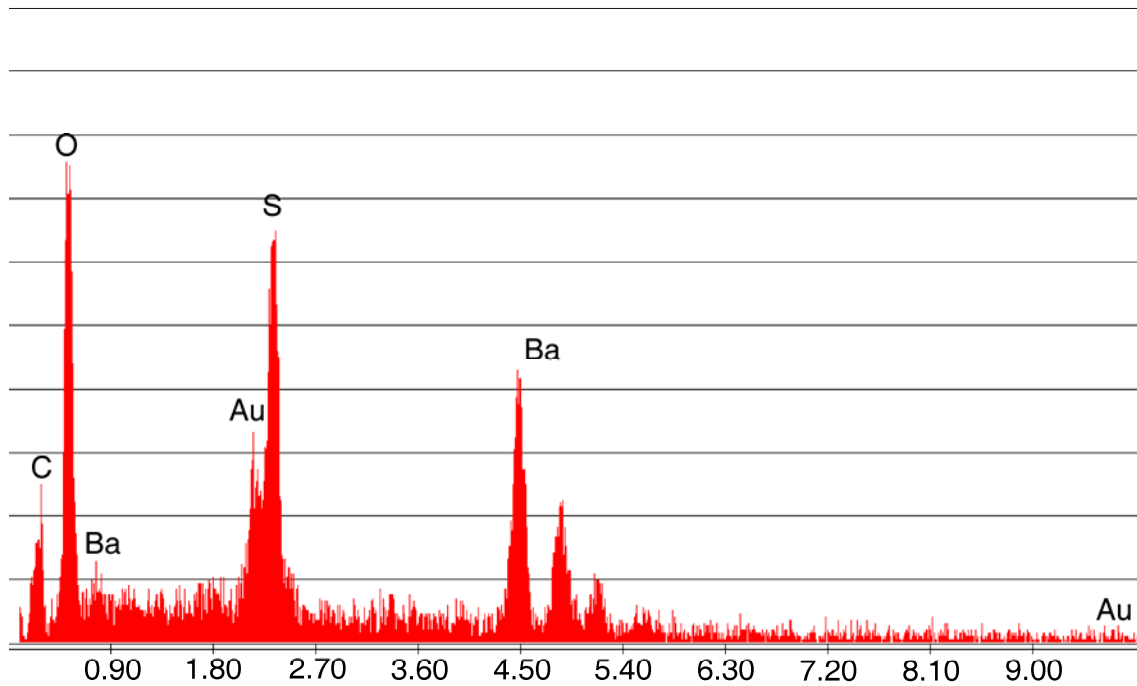
**Table 12: Comparison of measured mean diameters  $d_{50}$  to two standard particles [ $\mu\text{m}$ ]**

	Standard	Aello	CILAS
1. Standard	1.998	1.32	1.72
2. Standard	9.727	4.86	9.16

Table 12 gives the measured mean diameters. It can be seen that the mean diameters obtained with CILAS are in acceptable range. Diameters measured by the Aello device were too small in both cases.

### 3.6 X-ray spectrum (EDX analysis) of particles

As already mentioned, an integrated EDX-analysis of X-ray spectra in the high resolution scanning electron microscope (SEM, Philips, XL series) was used for the chemical analysis of the precipitated particles. With this, the chemical composition of the particles is determined by the X-ray spectra detected.



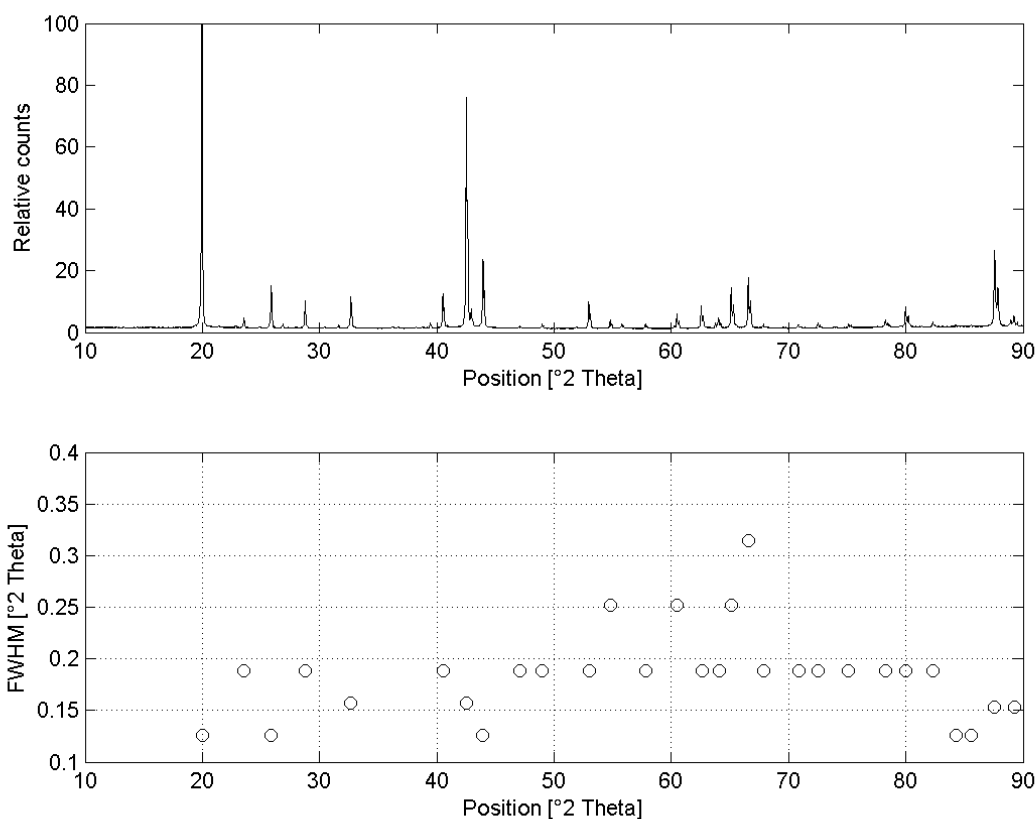
**Figure 14: X-ray spectrum (EDX analysis) of BaSO<sub>4</sub> particles precipitated at  $S_a = 1336$  and feed rate of 80 ml/min.**

Figure 14 shows the X-ray spectrum (EDX analysis) of the barium sulfate precipitate particles. The gold peak results from gold with which the sample was sputtered to increase conductivity for scanning electron microscopy (SEM) analysis. The carbon peak originates from the base material on which the particle sample was prepared for examination. It can be seen that the particles indeed consist of sufficiently pure BaSO<sub>4</sub>.

### 3.7 X-ray powder diffractometry (XRD)

Information about the crystal structure and crystallite elements of solid materials as well as crystallite defects, substrate orientation, or mechanical strains can be gathered

with X-ray diffraction. The measurements are non-destructive. Typical interatomic distances in crystalline solids are in the order of a few angstroms, which is the wavelength of X-rays. If irradiated with X-rays, oscillations of the electrons of the atoms in the crystal structure are activated, emitting secondary rays with the same frequency. Emitted rays from neighbouring atoms interfere, creating zones of diffraction minima and maxima. The angle of diffraction is called the theta angle and measured in degrees. From the picture obtained the crystallite structure of the sample investigated can be determined. A diffraction pattern records the X-ray intensity as a function of the 2-theta angle.



**Figure 15: Top: Diffraction pattern of the experiment with potassium sulfate feed of 0.01 mol/l to barium chloride provided in the vessel at 0.05 mol/l with a feed rate of 80 ml/min. Bottom: Determination of peak width (FWHM [ $^{\circ}2\text{Theta}$ ]) for the  $\text{BaSO}_4$  sample.**

The device used was the X-Ray Diffraction System X'Pert Pro (PANalytical). For preparation, the precipitated particles were filtered through a 0.2  $\mu\text{m}$  membrane filter, washed and dried. For measurement, a small amount (covering the tip of a spatula) of the dry powder was given onto the sample holder of the XRD measuring device. Figure 15 (top) shows the diffraction pattern of particles precipitated in an

experiment with a potassium sulfate feed of 0.01 mol/l to barium chloride provided in the vessel at 0.05 mol/l with a feed rate of 80 ml/min.

Scattered rays also interfere with neighbouring planes in a way that for some angles, the rays are cancelled out. For crystallites smaller than 1 $\mu\text{m}$ , the canceling-out effect is reduced due to missing planes. In this case the peaks of the diffraction pattern show a broadening compared to the inherent width dictated by the uncertainty principle which is only broadened by instrumental effects. This additional broadening in diffraction peaks further than the inherent peak width can be used to determine crystallite sizes if smaller than 1 $\mu\text{m}$ . Ideally, the peak of a mono-crystal would be of zero width. For estimation of the peak width due to instrumental effects, the peak widths of the sample are compared with the ones from a reference mono-crystal. Here, the instrumental broadening of the signal was measured using a sample of NIST SMR66a (LaB6). Figure 15 shows the peak counts and widths of precipitated particles. The example chosen consists of dendritic particles, precipitated with potassium sulfate feed of 0.01 mol/l to barium chloride provided in the vessel at 0.05 mol/l with a feed rate of 80 ml/min. The peak widths are of the same order of magnitude as those of the reference. It can be concluded that no nano-agglomerates or nanoparticles are present. Hence, agglomeration can be excluded for the precipitated particles at  $S_a < 1336$ .

### **3.8 Influence of KCl excess on particle morphology**

For the reaction system of barium chloride and potassium sulfate, potassium and chloride ions are accumulated and remain dissolved in the liquid phase during and after precipitation. To make sure that these ion species do not influence the particle morphologies of the barium sulfate crystals, i.e. that these are due to the influence of barium and sulfate ion concentrations and excess, experiments with solute potassium chloride in excess (KCl) were performed and particle morphologies were determined using scanning electron microscopy (SEM).

Table 13 contains all conditions chosen in these experiments. For all three experiments barium chloride was fed to the reactor with a feed rate of 80 ml/min. In the potassium sulfate solution provided in the vessel an excess of potassium chloride was dissolved as specified. The reference experiment with no extra KCl contained in the solution (experiment 1) is the same as listed in Table 10.



**Table 13: Precipitation experiment conditions for excess of KCl in solution**

Experiment number (Figure 16)	concentration of $K_2SO_4$ in vessel [mol/l]	concentration of $BaCl_2$ in feed [mol/l]	feed rate [ml/min]	$S_a$ [-]	concentration of excess KCl (in vessel) [mol/l]
1	0.1	0.01	80	527	0.0
2	0.1	0.01	80	527	0.01
3	0.1	0.01	80	527	0.1

Figure 16 shows the resulting particle morphologies. Figure 16.1 is the reference experiment without extra KCl in the solution. In Figure 16.2 the excess of KCl at the beginning of the experiment in the vessel (dissolved in the potassium sulfate solution) is 0.01 mol/l, in Figure 16.3 it is 0.1 mol/l. These experiments were only meant as a quick check on a possible influence of the potassium chloride ions on the particle morphologies; hence the SEM images do not provide enough information about the influence on the particle size. Nevertheless, no significant influence of potassium chloride excess can be observed on the particle morphologies. In all three cases, the particles are dendrites, with one elongated axis and branches arising from it in the same manner.

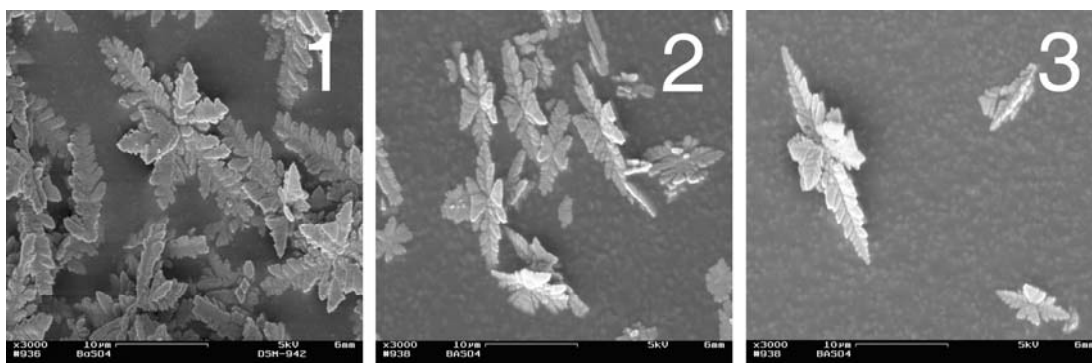


**Figure 16: Particle morphologies obtained for varying excess of KCl in the solution, provided in the vessel at  $t=0$  as listed in Table 13.**

Buchanan and Heymann (1948) made Zeta-potential measurements for barium sulfate particles where they found that an excess of KCl has no influence on the Zeta-potential of  $BaSO_4$ . Kucher et al. (2006) also stated that chloride and potassium ions do not affect particle charge by adsorbing on the particle surface. Benton et al. (1993) reported that not the presence of counter ions but the concentration of barium ions and the barium to sulfate ion ratio controlled the particle morphology in their experiments. These results can be taken as a verification that potassium and chloride

ions have no influence on the precipitated particle morphologies described in Chapter 4. The morphologies of the barium sulfate particles are due to the influence of barium or sulfate ion excess and their resulting behaviour on the particle surface only.

## 4 Experimental results and discussion

In this Chapter, the morphologies and the measured mean particle lengths and size distributions for the experimental series listed in Chapter 3 are presented and discussed. SEM images of the particles precipitated are presented to visualise the morphologies.

### 4.1 Particle morphologies

In the following, the particle morphologies of the experiments are discussed by use of the SEM-pictures obtained.

#### 4.1.1 High supersaturation

Figure 17 shows particles precipitated at high supersaturation ( $S_a = 1336$ ) and varying feed rates as listed in Table 9. The reaction conditions were stoichiometric with 0.1 mol/l concentration of barium chloride in the vessel and potassium sulfate in the feed. The morphology of the particles are small agglomerated platelets. Compared with the values presented in Chapter 2.11, particles precipitated at  $S_a = 1336$  can be expected to be in the homogeneous nucleation region with diffusion controlled growth, and indeed they are small (about 1  $\mu\text{m}$  or smaller) and rather irregularly shaped when compared to the dendritic morphologies shown in the following subchapters.

No significant influence of the feed rate on particle shape can be observed for this high supersaturation region. Obviously, slower feeding does not suffice to decrease the local supersaturation ratio so that precipitation is out of the homogeneous nucleation region.

For all following experiments at lower supersaturation no agglomeration of particles could be detected. The scanning electron microscopy (SEM) images showed no agglomeration, and also the X-ray diffraction (XRD) measurements (Chapter 3.7) suggest that the particles have grown from one crystal and not to consist of agglomerated particles.

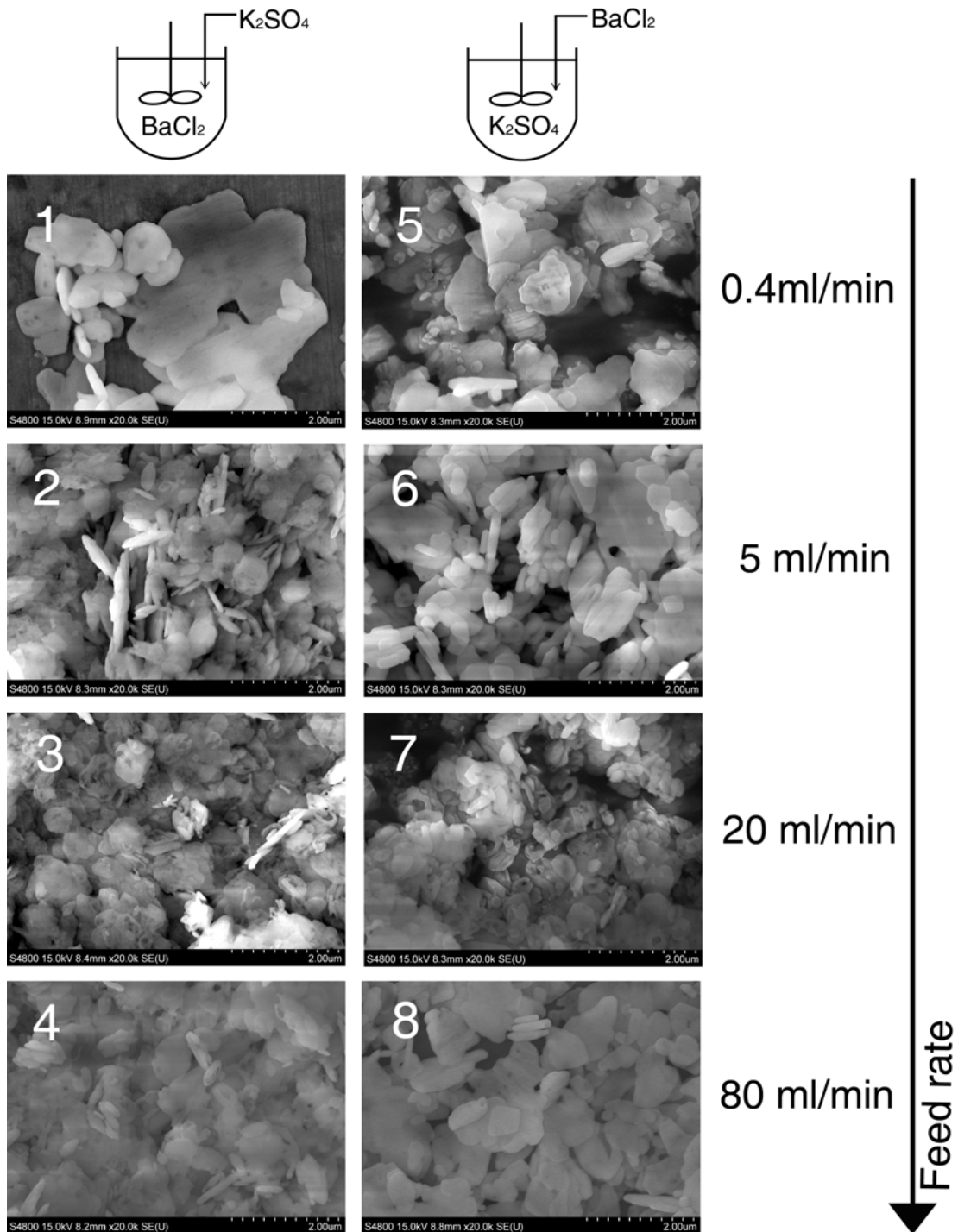


**Figure 17: Particle morphology at  $S_a = 1336$  and  $R = 1$ . Feed rates and feed sequence as specified (ref. Table 9).**

#### 4.1.2 Low feed concentration

Figure 18 shows particle morphologies for varying excess of barium or sulfate ions, respectively, expressed in terms of the reactant ratio  $R$ .

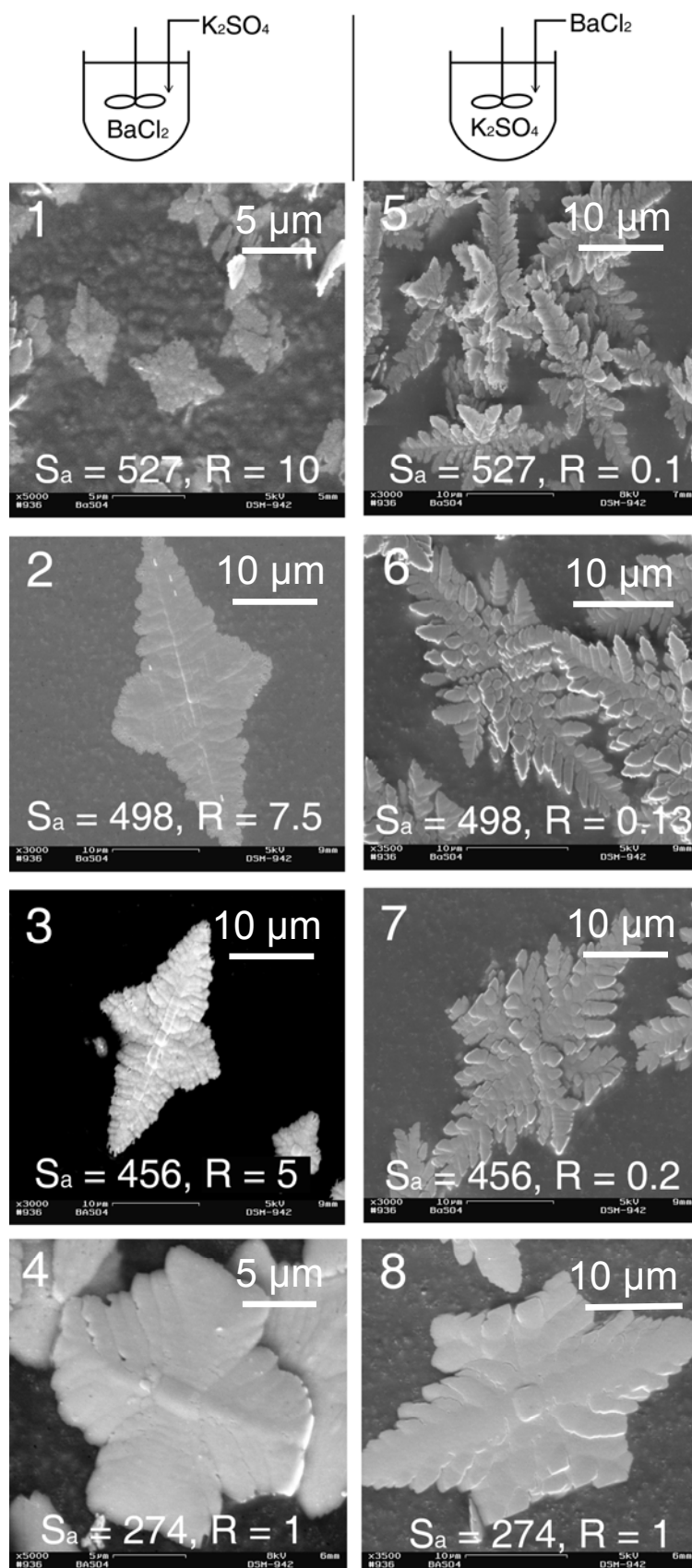


**Figure 18:** Particle morphologies obtained at varying reactant feed ratio  $R$  as indicated. Feed rate of 80 ml/min with lower concentration in the feed (first four rows of Table 10, same order as here). Supersaturation level changes because concentrations were chosen so that the amount of precipitated  $\text{BaSO}_4$  was the same for all experiments.

Concentrations were chosen in a way that the precipitated mass was kept constant, and the concentration in the feed was always equal to or lower than that of the second reactant in the tank. The first four entries in Table 10 list the feed and tank concentrations of the reactants used. Figure 18.1 to Figure 18.4 show particle shapes resulting for the case of different values of  $R > 1$  and potassium sulfate feed. Figure 18.5 to Figure 18.8 show the reverse experiments for  $R < 1$ , with potassium sulfate solution as feed and barium chloride reactant being provided in the vessel.

At  $R = 1$  and  $\text{BaCl}_2$ -feed, the particles precipitated are flat, four armed stars with one elongated axis, the stems in the other axis short and truncated. For  $\text{K}_2\text{SO}_4$ -feed, the particles resemble a flat four-armed star with symmetrical arms. The particles are generally larger for barium sulfate feed.

For  $R > 1$ , particles grow in a dendritic shape but flat with a very rough surface, like four-armed stars with one longer and one shorter axis. Overall, there does not seem to be much influence of the ion ratio on the particle shape within the supersaturation range investigated.

For  $R < 1$ , the particles change from flat to three-dimensional appearance as secondary dendrite branches start growing away from one main particle axis.

In Figure 19, particle morphologies for varying feed rates are shown at a theoretical initial supersaturation level of  $S_a = 527$  as listed in Table 10. The concentrations were chosen so that for potassium sulfate feed the ion ratio results in  $R = 10$  (Figure 19.1 to Figure 19.4) and for barium chloride feed,  $R = 0.1$  (Figure 19.5 to Figure 19.8).

For  $R = 10$ , particles grow along two axes, and are flat along the third. The particle surface is a plane at low feed rates, but gets more covered with growth structures for increasing feed rate. The shape varies from dendritic for the fastest feed rate, to flat platelets with jagged brims for medium and platelets for the slowest feed rate. For decreasing feed rate, the edges of the particles get sharper.

For  $R = 0.1$ , the particles grow into all three dimensions. As described above, for the fastest feed rate, the particles are dendrites with one elongated axis and branches arising from it. For decreasing feed rate, the number of arms decrease and the edges get sharper. For the slowest feed rate, the particles grow blocklike, the three planes equally developed. In general, particles seem to be bigger than for  $R = 10$ .

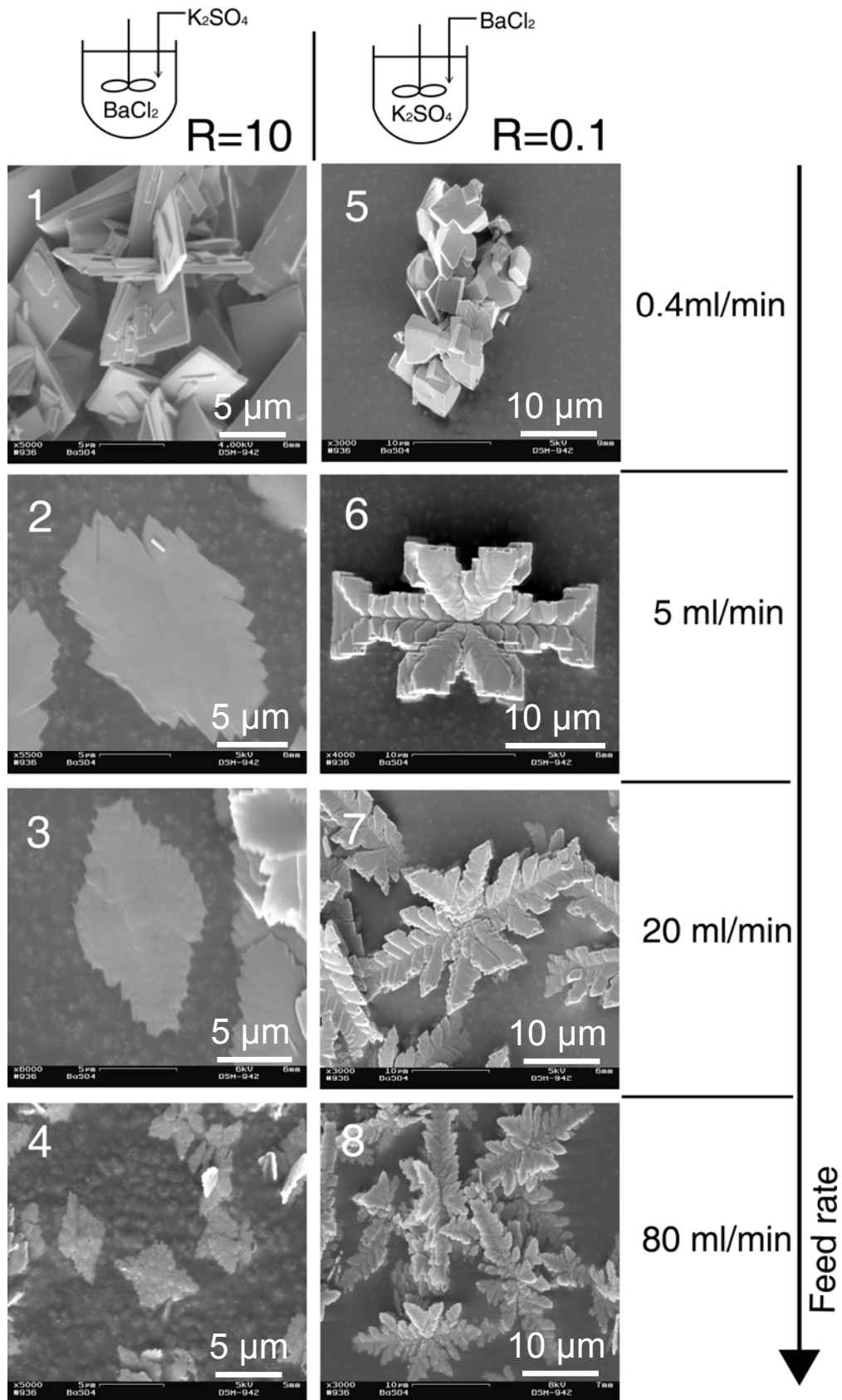


Figure 19: Particle morphologies for varying feed rate at  $S_a = 527$  with lower concentration in the feed (Table 10). Feeding sequences, ion ratios and feed rates as indicated.

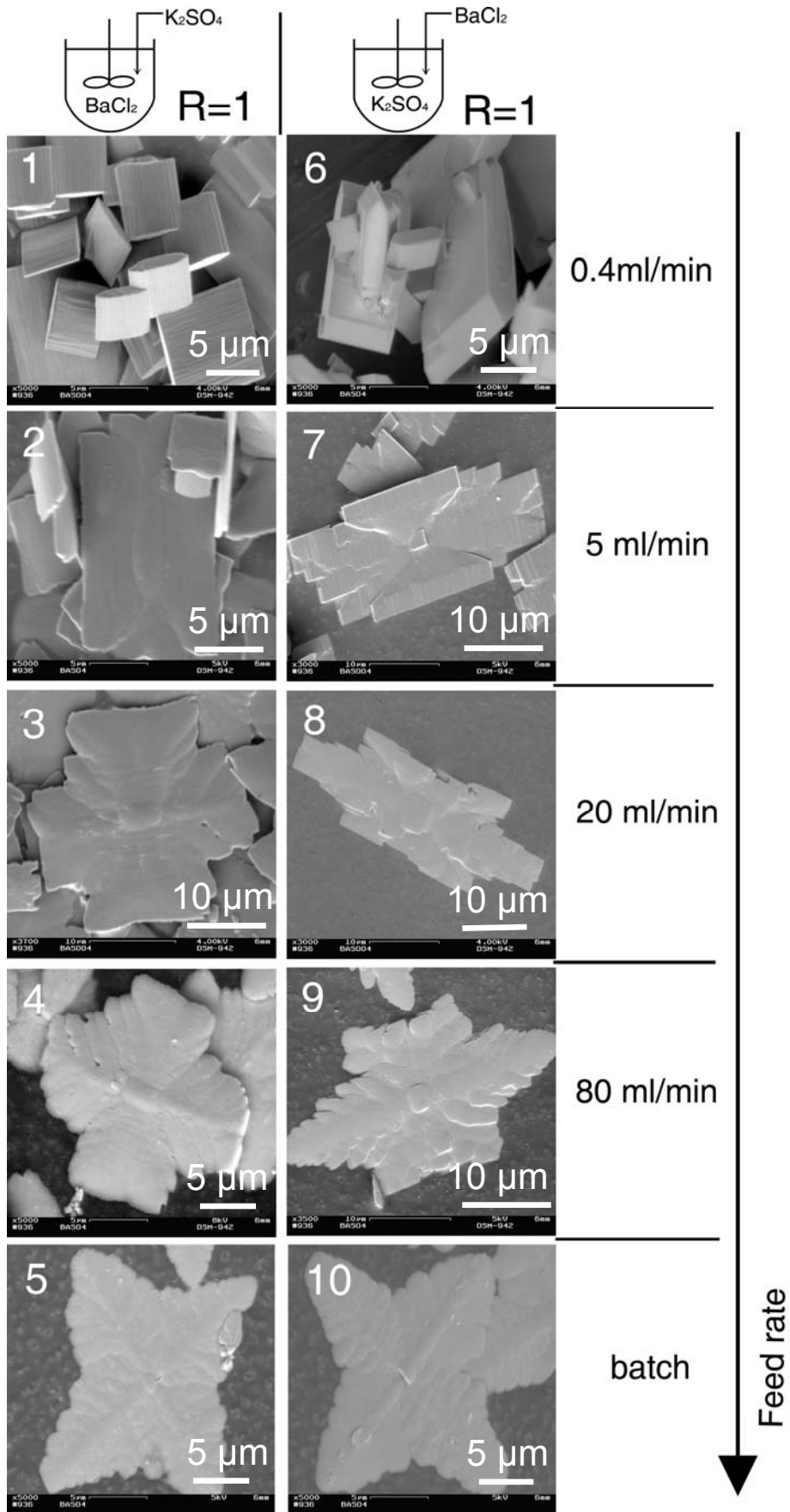


Figure 20: Particle morphologies for varying feed rate at  $S_a = 274$  and  $R = 1$  (Table 10). Feed rates and sequence as specified.



Figure 20 shows particle morphologies for varying feed rates and stoichiometric precipitation with 0.01 mol/l concentration for both ion solutions, leading to a theoretical initial supersaturation of  $S_a = 274$  and an ion ratio of  $R = 1$ , as listed in Table 10. Figure 20.1 to Figure 20.5 show the particle forms for potassium sulfate feed. Figure 20.6 to Figure 20.10 refer to the reverse case, i.e. barium chloride was fed to the reactor.

For slow feed, the particles were lenticular for potassium sulfate feed. For the reverse case, the crystals were also lenticular-shaped but with sharpened rims. For  $K_2SO_4$ -feed, structures like growth of different surface layers can be seen. For barium chloride feed, the edges are sharper, and the surfaces are plainer.

For increasing feed rate, excrescences appear up to a dendritic appearance, but the particles remain flat. Figure 20.5 and Figure 20.10 show the batch experiments for both feeding sequences that are carried out for comparison. Here, the same morphology for both sequences can be observed, as already reported in literature for batch operation (Aoun et al., 1999). For semi-batch operation however, differences in morphology are present for the two feeding sequences. For potassium sulfate feed, particles have the shape of a “cross” with two main axes of equal length. For barium chloride feed, the particles show one dominant growth direction, leading to elongated particles. The particles are bigger than for potassium sulfate feed.

For both experiments with the lowest feed rate (Figure 19.1, Figure 19.5, Figure 20.1, and Figure 20.6) the particles seem to be grown together at different angles like it can happen if growth occurs on imperfections in the crystal lattice. New growth layers of different orientation appeared, leading to what seems to be primary particles growing on particles. This phenomenon is not necessarily caused by agglomeration but by continued growth in different growth directions, as it was also observed in literature, although for higher concentrations (Fitchett and Tarbell, 1990).

#### 4.1.3 Higher feed concentration

Figure 21 and Figure 22 show SEM-pictures of particles precipitated with the experimental conditions listed in Table 11. For all of these experiments, the concentration in the feed was higher than of the salt solution provided in the vessel. The concentration ratio was the same as for the experiments with low feed concentrations above, but concentrations of feed and in the tank are reversed so that the feed concentration is the higher one in each case.

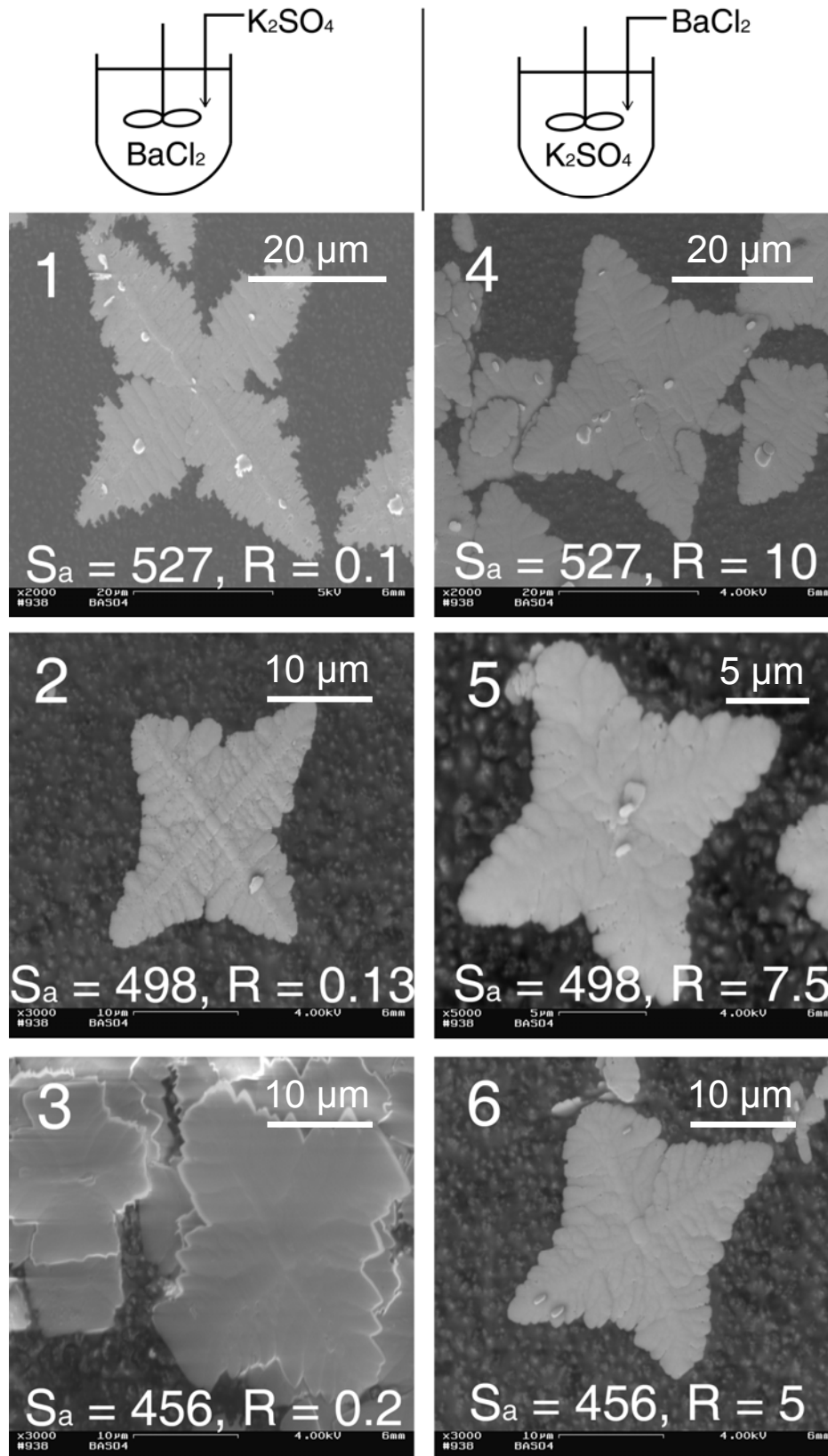


**Figure 21: Particle morphologies for varying  $R$  as indicated at a feed rate of 80 ml/min with higher concentration in the feed (Table 11). Amount of precipitated  $\text{BaSO}_4$  was the same for all experiments.**

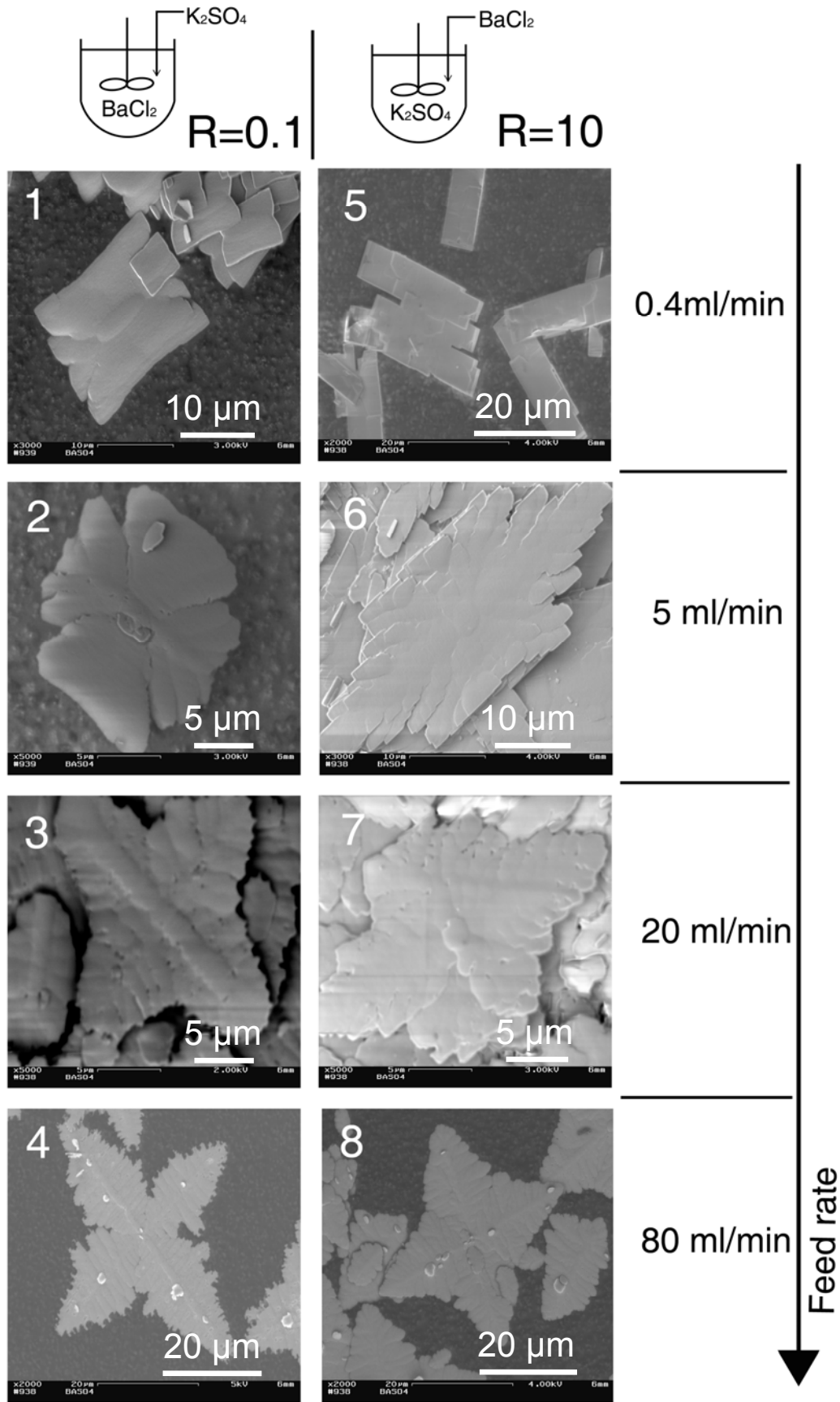


Figure 22: Particle morphologies for varying feed rate at  $S_a = 527$  with higher concentration in the feed (Table 11). Feed rate and sequence as specified.

In Figure 21 it can be seen that for ion solution provided in the vessel of 0.01 mol/l and 80 ml/min feed rate, all experiments with this feed rate lead to morphologies that look like the four-armed stars like for the case of  $S_a = 275$  and  $R = 1$ , batch case (Figure 20.5 and Figure 20.10), regardless of the concentration in the vessel.

Figure 22 shows the particle morphologies for varying feed rates and higher concentration in the feed as listed in Table 11. It is the direct reverse feeding sequence as for the experiments of Figure 19. Similar morphologies to the experiments shown in Figure 20 ( $S_a = 275$  and  $R = 1$ ) can be observed. In Figure 20 also the ion species provided in the vessel had the same concentration like the feed of 0.01 mol/l. This similarity in morphology occurs for both possible feeding sequences for the ion species, but always for higher feed rate than for the stoichiometric conditions: For 80 ml/min, the morphology of the experiments with the higher feed concentrations are equivalent as for the batch case of Figure 20. For feed rate 20 ml/min, the morphology is the same as for 80 ml/min in Figure 20. For 5 ml/min feed rate, it is the same as for 20 ml/min of Figure 20, and for 0.4 ml/min the morphology of the particles is the same as for 5 ml/min in Figure 20.

## 4.2 Discussion of influences on morphologies

Concerning the dependence on supersaturation, the particle shapes observed are consistent with the literature reports which are mentioned in the introduction. They show sharper edges at lower supersaturation, small particles at high supersaturation, and dendritic growth for intermediate stages of supersaturation. Influences of ion ratio, feed rate and feeding sequence will be discussed separately in the following subchapters. They could only be identified for low to medium supersaturation levels. At high supersaturation ( $S_a = 1336$ , Figure 17), no influence was detectable according to the SEM images.

### 4.2.1 Influence of ion excess

Changes reported in particle morphology for ion excess are smaller particles for  $R > 1$  than for  $R < 1$ , which is also the result for all experimental series for  $R > 1$  in this work, where the particles are mostly smaller in comparison for the reverse case at the same supersaturation level.

Not reported yet in the literature is the growth into the third dimension observed here for  $R < 1$  in comparison to flat particles for  $R > 1$  for the same supersaturation. Apparently, growth into the third dimension gets hindered in case of barium ion excess and probably enhanced for sulfate ion excess. A possible reason could be the

difference in diffusion of the ions to the particle surface. Diffusion coefficients calculated from the conductivity of ions at infinite dilution (Atkins, 1996) are  $D_{Ba} = 8.47 \times 10^{-10} \text{ m}^2/\text{s}$  for barium ions, and  $D_{SO_4} = 1.1 \times 10^{-9} \text{ m}^2/\text{s}$  for sulfate ions. Hence, the diffusion of barium ions is slower, which could explain the growth of arms into the bulk for sulfate excess as they grow to the higher concentration of barium ions. Nevertheless, this would only be of interest for the region of diffusion-controlled growth. For the very slow dosing where integration-controlled growth can be assumed to be dominant, the particles are cubes for sulfate excess (Figure 19.5) and platelets for barium excess (Figure 19.1). It seems that the adsorption of ions on the particle surface and the resulting electrical potential forces have also influence on the ion movement to and the attachment on the surface and therefore on the face growth rates for ion excess. As mentioned in Chapter 2.5, the preferred ion species adsorbed on the barium sulfate particles are barium ions. For excess of barium ions in the electrolyte solution, it is possible that in addition to the layer of barium ions near the surface, the concentration of sulfate ions in the vicinity of the particle is additionally decreased, hindering the growth on certain particle faces. Vice versa, for excess of sulfate ions, the effect of the barium ion layer near the surface could be reduced by a higher concentration of sulfate ions, leading to an increase in growth rate for certain faces.

Yet, for semi-batch feeding, the influence of ion excess is only crucial for the ion species provided in the vessel. A high concentration of ionic species in the feed does not have the same effect as if the same ion species is provided with high concentration in the vessel, as will be discussed in the following two subchapters.

#### 4.2.2 *Influence of feeding sequence*

Figure 20 shows the influence of the feeding sequence on the particle morphologies for precipitation in a semi-batch reactor. Precipitation was stoichiometric, and all experiments of this series had the same theoretical initial supersaturation. For batch experiments, no influence of the feeding sequence can be detected. Yet, for semi-batch the morphologies observed are different for the different feeding strategies as described earlier, as well as mean particle diameters being smaller for potassium sulfate feed (particle size distributions please ref. to Chapter 4.4). Influence on morphology for the different feeding sequences results from the fact that the ions of the salt solution provided in the vessel are present in excess at the beginning of the

experiment even if stoichiometric concentrations were chosen, and thus, nucleation and growth rates get influenced by the feeding sequence for semi-batch precipitation. Comparison of the pictures of Figure 18.1-3 with Figure 21.4-6 and Figure 18.5-7 with Figure 21.1-3 give morphologies for reverse sequences for non-stoichiometric semi-batch feeding. Here the influence of feeding sequence is very strong. As can be seen, if the higher concentrated ion species is in the feed (“high feed concentration”) there is nearly no effect on the particle morphologies for faster feed rate as already described in Chapter 4.2.1. For all experiments the resulting morphology was the same as the batch experiment at lower supersaturation.

When comparing Figure 19 and Figure 22, one can conclude that high feed concentrations at low feed rates lead to the same morphologies as low feed concentrations at high feed rates (such as those shown in Figure 20).

It seems that the concentration of the salt solution provided in the vessel defines the morphologies in all cases. The feed concentration has not the same influence as the ion excess would have if the higher concentration would be provided in the vessel. This is due to the fact that the ions provided in the vessel are present in excess in comparison to the ions in the feed. It can be concluded that increasing the concentration of the fed salt solution has the same influence on the morphology as increasing the feed rate for a lower concentrated feed solution.

#### 4.2.3 *Influence of feed rate*

Lower feed rate means less amount of reactant fed per unit of time, leading to a lower concentration level in the reactor and thus a lower supersaturation. The dominant precipitation mechanisms are supposed to change accordingly as mentioned in Chapter 2. And indeed, the expected behaviour can be seen for the two feed rate series that were carried out. At  $S_a = 527$ , precipitation mechanisms are supposed to be homogeneous nucleation and diffusion-controlled growth. The fact that particles are rather big, showing dendritic behaviour at the highest feed rate, leads to the conclusion that the influence of homogeneous nucleation is still low, though. The reason lies in the lower overall supersaturation during the semi-batch precipitation in comparison to batch, since even at the highest semi-batch feed rate investigated it still took more than four minutes until all liquid was pumped into the vessel. Therefore, it can be assumed that the theoretical supersaturation of  $S_a = 527$  was not reached. This is also true for the morphologies of the particles precipitated for lower feed rates in both series. For lower feed rate and lower concentration in the

feed, they have sharper edges, less dendritic branches, up to cuboid shapes for the lowest feed rate, where growth seems to have shifted to the polynuclear mechanism forming plain surfaces (Figure 19). It can be seen that for the lowest feed rate, particles are not agglomerated but rather seem to have grown on to another, assumingly by surface nucleation events that lead to new growth sites of different orientation (Figure 19.1, Figure 19.5, Figure 20.1, and Figure 20.6). It can be concluded that for lower feed rate, nucleation has shifted to the heterogeneous mechanism. Comparing the compact cuboidal shapes for low and dendritic forms for high feed rates, the crystals' structure seems to have a higher long-range order in case of the slower dosing.

The concentration of the salt solution provided in the vessel defines the possible morphologies. Increasing the feed rate has the same influence on the morphology as increasing the fed salt solution concentration, as can be seen if comparing Figure 20 with Figure 22.

Figure 23 illustrates the influence of the feed rate using the experiments at  $S_a = 274$  and  $R = 1$  as listed in Table 10 (lower feed concentration). Lines of constant supersaturations and  $R = 1$  as indexed are plotted. Supersaturation values are calculated using Eq. (13). The precipitation regions defined by Li et al. (2007) are also indicated as described in Chapter 2, namely the growth region (I), the transition regions combined (II), and the nucleation region (III).

Precipitation experiments for different feeding policies are shown as trajectories of the changing barium and sulfate ion concentrations and the resulting supersaturations and ion ratios during precipitation, together with the particle shapes obtained.

For the trajectories, the diagram does not give quantitative values. A figure with quantitative, calculated trajectories will be shown in Chapter 6.3.2 (Figure 49). The trajectories shown here in Figure 23 are meant as a qualitative visual impression of the conditions leading to the different particle morphologies for the different feeding policies. Pictures of the resulting particle shapes are included for the different trajectory paths.

The trajectories in the right and left hand corner are for barium chloride and potassium sulfate feed, respectively. All trajectories start at  $S_a = 1$  and the concentration of the ion species provided in the tank, i.e. 0.01 mol/l. Depending on the feed rate, they reach a maximum supersaturation before they all aim for the solubility point at  $R = 1$ . The cross labelled  $e$  indicates the batch conditions, i.e. the

highest possible supersaturation  $S_a = 274$ . It can be seen clearly how regions change for changing flow rate, despite the same starting points of the experiments.

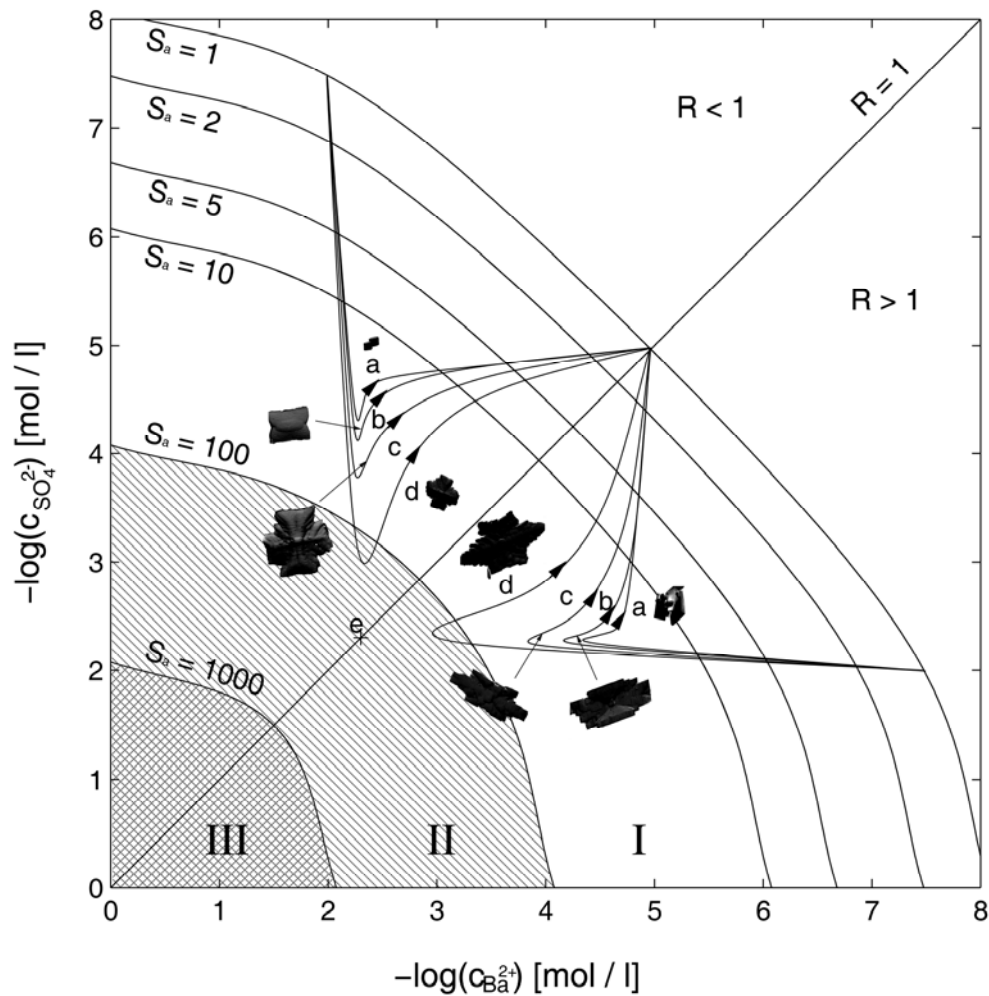


**Figure 23: Trajectories of the changing barium and sulfate ion concentrations ( $S_a = 274$  and  $R = 1$ ) with particle shapes. Feed rates: a) 0.4 ml/min, b) 5 ml/min, c) 20 ml/min, d) 80 ml/min; e) initial point for batch precipitation; I: growth region, II: transition region, III: nucleation region as stated by Li et al. (2007).**

The findings above are only valid for theoretical initial supersaturations of less than approximately  $S_a = 1000$ . For higher concentrations, reduction of feed rate does not change the particle morphologies significantly as can be seen in Figure 17. Here, concentrations are so high the mixing in the vessel does not suffice to prevent high local supersaturation peaks where homogeneous nucleation occurs, leading to the formation of small and agglomerating particles.

In summary it can be stated that the particles' morphology is influenced on the one hand by the concentration of the salt solution provided in the vessel, and on the other hand by the feed concentration in combination with the feed rate. The concentration



of the inlet feed is formed by the actual concentration of the ion solution in the feed in combination with the feed rate.

#### 4.2.4 *Influencing particle morphology by feeding policy*

The dependencies stated above at theoretical initial supersaturations  $S_a < 1000$  for semi-batch precipitation in a stirred vessel with one feed can be summarized to the following concerning the resulting particle morphologies:

- Slow dosing with higher feed concentration gives equivalent results as faster dosing with lower feed concentration.
- High concentrations in the feed do not influence the morphology as much as high concentrations in the vessel. Morphologies are therefore best influenced by high vessel concentrations in combination with lower feed concentrations. Trying to influence the morphology by using higher feed concentrations is ineffective. The same effect can be achieved (more reliably) by lower feed concentration in combination with higher feed rate.
- Smaller and flatter crystals are achieved for potassium sulfate feed.
- Larger and more star-like shapes are achieved for barium chloride feed.
- The intensity of the shape characteristics increases for increasing ion ratio  $R$  or  $1/R$  for barium or sulfate excess, respectively.

In conclusion, the following recommendations for the feeding policy of choice for achievement of particles of specified morphology for un-seeded precipitation can be given:

- For cuboid particles, barium chloride feed of lower concentration than the potassium sulfate solution in the vessel should be dosed to the reactor at very low feed rates.
- For flat platelets, potassium sulfate feed of lower concentration than the barium chloride in the vessel should be dosed to the reactor at very low feed rates.
- For star-like crystals with dendritic branches in all space directions, barium chloride feed of lower concentration than the potassium sulfate in the vessel should be dosed to the reactor at higher to medium feed rates.
- Flat dendrites can be achieved by one of the following:
  1. For star-like but flat (“two-dimensional”) crystals, one can chose either batch precipitation of lower concentrations, or high to medium feed rates

at higher concentration in the feed. Both possibilities are independent of feed sequence.

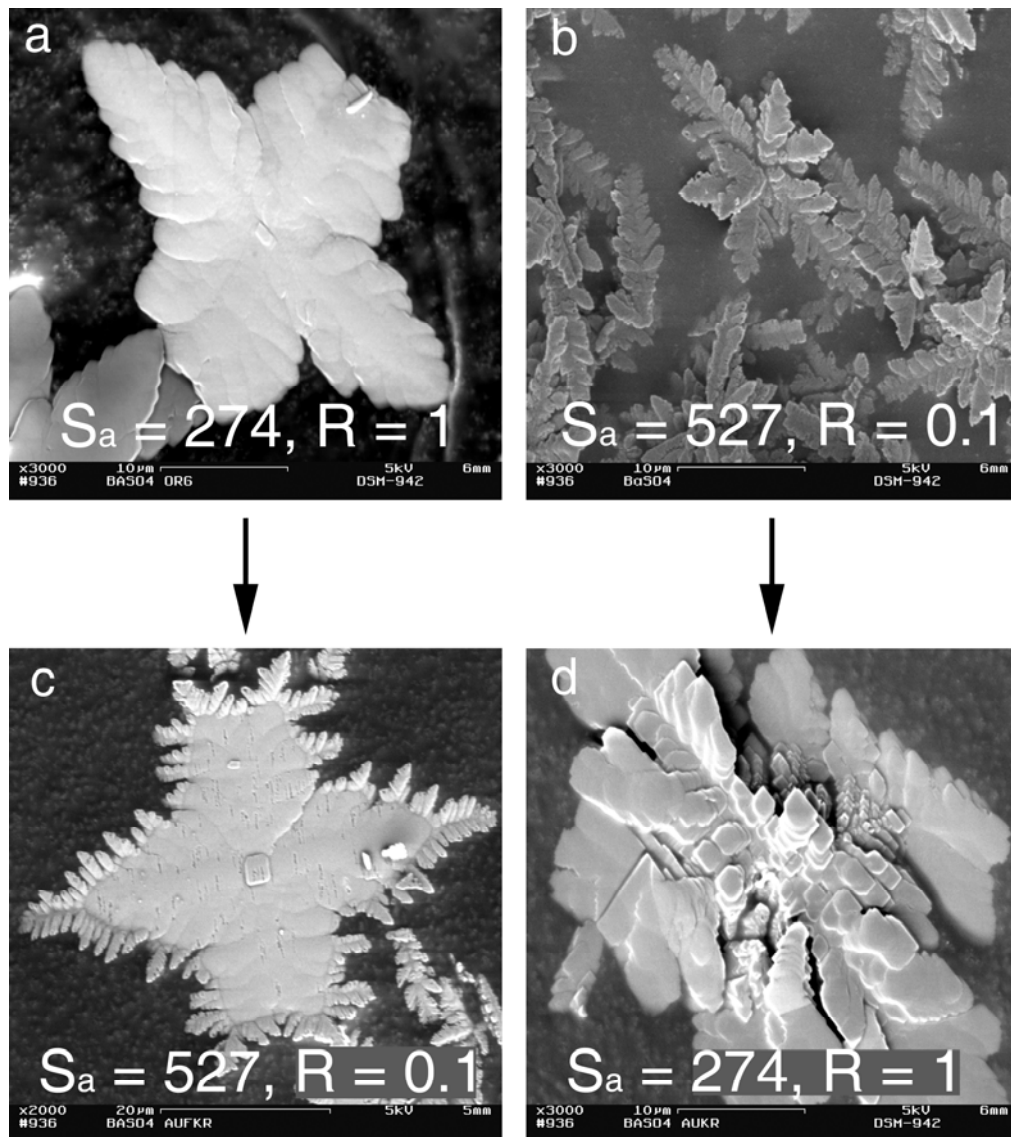
2. For cross-like flat crystals with two equal axis lengths, potassium sulfate should be in the feed either dosed to the vessel at medium feed rates for stoichiometric conditions or dosed at higher feed rates for  $R < 1$ .
3. For elongated flat dendrites, barium chloride should be in the feed dosed at medium feed rates for stoichiometric conditions.

For seeded precipitation, the resulting particle sizes and morphologies are dependent on the characteristics of the seed crystals as discussed in the next subchapter.

### 4.3 Seeded precipitation

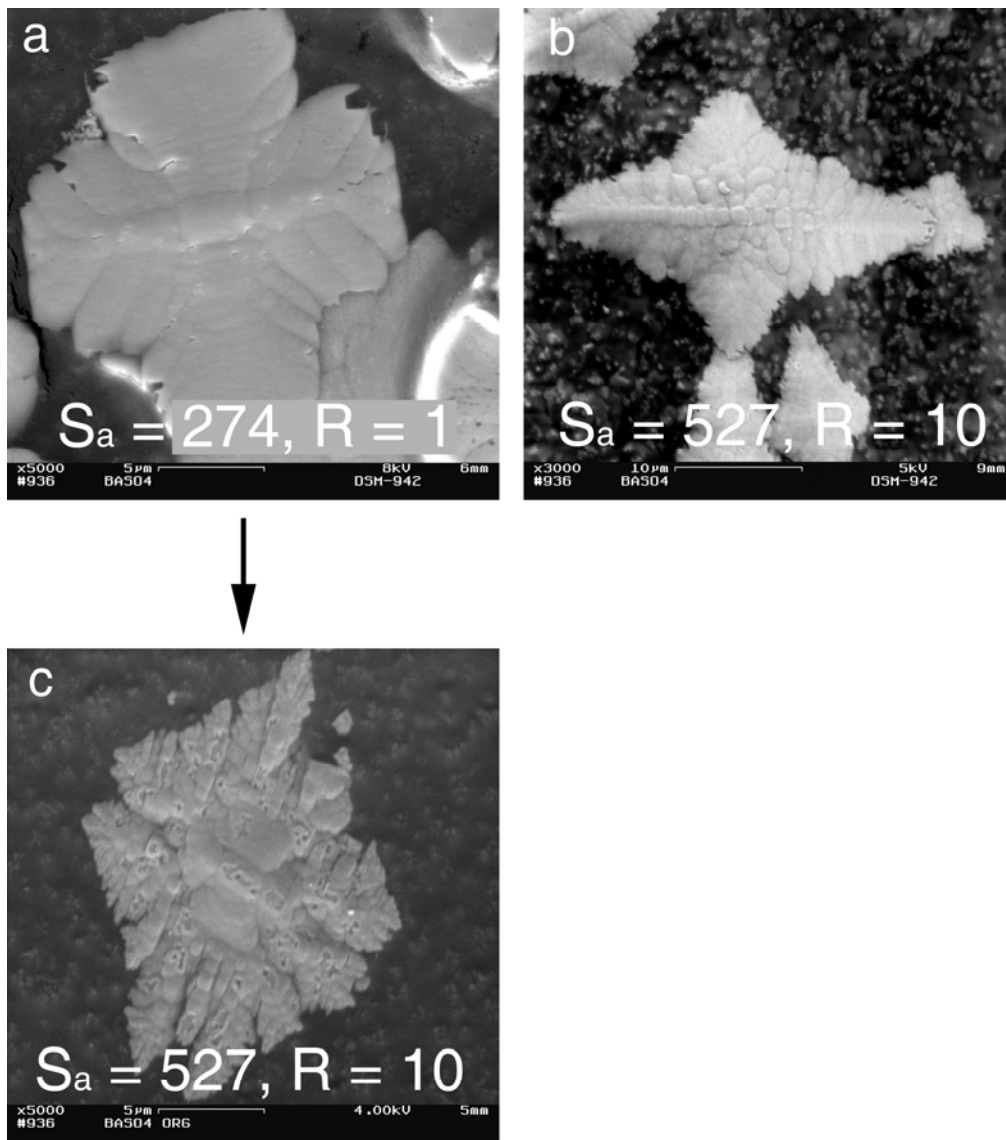
Figure 24 to Figure 26 show particle morphologies for seeded precipitation experiments. In all three cases, the pictures on top show the original particles if precipitated without seeds for the experimental conditions used as they were described in the previous subchapters. The picture(s) below show the product particles grown on the specified seeds.

In Figure 24c the seed particles were precipitated at medium supersaturation ( $S_a = 274$ ) and  $R = 1$  with barium chloride feed and potassium sulfate provided in the vessel. The seeded precipitation was then carried out at  $S_a = 527$  and  $R = 0.1$ , also with barium chloride feed. In Figure 24d, the two experimental conditions were reversed: First seed particles were precipitated for  $S_a = 527$  and  $R = 0.1$  and barium chloride feed. Seeded precipitation was carried out with  $S_a = 274$  and  $R = 1$ , also with barium chloride in the feed. Figure 24a and b show the crystal morphologies obtained in case of non-seeded precipitation for the two experimental conditions.



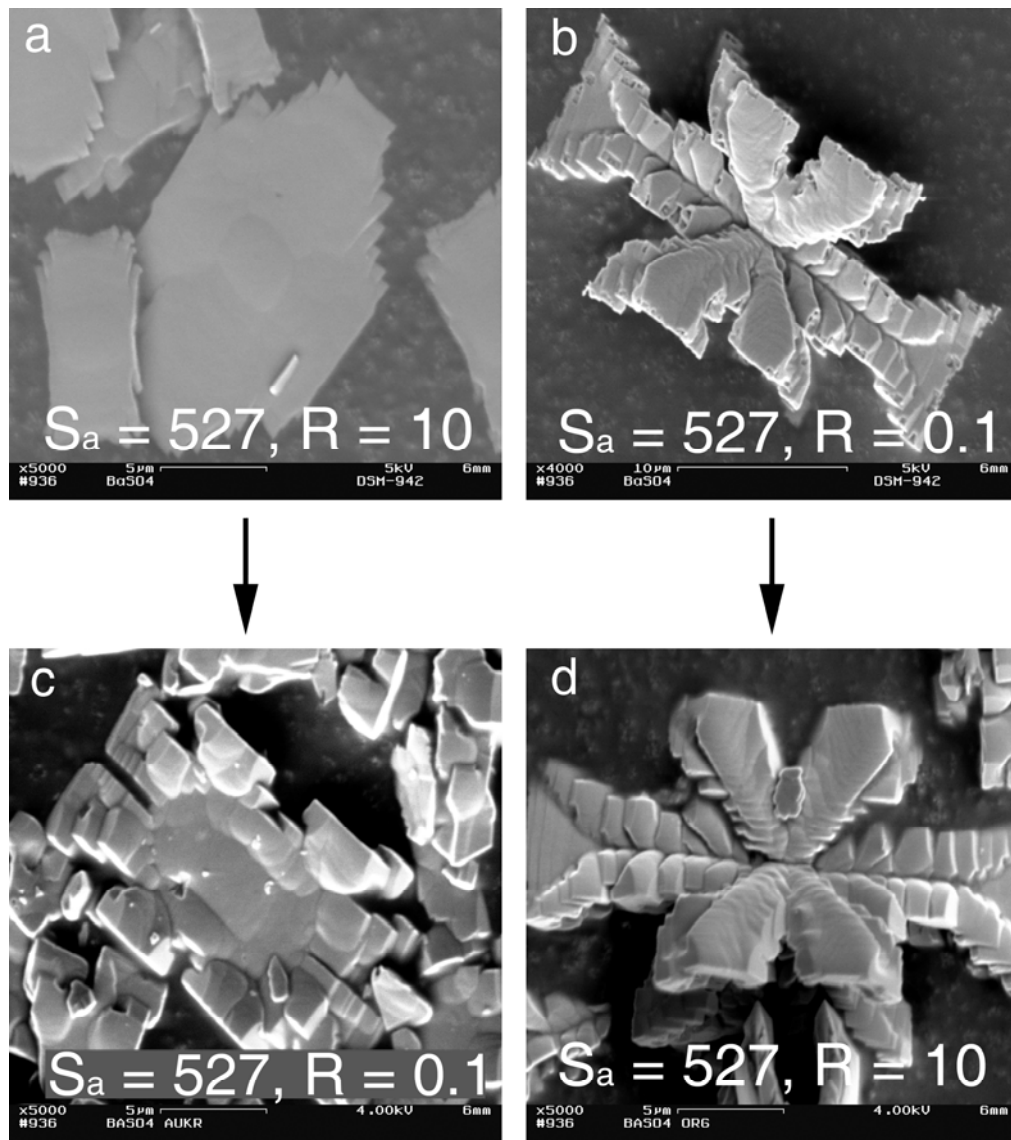
**Figure 24:** In all cases: barium chloride feed, 80 ml/min feed rate. Operation conditions as listed in the images. a: Seed crystal as used in c. b: Seed crystal as used in d. c: resulting particle of seeded precipitation (Figure 24a shows seed crystal); d: resulting particle of seeded precipitation (Figure 24b shows seed crystal).

Figure 25c shows the resulting particulate product for seed precipitation for the experimental conditions  $S_a = 527$  and  $R = 10$ , potassium sulfate feed. Seed crystals were precipitated at  $S_a = 274$  and  $R = 1$ , potassium sulfate feed (Figure 25a).



**Figure 25:** In all cases: potassium sulfate feed, 80 ml/min feed rate. Operation conditions as listed in the images. a: Seed crystal as used in c. b: Particle precipitated in conditions of c for comparison. c: resulting particle of seeded precipitation (Figure 25a shows seed crystal).

Figure 26c shows the product of seeded precipitation with seed particles produced at  $S_a = 527$  and  $R = 10$ , potassium sulfate feed, as shown in Figure 26a. Seeded precipitation was then carried out at  $S_a = 527$  and  $R = 0.1$ , barium sulfate feed. Feed rate in both cases was 5 ml/min. Figure 26b shows the original, non-seeded particles that form at the conditions that were used for the seeded precipitation experiment. In Figure 26d, the reversed seed precipitation was carried out: Seed crystals were produced at  $S_a = 527$  and  $R = 0.1$ , barium sulfate feed (Figure 26b shows a seed crystal). Seeded precipitation was carried out at  $S_a = 527$  and  $R = 10$ , potassium sulfate feed. Feed rate was also 5 ml/min in all cases.



**Figure 26:** For a and d: potassium sulfate feed. For b and c: barium chloride feed. In all cases 5 ml/min feed rate. Operation conditions as listed in the images. a: Seed crystal as used in c. b: Seed crystal as used in d. c: resulting particle of seeded precipitation (Figure 26a shows seed crystal); d: resulting particle of seeded precipitation (Figure 26b shows seed crystal).

In Figure 24c and Figure 25c the original particles can be clearly identified in the middle of the new particle. Their original shapes did not change during seeded precipitation. In Figure 24d, Figure 26c, and Figure 26d, it is harder to detect the seed crystals' original shape, as the particles were partly overgrown during seeded precipitation. Still their original shape can be identified. It has already been stated that the initial concentrations of a semi-batch precipitation operation determines the initial crystal morphology (van Leeuwen (1998), Wong et al. (2001)). Van Leeuwen (1998) observed in his experiments that initial supersaturation, i.e. the supersaturations, at which the particle was formed, dominates the morphology of the particle. For this the author precipitated particles at a higher supersaturation and let

them grow in a lower supersaturation region, choosing time and amount of growing material in a way that supersaturation for the growth experiments was held nearly constant, leading to only small amounts of precipitate growing on the particles. Van Leeuwen's experiments showed that the original morphology of the seed also gets preserved, if growth of the particle is continued in a solution of much lower supersaturation than the one it was precipitated in. The present work shows that this is also true if the conditions of seeded precipitation are different with regard to higher supersaturation, or ion species in excess, in the sense that the original seed crystals' original shape is not changed under the newly grown layers.

Under the conditions of the seeded precipitation of Figure 25c, the particle grew further, showing the flat morphology shape of the particle that would nucleate and grow under these conditions. In Figure 24c, new dendritic arms were precipitated at the sides of the seed particle that show the exact growth morphology as the particles nucleated and grown in the experimental conditions used (Figure 24b). For seeded precipitation shown in Figure 26c, the seed crystals were flat (Figure 26a). Only during the seeded precipitation they grew into the third dimension as could be expected when looking at the particle growth morphology for these experimental conditions (Figure 26b). In the reverse case, the branches of the dendritic seed crystal (Figure 26b) got overgrown during seeded precipitation (Figure 26d). In Figure 24d, the seed particle grew in shape of an elongated dendrite with several arms growing away from the main crystal axis (Figure 24b). When used as seed crystals, new layers of barium sulfate grew on the branches, showing the characteristic flat shape that was observed for the experimental conditions used as in Figure 24a. Thus, the branches got covered, nearly growing together to one continuous layer. This shows that albeit the original shape of the seed crystals gets preserved, the new layers during seeded precipitation grow in a pattern that is characteristic for the experimental conditions. In Chapters 4.1 and 4.2 definite reproducible growth morphologies are identified for certain precipitation conditions of the experimental set-up used. Apparently, these growth morphologies can also be observed if precipitation is carried out using differently shaped seed crystals.

Further, it can be concluded that particles grown in a certain experimental environment have active growth sites that are defined by the experimental conditions of the original solution the particle was precipitated in, as can be seen in Figure 24c. During precipitation of the seed crystal, the growth morphology of the experimental conditions lead to a flat dendrite, growing in two directions with the active growth

sites along the rim of the particle. Upon seeded precipitation, the seed crystal only grew further on the outer rim. The flat surface did not grow any branches. This is consistent with Liu et al.'s (1976) statement about active growth sites on seed crystals. Liu et al. concluded from their kinetic experiments concerning growth of seed crystals that for different seed crystal morphologies the crystals may contain quite different numbers of active sites per unit area for growth (or dissolution), leading to different densities of active growth sites on surfaces for differently shaped crystals. Van Leeuwen (1998) also noticed that his dendritic particles continued growing at the branches, and he formulated the theory that this is because they reach deeper into the bulk solution where the concentration of precipitant is higher. From the experiments of the present work it can be concluded that this is not the main reason. If exposed to other precipitation conditions, the particles grow on the active growth sites that were defined by the morphology of the original supersaturation. Thus, it can be concluded that for van Leeuwen's (1998) particles the active growth sites were on the branches of the dendrites, thus leading to their further growth.

Van Leeuwen (1998) also raised the question as to whether the particle would be totally overgrown and therefore would lose its shape, if the amount of available precipitant in the growth solution would be equivalent or higher to the amount used in the particle. From the figures presented here, e.g. by comparison of Figure 24c and d, it can be seen that this depends on the active growth sites of the original particle, as well as the growth morphology determined by the seeded precipitation conditions. While the seed crystal in Figure 24d gets overgrown by the more flat growth layers of the growth solution, in Figure 24c the original particle does not get overgrown in a noticeable manner.

#### 4.4 Particle sizes and size distributions

For laser particle sizers, it is appropriate to use the mass weighted mean particle length  $d_{43}$  for characterization of the particles (Marchisio et al., 2002), calculated by the fourth and third moment:

$$d_{43} = \frac{\mu_4}{\mu_3} = \frac{\int_L^{L_{\max}} L^4 \cdot q_3(L) dL}{\int_{L^*}^{L_{\max}} L^3 \cdot q_3(L) dL}. \quad (89)$$

Table 14 lists the median diameters  $d_{50}$  evaluated by the Aello and CILAS devices, Table 15 the mass weighted mean diameters  $d_{43}$  for the CILAS experimental results, calculated from the PSDs measured using Eq. (89).

**Table 14: Median particle diameters  $d_{50}$  as measured by Aello and CILAS devices for the experimental conditions as listed in Table 10.**

no. (same as in Table 10)	concentration of reactant [mol/l]		feed rate [ml/min]	$S_a$ [-]	Median particle diameter $d_{50}$ [ $\mu\text{m}$ ]					
	in vessel	in feed			$\text{K}_2\text{SO}_4$ feed			$\text{BaCl}_2$ feed		
					R	Aello	CILAS	R	Aello	CILAS
1	0.1	0.01	80	527	10	<b>5.97</b>	<b>6.20</b>	0.1	<b>5.36</b>	<b>8.04</b>
2	0.075	0.01	80	498	7.5	<b>5.80</b>	<b>6.96</b>	0.13	<b>6.40</b>	<b>12.16</b>
3	0.05	0.01	80	456	5	<b>4.45</b>	<b>7.12</b>	0.2	<b>5.66</b>	<b>16.27</b>
4	0.01	0.01	80	274	1	<b>4.44</b>	<b>10.57</b>	1	<b>4.79</b>	<b>19.31</b>
5	0.1	0.01	20	527	10	<b>3.64</b>	<b>5.59</b>	0.1	<b>5.48</b>	<b>11.26</b>
6	0.1	0.01	5	527	10	<b>3.12</b>	<b>7.69</b>	0.1	<b>5.93</b>	<b>13.79</b>
7	0.1	0.01	0.4	527	10	<b>2.90</b>	<b>5.57</b>	0.1	<b>5.53</b>	<b>24.38</b>
8	0.01	0.01	20	274	1	<b>3.87</b>	<b>14.53</b>	1	<b>5.54</b>	<b>15.27</b>
9	0.01	0.01	5	274	1	<b>4.19</b>	<b>11.53</b>	1	<b>8.05</b>	<b>23.67</b>
10	0.01	0.01	0.4	274	1	<b>1.39</b>	<b>15.31</b>	1	<b>3.42</b>	<b>26.92</b>
11	0.01	0.01	batch	274	1	<b>5.54</b>	<b>11.86</b>	1	<b>5.80</b>	<b>12.94</b>

**Table 15: Particle diameters  $d_{43}$  (Eq. (89)) as measured by the CILAS device for the experimental conditions as listed in Table 10.**

no. (same as in Table 10)	concentration of reactant [mol/l]		feed rate [ml/min]	$S_a$ [-]	Mass weighted particle diameter $d_{43}$ [ $\mu\text{m}$ ]			
	in vessel	in feed			$\text{K}_2\text{SO}_4$ feed		$\text{BaCl}_2$ feed	
					R	CILAS	R	CILAS
1	0.1	0.01	80	527	10	<b>8.17</b>	0.1	<b>16.4</b>
2	0.075	0.01	80	498	7.5	<b>19.9</b>	0.13	<b>20.3</b>
3	0.05	0.01	80	456	5	<b>14.5</b>	0.2	<b>26.6</b>
4	0.01	0.01	80	274	1	<b>15.3</b>	1	<b>35.0</b>
5	0.1	0.01	20	527	10	<b>9.24</b>	0.1	<b>22.0</b>
6	0.1	0.01	5	527	10	<b>12.0</b>	0.1	<b>23.4</b>
7	0.1	0.01	0.4	527	10	<b>17.1</b>	0.1	<b>51.8</b>
8	0.01	0.01	20	274	1	<b>23.0</b>	1	<b>33.3</b>
9	0.01	0.01	5	274	1	<b>20.0</b>	1	<b>45.7</b>
10	0.01	0.01	0.4	274	1	<b>38.0</b>	1	<b>77.3</b>
11	0.01	0.01	batch	274	1	<b>18.1</b>	1	<b>20.8</b>

Figure 27 shows the median length measured by the particle laser scatter device (CILAS) for experiments at different feed rates (600 ml/min referring to the batch



experiment). The same dependency for stoichiometric as well as non-stoichiometric conditions seems to be present depending on the barium and sulfate ion species in the vessel and the feed, respectively, although the data is rather scattered. For barium chloride feed there seems to be an overall increase in median particle size for decreasing feed rate, whereas for potassium sulfate feed, no significant influence can be detected.

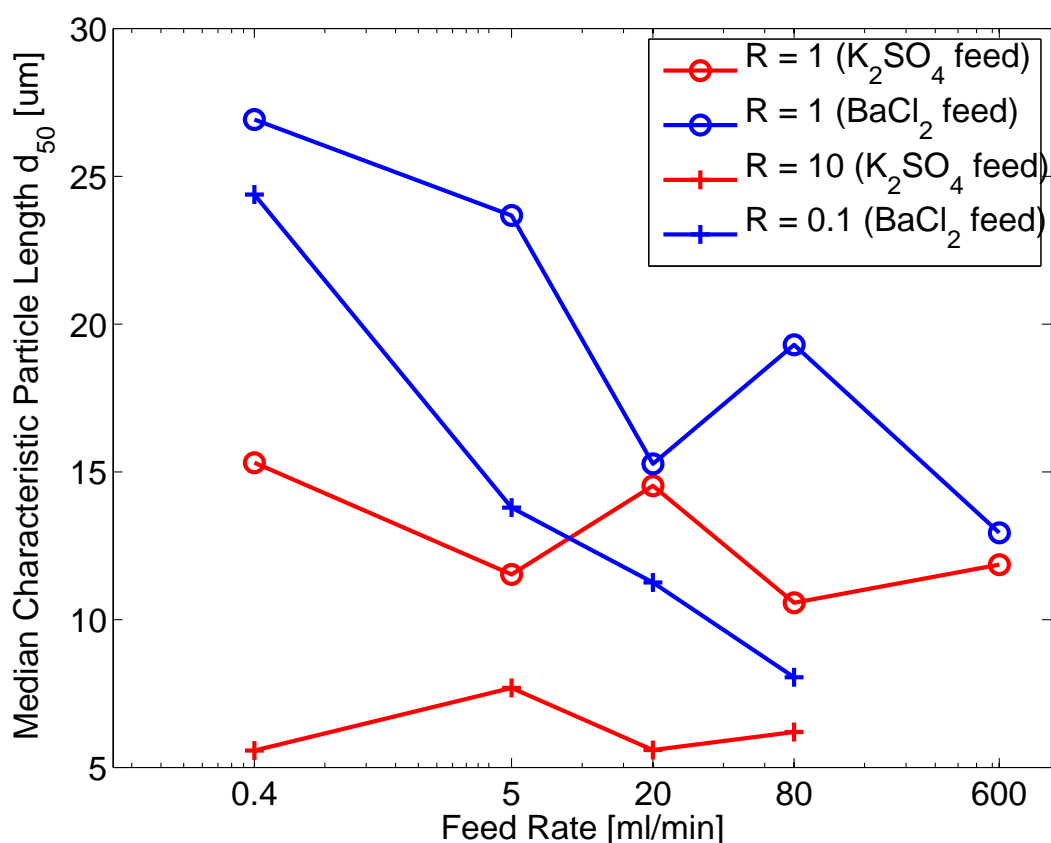


**Figure 27: Dependence of measured median particle size on feed rate.**

Figure 28 to Figure 38 show the measured PSDs and median diameters over time for the experiments listed in Table 10. On the left are the PSDs, on the right the median particle diameters over time for the experimental conditions as stated in the figure captions. All shown PSDs and mean particle sizes over time are averaged from several experimental runs. In Figure 39 (top), the main peak of the averaged PSD shows an additional bulge which results from different particle size peaks of the different experimental runs where each single run had only one PSD peak.

The median diameters measured over time with the Aello measuring device do not seem very trustworthy with regard to quantitative analysis. For the particles precipitated, the median diameters  $d_{50}$  evaluated by the Aello device were smaller than the median diameters calculated from the PSDs measured by the CILAS device

as it is shown in Table 14. As already stated in Chapter 3.5, the Aello device gives smaller particle sizes for standard spherical particles, thus a systematic error could be the reason here. Additionally, it is possible that the dendritic, flat particles moved through the narrow measuring slot of the Aello probe in an oriented way, thus leading to a smaller mean diameter than the real particles would otherwise give. Also, unfortunately the calculated mean diameter seems to fluctuate between two numerical solutions, as can be seen in Figure 32 (bottom) and Figure 35 (bottom).

For experiments with higher concentrations (Table 9), the particle concentrations were too high for the Aello device to give a mean diameter. The value of zero for the median particle diameter at the beginning of some experiments does not necessarily mean that no particles were present, as the concentration of particles was too low for the device to recognize a signal. The measurements gained with the Aello device showed good reproducibility from one experimental run to the next, but all in all the results were not considered to be significant in a quantitative way due to the problems of the data evaluation mentioned.

All in all it can be seen that the mean diameter is smaller for  $K_2SO_4$ -feed in comparison to  $BaCl_2$ -feed. This is easily explained for the  $Ba^{2+}$  ion excess that is present if barium chloride is provided in the vessel.  $Ba^{2+}$  ion excess leads to smaller particle sizes, as stated in the literature and mentioned in Chapter 2. Only in one case, measured mean particle sizes for  $BaCl_2$ -feed are smaller (Figure 28.1, bottom), but this finding is not confirmed by the PSD-measurements of the CILAS device, which seem to be more trustworthy. It could be that the orientation of the dendritic particles in the measuring zone of the Aello-probe had an influence on this result. For nearly all experiments, the particle size increases throughout the feeding process. This makes sense as during the feeding new reactant is added to the vessel and the particles grow further. For the batch case (Figure 38, bottom), there is a decreasing particle size for the time after the end of feeding time (at ca. 35 s). A possible explanation for this decrease could be the breakage of dendritic particles at the stirrer and reactor walls.

Because of the problems mentioned, the measuring results for the mean diameter over time are not taken into further consideration in this work.

The measured mean particle diameters by the CILAS device are always smaller for  $K_2SO_4$  feed than  $BaCl_2$  feed as listed in Table 14 and Table 15. This is consistent with the PSD peaks that are at smaller sizes for nearly all experiments with potassium sulfate feed.

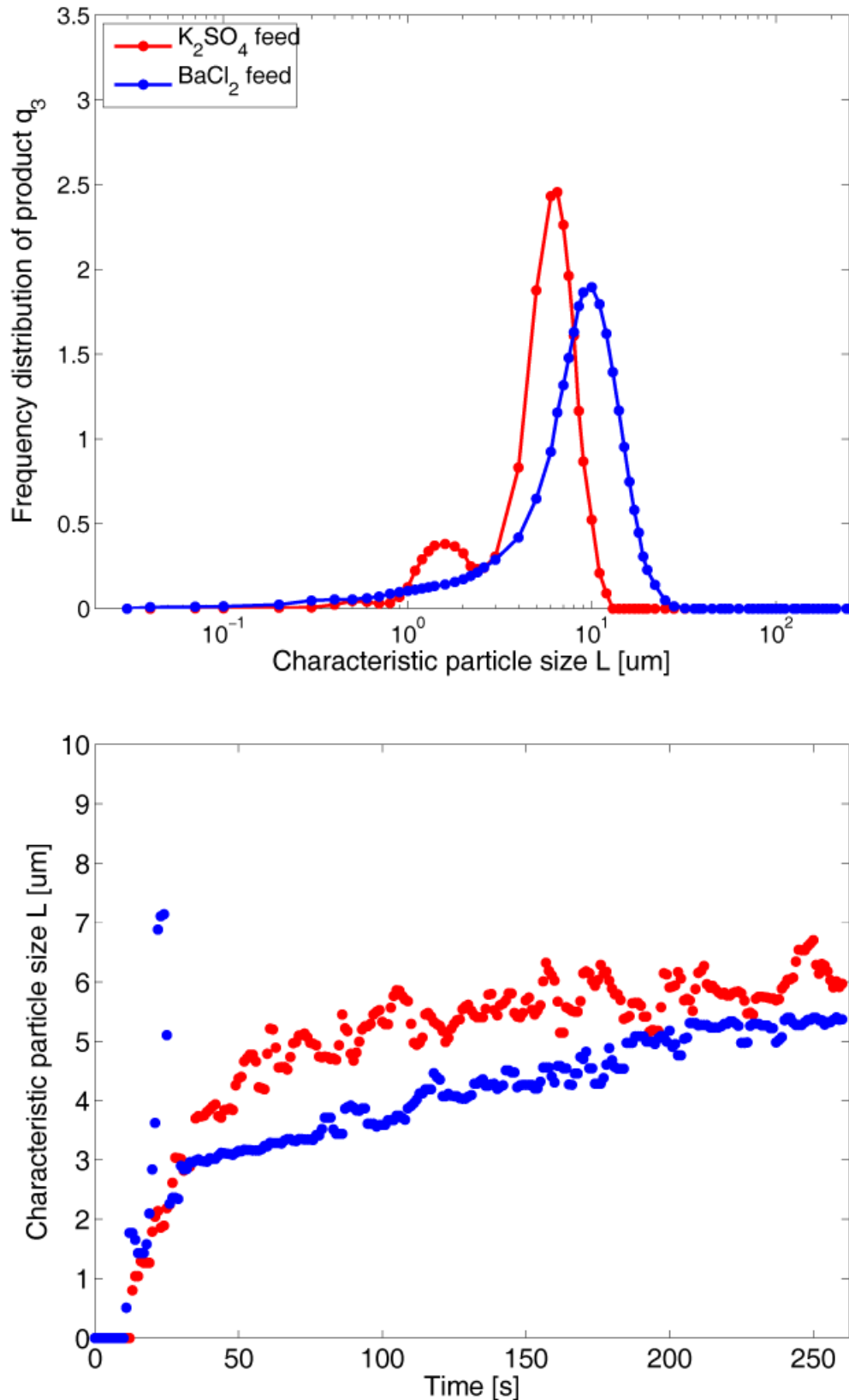


**Figure 28: Top: Measured particle size distributions (CILAS). Bottom: Mean particle diameter over time (Aello). Experimental conditions as in line 1 of Table 14:  $S_a = 527$ , feed rate 80 ml/min;  $\text{K}_2\text{SO}_4$  feed:  $R = 10$ , SEM image of morphology: Figure 18.1;  $\text{BaCl}_2$  feed:  $R = 0.1$ , SEM image of morphology: Figure 18.5.**

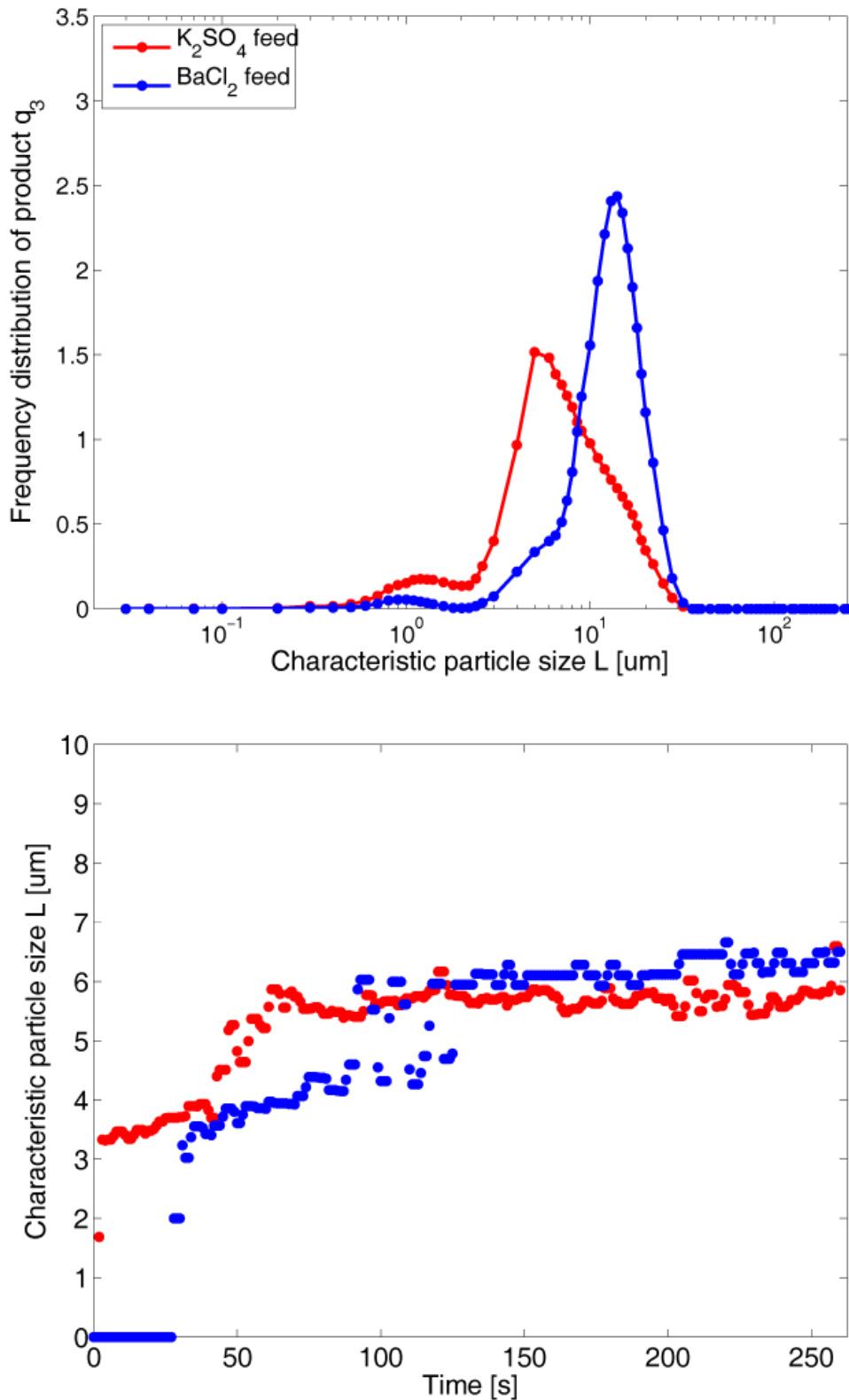


**Figure 29: Top: Measured particle size distributions (CILAS). Bottom: Mean particle diameter over time (Aello). Experimental conditions as in line 2 of Table 14:  $S_a = 498$ , feed rate 80 ml/min;  $\text{K}_2\text{SO}_4$  feed:  $R = 7.5$ , SEM image of morphology: Figure 18.2;  $\text{BaCl}_2$  feed:  $R = 0.13$ , SEM image of morphology: Figure 18.6.**

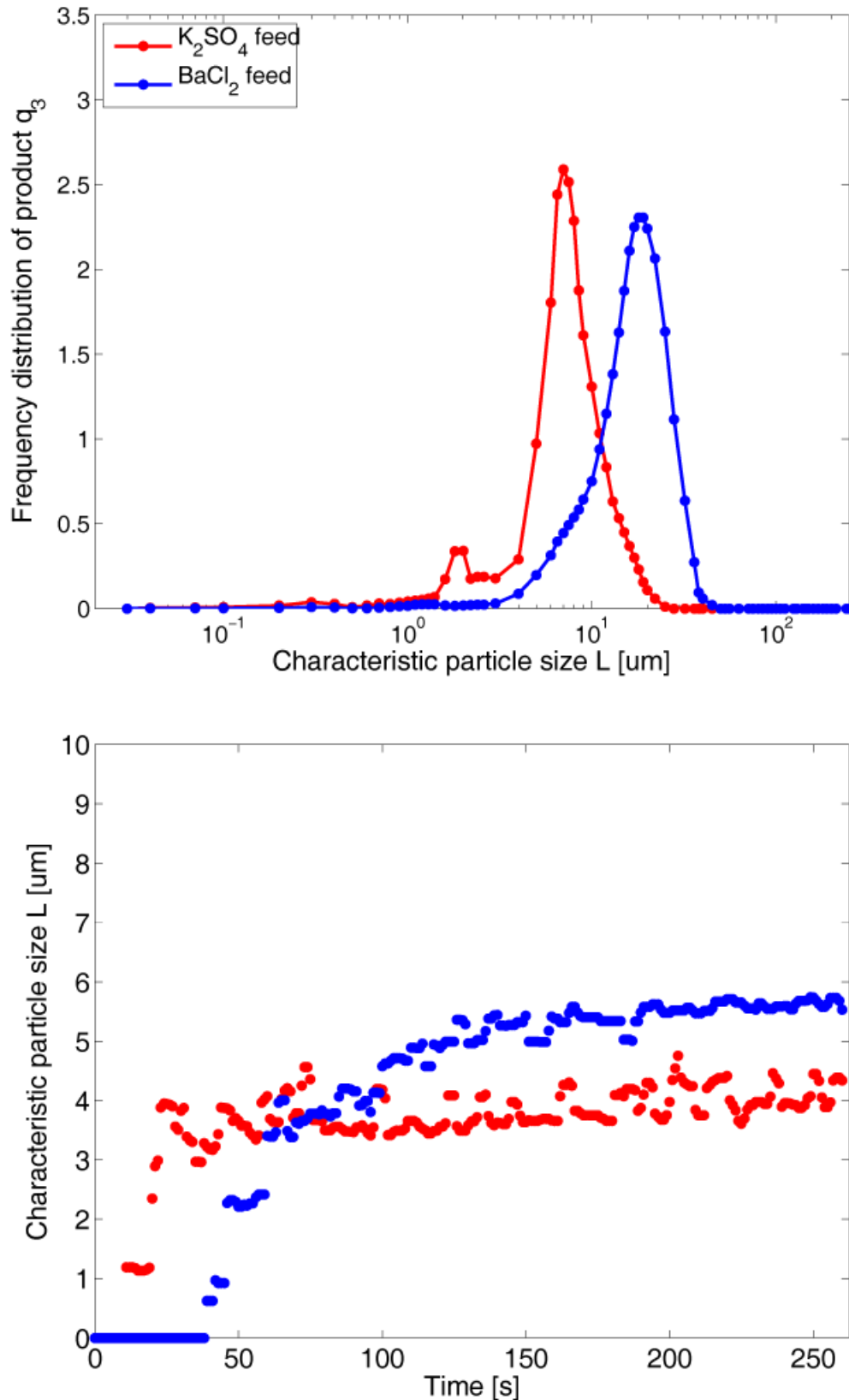


**Figure 30: Top: Measured particle size distributions (CILAS). Bottom: Mean particle diameter over time (Aello). Experimental conditions as in line 3 of Table 14:  $S_a = 456$ , feed rate 80 ml/min;  $\text{K}_2\text{SO}_4$  feed:  $R = 7.5$ , SEM image of morphology: Figure 18.3;  $\text{BaCl}_2$  feed:  $R = 0.13$ , SEM image of morphology: Figure 18.7.**

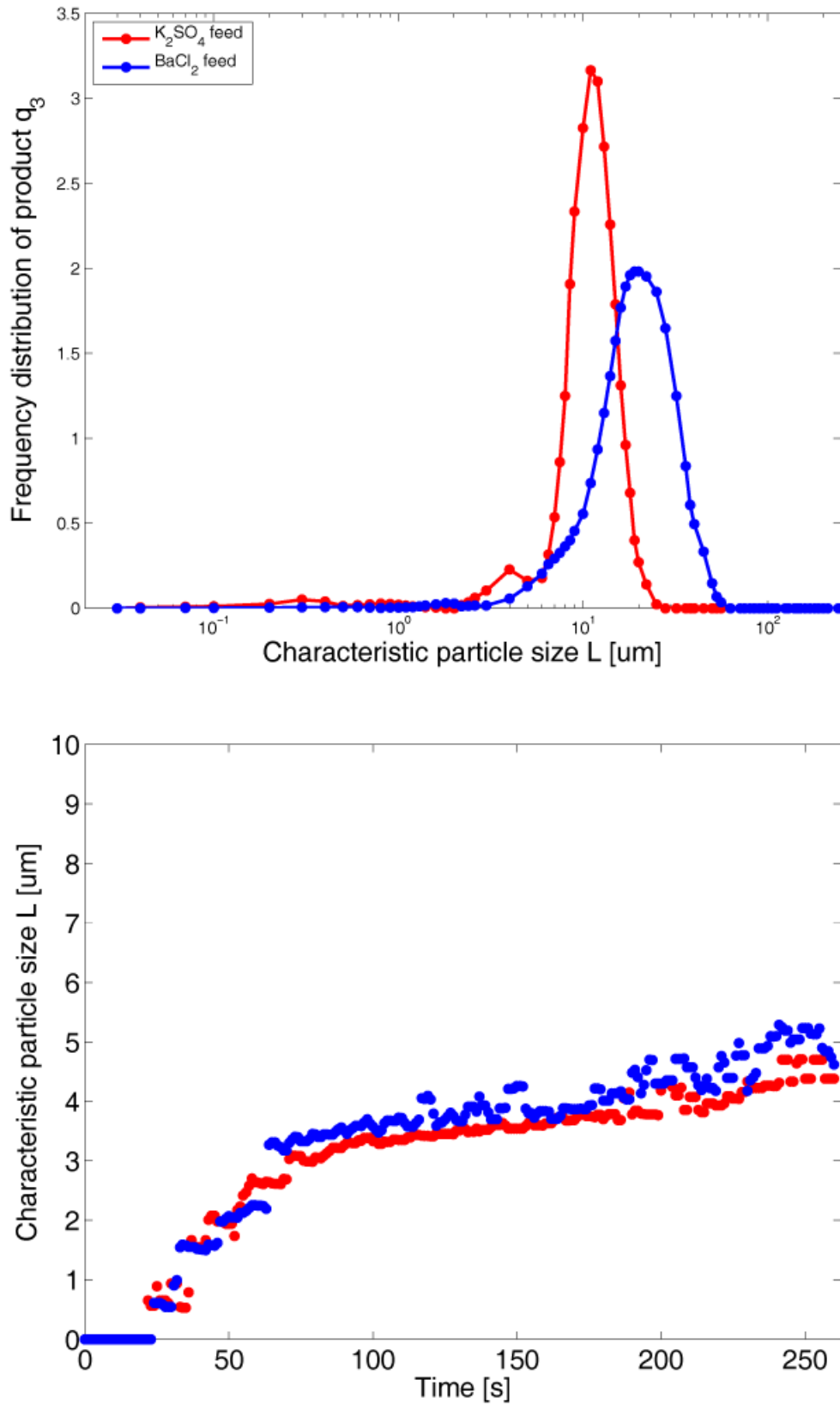


**Figure 31: Top: Measured particle size distributions (CILAS). Bottom: Mean particle diameter over time (Aello). Experimental conditions as in line 4 of Table 14:  $S_a = 274$ , feed rate 80 ml/min,  $R = 1$ ;  $\text{K}_2\text{SO}_4$  feed: SEM image of morphology: Figure 18.4;  $\text{BaCl}_2$  feed: SEM image of morphology: Figure 18.8.**

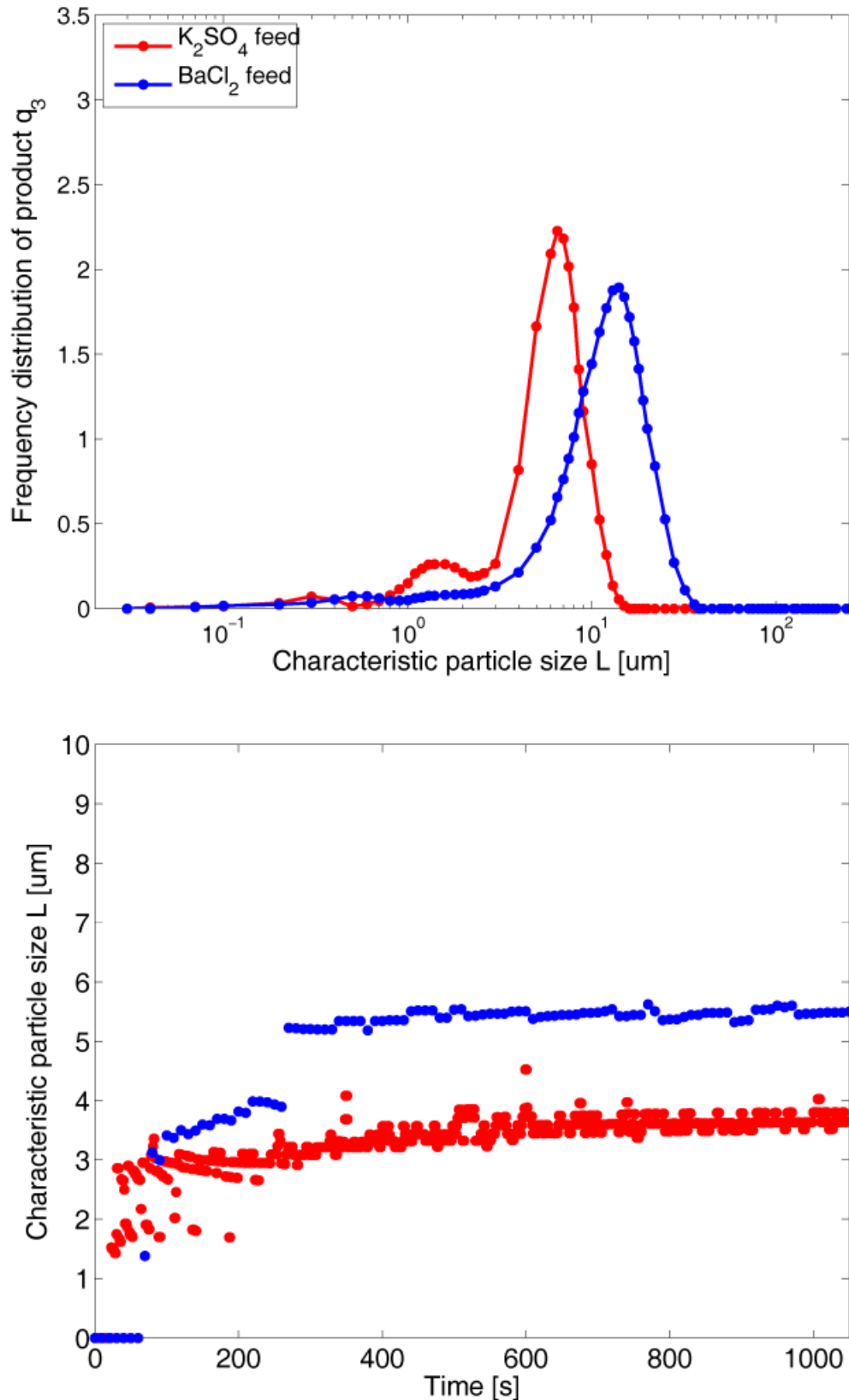


**Figure 32: Top: Measured particle size distributions (CILAS). Bottom: Mean particle diameter over time (Aello). Experimental conditions as in line 5 of Table 14:  $S_a = 527$ , feed rate 20 ml/min;  $\text{K}_2\text{SO}_4$  feed:  $R = 10$ , SEM image of morphology: Figure 19.3;  $\text{BaCl}_2$  feed:  $R = 0.1$ , SEM image of morphology: Figure 19.7.**

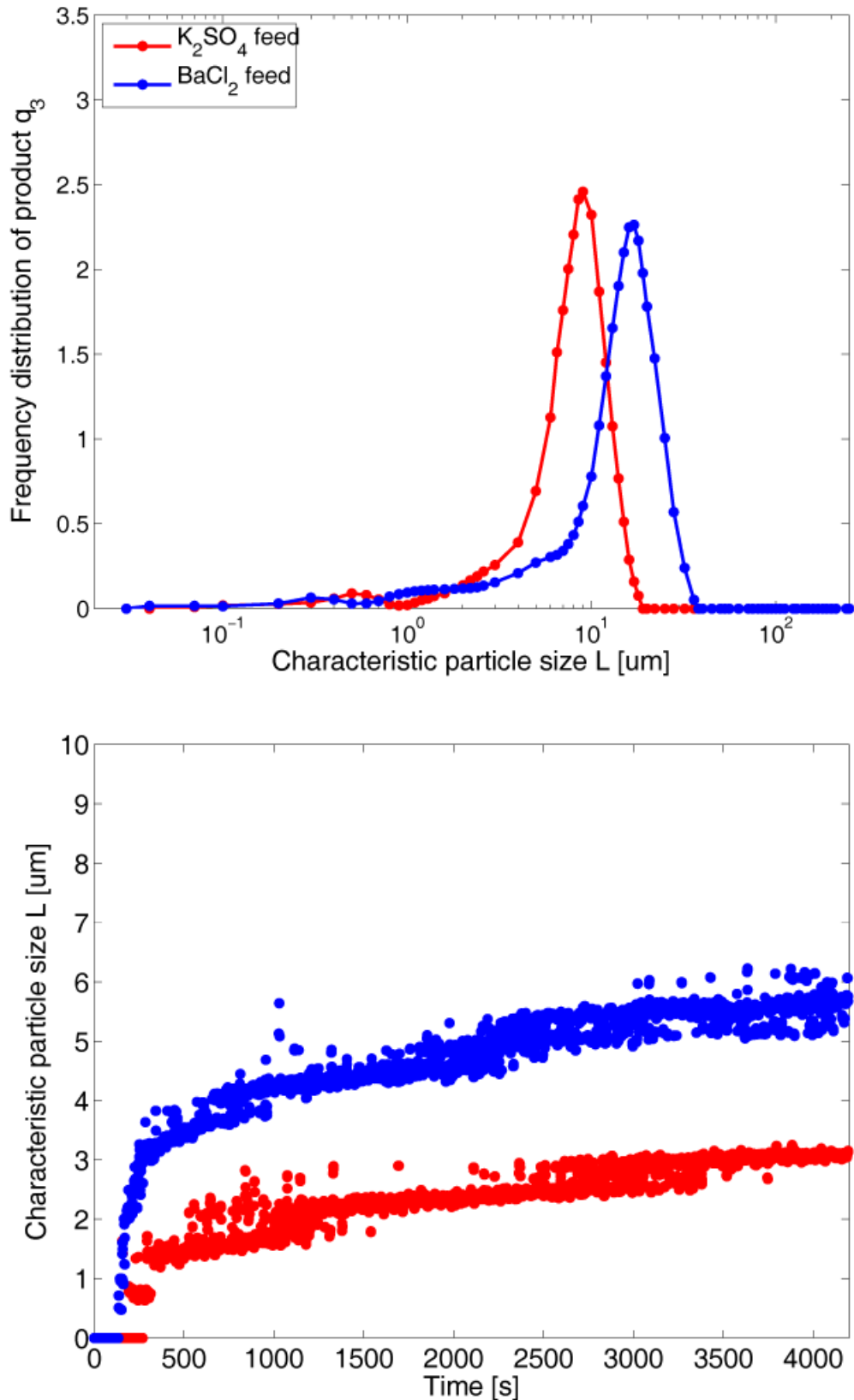


**Figure 33:** Top: Measured particle size distributions (CILAS). Bottom: Mean particle diameter over time (Aello). Experimental conditions as in line 6 of Table 14:  $S_a = 527$ , feed rate 5 ml/min;  $\text{K}_2\text{SO}_4$  feed:  $R = 10$ , SEM image of morphology: Figure 19.2;  $\text{BaCl}_2$  feed:  $R = 0.1$ , SEM image of morphology: Figure 19.6.



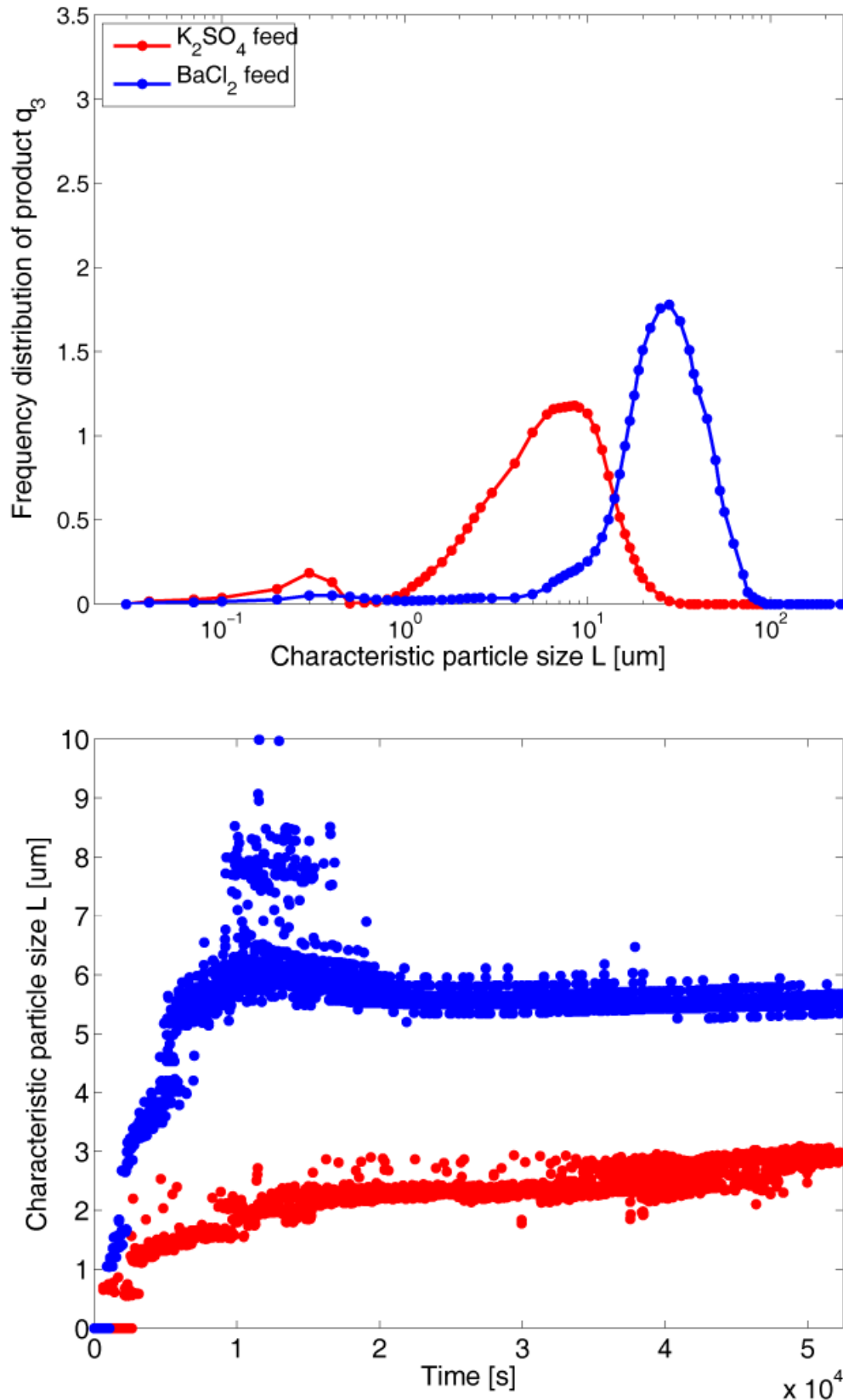


**Figure 34:** Top: Measured particle size distributions (CILAS). Bottom: Mean particle diameter over time (Aello). Experimental conditions as in line 7 of Table 14:  $S_a = 527$ , feed rate 0.4 ml/min;  $\text{K}_2\text{SO}_4$  feed:  $R = 10$ , SEM image of morphology: Figure 19.1;  $\text{BaCl}_2$  feed:  $R = 0.1$ , SEM image of morphology: Figure 19.5.

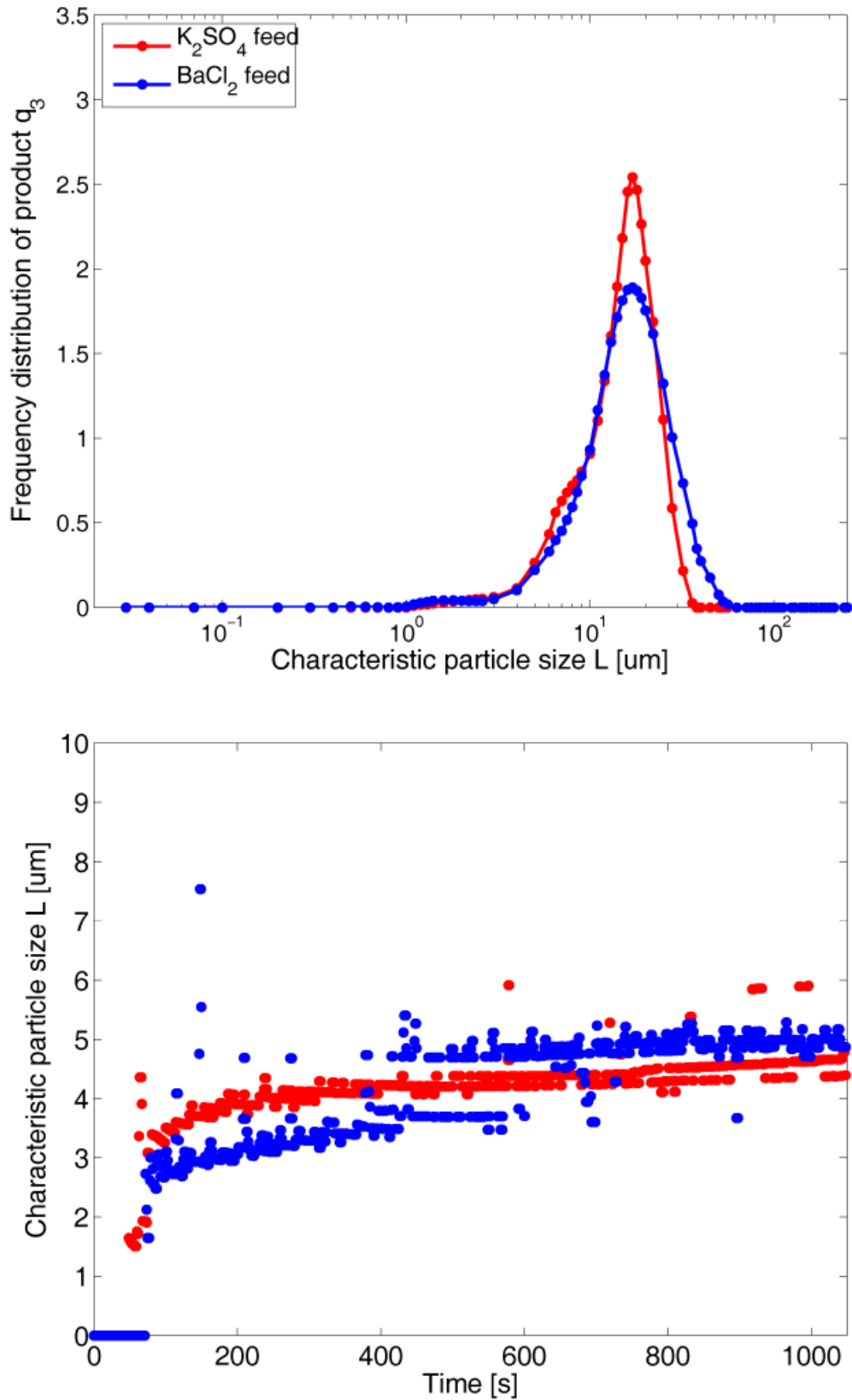


**Figure 35:** Top: Measured particle size distributions (CILAS). Bottom: Mean particle diameter over time (Aello). Experimental conditions as in line 8 of Table 14:  $S_a = 274$ , feed rate 20 ml/min,  $R = 1$ ;  $\text{K}_2\text{SO}_4$  feed: SEM image of morphology: Figure 20.3;  $\text{BaCl}_2$  feed: SEM image of morphology: Figure 20.8.

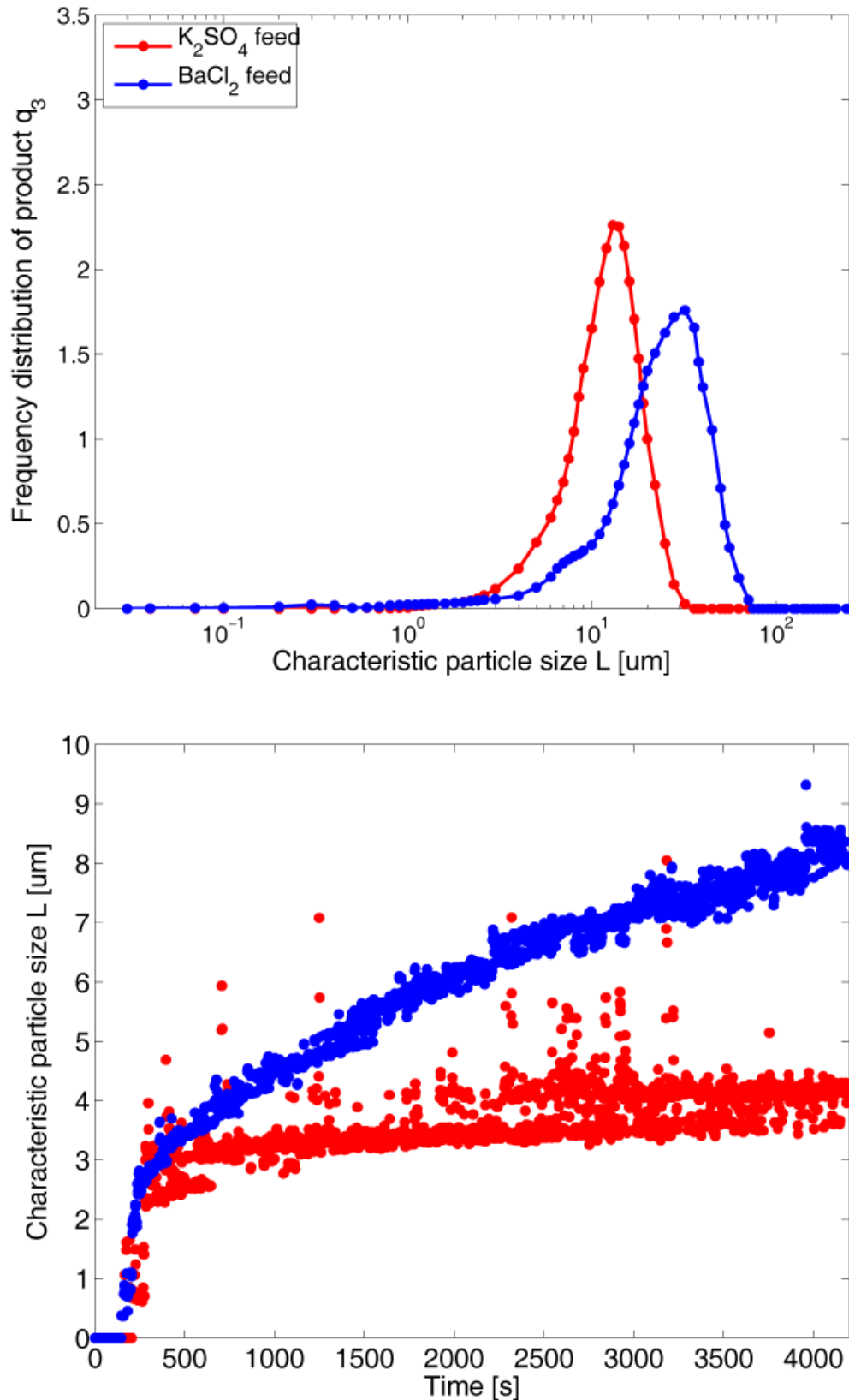


**Figure 36: Top: Measured particle size distributions (CILAS). Bottom: Mean particle diameter over time (Aello). Experimental conditions as in line 9 of Table 14:  $S_a = 274$ , feed rate 5 ml/min,  $R = 1$ ;  $\text{K}_2\text{SO}_4$  feed: SEM image of morphology: Figure 20.2;  $\text{BaCl}_2$  feed: SEM image of morphology: Figure 20.7.**

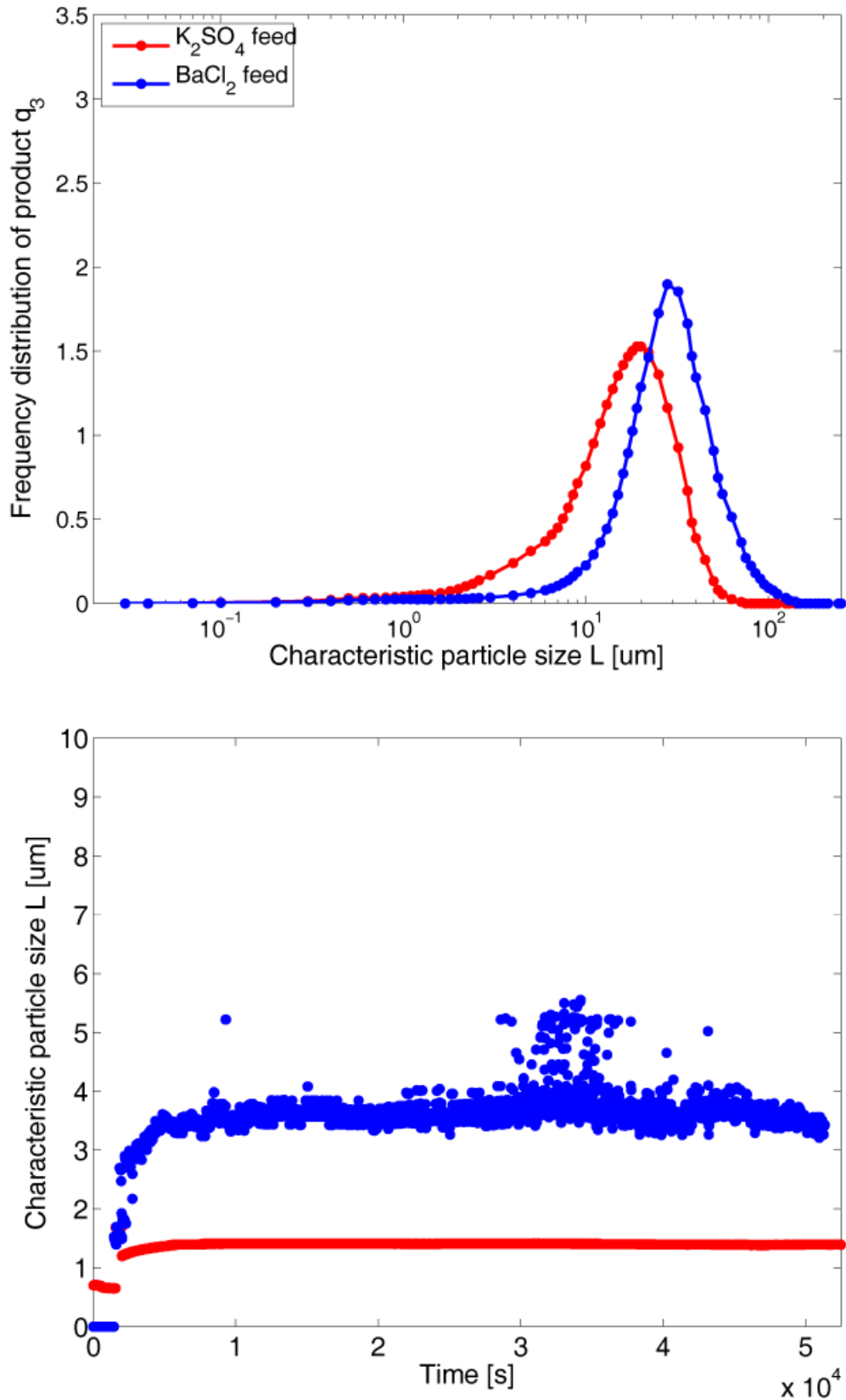


**Figure 37:** Top: Measured particle size distributions (CILAS). Bottom: Mean particle diameter over time (Aello). Experimental conditions as in line 10 of Table 14:  $S_a = 274$ , feed rate 0.4 ml/min,  $R = 1$ ;  $\text{K}_2\text{SO}_4$  feed: SEM image of morphology: Figure 20.1;  $\text{BaCl}_2$  feed: SEM image of morphology: Figure 20.6.

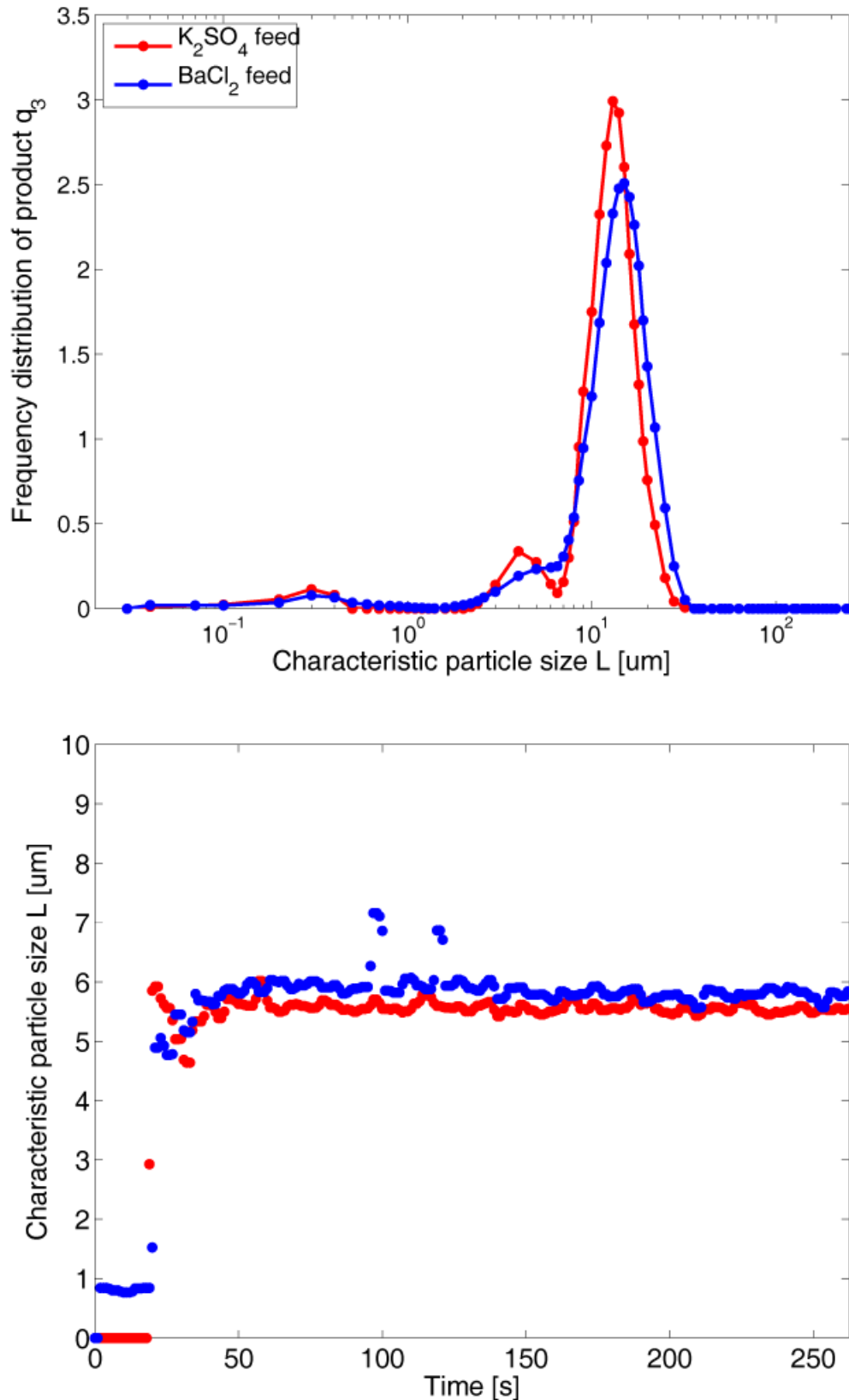


**Figure 38: Top: Measured particle size distributions (CILAS). Bottom: Mean particle diameter over time (Aello). Experimental conditions as in line 11 of Table 14:  $S_a = 274$ , batch operation,  $R = 1$ ;  $\text{K}_2\text{SO}_4$  feed: SEM image of morphology: Figure 20.5;  $\text{BaCl}_2$  feed: SEM image of morphology: Figure 20.10.**

## **5 Population balance model for simulating the particle size distribution**

Some of the experiments from Chapter 4 were simulated using a one-dimensional population balance equation model (1-D PBE) which is presented in this chapter.

The aim of the simulation was the investigation of the batch model kinetics from literature regarding their applicability to non-stoichiometric semi-batch precipitation of barium sulfate. It is known that excess of barium ions influences the size of precipitated particles (Eble, 2000). Often, kinetics from literature were derived for stoichiometric batch operation. Their ability to predict particle sizes for non-stoichiometric and semi-batch precipitation is therefore not guaranteed.

For the investigation, the influence of more sophisticated thermodynamic models for the driving force was investigated as well as the necessity discussed to include the non-stoichiometry into the nucleation and growth kinetics. Motivation for this was the observed differences in particle size distributions (PSDs) for different ions in excess upon semi-batch feeding. Only the more sophisticated thermodynamic models for the activity coefficients give non-symmetrical results concerning the supersaturation for barium or sulfate excess, respectively. One question investigated was to what extent this non-symmetry has influence on the observed different PSDs.

The 1-D PBE was developed to model particle size depending on precipitation kinetics since the particle size distributions measured via the CILAS device were available for quantitative analysis. Therefore, a 1-D PBE was chosen for the simulation model. Of course, by applying multi-dimensional population balances more particle properties could be considered. Given the necessary kinetic expressions even multi-dimensional growth could be predicted as shown in the SEM images of this work. Yet, solving multi-dimensional PBE systems is still challenging and prediction of multiple particle properties including kinetically driven crystal shapes a research field of its own (Borchert et al. (2009), Briesen (2006), Ramkrishna (2000)). Therefore, since for the aim of this work a 1-D PBE model is sufficient it was chosen to keep the necessary effort for the simulation low.

The model derived in this chapter considers nucleation and growth for the particle phase. It is used to model experiments at supersaturation levels where agglomeration was not observed in this thesis, as mentioned earlier. The 1-D PBE model is therefore suitable for the batch and semi-batch experiments as listed in Table 10.

Excluded are the experiments with high supersaturation as listed in Table 9. Here, agglomeration is present and would have to be considered.

The simulated results will be compared with the according experimental particle size distributions. All three activity coefficient models presented from Bromley and Pitzer and the extended Debye-Hückel model were used and the results shown and discussed in Chapter 6.

### 5.1 General population balance equation (PBE)

The crystals are described by a characteristic length  $L$ , and grow with growth rate  $G$ . Nuclei are formed of size  $L^*$  with nucleation rate  $r_N$ . No agglomeration or breakage is considered, as it has no impact for the supersaturation region used in the experiments as discussed earlier.

This gives the following population balance for the number density function  $f$  (Ramkrishna, 2000):

$$\frac{\partial f}{\partial t} + \frac{\partial}{\partial L}(Gf) = -\frac{q_{in}}{V} f, L^* < L < L_{max} \quad (90)$$

with  $f$  being the number density function of particles per unit volume,  $V$  the reactor volume, and  $q_{in}$  the feed rate (equivalent to the volume change over time).

For  $G \times f$  at the lower end of the length scale the following boundary condition holds:

$$G(L^*, t)f(L^*, t) = r_N. \quad (91)$$

The moment method for size-independent growth gives for the zero<sup>th</sup> moment:

$$\mu_0 = \int_{L^*}^{L_{max}} f dL \quad (92)$$

Thus, the time derivative can be expressed as follows:

$$\frac{d\mu_0}{dt} = \int_{L^*}^{L_{max}} \frac{\partial f}{\partial t} dL = \int_{L^*}^{L_{max}} \left( -G \frac{\partial f}{\partial L} - \frac{q_{in}}{V} \cdot f \right) dL \quad (93)$$

$$= [Gf]_{L^*}^{L_{max}} - \frac{q_{in}}{V} \int_{L^*}^{L_{max}} f dL \quad (94)$$

$$\frac{d\mu_0}{dt} = r_N - \frac{q_{in}}{V} \mu_0. \quad (95)$$

The first moment is defined by:

$$\mu_1 = \int_{L^*}^{L_{\max}} L f dL . \quad (96)$$

The corresponding time derivative is given by:

$$\frac{d\mu_1}{dt} = \int_{L^*}^{L_{\max}} L \frac{\partial f}{\partial t} dL = \int_{L^*}^{L_{\max}} \left( -GL \frac{\partial f}{\partial L} - \frac{1}{V} \frac{dV}{dt} \cdot Lf \right) dL \quad (97)$$

$$= -G \left\{ [Lf]_{L^*}^{L_{\max}} - \int_{L^*}^{L_{\max}} f dL \right\} - \frac{1}{V} \frac{dV}{dt} \int_{L^*}^{L_{\max}} Lf dL . \quad (98)$$

$$\frac{d\mu_1}{dt} = L^* r_N + G\mu_0 - \frac{1}{V} \frac{dV}{dt} \mu_1 \quad (99)$$

The second moment is defined as follows:

$$\mu_2 = \int_{L^*}^{L_{\max}} L^2 f dL , \quad (100)$$

for which the following time derivative results:

$$\frac{d\mu_2}{dt} = \int_{L^*}^{L_{\max}} L^2 \frac{\partial f}{\partial t} dL = \int_{L^*}^{L_{\max}} \left( -GL^2 \frac{\partial f}{\partial L} - \frac{1}{V} \frac{dV}{dt} \cdot L^2 f \right) dL \quad (101)$$

$$= -G \left\{ [L^2 f]_{L^*}^{L_{\max}} - \int_{L^*}^{L_{\max}} 2Lf dL \right\} - \frac{1}{V} \frac{dV}{dt} \int_{L^*}^{L_{\max}} L^2 f dL . \quad (102)$$

Finally, Eq. (102) can be expressed as:

$$\frac{d\mu_2}{dt} = L^{*2} r_N + 2G\mu_1 - \frac{1}{V} \frac{dV}{dt} \mu_2 . \quad (103)$$

The number distribution is denoted by  $q_0$ . To convert the number distribution function  $q_0$  into the volume cumulative curve  $Q_3(L)$ , as used by the experimental device, the following operation is performed (Stieß, 1995):

$$Q_3(L') = \frac{\int_{L^*}^{L'} L^3 \cdot q_0(L) dL}{\int_{L^*}^{L_{\max}} L^3 \cdot q_0(L) dL} , \quad (L' \leq L_{\max}) . \quad (104)$$

The histogram  $q_3(L)$  given by the experimental device is calculated out of  $Q_3(L)$  by Eq. (88).



## 5.2 Modelling of semi-batch BaSO<sub>4</sub> bulk precipitation

Due to the semi-batch feeding, the reactor volume  $V$  changes over time, thus the total mass balance equation is needed:

$$\frac{dV}{dt} = q_{in} \quad (105)$$

with  $q_{in}$  being the volumetric feed rate.

The component mole balance of ionic species are:

$$\frac{dc_{Ba^{2+},tot}}{dt} = \frac{q_{in}}{V} (c_{Ba^{2+},in} - c_{Ba^{2+},tot}) - r_s, \quad (106)$$

$$\frac{dc_{SO_4^{2-},tot}}{dt} = \frac{q_{in}}{V} (c_{SO_4^{2-},in} - c_{SO_4^{2-},tot}) - r_s, \quad (107)$$

$$\frac{dc_{Cl^-}}{dt} = \frac{q_{in}}{V} (c_{Cl^-,in} - c_{Cl^-}). \quad (108)$$

The concentration of K<sup>+</sup> ions can be calculated from the electroneutrality condition:

$$2c_{Ba^{2+}} - 2c_{SO_4^{2-}} + c_{K^+} - c_{Cl^-} = 0. \quad (109)$$

In Eqs. (106) and (107) the variable  $r_s$  denotes the mole flux from the liquid to the solid phase, i.e. the amount of precipitating product which disappears from the liquid solution per unit of time:

$$Vr_s = \frac{dn_s}{dt} = \frac{\rho_s}{M_s} \cdot \int_{L^*}^{L_{max}} k_v L^3 \frac{d}{dt}(Vf) dL, \quad (110)$$

where  $\rho_s$  is the solid density and  $M_s$  the molar mass of the precipitated particles, and  $k_v$  is the volume shape factor of the particles (Eq. (72)),

$$Vr_s = -\frac{\rho_s}{M_s} k_v \cdot V \int_{L^*}^{L_{max}} L^3 \frac{\partial}{\partial L}(Gf) dL \quad (111)$$

$$= -\frac{\rho_s}{M_s} k_v \cdot V \left\{ \left[ L^3 \cdot Gf \right]_{L^*}^{L_{max}} - \int_{L^*}^{L_{max}} 3L^2 \cdot Gf \cdot dL \right\}. \quad (112)$$

With the assumption that no particles reach the upper length scale boundary,  $Gf|_{L_{max}} = 0$  and thus

$$Vr_s = \frac{\rho_s}{M_s} k_v \cdot V \left\{ L^{*3} \cdot r_N + \int_{L^*}^{L_{\max}} 3L^2 \cdot Gf \cdot dL \right\}. \quad (113)$$

From Eq. (113) follows with Eq.(103):

$$\frac{dn_s}{dt} = \frac{\rho_s}{M_s} k_v \cdot V \{ L^{*3} \cdot r_N + 3G\mu_2 \} \quad (114)$$

and thus

$$r_s = \frac{\rho_s}{M_s} k_v \cdot \{ L^{*3} \cdot r_N + 3G\mu_2 \}. \quad (115)$$

Due to the different supersaturation levels and the ion ratios present in semi-batch operation, it is obvious that the shape factors for the observed particles vary for the different experiments. It can be assumed to change during the runtime of the experiments, also.

Ideally, the habit of the particles would be included into the simulation model, as the particle shape has crucial impact on the product quality. For this, the shape factor could be considered as a property of the population balance model. With particle size being the other property this would make the PBE two-dimensional. As already mentioned, solving multi-dimensional PBE models for determination of the crystal shape is still challenging as the problem size can get very large (Borchert et al. (2009), Briesen (2006)). Since the aim of the PBE model of this work was to generally investigate the influence of a higher sophisticated thermodynamic model for the driving force on simulated product properties, a 1-D PBE model with the particle size being the only monitored particle dimension was chosen to minimize computational efforts. The particle shape will be considered using a constant shape factor for every experiment. As already mentioned in Chapter 2.11.4, for semi-batch precipitation the initial concentrations, i.e. the initial local supersaturation dominates the morphology of the particle, thus a well-chosen constant shape factor for every run is a legitimate first assumption for the experiments. The shape factors used are specified later for the different calculations.

The difference between the total and the free amount of barium and sulfate ions is due to the ion complex formation as described in Eq. (10). The balances for total amount of barium and sulfate ions in the liquid solution are as follows:

$$c_{Ba^{2+},tot} = c_{Ba^{2+}} + c_{BaSO_4,(aq)}, \quad (116)$$

$$c_{SO_4^{2-},tot} = c_{SO_4^{2-}} + c_{BaSO_4,(aq)} \quad (117)$$

where  $c_{Ba^{2+}}$  and  $c_{SO_4^{2-}}$  are the molar concentrations of free barium and sulfate ions in the liquid phase, respectively.

### 5.3 Two-compartment mixing model

It was already stated that mixing effects have to be considered for bulk precipitation in a stirred tank reactor. In Chapter 2.10 the time scales involved in precipitation in a mixed vessel are discussed, which showed that the fast nucleation rate will lead to precipitation events occurring before the reactor content is completely mixed, forming concentration gradients near the inlet point that influence the resulting particle size distribution. This influence is higher for high reactant concentration where small-scale mixing affects the local supersaturation and therefore the nucleation close to the feed point is controlling the dynamics of the process (Vicum and Mazzotti, 2007).

An exact model of the flow field in the vessel would require a rigorous three-dimensional computational fluid dynamics approach (CFD). Because such a model is still a numerical challenge, more or less sophisticated semi-empirical mixing models for stirred tanks have been derived (Bałdyga et al. (1995), Taguchi et al. (1999), Vicum et al. (2003), van Leeuwen (1998)). Another approach is the use of CFD solvers to model the precipitation process as it was done elsewhere (Öncül et al. (2006), Piton et al. (2000), Marchisio et al. (2001), Vicum and Mazzotti (2007), Wei and Garside (1997)). Still, the combination of a CFD solver with a precipitation model is not a simple task and can be considered as research field of its own. Exact description of the flow field in the tank was not intended in this work. A far simpler mixing approach is sufficient for the purpose of the simulation of the 1-D PBE model, thus a simple mixing model was chosen to minimize the calculation effort. In a stirred tank reactor with one feed if the feed inlet point is away from the impeller zone, three zones of mixing intensity can be distinguished in general (Mersmann, 2001), namely the zone near the inlet with the highest supersaturation, the zone around the impeller with higher energy dissipation, and the bulk of the vessel. In the experiments described in Chapter 3.2, the feed inlet point was in the vicinity of the impeller and therefore into the impeller zone, making it possible to melt these two zones into one compartment. For their micromixing model for a double feed semibatch stirred tank reactor, Taguchi et al. (1999) distinguished between two zones

in their micromixing model, zone I being the feed inlet with locally mixing of feed and bulk and partially segregated fluid. Zone II represents the state of maximum mixedness after the feed mixed with the bulk suspension. This approach was also used by Chen et al. (1996) who distinguished between the feed inlet zone with segregated fluid elements and the well-mixed bulk. van Leeuwen et al. (1996, and van Leeuwen, 1998) also differentiate between the inlet zone where the feed stream is mixed with the bulk and the main bulk zone as the simplest model for a stirred tank reactor. Therefore, in the present work the vessel was modelled to consist of two compartments. The two compartments were defined to be the highly stirred inlet zone and the bulk zone, connected by an exchange flow rate  $q_{ex}$ . The two volumes add up to the total reactor volume:

$$V = V_B + V_E, \quad (118)$$

with  $V_B$  being the volume of the bulk zone and  $V_E$  the volume of the inlet volume. Figure 39 shows the principle of the two compartment mixing model.

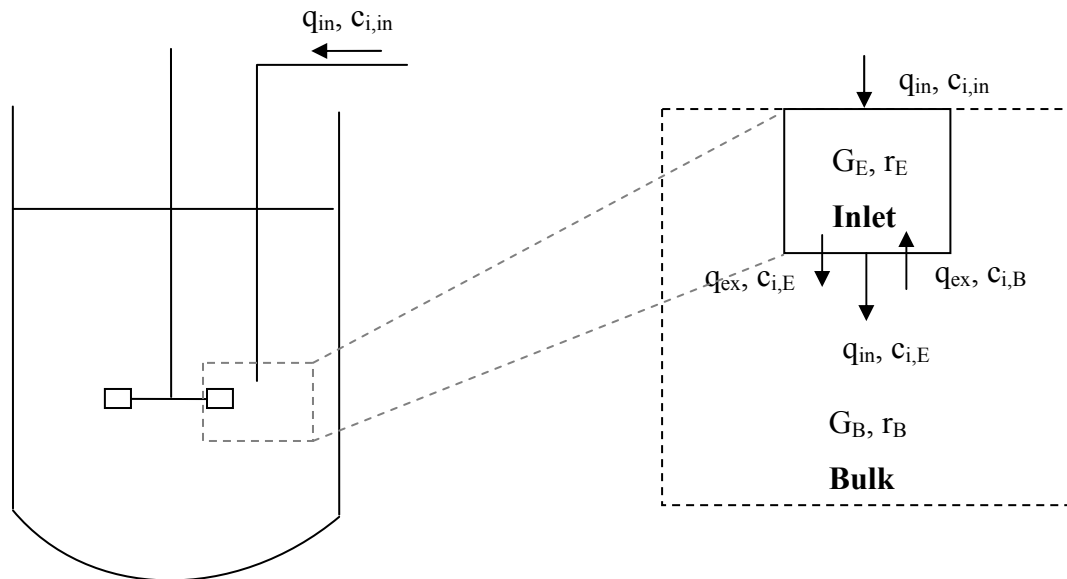


**Figure 39: Inlet and bulk compartments with inlet and exchange flows.  $G$ : growth rate,  $r$ : nucleation rate,  $q_{in}$ : feed flow to the vessel,  $q_{ex}$ : exchange flow rate between inlet and bulk compartments,  $c_i$ : concentration of ion species.  $E$ : inlet compartment,  $B$ : bulk compartment.**

It is assumed that the residence time in the inlet zone  $\tau_E$  can be expressed as fraction of the circulation time in the reactor  $\tau_c$  (van Leeuwen, 1998):

$$\tau_E = C_\tau \tau_c = C_\tau \frac{V}{N_Q N_{stirr} d^3}, \quad (119)$$

where  $V$  is the tank volume,  $N_Q$  the pumping number,  $N_{stirr}$  the number of stirrer revolutions, and  $d$  the impeller diameter.  $C_\tau$  is a constant depending on the distance between feed point and impeller.  $\tau_c$  is the circulation time in the reactor (Eq. (84)).

The pumping number for the geometry used is 0.67 (van Leeuwen, 1998).

In this work, the inlet volume was not determined by experiments but literature data was taken to estimate the volume and residence time. van Leeuwen (1998) did experiments to determine the volume of the inlet zone in dependence of the stirrer speed and values for the constant  $C_\tau$  for a stirred Rushton tank. The volume of the vessel was 2.4 l, the inlet feed rate 162 ml/min, and the number of stirrer revolutions up to 700 rpm. Taking his findings and applying them to the Rushton tank geometry used here leads to a minimum inlet volume of  $5 \times 10^{-3}$  ml for the very slow semi-batch feeding and approximately 7 ml for the batch experiments (assuming the inlet volume gets larger for higher feed rate). Baldyga et al. (1995) assumed the impeller region to be 5% of the total vessel volume for their stirred tank reactor. This would give a theoretical maximum value for the inlet region of 35 ml, assuming a total volume of 700ml that is reached at the end of the experiments in this work.

$C_\tau$  was estimated by van Leeuwen (1998) to 0.047 for a distance of 2 cm. For the distance of feed point to impeller of 1.5 cm as used here in this work the value would be approximately 0.035. These approximated values define the physically useful regions for  $V_E$  and  $C_\tau$ . For values of  $V_E$  and  $C_\tau$  inside this physically suitable range sensitivity analysis for the case of batch experiments (row no. 11 in Table 10) and also for slow feeding (row no. 10 in Table 10) showed no significant influence on the resulting PSD. Therefore, the volume of the inlet zone  $V_E$  was assumed to be constant at 2 ml and  $C_\tau$  to be 0.047. The residence time is therefore equal to 0.068 s for a tank volume of 350 ml, and the exchange rate  $q_{ex}$  between the two compartments inlet and bulk is equal to  $2.8 \times 10^{-5}$  [m<sup>3</sup> / s].

This leads to the following set of coupled balance equations:

$$V_B = V - V_E, \quad (120)$$

$$\frac{dV}{dt} = q_{in} \Rightarrow \frac{dV_B}{dt} = q_{in}, \quad (121)$$

$$\frac{dc_{i,E}}{dt} = -\frac{q_{in} + q_{ex}}{V_E} c_{i,E} + \frac{q_{in}}{V_E} c_{i,in} + \frac{q_{ex}}{V_E} c_{i,B} - r_{s,E}, \quad (122)$$

$$\frac{dc_{i,B}}{dt} = -\frac{q_{in} + q_{ex}}{V_B} (c_{i,E} - c_{i,B}) - r_{s,B}, \quad (123)$$

$$r_{s,E} = \frac{\rho_s}{M_s} k_v \cdot \{L^{*3} \cdot r_{N,E} + 3G_E \mu_{2,E}\}, \quad (124)$$

$$r_{s,B} = \frac{\rho_s}{M_s} k_v \cdot \{L^{*3} \cdot r_{N,B} + 3G_B \mu_{2,B}\}. \quad (125)$$

For the simulation results, a volume-weighted mean distribution was calculated from the results of the two compartments to give the overall particle size distribution of the product.

**Table 16: Used parameter values for simulation (refer also to Table 3)**

Temperature $T$ [K]	298
solid density $\rho_s$ [kg / m <sup>3</sup> ]	$4.48 \times 10^{-3}$
solid molar mass $M_s$ [kg / mol]	0.233
reaction equilibrium for complex formation $K_I$ (25 °C) [mol / kg]	$10^{-2.72}$
density of solvent (water) $\rho_{H_2O}$ [kg / m <sup>3</sup> ]	1000
shape factor $k_v$ [-]	0.06, 0.1, 1 (as specified)
solubility product $K_a$ [(mol / l) <sup>2</sup> ]	$10^{-9.96}$
number of grid points for discretisation $n$ [-]	100
minimum particle size (nuclei) $L^*$ (assumption)	1 nm
maximum particle size $L_{max}$ (same as the max. measuring range of the CILAS particle sizer)	2.5 mm

To compute the driving force of the precipitation reaction, supersaturation was calculated by Eq. (13). The activity coefficient was calculated by one of the three methods presented in Chapter 2.2. For application of the extended Debye-Hückel approach in this work it has to be said that the maximum theoretical ion strength of some experiments is  $0.165 \text{ kmol/m}^3$  which violates the validity range of the method (up to  $0.1 \text{ kmol/m}^3$ ). Nevertheless, the method is applicable because of the reduction of the ion strength in the reactor due to slower feeding for semi-batch operation. The

simulations done in this work showed that the maximum value of  $0.1 \text{ kmol/m}^3$  was never exceeded during experiments.

Table 17 shows the simulation times depending on the feed rate. They are equivalent to the end time of the feeding for the different experiments.

**Table 17: Simulation times depending on the feed rate**

feed rate	simulation time [s]
batch	262.5, end of feeding: 35
80 ml/min	262.5
20 ml/min	1050
5 ml/min	4200
0.4 ml/min	52500

#### 5.4 Growth and nucleation kinetics

Two different kinetic models for growth and nucleation from the literature were selected which will be presented in the following.

For barium sulfate precipitation, several kinetic models are available in the literature (Nielsen (1958, 1961), Vicum, 2003, Angerhöfer, 1994, Aoun, 1996, 1999, to name a few). Aoun et al. (1999) give a summary of kinetics expressions from the literature including the experimental conditions and the mechanism and concentration ranges for growth and nucleation rates. See also Petrova's PhD thesis (2008) for a summary of a number of kinetic models found in the literature.

The differences in the empiric and half-empiric models could be explained by the experimental conditions that varied for the different authors (e.g. precipitation system used, experimental set-up, measuring devices), but also by the dependency on the chosen characteristic length of the particles for which the growth kinetics were fitted (Judat, 2003), as well as the shape factors used for the validation.

Nucleation and growth rates are also influenced by excess of sulfate and barium ions. For non-stoichiometric conditions, Aoun et al. (1996) identified that both nucleation and crystal growth are significantly, and also differently, accelerated for  $R$  greater or smaller than one for the system barium chloride and potassium sulfate. Although in a later paper, Aoun et al. soften this statement (Aoun et al., 1999), there are many references in the literature that report findings of different influences of barium and

sulfate ion excess on the precipitation product. In general, the precipitated particles are smaller for barium excess, as also stated in Chapter 2.11.

Most models do not include an empirical approach to consider the dependence on ion ratio. The only model that explicitly includes the non-symmetrical behavior of the  $Ba^{2+}$  -  $SO_4^{2-}$  -  $Cl^-$  -  $K^+$  - electrolyte solution with respect to different ion ratios is from Aoun et al. (1996). There, the differences are considered empirically by fitted parameters to measured growth and nucleation rates for values of the ion ratio R in the range [0.1-10]. This model is used in this work and will be presented below.

Also, most of the kinetic models are derived for batch operation. It will be discussed to what extent such semi-empiric kinetics can be applied to the semi-batch operation in the following Chapter by applying the exemplary supersaturation-dependent nucleation and growth model presented in the next subchapter.

#### 5.4.1 Supersaturation-dependent nucleation and growth kinetics

For the supersaturation-dependent nucleation kinetics, a kinetic approach similar to Vicum et al. (2003) was chosen. In this work, it will be used for the investigations of the influence of different activity coefficient models in Chapter 6.

For nucleation, Vicum et al. differentiate between homogeneous and heterogeneous nucleation. By evaluating data from Nielsen (1961) they identified the transition from hetero- to homogeneous kinetics at  $S_a = 280$ . The nucleation rate is given by

$$r_N = R_{\max} \exp\left(\frac{-A_N}{\ln^2 S_a}\right), \quad (126)$$

with  $A_{N,het} = 40.0$ ,  $R_{max,het} = 3.75 \times 10^{11} \text{ m}^{-3}\text{s}^{-1}$  for heterogeneous nucleation and  $A_{N,hom} = 2254.0$ ,  $R_{max,hom} = 1.45 \times 10^{42} \text{ m}^{-3}\text{s}^{-1}$  for homogeneous nucleation kinetics.

For growth, Vicum et al. used a two-step model that includes the concentration at the particle surface. It was assumed that the molar mass transported to the particle has to be the same as the amount integrated into the solid phase.

These assumptions yield:

$$G = k_r \left( \left( \frac{c_{Ba^{2+},int} c_{SO_4^{2-},int}}{K_a} \right)^{1/2} \gamma_{\pm,int} - 1 \right)^2 = k_r (S_{a,int} - 1)^2, \quad (127)$$

$$= k_D (c_{i,tot,bulk} - c_{i,tot,int}), \quad (i = Ba^{2+}, SO_4^{2-}).$$

In this work, the integration rate coefficient  $k_r = 4 \times 10^{-11} \text{ (m s}^{-1}\text{)}$  was used (Wei and Garside, 1997). The mass-transfer coefficient  $k_D = 4.0 \times 10^{-8} \text{ (m s}^{-1}\text{) (m}^3 \text{ mol}^{-1}\text{)}$  is the



same as in Vicum et al. (2003) taken from Bałdyga et al. (1995). It is assumed to be the same for all ion species.

Eq. (127) was solved together with Eq. (10), (116) and (117) for the interface concentration for every time step using a predefined matlab numerical solver (using the Levenberg-Marquardt method) with the assumption that the interface concentrations of nonreactive ionic species are equal to the bulk concentrations, i.e.

$$c_{K^+,bulk} = c_{K^+,int} \quad \text{and} \quad c_{Cl^-,bulk} = c_{Cl^-,int}.$$

Due to the consideration of all possible growth and nucleation mechanisms with transitions depending on  $S_a$ , these kinetics are valid for the whole supersaturation range considered in this work.

#### 5.4.2 Supersaturation- and $R$ -dependent nucleation and growth kinetics

Aoun et al. (1996, 1999) fitted nucleation and growth rates for barium sulfate precipitation from barium chloride and potassium sulphate to own experiments using a batch stirred tank reactor at 22 °C. The range of maximum concentration during their experiments was 0.375 to 1.5 mol/m<sup>3</sup>.

For stoichiometric conditions, Aoun et al. (1999) derived for the nucleation rate

$$r_N = k_N \exp\left(\frac{-B}{\ln^2 \sqrt{c_{Ba^{2+}} c_{SO_4^{2-}} / K_a}}\right), \quad (128)$$

with  $k_N = (2.5 \pm 0.5) \times 10^{11} \text{ m}^{-3} \text{ s}^{-1}$  and  $B = (15 \pm 1)$ .

The growth rate given is

$$G = k_G \left( \sqrt{c_{Ba^{2+}} c_{SO_4^{2-}}} - \sqrt{K_a} \right)^g, \quad (129)$$

with  $k_G = (2.5 \pm 0.5) \times 10^{-7} \text{ m s}^{-1} (\text{mol m}^{-3})^{-g}$  and  $g = (2.1 \pm 0.1)$ .

The model was extended to non-stoichiometric batch experiments (Aoun et al., 1996). The authors observed, that for  $R = 1$  the growth and nucleation kinetics are the lowest, and increase for ion excess, i.e. the nucleation rate increases stronger for barium ion excess, whereas the growth rate is higher for sulfate ion excess.

The extension of the model to non-stoichiometric conditions was done by empirical consideration of the ion excess. For this, the initial ion ratio for batch experiments

$$R_0 = c_{Ba^{2+}}(t=0) / c_{SO_4^{2-}}(t=0) \quad (130)$$

was included into the rate equations, assuming ideal mixing at time  $t = 0$ , i.e.  $R_0 = R(t=0)$ . Since Aoun et al. did not consider ion complex formation of barium and

sulfate,  $R_0$  is also the highest possible and therefore the theoretical maximum initial ion ratio.

Additionally, the growth rate equation (Eq. (131)) is not symmetrical with respect to the ion species but weighs barium and sulfate ion concentrations differently.

For their kinetics, the authors fitted parameters to kinetic measurements for initial ion ratio  $R_0$  values in the range of [0.1-10].

They derived the following equations for the growth and nucleation rates for a given  $R_0$ :

$$G = k_G \left( c_{Ba^{2+}} - c_{Ba^{2+}}^* \right)^{1.15} \left( c_{SO_4^{2-}} - c_{SO_4^{2-}}^* \right)^{0.95} \quad (131)$$

where:

$$\text{for } R_0 \geq 1 : k_G = 1.05 \cdot 10^{-5} \times 10^{-1.57/R_0} \text{ m s}^{-1} (\text{mol m}^{-3})^{-2},$$

$$\text{for } R_0 \leq 1 : k_G = 2.73 \cdot 10^{-5} \times 10^{-1.99R_0} \text{ m s}^{-1} (\text{mol m}^{-3})^{-2},$$

$$r_N = k_N \exp \left[ \frac{-B}{\left( \ln \sqrt{c_{Ba^{2+}} c_{SO_4^{2-}} / K_a} \right)} \right], \quad (132)$$

where:

$$\text{for } R_0 \geq 1 : k_N = 2.5 \cdot 10^{11} \times R_0^{2.28} \text{ m}^{-3} \text{s}^{-1},$$

$$\text{for } R_0 \leq 1 : k_N = 2.5 \cdot 10^{11} \times R_0^{-1.05} \text{ m}^{-3} \text{s}^{-1},$$

and  $B = 14.9 + 67.57 |\log R_0|$  in all cases.

The kinetics take into account the fact that particle sizes are usually smaller for an excess of barium ions. Yet, in Eq. (131) the kinetic order of the absolute supersaturation of barium is higher than of sulfate. Still, due to the fitting of the growth constant  $k_G$  the overall growth rate is lower for barium excess than for sulfate excess (refer also to Figure 43 to see the change in overall growth rate depending on  $R$ ).

Actually, Aoun et al. (1996, 1999) fitted the nucleation and growth kinetics for experiments in batch operation mode for concentrations were the dominant mechanisms would be heterogeneous nucleation and integration limited growth, the latter also indicated by the kinetic order of the growth equations. Still, this model extends the kinetics usually presented in literature which only depend on supersaturation. It is used in this work as a possibility to identify kinetics that better describe the influence of non-stoichiometry on the particle sizes.

Although the model by Aoun et al. is able to reproduce their batch experiments well, integrating the initial ion ratio  $R_0$  is not quite satisfactory from a theoretical point of view. The dependence of the kinetics on the initial conditions in the batch reactor lacks a physical justification, especially if dealing with semi-batch precipitation.

To adapt the model to the semi-batch conditions in this work, the theoretical initial ion ratio  $R_0$  used in Eqs. (131) and (132) was substituted by the dynamic ion ratio  $R(t)$  present in the reactor at each moment of time:

$$R(t) = c_{Ba^{2+}, free}(t) / c_{SO_4^{2-}, free}(t). \quad (133)$$

The kinetic equations then are the following:

$$G = k_G (c_{Ba^{2+}} - c_{Ba^{2+}}^*)^{1.15} (c_{SO_4^{2-}} - c_{SO_4^{2-}}^*)^{0.95}, \quad (134)$$

with:

$$\text{for } R(t) > 1: k_G(t) = 1.05 \cdot 10^{-5} \times 10^{-1.57/R(t)} \text{ m s}^{-1} (\text{mol m}^{-3})^{-2},$$

$$\text{for } R(t) < 1: k_G(t) = 2.73 \cdot 10^{-5} \times 10^{-1.99R(t)} \text{ m s}^{-1} (\text{mol m}^{-3})^{-2},$$

$$\text{and for } R(t) = 1: k_G(t) = 2.8 \cdot 10^{-7};$$

$$r_N = k_N \exp \left[ \frac{-B}{\left( \ln \sqrt{c_{Ba^{2+}} c_{SO_4^{2-}}} / K_a \right)} \right], \quad (135)$$

with:

$$\text{for } R(t) > 1: k_N(t) = 2.5 \cdot 10^{11} \times R(t)^{2.28} \text{ m}^{-3} \text{ s}^{-1},$$

$$\text{for } R(t) < 1: k_N(t) = 2.5 \cdot 10^{11} \times R(t)^{-1.05} \text{ m}^{-3} \text{ s}^{-1},$$

$$\text{for } R(t) = 1: k_N(t) = 2.5 \cdot 10^{11} \text{ m}^{-3} \text{ s}^{-1},$$

$$\text{and } B = 14.9 + 67.57 |\log R(t)| \text{ in all cases.}$$

## 6 Simulation results and discussion

In this chapter, simulation results calculated with the one-dimensional population balance equation model (1-D PBE) introduced in Chapter 5 are presented and discussed in comparison to the experiments. The particle property considered is the particle size.

As already stated in Chapter 5 the aim of the simulation is the investigation of the applicability of barium sulfate batch kinetics from literature to non-stoichiometric semi-batch precipitation. The kinetics considered are for nucleation and growth rates valid for the whole supersaturation range as presented in Chapter 5.4.1. They are dependent on the supersaturation and were derived from stoichiometric batch experiments. The investigation wants to clarify the question of whether these kinetics can be applied to non-stoichiometric precipitation, as well. The focus lies on the ability of the model to describe the different particle size distributions (PSDs) observed in semi-batch experiments for barium or sulfate ions in excess, respectively. For this, some of the experiments were simulated and the resulting PSDs compared.

First, in the next two subchapters the applicability of the kinetics is validated using the results of the batch experiments. To simulate the experiments like they were performed and also to validate the mixing model used, the batch experiments were simulated as a very fast semi-batch as described earlier.

After validation, the kinetics will be applied to the simulation with three different sophisticated thermodynamic models. The extended Debye-Hückel model, the Bromley model, and the Pitzer model will be used to estimate the activity coefficients of barium and sulfate ions in solution and the results are then compared. Only the higher sophisticated thermodynamic models from Bromley (1973) and from Pitzer (1973) give non-symmetrical results concerning the supersaturation for barium or sulfate excess, respectively. Therefore, only they can be expected to contribute to the prediction of the different PSDs observed. The extended Debye-Hückel model is included as a reference. It is a less sophisticated model often used for calculations in literature.

After the discussion of the influence of higher sophisticated thermodynamic models for the relevant supersaturation range, the necessity of including the non-stoichiometry directly into the nucleation and growth kinetics will be investigated. Suitable dependencies of the kinetics for non-stoichiometric precipitation conditions will be identified and applied to an example. Since the experimental data available

does not enable the derivation of quantitative nucleation rates, the proposed kinetic model will be of qualitative nature.

### 6.1 Validation of supersaturation-dependent nucleation and growth kinetics

Figure 40 shows the the PSD of the batch experiments and the simulation using the nucleation and growth kinetics presented in Chapter 5.4.1 and the Pitzer model for the activity coefficients. Calculation was done using the mixing model presented in Chapter 5.3 with an assumed feed rate of 600 ml/min. Like the experiments, the simulation was done for a total experimental time of 262.5s, the first 35 s being the feeding time of the second reactant into the vessel. The shape of the particles is shown to be flat, dendritic particles (Figure 20.5 for  $K_2SO_4$  feed and Figure 20.10 for  $BaCl_2$  feed), thus the volume shape factor of 0.06 from Fitchett and Tarbell (1990) derived for this shape was used.

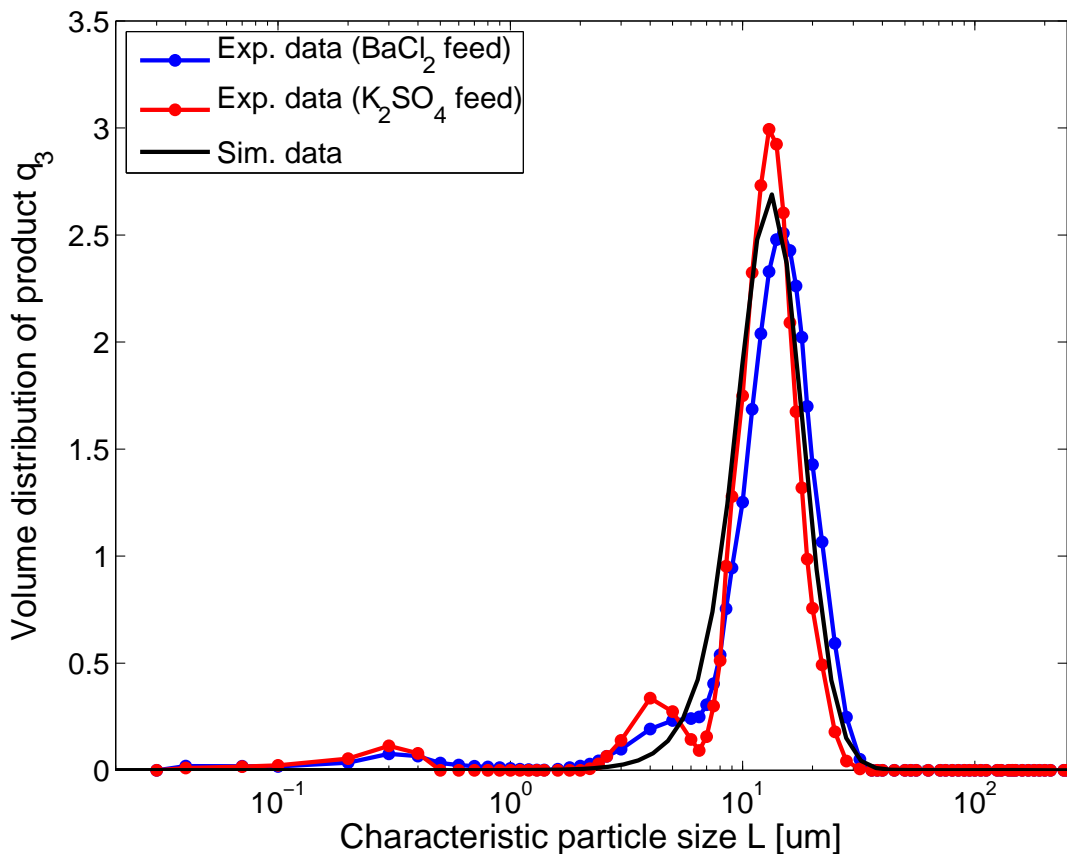


**Figure 40: Simulated particle size distribution in comparison to the batch experiments calculated as a very fast semi-batch ("a" in Table 19) using Pitzer method and kinetics from Eqs. (126) and (127).**

Table 18 gives the experimental mean diameters  $d_{43}$  in comparison with the calculated  $L_{43}$ .

**Table 18: Experimental and calculated mean diameters for the batch precipitation (Pitzer model)**

mean diameters [ $\mu\text{m}$ ]	$\text{K}_2\text{SO}_4$ feed	$\text{BaCl}_2$ feed
$d_{43}$	18.1	20.8
$L_{43}$	20.43	20.44

The calculated PSDs for both  $\text{K}_2\text{SO}_4$ -feed and  $\text{BaCl}_2$ -feed form nearly the same curve. Therefore, in Figure 40 one simulation line was plotted for both feeding sequences although the calculated values differ slightly. The difference can be seen for the values of mean diameters for the two feeding sequences in Table 18.

Agreement between experiments and simulation using the stated kinetics is acceptable. They are from the literature and were derived for stoichiometric batch experiments. The good fit of the kinetics in the simulation of the experimental results in this work justify the assumption that they can be used in principle for the semi-batch experiments in this work, too.

## 6.2 Validation of the supersaturation- and $R$ -dependent kinetics

The supersaturation- and  $R$ -dependent kinetics as presented in Chapter 5.4.2 derived by Aoun et al. (1996) are one possibility to include the non-stoichiometry directly into the nucleation and growth kinetics. In this subchapter, their applicability to the experiments of this work will be discussed. The batch experiment was chosen since Aoun et al. (1996, 1999) derived the kinetics for batch precipitation in a stirred vessel. Unfortunately, the batch experiment is not the best example to prove validity if simulated as a very fast semi-batch operation. Due to the fact that the theoretical initial ion ratio  $R_0$  is equal to 1, the growth and nucleation constants  $k_G$  and  $k_N$  have the same values for both feeding sequences. For semi-batch operation, the ion solution in the vessel is present in excess at the beginning of the experiment. Because of the different kinetic orders in the growth equation (Eq. (131)), the growth rate for the case of sulfate feed is higher and thus, gives greater particle sizes than for barium chloride feed. This contradicts the experimental results that show greater particle sizes for the case of barium feed. It also contradicts the already mentioned knowledge that barium sulfate particles are usually smaller if precipitated in barium excess (Eble, 2000). Therefore, it is clear to see that the case of semi-batch precipitation with ion solutions of stoichiometric concentration is not covered by the original  $R_0$ -dependent model from Aoun et al. (1996). The approach using the theoretical initial ion ratio  $R_0$  only makes sense for a batch operation with the

assumption of mixed ion species at time  $t=0$ . It cannot be applied to the case where the second ion solution is not present at  $t=0$  but is fed to the reactor in a finite amount of time as it is done for semi-batch precipitation. It was said before that the approach of using a dependence on the theoretical initial ion ratio  $R_0$  for the kinetics lacks a physical justification. The example shows why the growth kinetics of Aoun et al.'s (1996) model should not be applied to semi-batch operation. Instead of the theoretical initial ion ratio  $R_0$  the dynamic  $R(t)$  present in the reactor will be used giving the approach already presented in Chapter 5.4.2. It will be applied and discussed later. First, Aoun et al.'s stoichiometric kinetics (1999) will be applied to batch operation with assumed mixed ion solutions at time  $t=0$ .

### 6.2.1 Application of Aoun et al.'s (1999) kinetics (ideal mixed batch)

To show the agreement of Aoun et al.'s kinetics to the experiments it will be first applied to a simulated batch operation in an ideal mixed vessel. Since the ion ratio of barium to sulfate is equal to 1 at all times in this case, the non-stoichiometric kinetics (Aoun et al., 1996) reduce to the stoichiometric ones (Aoun et al., 1999). For the simulation, the latter were taken for the population balance model presented in Chapter 5 with the assumption of ideal mixed tank volume at all times. As in the previous subchapter, the volume shape factor for calculation had a value of 0.06 (Fitchett and Tarbell, 1990). The activity coefficient model was the Pitzer method. The resulting particle size distribution (PSD) is shown in Figure 41.

As can be seen, the particles in the simulated PSD are larger than the experimental ones. One reason for this could be the already mentioned fact that the growth term of Aoun et al.'s model was derived for a supersaturation level where integration limited growth plays a dominant role. The kinetic order of "2" in the growth kinetics ( $g$  in Eq. (129)) gives too great values for the growth rate if diffusion limited growth is dominant as can be assumed here. Thus, the growth rate calculated is too high leading to the observed bigger particles in the simulated PSD.

Considering this, the resulting simulated PSD seems to be in a reasonable range in comparison to the experiments.

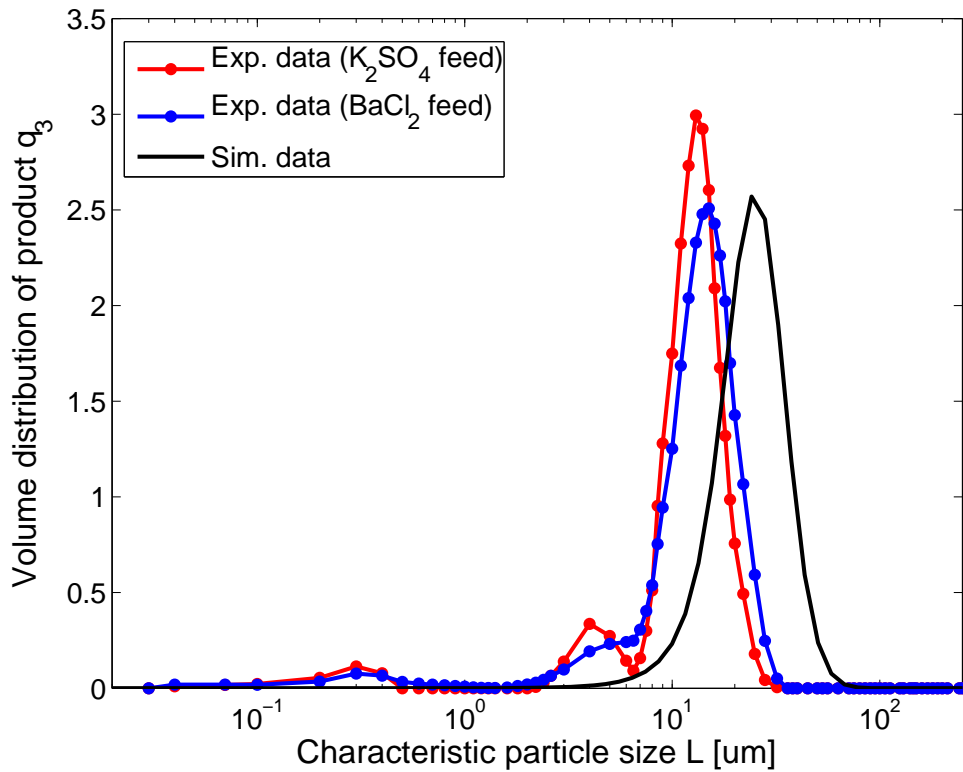


**Figure 41:** Simulated particle size distribution in comparison to the batch experiments calculated for an ideal mixed vessel using Pitzer method and Aoun et al.'s (1999) stoichiometric nucleation and growth kinetics (Eqs. (128) and (129)).

### 6.2.2 Application of $R(t)$ -adapted kinetics to batch experiments

Since the original  $R_0$ -approach cannot be applied (as stated above), the adapted  $R(t)$ -dependent kinetics were used instead. Figure 42 shows the simulated particle size distributions (PSDs) in comparison to the batch experiments calculated as a very fast semi-batch using Aoun et al.'s (1996) to  $R(t)$  adapted kinetics (Eqs. (134) and (135)). The simulation parameters were the same except for the activity coefficient model. Giving symmetrical supersaturation values in regard to barium and sulfate ion excess, the extended Debye-Hückel method was chosen here on purpose to be sure the differences in PSDs for the two feeding sequences are due to the  $R$ -dependence of the kinetics, only. The results show that the fit of the simulated PSDs are not good. The peaks are at too great values and are far too distinguished in comparison to the batch experiment. The peaks of the simulated PSDs are both at greater values than the experimental ones, the particle sizes for barium chloride feed being much greater. The reason for this discrepancy should be discussed in more detail. The influence of the growth term being one possible reason for the particle sizes being greater than the



experimental ones was already discussed above for the batch simulation. This does not necessarily explain the much greater sizes for barium chloride feed, though.

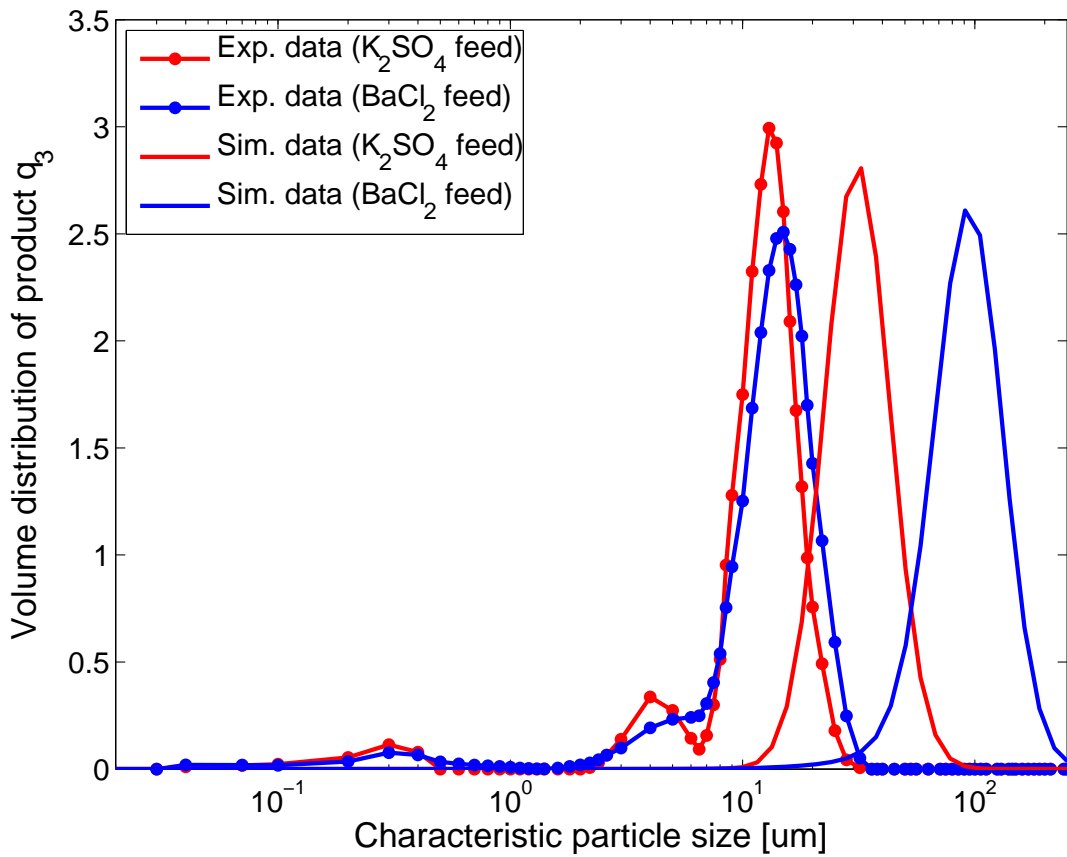


**Figure 42: Simulated particle size distribution in comparison to the batch experiments calculated as a very fast semi-batch ("a" in Table 19) using ext. Debye-Hückel method and Aoun et al.'s (1996) adapted kinetics (Eqs. (134) and (135)).**

For the  $R(t)$ -dependent kinetics, also the impact of the changes made to the original model by using the dynamic  $R$  have to be considered. Figure 43 shows the growth rate from Aoun et al.'s  $R$ -dependent model (1996) for the range of  $R$  from 0.1 to 10 at a constant supersaturation  $S_a = 100$  which is about the maximum of Aoun et al.'s investigated concentration range. If  $R$  moves away from 1, both growth rate and nucleation rate increase. Using  $R(t)$  instead of  $R_0$ , both kinetics can be assumed to be faster than predicted by Aoun et al., because for the semi-batch approach, i.e. starting with only one ionic solution in the vessel,  $R(t)$  is far from 1 at the beginning of the experiment. Thus, the kinetics are far too high in comparison to Aoun et al.'s original kinetics which were meant for batch if started in a mixed vessel. But, since both nucleation and growth rates are increased by using the dynamic  $R(t)$ , this does not have to be the reason for the great particle sizes calculated.

The main reason for the extraordinary great particle sizes calculated for barium chloride feed may lie in the asymmetry of growth rate for increasing barium and sulfate ion excess of Aoun et al.'s model. In Figure 43 the asymmetry with respect to  $R$  favours a higher growth rate for sulfate excess, i.e.  $R < 1$ . It will be shown later that the growth rate can be assumed to be constant for constant supersaturation regardless of the species of ions in excess (Chapter 6.4.2, Figure 56). Considering Eq. (131) the discrepancy between the reversed concentrations of barium and sulfate already present in Figure 43 will increase for increasing supersaturation, leading to an even higher growth rate for sulfate excess in comparison to barium excess for the same supersaturation level. Thus, in Figure 42 the greater particle sizes for barium feed result from the impact of the increase of overall growth rate for the sulfate excess being present in the vessel at the beginning of the simulation.

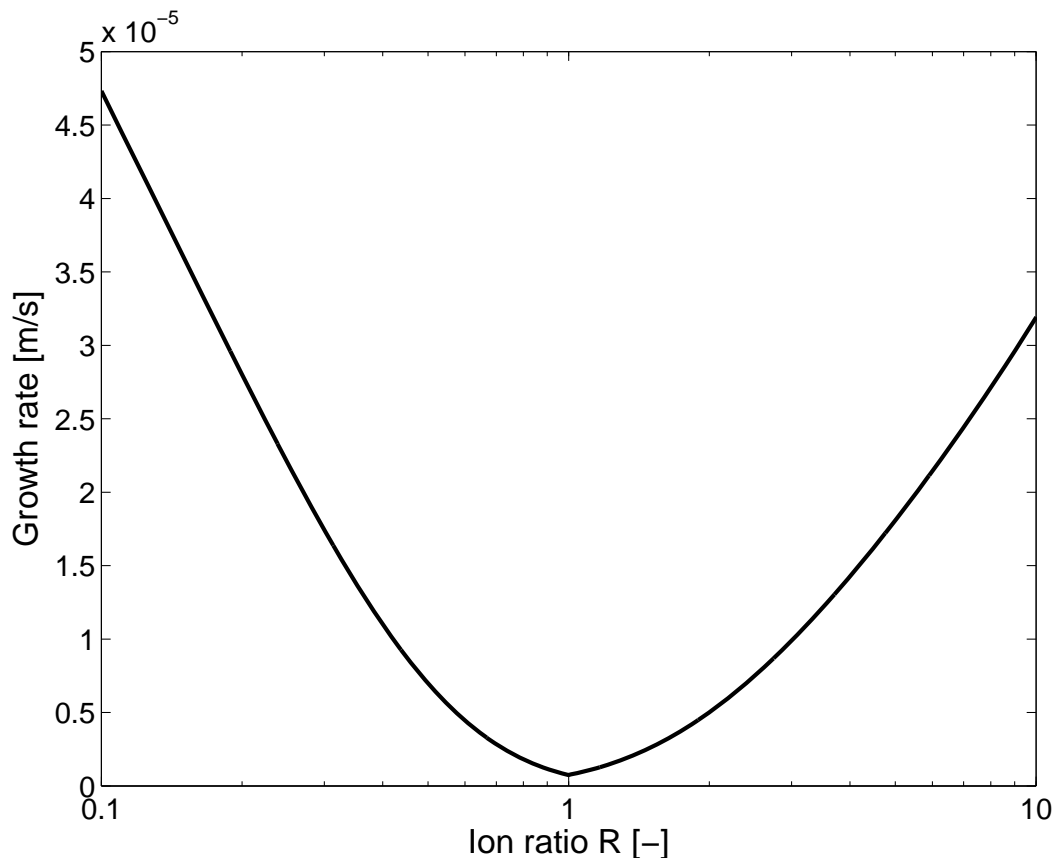


**Figure 43: Growth rate calculated with the  $R$ -dependent approach of Aoun et al. (1996) for a constant supersaturation of  $S_a = 100$ .**

It can be concluded, though, that in a qualitative way the kinetics from Aoun et al. (1996) with the adaption to  $R(t)$  can be used to describe the two different PSDs for the different feeding sequences as observed in the experiments in Chapter 4. They will be applied to semi-batch precipitation in the following.

### 6.2.3 Application of $R(t)$ -adapted kinetics to semi-batch experiments

Figure 44 shows the experimental and calculated PSDs of the particulate product for the semi-batch conditions of a theoretical initial supersaturation  $S_a = 527$  and 80 ml/min feed rate ("d" in Table 19). The dynamic  $R(t)$  was taken for nucleation and growth rate constants (Eqs. (133) to (135)) with the same simulation parameters as in the previous subchapter. The lines with markers show the experimental results for the two feeding sequences, the lines without markers show the simulation results as specified in the figure's legend.

The simulations give the right trend for the two feeding sequences with the distribution for potassium sulfate feed having smaller particle sizes. The peaks display far too great particle sizes, though. The reasons can be assumed to be the same as those already discussed above for the batch experiment.

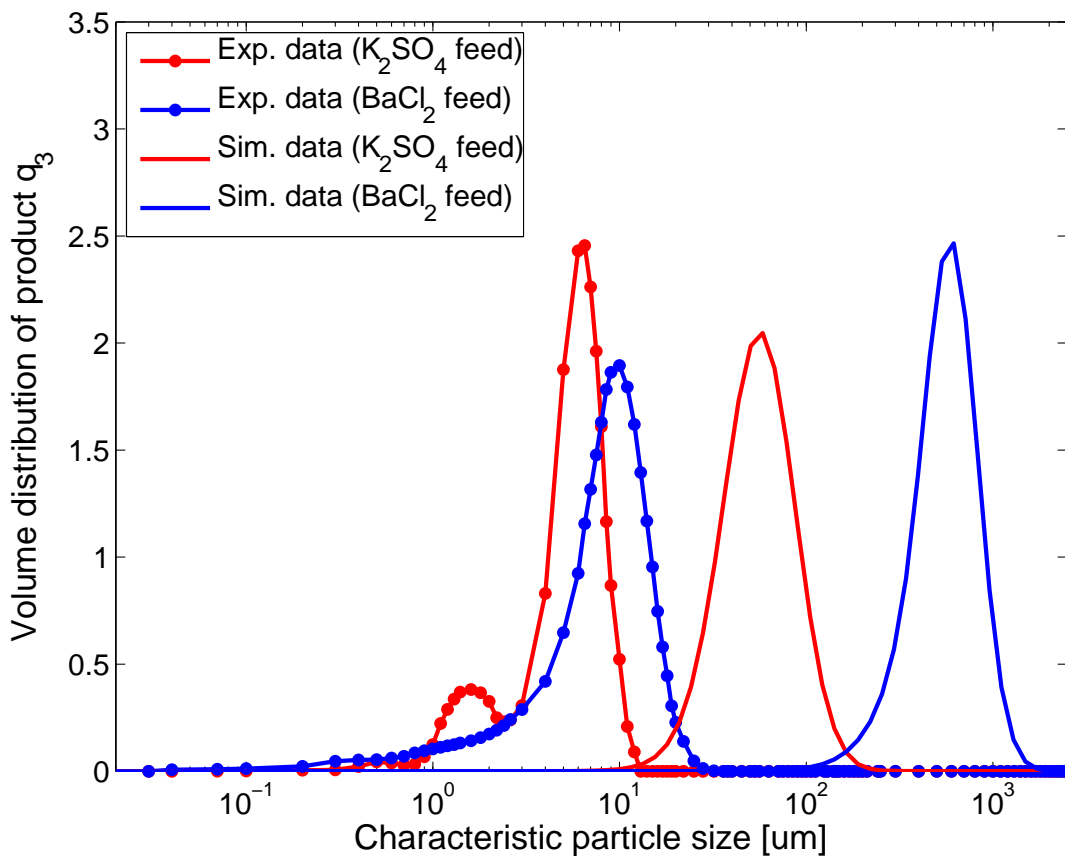


**Figure 44: Comparison of simulated and experimental particle size distributions (volume distribution function  $q_3$ ) of the particles precipitated using the  $R$ -dependent kinetics from Aoun et al. (1996, Eqs. (133) to (135)). The operation condition was semi-batch, theoretical initial  $S_a = 527$ . 80 ml/min feed rate ("d" in Table 19).**

In general, the adapted kinetics from Aoun et al. strongly overestimate the particle sizes. Still, in principle it can be used to describe the two different PSDs for the different feeding sequences.

### 6.3 Influence of the thermodynamic model

The influence of the thermodynamic model on differences in simulated particle size distributions (PSDs) will be investigated in the following. For highly sophisticated activity coefficient approaches it is of importance whether barium or sulfate ions are present in excess since they predict different supersaturation values accordingly. The question is how much influence this difference has on the resulting PSDs. All three activity coefficient models presented in the theory chapter (2.2) will be applied and compared. First, a case study with high concentrations will be presented. After that, the simulation results will be compared to an example experiment.

#### 6.3.1 Simulation studies

For this case study the simulation model presented in Chapter 5 was applied with the conditions listed in Figure 45. Kinetics used are the  $S_a$ -dependent nucleation and growth rates as presented in Chapter 5.4.1. The experimental conditions are theoretical and for discussion of the influence of activity coefficient models only.

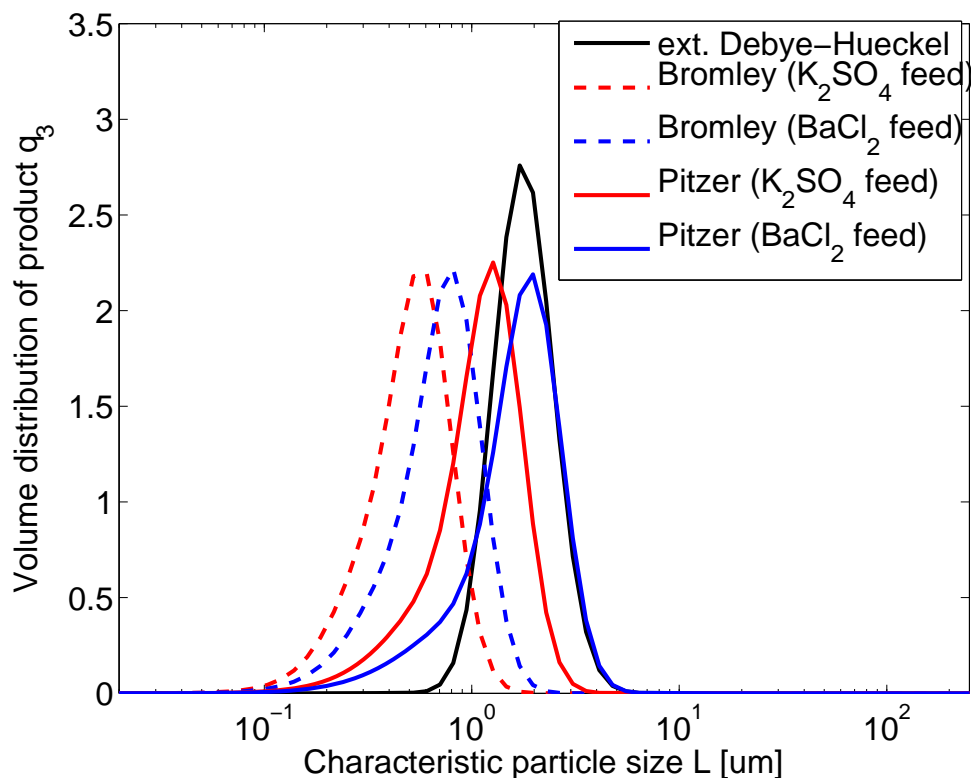


**Figure 45:** Calculated particle size distributions with three different activity coefficient models for the theoretical initial concentrations of  $0.5 \text{ kmol/m}^3$  in the tank and  $0.1 \text{ kmol/m}^3$  in the feed for a feed rate of  $80 \text{ ml/min}$ .

From the supersaturation diagram (Figure 2) it can be seen that the difference in activity coefficient for the three models is higher for high supersaturation. Therefore,

high concentrations were chosen for this case study to assure great influence of the thermodynamic model on the resulting PSDs. No experiment with such high initial supersaturations was carried out.

The shape factor was set to 1 for both feeding sequences. It is an arbitrary value, as the absolute value was not important. The same shape factor was chosen on purpose for all calculations to be able to see the influence of the thermodynamic model on the resulting PSDs.

In semi-batch operation, the tank initially contains one of the two ion solutions, i.e. either barium chloride or potassium sulfate. The other reactant is fed with constant feed rate to the vessel. This gives two experiments for each concentration ratio. Figure 45 shows simulated particle size distributions (PSD) for the conditions mentioned.

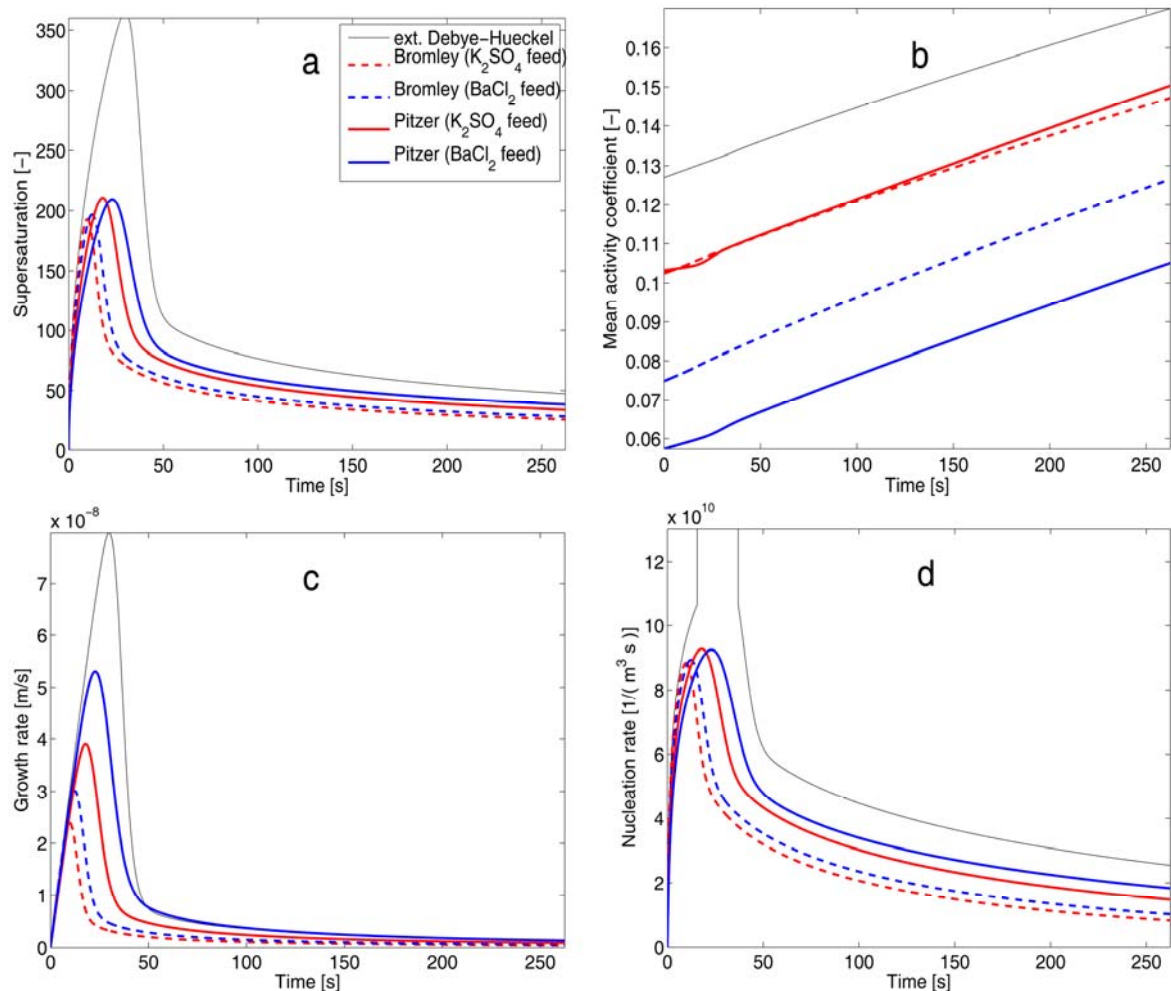


**Figure 46: Simulated supersaturation, activity coefficients, growth and nucleation rates with all three models for the theoretical initial concentrations of 0.5 kmol/m<sup>3</sup> in the tank and 0.1 kmol/m<sup>3</sup> in the feed for a feed rate of 80 ml/min. (In d, the peak was cut for a better observation of the other curves' slopes, as explained in the text.)**

For the extended Debye-Hückel model both feeding sequences result in the same distribution, as it is a symmetrical model with regard to barium or sulfate excess, thus only one line is shown for both feeding sequences. For the Bromley and Pitzer approaches, two PSD lines for the two different feeding possibilities are obtained as specified in the legend. For both methods, barium feed leads to greater particle sizes. This is to be expected, as for semi-batch operation in this case sulfate excess predominates in the tank. The particles are smaller for the Bromley approach. Surprisingly, the PSD for the extended Debye-Hückel approach is of a size range similar to that of the Pitzer model. This has to be explained by the dynamics of the process as outlined below.

Figure 46 compares the simulated dynamics of activity coefficients, supersaturation, growth, and nucleation rates based on the three different activity coefficient models discussed in Chapter 2.2.

Figure 46b shows the activity coefficients versus time. The activity coefficient for the extended Debye-Hückel approach is highest, followed by those of the Bromley and Pitzer approaches for sulfate feed. The activity coefficients calculated from the Bromley and Pitzer models for the barium feed are the lowest, and show greater difference than for sulfate feed, as can be expected from the supersaturation diagram (Figure 2), that shows a greater difference of activity coefficients for Pitzer and Bromley methods for the case of sulfate excess. In accordance with the activity coefficients, the supersaturation increase is highest for the extended Debye-Hückel model, and lowest for the Pitzer model for the case of barium feed (Figure 46a).

The further development of the supersaturation is due to the interacting dynamic influences of the supersaturation, the growth rate, and the nucleation rate. Higher supersaturation leads to a higher nucleation rate, with more particles being formed that consume the existing ions in solution upon growth. At the beginning, the growth rates for all models are of similar magnitude (Figure 46c). It is noticeable that this means that for some cases the growth rate is higher although the supersaturation is lower. This can be explained by the two-step growth model, as the impact of diffusion-controlled growth increases for higher supersaturation, thus giving a lower growth rate than the possible integration-controlled growth, which has a parabolic growth law. For the case of the extended Debye-Hückel model, supersaturation reaches such a high level that growth is significantly higher than for the other activity

coefficient approaches. For values of supersaturation above 280, the nucleation rate reaches into the region of homogeneous nucleation for extended Debye-Hückel model only (Figure 46d, black line). The maximum of the nucleation rate for this model lies at approx. 40 s of operation time and goes up to  $10^{14}$  ( $\text{m}^{-3} \text{s}^{-1}$ ). The peak was cut for a better observation of the other curves' slopes. These two effects of the extended Debye-Hückel model result in PSD sizes that are comparable to the ones of the Pitzer approach, although the activity coefficients for e.g. barium feed for Pitzer are half of the value than the ones for the extended Debye-Hückel model. Thus, a sophisticated thermodynamic model is indispensable to predict the correct phenomena occurring during the precipitation process. In case of the PSD, however, the assumption that the particle sizes are shifted into the same direction if the accuracy of the activity model increases is not valid, since for such a semi-batch experiment the resulting PSD is strongly influenced by precipitation dynamics.

### 6.3.2 Comparison with experimental results

In this subchapter, the batch nucleation and growth kinetics will be applied to semi-batch precipitation with thermodynamic models differing in sophistication. The simulations of particle size distributions (PSDs) using the three activity coefficient models will be compared with experimental results. The focus lies on the ability of the models to predict the two different PSDs for barium and sulfate excess, respectively.

The simulation model presented in Chapter 5 was applied with the  $S_a$ -dependent nucleation and growth kinetics from Chapter 5.4.1. The feed inlet volume of the mixing-model was the same size as for the batch example since no significant influence on the PSD was seen as already mentioned in Chapter 5.3. Table 19 lists the operation conditions for the simulations. Again, the same shape factor was chosen for both feeding sequences to focus on the influence of the thermodynamic models.

For discussion of the influence of the activity coefficient model the simulation of line "d" in Table 19 is taken as a typical example. The shape factor was set to 0.06 according to the particle shape of the potassium sulfate feed experiment. The influence of the activity coefficient models on the PSDs is minimal and can only be seen for high magnification (Figure 47, right). Showing greater particle sizes for barium chloride feed, the tendency of the simulated PSDs is correct. Overall, the

agreement between simulation and experiment is not satisfactory with two observed discrepancies for the example in Figure 47:

1. The simulated PSD seem to give a better fit for barium chloride feed.
2. The influence of the barium or sulfate ion excess is negligibly small in the simulation, whereas for the experiment two distinctive PSD peaks can be seen for reversed concentration conditions.

**Table 19: Operating conditions of precipitation experiments used for simulation**

concentration of reactant [mol/l]		feed rate [ml/min]	$S_a$ [-]	Ba <sup>2+</sup> / SO <sub>4</sub> <sup>2-</sup> ion ratio R [-]		labelling in Figure 49
in vessel	in feed			K <sub>2</sub> SO <sub>4</sub> feed	BaCl <sub>2</sub> feed	
0.01	0.01	600 (batch)	274	1	1	a
0.01	0.01	80	274	1	1	b
0.01	0.01	0.4	274	1	1	c
0.1	0.01	80	527	10	0.1	d
0.1	0.01	0.4	527	10	0.1	e

The reason why one feeding sequence is better described than the other is linked to the second discrepancy, i.e. the little influence of the activity coefficient model on the PSDs. But also, it was mentioned above that the same shape factor was used for both feeding sequences and the used shape factor of 0.06 is for flat dendritic particles and therefore better suitable for the case of potassium sulfate feed. For the according SEM image please refer to Figure 19.4 (page 69). The shape of the particles for barium sulfate feed (Figure 19.8) would be better described by star-like and therefore would require a different shape factor. The influence of the shape factor on the resulting PSD for this example is presented in Chapter 6.4.1. Thus, the simulated PSDs actually overestimate the particle sizes, i.e. the peak is shifted to greater values. This first discrepancy is discussed in more detail in Chapter 6.4.1. The focus of this chapter lies on the influence of the activity coefficient. Let us therefore discuss the second type of discrepancy, namely the weak influence of the feeding policy, i.e. the ion excess on the simulated PSD.



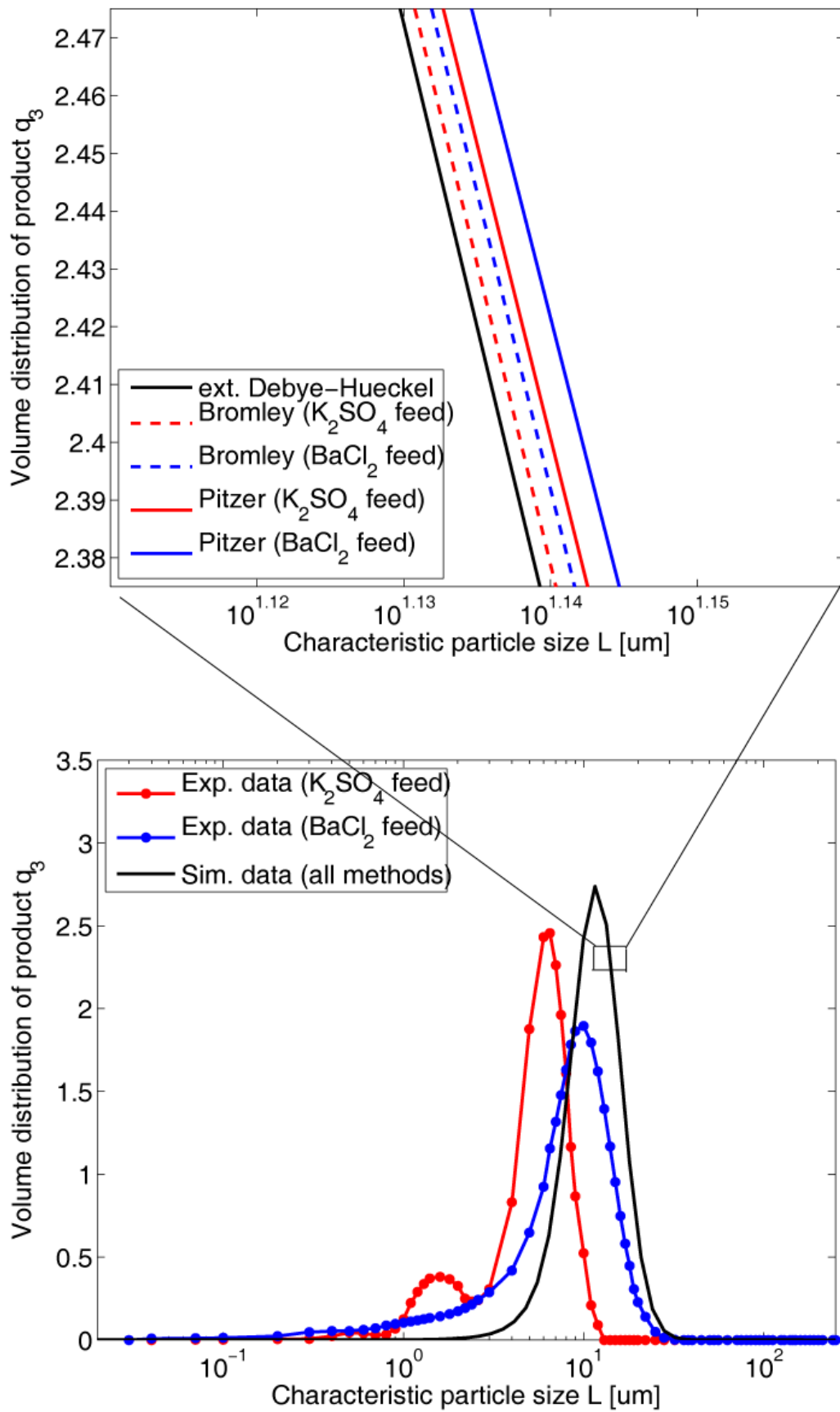
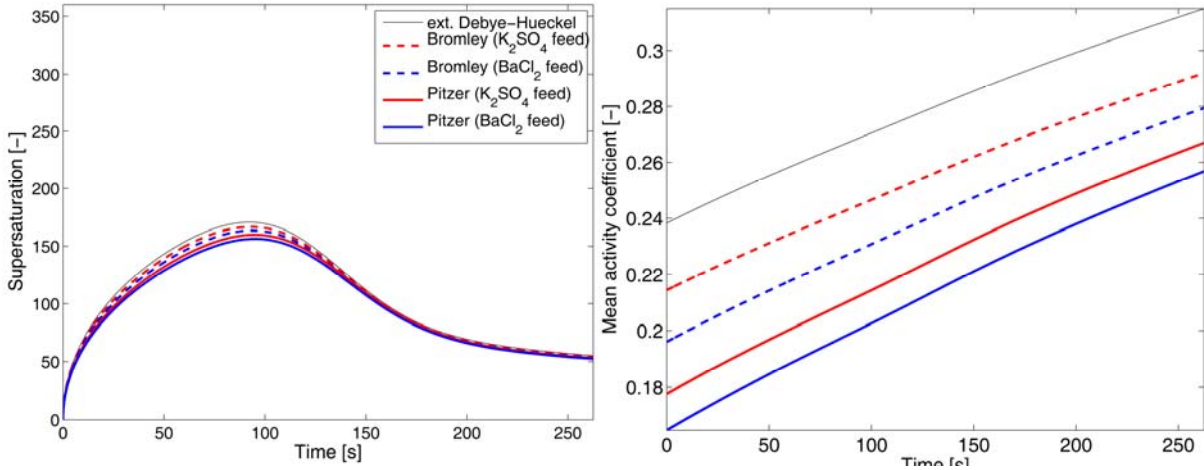


Figure 47: Simulated particle size distributions for the three activity coefficient models in comparison to the experiments. Theoretical initial  $S_a = 527$ ; 80 ml/min feed rate ("d" in Table 19).

Figure 48 compares the simulated supersaturations and activity coefficients for all three models over the operation time. It can be seen that the differences are not very pronounced.



**Figure 48: Differences in simulated supersaturations and activity coefficients. Theoretical initial  $S_a = 527$ ; 80 ml/min feed rate ("d" in Table 19).**

In the experiments, the PSD were smaller for barium excess. As already mentioned, barium ions preferentially adsorb on the barium sulfate particle surface, forming a positive charge and changing the interfacial tension, influencing the nucleation strongly (Eble, 2000). The resulting electrical potential forces also have influence on the movement of ion to and attachment on the surface and therefore on growth and nucleation rates for ion excess. The amount and charge of attached ions on the particle surface is dependent on the supersaturation and the ion ratio  $R$ .

The idea of the model formulated in Chapter 5 using Eqs. (126) and (127) for growth and nucleation rates is to describe nucleation and growth by supersaturation dependent kinetics. The influence of ion excess is captured by detailed activity coefficient models that determine the actual supersaturation  $S_a$ . As shown in the previous section, this causes an asymmetric dependence of the model on the excess ratio  $R$ . However, the effect is quite small compared to the experiments.

Further, at first glance it is surprising that in Figure 47 there is hardly any difference between the predictions based on different activity coefficient models. But this can be explained by having a closer look at the conditions during the experiments. Figure 49 shows the trajectories of the ion concentrations calculated for the five experimental conditions as given in Table 19. Two different concentration ratios were used, each with different feed rates. Every set was done for the two feeding

sequences, i.e. barium chloride in the feed and potassium sulfate in the vessel versus potassium sulfate in the feed and barium chloride in the vessel with the appropriate concentrations. The supersaturation diagram was calculated using the Pitzer approach for predicting the activity coefficient. The thick solid lines represent the experiments with lowest feed rate of 0.4 ml/min, the dashed lines refer to 80 ml/min, and the dotted lines are for the batch equivalent experiment (feed rate 600 ml/min). The cross marks the ideal batch point for instantaneous mixing without barium sulfate complex formation. The circle marks the ideal batch point if complex formation is considered, as it is done in this work. The diagonal bisecting line represents the  $R = 1$  line. Also included are the lines for  $R = 0.1$  and  $10$  as specified. In the lower triangle, the values are for barium feed experiments, in the upper triangle for sulfate feed. All trajectories do not cross the line at  $R = 1$ .

The start of all trajectories is on the rim of the diagram where the concentration of the ion species in the feed is smallest, marking the beginning of the experimental runs. Upon feeding, the concentration of the feed ion species increases as implied by the arrows, leading to higher supersaturation levels. After reaching a maximum supersaturation, the trajectories run backwards and up to lower concentrations of the ionic species in the tank as indicated by the arrows. It can be seen that the batch trajectory ("a" from Table 19) runs straight to the ideal batch point, and after that on the  $R = 1$  line during the time after feeding is terminated. The other trajectories do not reach that far and have their turning point at lower supersaturations, although all experiments for the same concentration ratio run on the same path at the beginning. Thus, although starting with the same experimental conditions regarding concentrations, volumes of reactants and experimental set-up, the varied feed rates and reversed feeding sequences lead to different trajectories in the supersaturation diagram with different supersaturation peaks reached, also explaining the diverse morphologies and sizes of the resulting particles as described in Chapter 4.

Still, all trajectories run in regions where the three activity coefficient models give similar results, as also shown in Figure 48. Thus, the experiments are in supersaturation regions where the impact of the complexity of the activity coefficient model is negligible and the supersaturation-only based growth and nucleation rates are not much influenced. This is why the influence of activity coefficients in the model is too small on the resulting simulated particle size distributions for the different feeding sequences of the experiments discussed here.

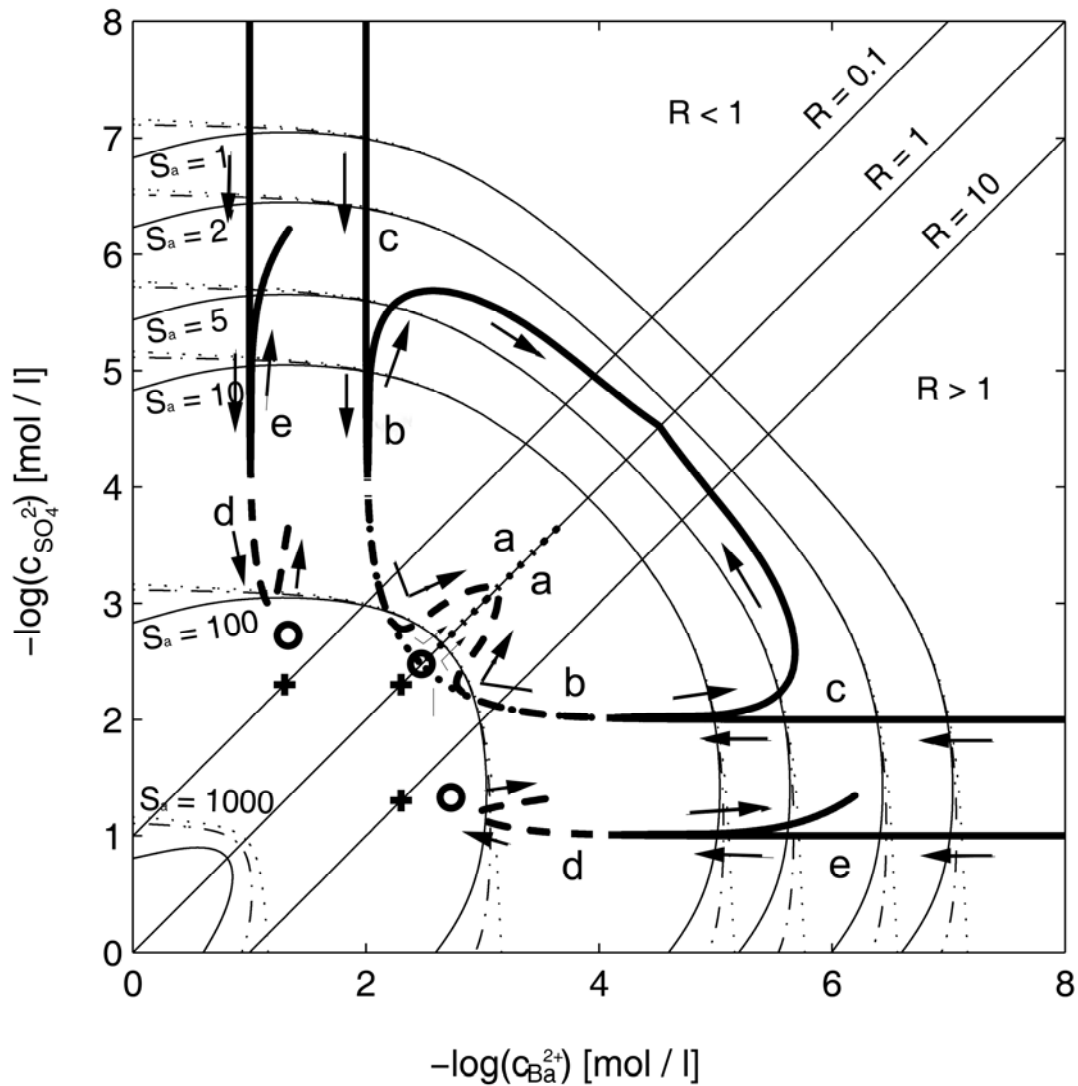


**Figure 49:** Simulated trajectories in the supersaturation diagram (lines of constant  $S_a$  calculated with Pitzer model) for the experiments listed and specified in Table 19 and discussed in the text.

#### 6.4 Influence of kinetics

As seen above, the influence of the thermodynamic model on the simulation does not suffice to describe the two distinctive peaks for the reversed concentrations of barium and sulfate for non-stoichiometric semi-batch feeding.

It was mentioned in Chapter 2 that for fast precipitation of barium sulfate the crystals form metastable, kinetically controlled morphologies. It seems that the influence of particle shapes on particle size distributions (PSDs) has to be considered in the simulation by other means.

The most accurate solution would be to simulate the growth with different growth rates of different faces including all influences of ion excess and adsorption of potential-determining ions of the crystal surface. Such a multi-dimensional model is highly sophisticated and would require a lot of experimental data not easily available. For this work, a one-dimensional population balance model (1-D PBE) for simulation of the PSDs was chosen. In this model, kinetically controlled crystal morphologies can be taken into account by the use of appropriate shape factors, if these are known. In previous works, possible solutions for the prediction of particle size distributions (PSDs) for non-stoichiometric precipitation systems independent of particle morphologies were discussed (Steyer et al., 2010). Such an approach is possible but requires extensive empirical validation.

For the particles precipitated in this work, shape factors were estimated as listed in Table 20. The resulting simulated PSDs using these shape factors in comparison to the experiments will be discussed next.

#### 6.4.1 Shape factors

For the investigation of the thermodynamic model the same shape factor was used on purpose to see the influence of the asymmetry of the sophisticated thermodynamic model. In this subchapter, different shape factors for the two feeding policies are used in the simulation of some semi-batch examples and the resulting PSDs are discussed.

**Table 20: Volume shape factors used for simulation (according to Eq. (72), estimated from SEM images)**

concentration of reactant [mol/l]		feed rate [ml/min]	$S_a$ [-]	K <sub>2</sub> SO <sub>4</sub> feed		BaCl <sub>2</sub> feed		line in Table 10	No.
in vesse l	in feed			$k_v$ [-]	SEM image	$k_v$ [-]	SEM image		
0.01	0.01	batch (600)	274	0.06	Figure 20.5	0.06	Figure 20.10	11	1
0.01	0.01	80	274	0.09	Figure 20.4	0.01	Figure 20.9	4	2
0.01	0.01	20	274	0.04	Figure 20.3	0.006	Figure 20.8	8	3
0.01	0.01	0.4	274	0.2	Figure 20.1	0.1	Figure 20.6	10	4
0.1	0.01	80	527	0.06	Figure 19.4	0.004	Figure 19.8	1	5
0.1	0.01	20	527	0.06	Figure 19.3	0.004	Figure 19.7	5	6
0.1	0.01	0.4	527	0.1	Figure 19.1	1	Figure 19.5	7	7

Volume shape factors were estimated using Eq. (72) from the according SEM images with the assumption that flat particles have a thickness of 1  $\mu\text{m}$ . This seemed appropriate according to observations from some of the SEM pictures. The longest particle axis was taken as the characteristic particle length. Table 20 lists the volume shape factors with reference to the particles' SEM images.

It was shown earlier that agreement of the simulation model used with the kinetics discussed is good for the case of stoichiometric batch operation. Figure 50 shows the PSDs of experiment and simulation in comparison for a semi-batch experiment with stoichiometric initial conditions (no. 2 in Table 20). The peaks of the simulated PSDs are in the range of the experimental one, making it a quite good fit.

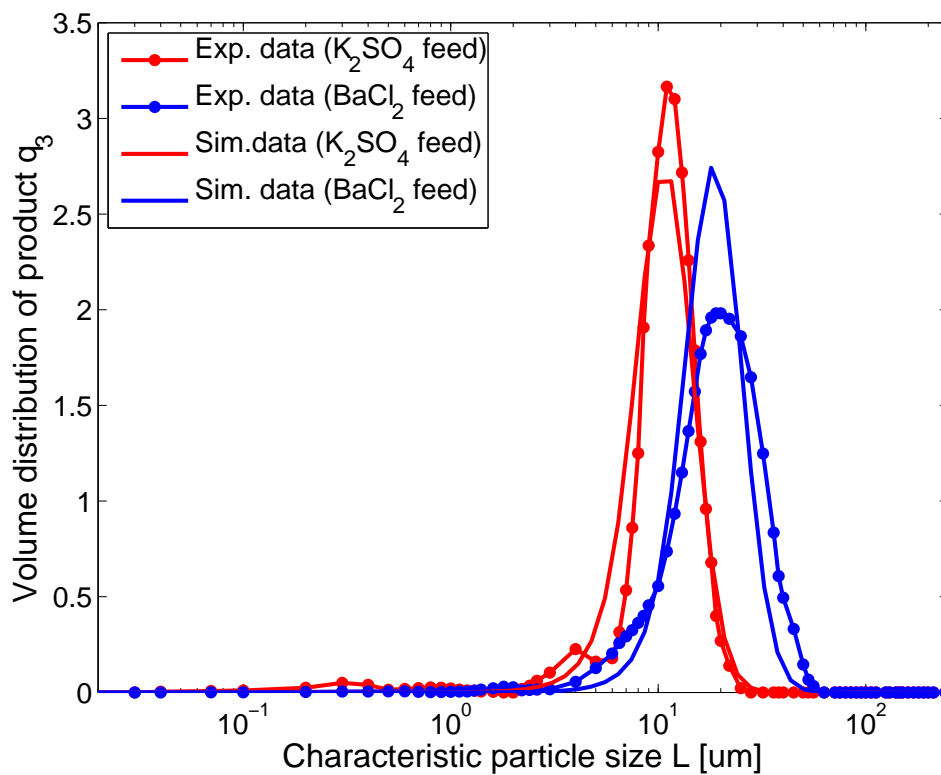


**Figure 50: Simulated PSD in comparison to the experiments using Pitzer method and kinetics from Eqs. (126) and (127) for stoichiometric ion ratio.  $S_a = 274$ , 80 ml/min feed rate (no. 2 in Table 20).**

Figure 51 shows the PSDs for specific times during these simulated experiments as well as the experimental results of the product particles. For better clarity the cumulative curve  $Q_3$  is chosen for this figure. It can be seen that the PSDs for the two different feeding policies are nearly the same for approx. the first 90 s of the simulation. Then, the PSDs of the two experiments develop differently, with resulting smaller particle sizes for the case of  $\text{K}_2\text{SO}_4$  feed. The calculated intermediate PSDs results are shown for additional insight into the possible process.

Unfortunately, there are no intermediate experimental results for PSDs the simulations can be quantitatively compared to. Therefore, only the PSDs of the products will be used in the following to evaluate the applicability of the model kinetics on the experiments.

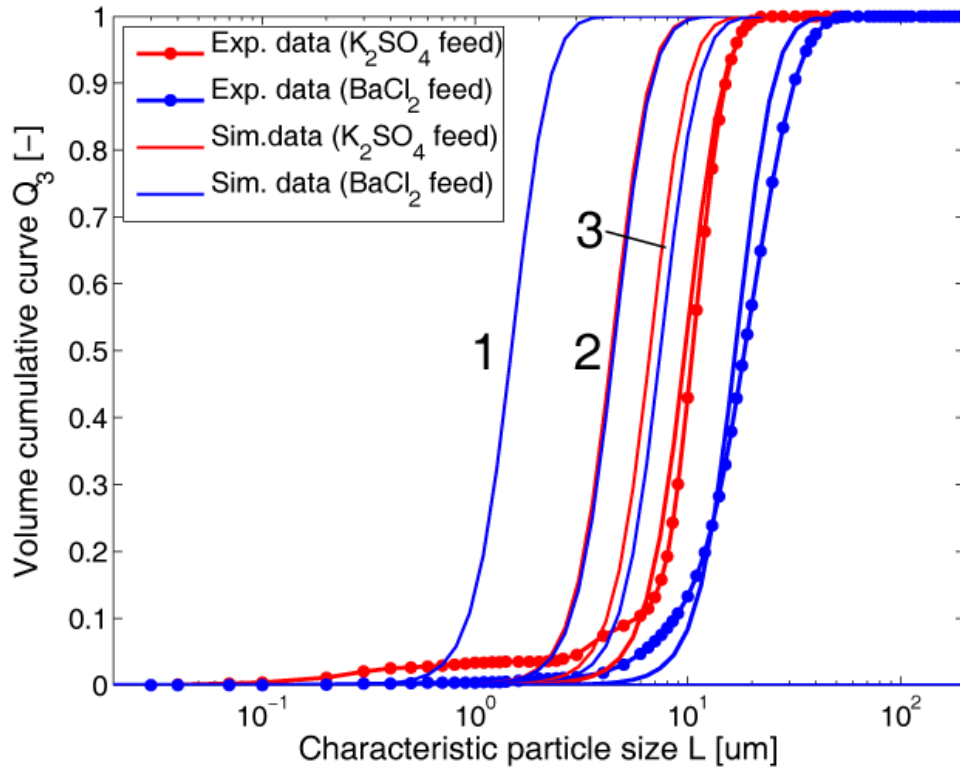


**Figure 51: Simulated cumulative curve for different times. Same experimental conditions as in Figure 50:  $S_a = 274$ , 80 ml/min feed rate (no. 2 in Table 20). 1: at  $t=50$  s, 2: at  $t=90$  s; 3: at  $t=120$  s. Thick lines are for simulated product PSDs.**

The same can be seen in Figure 52 for a stoichiometric semi-batch example of slower feed rate (no. 3 in Table 20). The fit is still acceptable but not as good as for faster feeding. Still, it seems for stoichiometric ion ratio of ion solutions the fit of simulated particle sizes are in good range for semi-batch operation.

Figure 53 shows the resulting PSDs in comparison to the experiments for the non-stoichiometric semi-batch example discussed in the previous subchapters (no. 5 in Table 20). The PSD peaks for barium or sulfate feed show the right tendency but simulation overestimates the particle sizes for non-stoichiometric conditions as already discussed in Chapter 6.3.2.

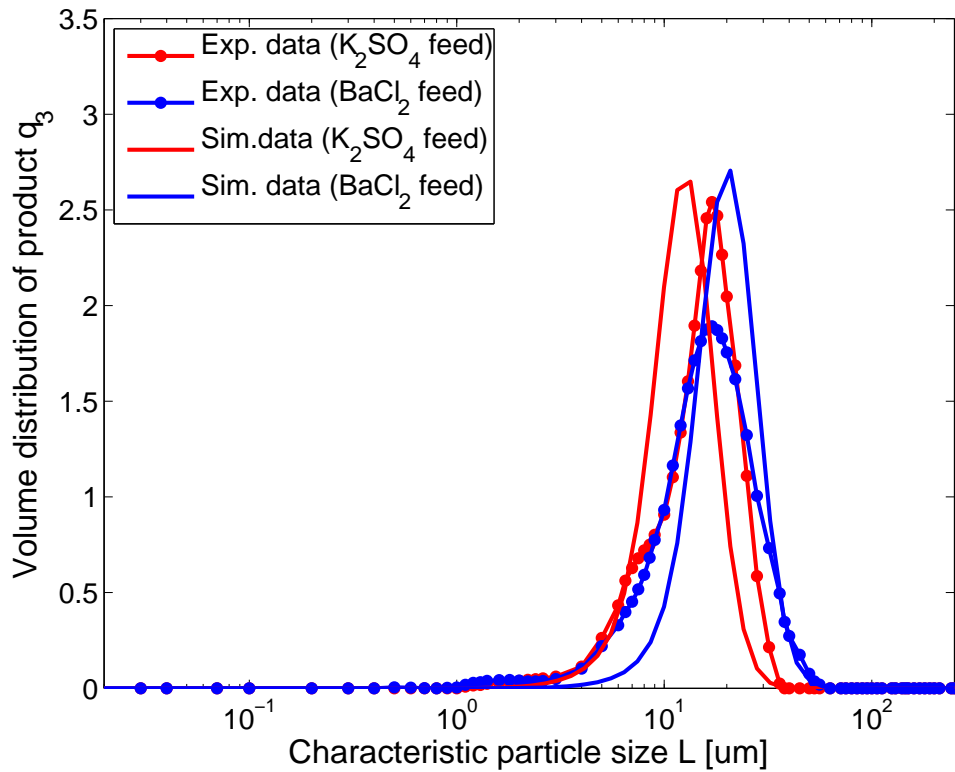


Figure 52: Simulated particle size distribution in comparison to the experiments using Pitzer method and kinetics from Eqs. (126) and (127) for stoichiometric ion ratio.  $S_a = 274$ , 20 ml/min feed rate (no. 3 in Table 20).

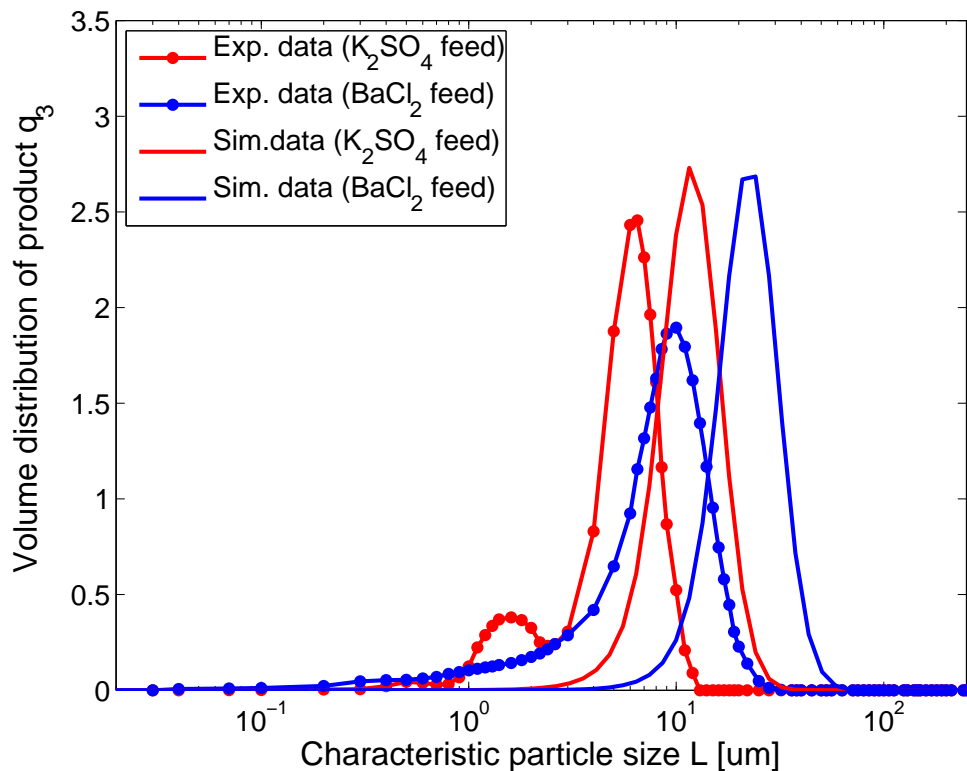
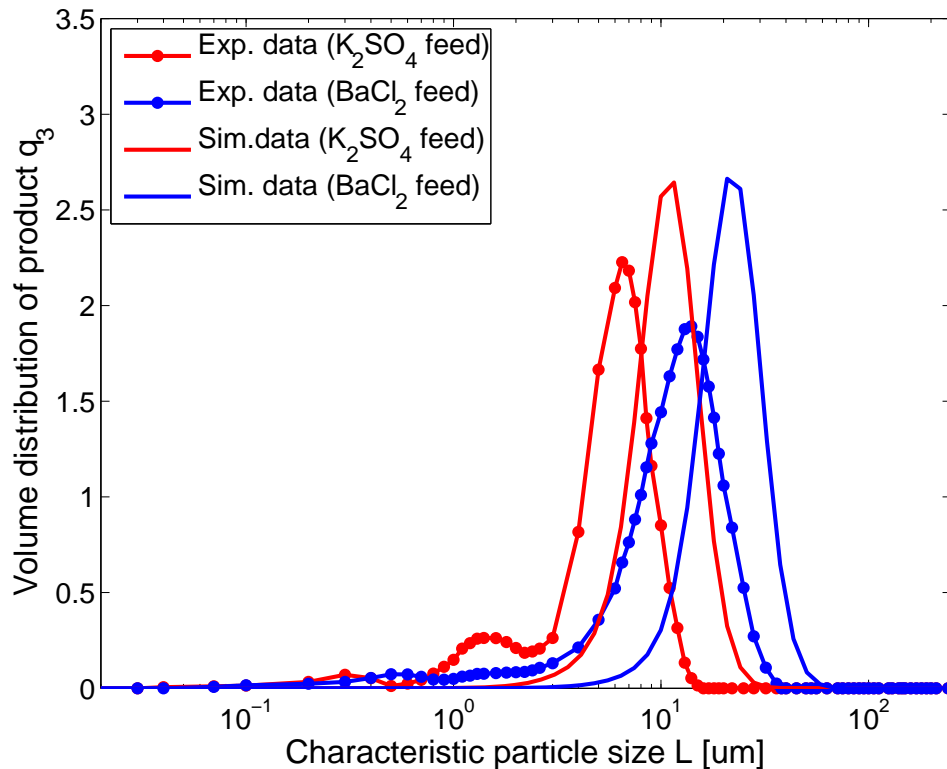


Figure 53: Simulated particle size distribution in comparison to the experiments using Pitzer method and kinetics from Eqs. (126) and (127).  $S_a = 527$ , 80 ml/min feed rate (no. 5 in Table 20).





**Figure 54: Simulated particle size distribution in comparison to the experiments using Pitzer method and kinetics from Eqs. (126) and (127).  $S_a = 527$ , 20 ml/min feed rate (no. 6 in Table 20).**

In Figure 54 particle sizes were simulated for non-stoichiometric conditions at a slower feed rate as specified. The particle sizes are shifted to greater values for this example, too.

Figure 55 shows the simulated particle sizes for stoichiometric operation at the lowest feed rate of 0.4 ml/min. Here, the particle sizes are highly underestimated. The simulation model does not seem able to predict the particle sizes. This could also be due to the growth of new layers with different orientation starting on face imperfections already mentioned and as seen in the SEM images for these experiments which could lead to smaller simulated than measured particle sizes. Thus, caution has to be taken if applying the simulation model to the experiments at the lowest feed rate of 0.4 ml/min. The results shown in Figure 55 were not included into the evaluation of the nucleation and growth kinetics.

It can be concluded that using the nucleation and growth rates discussed the PSDs for non-stoichiometric semi-batch precipitation cannot be predicted correctly. It seems either predicted growth is too high, or nucleation rate is underestimated, or both.

This will be discussed further in the next chapter where the dependence of nucleation and growth rates on the non-stoichiometry, i.e. barium or sulfate ion excess will be discussed.

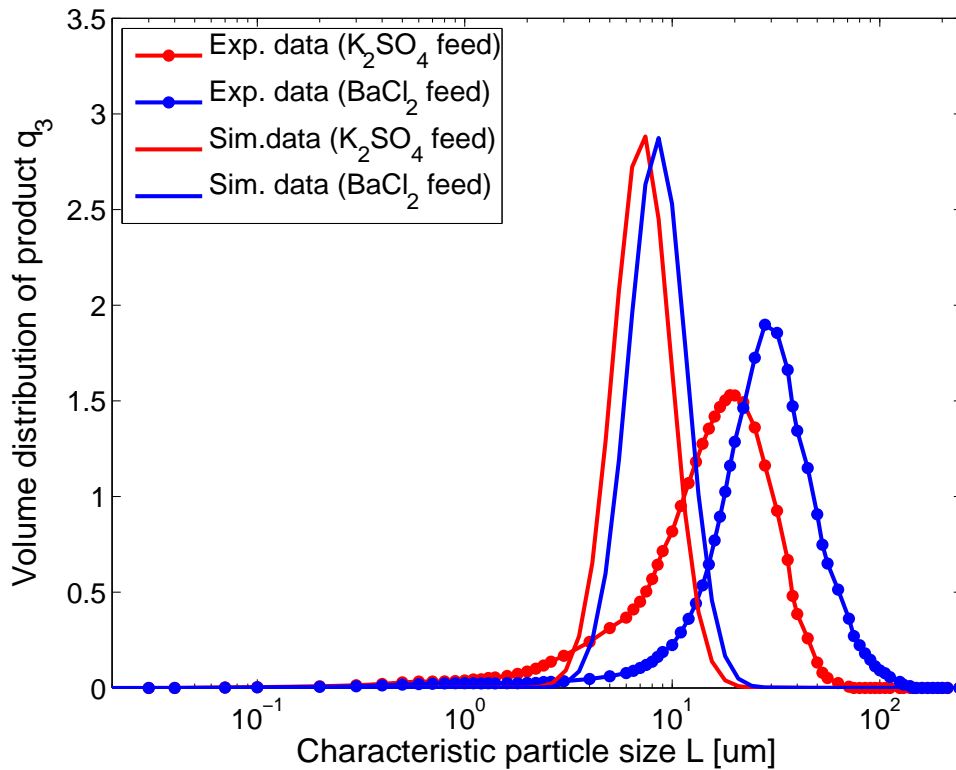


**Figure 55: Simulated PSDs in comparison to the experiments using Pitzer method and kinetics from Eqs. (126) and (127) for stoichiometric ion ratio.  $S_a = 274$ , 0.4 ml/min feed rate (no. 4 in Table 20).**

#### 6.4.2 Sensitivity of nucleation and growth rates to $R$

The results above showed that the influence of the thermodynamic model on different PSDs for barium or sulfate excess for non-stoichiometric semi-batch precipitation is negligible for the supersaturation range investigated here. The two different PSDs can only be predicted by consideration of the kinetically controlled particle shape in the simulation model.

Stoichiometric precipitation can be described well if shape factors of particles are known.

For non-stoichiometric conditions the use of correct shape factors leads to two different PSDs for the two different feeding sequences but prediction of particle sizes is not satisfactory. The influence of ion excess on the precipitation kinetics discussed above should be included for a better model prediction for non-stoichiometric semi-batch precipitation.

One way for taking into account the influence of ion excess is by directly integrating the ion ratio  $R$  into the kinetics like it was done by Aoun et al. (1996). As already shown, the growth term of the Aoun et al.'s model has too strong an impact on the resulting PSD, leading to too great particle sizes in the simulation. It is worth considering whether the empirical extension of the kinetics by including the dependence on the ion ratio  $R$  is really necessary for both nucleation and growth kinetics. It was already stated that for barium sulfate precipitation the nucleation rate is influenced more strongly than the growth rate by ion excess (Eble, 2000). This will be shown with literature data in the following.

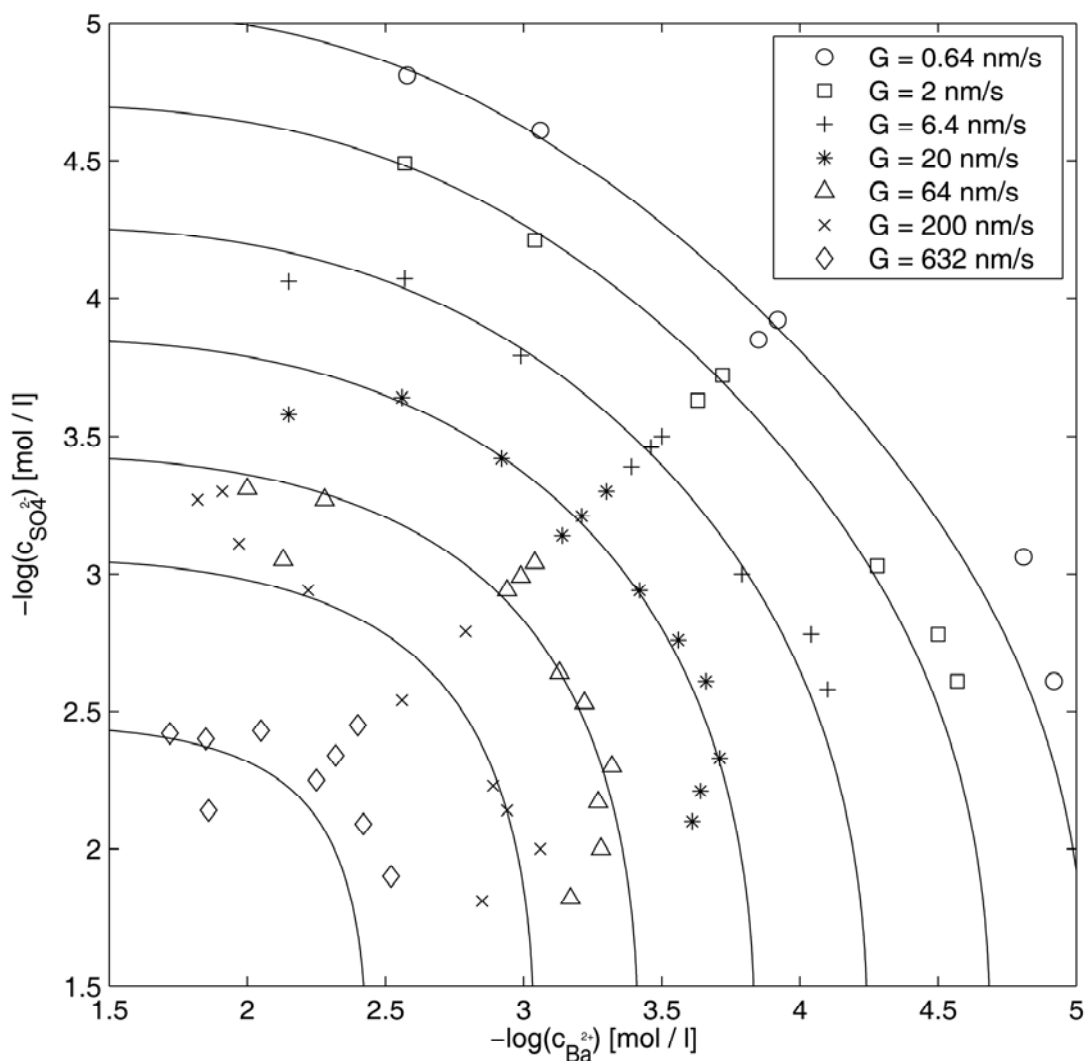


**Figure 56: Growth rate data from Nielsen and Toft (1984) in a supersaturation diagram (calculated with Pitzer model).**

For constant supersaturation Aoun et al.'s growth rate predicts a dependence on  $R$  (see also Figure 43), whereas the  $S_a$ -dependent growth kinetics as used in this work are constant. Experimental results by Nielsen and Toft (1984) support the latter

approach as can be seen in Figure 56. It shows experimental data from Nielsen and Toft for growth rates at non-stoichiometric conditions. The solid lines are for constant supersaturation, calculated with the Pitzer approach. Identical symbols indicate identical growth rates as measured by Nielsen and Toft (1984). It can be seen that although it could be interpreted that for lower supersaturations growth rates are higher for sulfate excess than for barium excess, overall the assumption of constant growth rates for constant supersaturation can be seen as sufficient to describe the growth rates for non-stoichiometric conditions.

Concluding from these literature data as presented in Figure 43 and Figure 56, as a good first approach the growth rate seems to be appropriately described by a supersaturation-dependent model as given by Eq. (127) for non-stoichiometric precipitation. There seems to be no explicit need to extend the growth kinetics to include the ion ratio as it was done by Aoun et al. (1996).

Now we come to the behaviour of the nucleation rate. Figure 57 shows the nucleation rate of the  $R$ -dependent kinetic approach of Aoun et al. (1996). The figure is for a constant supersaturation of 100, which implies different concentration ratios for barium and sulfate excess if the supersaturation is calculated using the Bromley or Pitzer models for the activity coefficient. The range of the ion ratio  $R$  goes from 0.1 to 10 like in the work from Aoun et al. (1996). The kinetics of Aoun et al. are calculated using the extended Debye-Hückel approach, for excluding non-symmetric influences of the activity coefficient. The differences for  $R$  greater or smaller 1 are therefore only due to the  $R$ -dependence of the kinetic approach as measured by Aoun et al. The nucleation rate is not constant for the considered region but shows a noticeable change if  $R$  is not equal to 1. Also, the influence of barium and sulfate ion excess is asymmetrical with a ratio of 16.9 for the values at  $R = 0.1$  and  $R = 10$ . For higher excess of ions, the impact can be assumed to increase accordingly.

Hence, for nucleation kinetics, influence of ion excess of barium and sulfate concerning change of kinetics and non-symmetry with regard to the two ionic species is not predictable by a supersaturation-dependent model only. The ion ratio of barium and sulfate has to be considered as well.

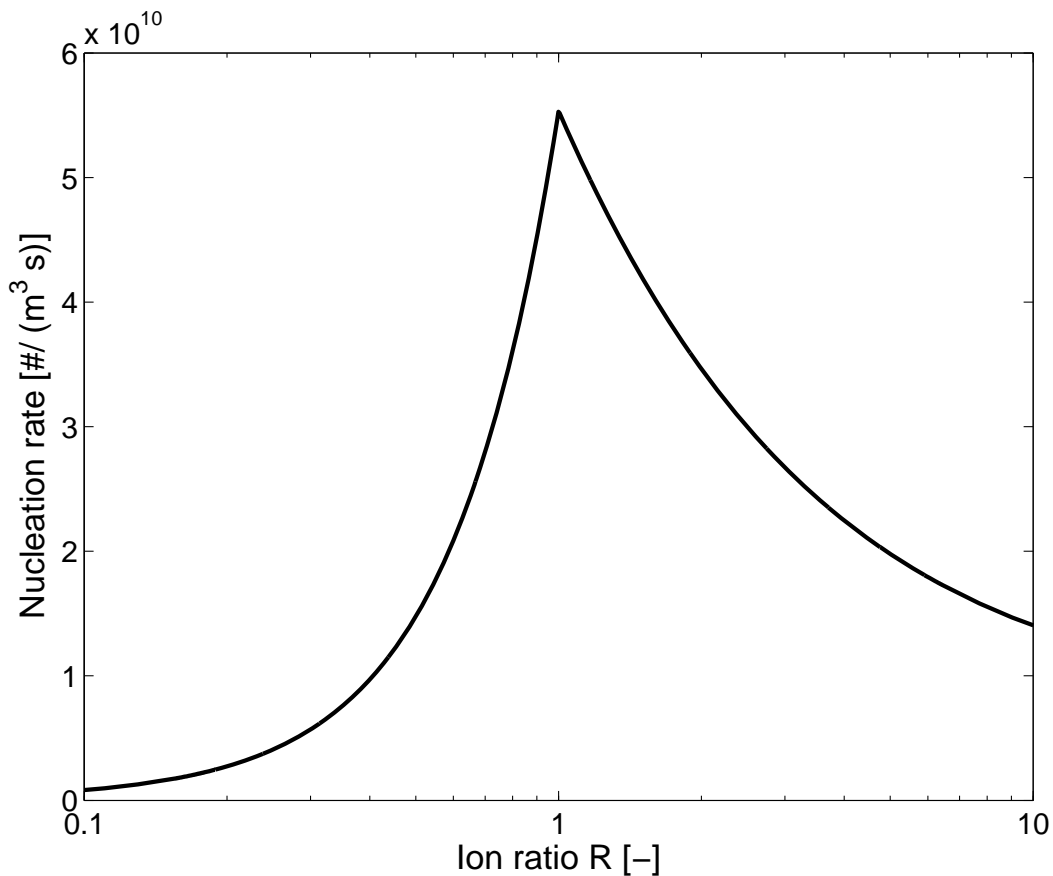


**Figure 57: Nucleation rate calculated with the  $R$ -dependent approach of Aoun et al. (1996) for a constant supersaturation of  $S_a = 100$ .**

This conclusion is consistent with the work of Eble (2000) who determined that the adsorption of potential-determining ions on the crystal surface result in a change of interfacial tension for ion excess which influences the nucleation strongly.

### 6.5 Proposed kinetic model with $R$ - $S_a$ -dependent nucleation

In the previous chapter it was discussed that nucleation kinetics should be dependent on the ion ratio of barium and sulfate, whereas the growth rate can be described by a supersaturation-dependent kinetic model. In the following a quick check whether such a model based on supersaturation-dependent growth rate and a supersaturation as well as ion ratio-dependent nucleation rate would be appropriate to predict the different particle size distribution (PSD) peaks for the reversed feed sequences will be performed. For this, the experimental conditions as used for Figure 47 (no. 5 in Table 20) was calculated with the simulation model of Chapter 5 using the supersaturation-dependent growth rate from Eq. (127) and the adapted nucleation rate from Aoun et al. (1996) as given by Eq. (135). Simulation was done using the

shape factors as listed in Table 20 and the extended Debye-Hückel method for calculation of the activity coefficients.

Figure 58 shows the resulting PSDs for the batch conditions calculated as a very fast semi-batch as described earlier. The fit for barium sulfate feed is agreeable. For potassium sulfate feed the particle sizes are underestimated by the simulation. The predicted nucleation rate seems to be too high in this case.

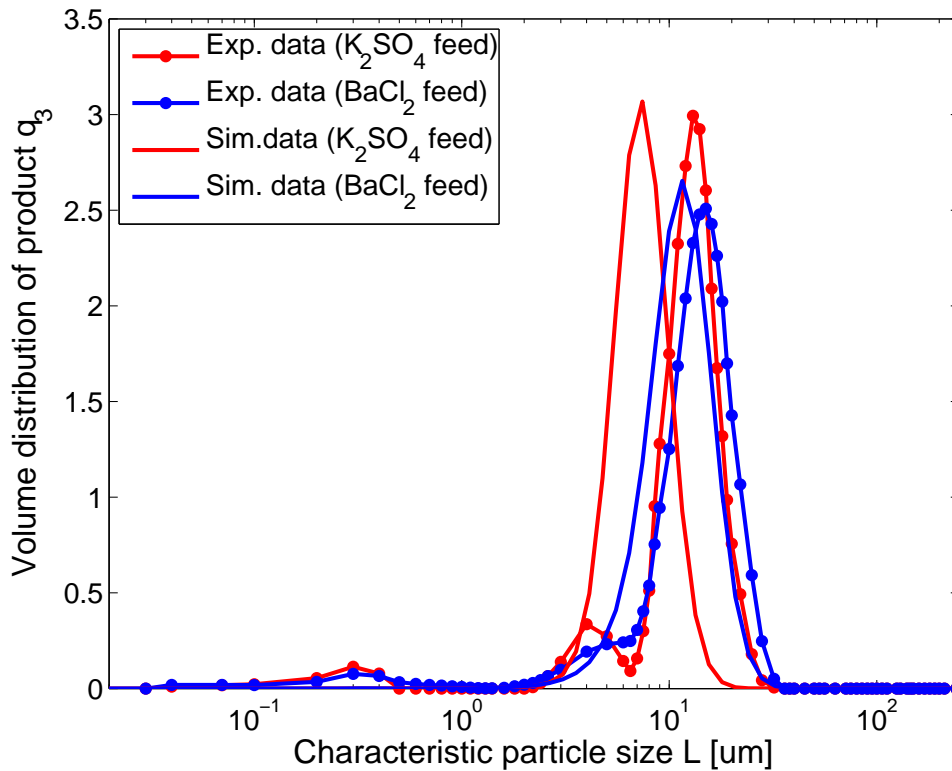


**Figure 58: Simulated PSDs in comparison to the batch experiments. Growth and nucleation kinetics by Eq. (127) and Eq. (135) as specified in the text (no. 1 in Table 20).**

In Figure 59 the results for the semi-batch example of  $S_a = 527$ , 80 ml/min feed rate (no. 5 in Table 20) is presented.

Again, the nucleation rate is too high for potassium sulfate feed giving too small particle sizes like it is for the batch experiment. For barium chloride feed on the other hand, nucleation seems to be too low. Here, the predicted particle sizes are too great.

The reasons for the discrepancy between simulated and experimental PSDs will not be discussed in more detail, as the used nucleation kinetics were not derived for these precipitation conditions originally. Better quantitative agreement could be achieved by appropriate parameter fitting. Nevertheless, the result is sufficient to affirm the

principle applicability of the proposed “mixed” kinetic model to non-stoichiometric precipitation.

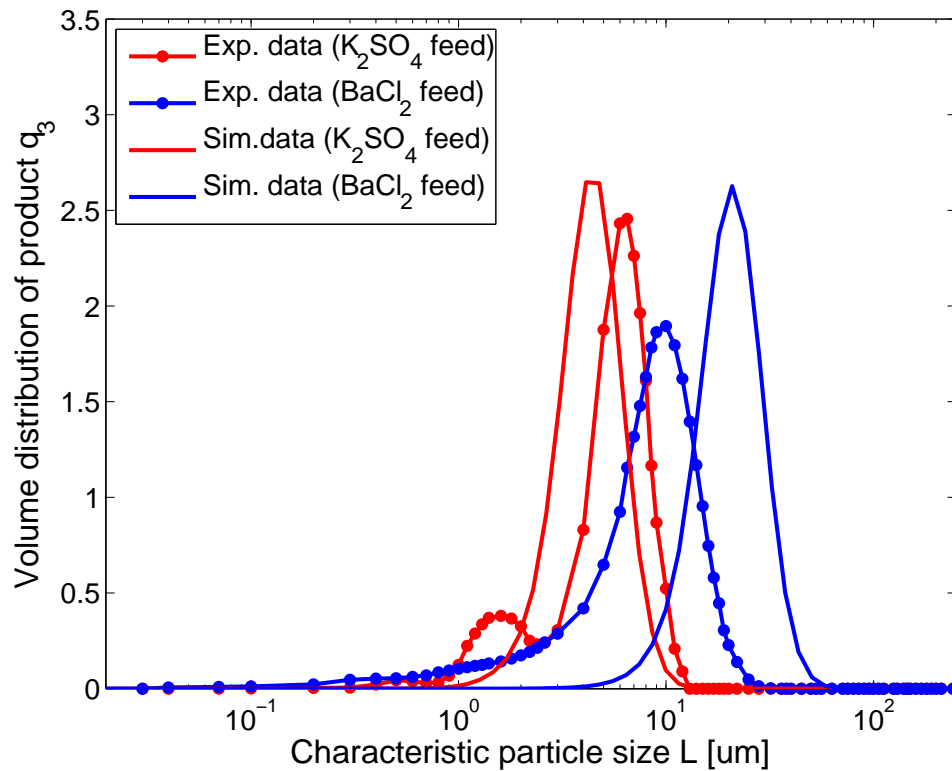


**Figure 59:** Simulated PSD in comparison to the experiments using ext. Debye-Hückel method and “mixed” kinetics as specified in the text.  $S_a = 527$ , 80 ml/min feed rate (no. 5 in Table 20).

All in all it can be concluded that implementing an  $R$ -dependent nucleation rate is a possible way of deriving a precipitation model that is able to predict particle sizes for stoichiometric as well as non-stoichiometric precipitation of barium sulfate.

## 7 Summary and conclusion

The dependency of particle sizes and morphologies for barium sulfate precipitation on the feeding policy and initial ion ratio was investigated and a strong influence was found for initial supersaturation values  $S_a < 1000$ . Depending on the experimental conditions of semi-batch operation, the observed crystal populations had different particle size distributions (PSDs) for the same concentration ratio, depending on whether barium or sulfate ions were present in excess. Influence of the feed rate on the morphology was explained by the shift of the real initial supersaturation to different values for varying feed rates. For a lower feed rate, the dominant nucleation mechanism changes to heterogeneous nucleation, and the growth mechanism changes from diffusion-controlled to integration-controlled kinetics giving plain surfaces and a higher long-range order of the crystal. For excess of barium ions, growth occurred mainly in two dimensions, leading to flat particles, whereas for excess of sulfate ions, growth into the third dimension was present. Changes in morphology for different ion ratios  $R$  were explained by the effect of the excess ions on the growth rates of crystal faces which are influenced differently by excess of ions, presumably by excess ions attaching to the particle surface that hinder growth of that face. The influence of the feeding sequence on the particle morphology can be explained by the excess of the ion species provided in the vessel at the beginning of the experiment, as it is present for semi-batch operations. This also explains the observed result that the influence of ion excess is only crucial for the ion species provided in the vessel. A higher concentration of one ion species in the feed does not have the same effect as if the same ion species is provided with higher concentration in the vessel.

The concentration of the inlet feed is defined by the concentration in combination with the feed rate. Higher concentrated feed has to some extent the same effect as lower feed concentration at higher feed rate. Recommendations for feed policies to achieve specified particle morphologies valid for the experimental set-up of this work are given.

The experimental conditions also influence the active growth sites of a seed crystal. For seeded precipitation, great care should be taken to properly characterize the seed crystals used, as the properties of the precipitates depend on the morphology and active growth sites of the seeds. The seed crystal's morphology gets preserved while seed crystals grow with the growth morphology that is influenced by the



experimental conditions of the seeded precipitation. Growth of seed crystals depends on their morphology which defines the existing growth sites on which growth continues. Depending on the active growth sites of the seed crystal and the growth morphology of the seeded precipitation, seed crystals do not necessarily get covered with new growth layers upon growth, but can show dendritic branches that start at the outer rim. It can be concluded, that the shape and thus the size of seeded precipitates is not only dependent on the precipitation conditions like supersaturation and ion ratio, but also on the morphology of the seed crystals. This is a very important knowledge for operations where the size of the particles is the key information about the process, like it is for growth kinetic experiments by seeded precipitation.

For simulating barium sulfate precipitation with a one-dimensional population balance equation model, the difference in influence on the particle size distributions of the activity coefficient for calculation with the three different approaches is negligibly small. Thus, even the extended Debye-Hückel model gives approximately the same PSD results for a model including ion complex formation. Due to the simpler structure of this activity coefficient model, this could be advantageous for faster simulation, if e.g. considering a model based process control scheme. For higher concentration ratios of reactants, however, this simplest activity coefficient model gave a different prediction of precipitation regions reached, predicting homogeneous nucleation due to the high supersaturation. In this case, a more sophisticated thermodynamic approach for the supersaturation helps the right prediction of phenomena occurring during precipitation.

For modelling non-stoichiometric semi-batch precipitation kinetics have to be used that take into account the differences in PSDs that result from the different ion ratios. The influence of barium and sulfate ion excess because of changes of interfacial tension due to attachment of potential-determining ions on the crystal surface have to be included into the model in addition to the thermodynamic driving force to predict the influence on nucleation kinetics. For the growth rate, it was shown that a supersaturation-dependent model should be sufficient as the non-symmetry with regard to barium and sulfate excess can be assumed to be negligible. For the nucleation rate, however, the non-symmetry concerning the ion ratio and the overall change of the rate for increasing ion excess of barium and sulfate are significant. Nucleation kinetics dependent on the barium to sulfate ion ratio adapted from Aoun

et al.'s (1996) were suggested as possibility to account for the dependence on barium or sulfate ion excess. The computational results shown are for kinetic parameters taken from the literature and are thus satisfactory as a first result.

The results of this thesis show that when performing morphology experiments of barium sulfate in semi-batch reaction mode, as well as for producing barium sulfate in industry, it is necessary to consider the rate at which the feed is added to the tank, as well as the feeding sequence, as these two factors can have a great influence on the particle shape and size. As an advantage, semi-batch mode gives more possibilities to influence the particle properties by the operating parameters than the common batch procedure. The knowledge about the effects reported could be used to produce particles or seed crystals with specific properties, well-defined shapes, and specific morphologies, as they might be of interest for applications in pharmacy, catalysis or material science.

Reliable quantitative measurements describing the ion excess influence on growth rates of different crystal faces are still lacking, though, which would be needed to give quantitative estimations of the morphology changes. For one-dimensional population balance modelling, nucleation kinetics dependent on the ion excess would have to be determined to improve the kinetic modelling of semi-batch precipitation, e.g. by an empirical rate law that includes the ion ratio of barium and sulfate.

**List of symbols**

$a$	[m]	smallest possible distance between ions
$a$	[m <sup>2</sup> / m <sup>3</sup> ]	specific particle surface
$A$	[(m <sup>3</sup> /mol) <sup>1/2</sup> ]	parameter of extended Debye-Hückel law
$a_i$	[-]	activity of ion species $i$
$A_m$	[(kg/mol) <sup>1/2</sup> ]	temperature-dependent constant of Debye-Hückel limiting law and Bromley model
$A_N$	[-]	parameter for nucleation model
$A_p$	[m <sup>2</sup> ]	surface of crystal
$A_{\ominus}$	[(kg/mol) <sup>1/2</sup> ]	temperature-dependent constant of Pitzer model
$b$	[-]	parameter of Pitzer model
$B$	[-]	nucleation rate constant
$B$	[(m/mol) <sup>1/2</sup> ]	parameter of extended Debye-Hückel law
$B_{ca}$	[kg/mol]	exchange parameter of Bromley model
$B_{ij}^P$	[kg/mol]	parameter of Pitzer model
$B_{ca}^*$	[kg/mol]	exchange parameter of Bromley model
$B_{ca}'^P$	[(kg/mol) <sup>2</sup> ]	parameter of Pitzer model
$c_i$	[mol / m <sup>3</sup> ]	concentration of ions of species $i$
$C_{ij}$	[-]	parameter of Pitzer model
$C_{ij}^{\ominus}$	[-]	parameter of Pitzer model
$C_{\tau}$	[-]	constant in Eq. (119)
$d$	[m]	impeller diameter
$d$	[m]	mean particle size
$f$	[#/(m <sup>3</sup> m)]	number density function
$f(I_m)$	[-]	correlation function for Pitzer model
$F_i$	[-]	interaction parameter between cations and anions, Bromley model
$G$	[m / s]	growth rate
$G^E$	[J]	Gibbs free energy
$I_c$	[mol / m <sup>3</sup> ]	ionic strength based on concentrations
$I_m$	[mol / kg]	ionic strength based on molality
$K_a$	[-]	activity based solubility product

---

$k_D$	$[(\text{m} / \text{s})(\text{m}^3 / \text{mol})]$	mass-transfer coefficient of growth model
$k_G$	$[(\text{m}/\text{s})(\text{m}^3 / \text{mol})]$	growth rate constant
$K_I$	$[\text{mol} / \text{kg}]$	reaction equilibrium
$k_r$	$[\text{m} / \text{s}]$	integration rate coefficient of growth model
$K_c$	$[-]$	concentration based solubility product
$k_N$	$[[\# / (\text{m}^3 \text{ s})]$	nucleation rate constant
$k_v$	$[-]$	volume shape factor of the particles as defined by Eq. (72)
$L$	$[\text{m}]$	characteristic crystal length
$L^*$	$[\text{m}]$	size of nuclei
$M_s$	$[\text{kg} / \text{mol}]$	molar mass of the precipitated particles
$m_i$	$[\text{mol} / \text{kg}]$	molality of species $i$
$\tilde{m}_{LM}$	$[\text{kg}]$	mass of solvent
$N$	$[\#]$	number of molecules / ions in a cluster
$\bar{N}$	$[\text{m}^{-3}]$	average crystal concentration
$n_i$	$[\text{mol}]$	mole number of component $i$
$N_Q$	$[-]$	pumping number
$n_s$	$[\text{mol}]$	mole number of material flux from liquid to solid phase
$N_{stirr}$	$[1 / \text{s}]$	number of stirrer revolutions
$PSD$		particle size distribution
$q$	$[-]$	parameter of Pitzer model
$q_{ex}$	$[\text{m}^3 / \text{s}]$	exchange flow rate between inlet and bulk compartments
$q_{in}$	$[\text{m}^3 / \text{s}]$	feed rate
$q_0$	$[1 / \text{m}]$	number distribution function
$q_3$	$[1 / \text{m}]$	volume distribution function
$Q_3$	$[-]$	volume cumulative curve
$r_N$	$[\# / (\text{m}^3 \text{ s})]$	nucleation rate
$r_s$	$[\text{mol} / (\text{m}^3 \text{ s})]$	material flux from liquid to solid phase
$R$	$[-]$	concentration ratio of barium to sulfate ions
$R_{max}$	$[1 / (\text{m}^3 \text{ s})]$	parameter for nucleation model
$\bar{R}$	$[\text{J} / (\text{K mol})]$	universal gas constant

$S_a$	[-]	activity based supersaturation ratio
$T$	[K]	temperature
$V$	[m <sup>3</sup> ]	total volume of the reactor
$V_B$	[m <sup>3</sup> ]	volume of the bulk zone
$V_E$	[m <sup>3</sup> ]	volume of the inlet volume
$V_p$	[m <sup>3</sup> ]	volume of the crystal
$z_i$	[-]	number of charges of ion species $i$
$\bar{z}_{ca}$	[-]	arithmetic mean ion charge

### Greek symbols

$\alpha_n$	[-]	parameter of Pitzer model
$\beta_{ij}^{(x)}$	[-]	parameter of Pitzer model, $x = [0,1]$
$\gamma_i$	[-]	ionic activity coefficient of ion species
$\gamma_s$	[J/m <sup>2</sup> ]	interfacial tension
$\gamma_{\pm}$	[-]	mean ionic activity coefficient of barium sulfate
$\gamma_{\pm}^{sat}$	[-]	saturation activity coefficient
$\varepsilon$	[m <sup>2</sup> s <sup>-3</sup> ]	local turbulent energy dissipation rate
$\lambda_{ij}(I_m)$	[-]	binary interaction term, Pitzer model
$\mu_{ijk}$	[-]	triplet interaction term, Pitzer model
$\mu_i$	[J/kmol]	chemical potential of component $i$
$\nu_i$	[-]	stoichiometric coefficient of component $i$
$\nu$	[-]	sum of molality ratios, Pitzer model $\rho_s$ [kg / m <sup>3</sup> ] density of the particles
$\rho_{H_2O}$	[kg / m <sup>3</sup> ]	density of water
$\tau_c$	[s]	circulation time in the reactor
$\tau_E$	[s]	residence time in inlet zone
$\tau_G$	[s]	characteristic time constant for growth
$\tau_M$	[s]	characteristic time constant for macromixing
$\tau_N$	[s]	characteristic time constant for nucleation
$\tau_w$	[s]	characteristic time constant for micromixing
$\Phi$	[-]	molar affinity

---

$\Phi_{ij}$	[-]	parameter of Pitzer model
$\Phi_v$	[-]	sphericity of a particle as defined by Eq. (75)
$\Psi_{ijk}$	[-]	triplet interaction term, Pitzer model

### Subscripts

0	initial, at time t=0
a	activity based
a	anion
aa	anion-anion
A	surface area
aq	dissolved in water
B	bulk volume
Ba <sup>2+</sup>	barium ions
BaSO <sub>4</sub>	barium sulfate ion complex formed in solution
c	cation
c	concentration based
ca	cation-anion
cc	cation-cation
Cl <sup>-</sup>	chloride ions
E	inlet volume
free	free ions in solution
GG	equilibrium state
i	component <i>i</i>
int	interface solid-liquid
K <sup>+</sup>	potassium ions
het	heterogeneous nucleation
hom	homogeneous nucleation
L	liquid phase
m	molality based
M	anion
p	crystal (solid phase)
s	precipitating substance, solid phase
SO <sub>4</sub> <sup>2-</sup>	sulfate ions
tot	total

---

V	volume
X	anion
$\pm$	mean

**Superscripts**

*	solid (equilibrium) state
l	liquid phase
sat	saturated

## References

- Adityawarman, D.; Niemann, B.; Sundmacher, K. Dynamic Process Model for Nano-particle Precipitation in Microemulsion Systems. *Chem. Eng. Technol.* **2008**, *31*, 1-7.
- Angerhöfer, M. *Untersuchungen zur Kinetik der Fällungsreaktion von Bariumsulfat*. Ph.D. Thesis, Technical University Munich, Germany, 1994.
- Aoun, M.; Plasari, E.; David, R.; Villiermaux, J. Are Barium Sulphate Kinetics Sufficiently Known for Testing Precipitation Reaction Models? *Chem. Eng. Sci.* **1996**, *51*, 2449-2458.
- Aoun, M.; Plasari, E.; David, R.; Villiermaux, J. Simultaneous Determination of Nucleation and Growth Rates from Batch Spontaneous Precipitation. *Chem. Eng. Sci.* **1999**, *54*, 1161-1180.
- Archibald, D.; Gaber, B.; Hopwood, J.; Mann, S.; Boland, T. Atomic Force Microscopy of Synthetic Barite Microcrystals. *J. Cryst. Growth* **1997**, *172*, 232-248.
- Atkins, P.W. *Physikalische Chemie*; Second Edition, VCH, Weinheim, 1996.
- Bala, H.; Fu, W.; Guo, Y.; Zhao, J.; Jiang, Y.; Ding, X.; Yu, K.; Li, M.; Wang, Z. In Situ Preparation and Surface Modification of Barium Sulfate Nanoparticles. *Colloids Surf. A* **2006**, *274*, 71-76.
- Bałdyga, J.; Makowski, Ł.; Orciuch, W. Interaction between Mixing, Chemical Reactions, and Precipitation. *Ind. Eng. Chem. Res.* **2005**, *44*, 5342-5352.
- Bałdyga, J.; Orciuch, W. Closure Problem for Precipitation. *Trans IChemE* **1997**, *75* (A), 160-170.
- Bałdyga, J.; Orciuch, W. Barium Sulphate Precipitation in a Pipe – an Experimental Study and CFD Modelling. *Chem. Eng. Sci.* **2001**, *56*, 2435-2444.
- Bałdyga, J.; Podgórska, W.; Pohorecki, R. Mixing-Precipitation Model with Application to Double Feed Semibatch Precipitation. *Chem. Eng. Sci.* **1995**, *50* (8), 1281-1300.
- Benton, W.J.; Collins, I.R.; Grimsey, I.M.; Parkinson, G.M.; Rodger, S.A. Nucleation, Growth and Inhibition of Barium Sulfate-controlled Modification with Organic and Inorganic Additives. *Faraday Discuss.* **1993**, *95*, 281-297.
- Bernard-Michel, B.; Pons, M.N.; Vivier, H. Quantification, by Image Analysis, of Effect of Operational Conditions on Size and Shape of Precipitated Barium Sulphate. *Chem. Eng. J.* **2002**, *87*, 135-147.



- Bisker-Leib, V.; Doherty, M.F. Modeling the Crystal Shape of Polar Organic Materials: Prediction of Urea Crystals Grown from Polar and Nonpolar Solvents. *Cryst. Growth Des.* **2001**, *1* (6), 455-461.
- Black, S.N.; Bromley, L.A.; Cottier, D.; Davey, R.J.; Dobbs, B.; Rout, J.E. Interactions at the Organic/Inorganic Interface: Binding Motifs for Phosphonates at the Surface of Barite Crystals. *J. Chem. Soc. Faraday Trans.* **1991**, *87* (20), 3409-3414.
- Borchert, C.; Nere, N.; Ramkrishna D.; Voigt, A.; Sundmacher, K. On the prediction of crystal shape distributions in a steady-state continuous crystallizer. *Chem. Eng. Sci.* **2009**, *64*, 686-696.
- Bosbach, D.; Hall, C.; Putnus, A. Mineral precipitation and dissolution in aqueous solution: in-situ microscopic observations on barite (001) with atomic force microscopy. *Chem. Geol.* **1998**, *151*, 143-160.
- Briesen, H. Simulation of Crystal Size and Shape by Means of a Reduced Two-dimensional Population Balance Model. *Chem. Eng. Sci.* **2006**, *61*, 104-112.
- Bromley, L.A. Thermodynamic Properties of Strong Electrolytes in Aqueous Solutions. *AIChE J.* **1973**, *19* (2), 313-320.
- Buchanan, A.S.; Heyman, E. The Electrokinetic Potential of Barium Sulphate. *Proc. R. Soc. London, Ser. A* **1948**, *195* (1041), 150-162.
- Cardew, P.T. The growth shape of crystals. *J. Cryst. Growth* **1985**, *73*, 385-391.
- Chen, J.; Zheng, C.; Chen, G. Interaction of Macro- and Micromixing on Particle Size Distribution in Reactive Precipitation. *Chem. Eng. Sci.* **1996**, *51* (10), 1975-1966.
- D'Ans, J.; Lax, E. *Taschenbuch für Chemiker und Physiker, Bd. 3: Elemente, anorganische Verbindungen und Materialien, Minerale*; Springer, Berlin, 1998.
- Debye, P.; Hückel, E. Zur Theorie der Elektrolyte: I. Gefrierpunktserniedrigung und verwandte Erscheinungen / II. Das Gesetz für die elektrische Leitfähigkeit. *Phys. Z.* **1923**, *24*, 185-206 / 305-325.
- Dirksen, J.A.; Ring, T.A. Fundamentals of Crystallisation: Kinetic Effects on Particle Size Distributions and Morphology. *Chem. Eng. Sci.* **1991**, *46* (10), 2389-2427.
- Dunn, K.; Daniel, E.; Shuler, P.J.; Chen, H.J.; Tang, Y.; Yen, T.F. Mechanisms of Surface Precipitation and Dissolution of Barite: A Morphology Approach. *J. Colloid Interface Sci.* **1999**, *214*, 427-437.
- Eble, A. *Precipitation of Nanoscale Crystals with Particular Reference to Interfacial Energy*. Ph.D. Dissertation, Technical University Munich, Germany, 2000.

- Felmy, A.R.; Rai, D.; Amonette, J.E. The Solubility of Barite and Celestite in Sodium Sulfate: Evaluation of Thermodynamic Data. *J. Solution Chem.* **1990**, *19* (2), 175-185.
- Felmy, A.R.; Weare, J.H. The Prediction of Borate Mineral Equilibria in Natural Waters: Application to Searles Lake, California. *Geochim. Cosmochim. Acta* **1986**, *50*, 2771-2783.
- Filippov, V.K.; Kalinkin, A.M.; Vasin, S.K. Thermodynamics of Phase Equilibria of Aqueous (Lithium Sulfate + Cesium Sulfate), (Sodium Sulfate + Cesium Sulfate), and (Potassium Sulfate + Cesium Sulfate) at 298.15 K using Pitzer's Model. *J. Chem. Thermodyn.* **1987**, *19*, 185-193.
- Fischer, R.B.; Rhinehammer, T.B. Rapid Precipitation of Barium Sulfate. *Anal. Chem.* **1953**, *25* (10), 1544-1548.
- Fitchett, D.E.; Tarbell, J.M. Effect of Mixing on the Precipitation of Barium Sulphate in an MSMR Reactor. *AIChE J.* **1990**, *36* (4), 511-522.
- Gunn, D.J. and Murthy, M.S. Kinetics and Mechanisms of Precipitation. *Chem. Eng. Sci.* **1972**, *27*, 1293-1313.
- Hartmann, P. and Perdock, W.G. On the Relations Between Structure and Morphology of Crystals III. *Acta. Cryst.* **1955**, *8*, 525-529.
- Hennessy, A.J.B.; Graham, G.M. The Effect of Additives on the Co-crystallisation of Calcium with Barium Sulphate. *J. Cryst. Growth* **2002**, *237-239*, 2153-2159.
- Jaworski, Z.; Nienow, A.W. CFD Modelling of Continuous Precipitation of Barium Sulphate in a Stirred Tank. *Chem. Eng. J.* **2003**, *91*, 167-174.
- Jenkins, R.; Snyder, R.L. *Introduction to X-ray Powder Diffractometry*, Volume 138 from Chemical Analysis, a series of monographs on analytical chemistry and its application; John Wiley & Sons, Inc., New York, 1996.
- Jones, F.; Oliviera, A.; Parkinson, G.M.; Rohl, A.L.; Stanley, A.; Upson, T. The Effect of Calcium Ions on the Precipitation of Barium Sulphate 1: Calcium Ions in the Absence of Organic Additives. *J. Cryst. Growth* **2004**, *262*, 572-580.
- Jones, F.; Oliviera, A.; Parkinson, G.M.; Rohl, A.L.; Stanley, A.; Upson, T. The Effect of Calcium Ions on the Precipitation of Barium Sulphate 1: Calcium Ions in the Presence of Organic Additives. *J. Cryst. Growth* **2004**, *270*, 593-603.
- Jones, F.; Oliviera, A.; Rohl, A.L.; Parkinson, M.I.; Ogden, M.I.; Reyhani, M.M. Investigation into the Effect of Phosphonate Inhibitors on Barium Sulfate Precipitation. *J. Cryst. Growth* **2002**, *237-239*, 424-429.

- Judat, B. *Über die Fällung von Bariumsulfat – Vermischungseinfluss und Partikelbildung*. Ph.D. Thesis, Universität Fridericiana Karlsruhe, Germany, 2003.
- Judat, B.; Kind, M. Morphology and Internal Structure of Barium Sulfate – Derivation of a New Growth Mechanism. *J. Colloid Interface Sci.* **2004**, *269*, 341-353.
- Judat, B.; Racina, A.; Kind, M. Macro- and Micromixing in a Taylor-Couette Reactor with Axial Flow and their Influence on the Precipitation of Barium Sulfate. *Chem. Eng. Technol.* **2004**, *27* (3), 287-292.
- Kucher, M.; Babic, D.; Kind, M. Precipitation of Barium Sulfate: Experimental Investigation about the Influence of Supersaturation and Free Lattice Ion Ratio on Particle Formation. *Chem. Eng. Process.* **2006**, *45*, 900-907.
- Li, S.; Xu, J.; Luo, G. Control of Crystal Morphology through Supersaturation Ratio and Mixing Conditions. *J. Cryst. Growth* **2007**, *304*, 219-224.
- Liu, S.T.; Nancollas, G.H. Scanning Electron Microscopic and Kinetic Studies of the Crystallization and Dissolution of Barium Sulfate Crystals. *J. Cryst. Growth* **1976**, *33*, 11-20.
- Luckas, M.; Krissmann, J. *Thermodynamik der Elektrolytlösungen: Eine einheitliche Darstellung der Berechnung komplexer Gleichgewichte*; Springer Verlag, Berlin, 2001.
- Mangold, M.; Bück, A.; Schenkendorf, R.; Steyer, C.; Voigt, A.; Sundmacher, K. Two State Estimators for the Barium Sulfate Precipitation in a Semi-Batch Reactor. *Chem. Eng. Sci.* **2009**, *64* (4), 646-660.
- Marchisio, D.L.; Barresi, A.A.; Garbero, M. Nucleation, Growth, and Agglomeration in Barium Sulfate Turbulent Precipitation. *AIChE J.* **2002**, *48* (9), 2039-2050.
- Marchisio, D.L.; Fox, R.O.; Barresi, A.A.; Garbero, M.; Baldi, G. On the Simulation of Turbulent Precipitation in a Tubular Reactor via Computational Fluid Dynamics (CFD). *Trans IChemE* **2001**, *79* (A), 998-1004.
- Mersmann, A. *Crystallization Technology Handbook*; Second Edition, Marcel Dekker, Inc., New York, 2001.
- Monnin, C. A Thermodynamic Model for the Solubility of Barite and Celestite in Electrolyte Solutions and Seawater to 200 °C and to 1 kbar. *Chem. Geol.* **1999**, *153*, 187-209.
- Murthy, M.S. Theory of Crystal Growth in Phase Transformations: Precipitation of Barium Sulfate. *Chem. Eng. Sci.* **1994**, *49* (14), 2389-2393.

- Myers, D. *Surfaces, Interfaces, and Colloids, Principles and Application*; Second Edition, John Wiley & Sons, Inc., New York, 1999.
- Nielsen, A.E. The Kinetics of Crystal Growth in Barium Sulfate Precipitation. *Acta Chem. Scand.* **1958**, *12* (5), 951-958.
- Nielsen, A.E. Homogeneous Nucleation in Barium Sulfate Precipitation. *Acta Chem. Scand.* **1961**, *15* (2), 441-442.
- Nielsen, A.E. *Kinetics of Precipitation*; Pergamon, Oxford, 1964.
- Nielsen, A.E.; Toft, J.M. Electrolyte Crystal Growth Kinetics. *J. Cryst. Growth* **1984**, *67*, 278-288.
- Niemann, B.; Rauscher, F.; Adityawarman, D.; Voigt, A.; Sundmacher, K. Microemulsion-assisted Precipitation of Particles: Experimental and Model-based Process Analysis. *Chem. Eng. Process.* **2006**, *45*, 917-935.
- Öncül, A.A.; Sundmacher, K.; Thévenin, D. Numerical Investigation of the Influence of the Activity Coefficient on Barium Sulphate Crystallization. *Chem. Eng. Sci.* **2005**, *60*, 5395-5405.
- Öncül, A.A.; Sundmacher, K.; Seidel-Morgenstern, A.; Thévenin, D. Numerical and Analytical Investigation of Barium Sulphate Crystallization. *Chem. Eng. Sci.* **2006**, *61* (2), 652-664.
- Pagliolico, S.; Marchisio, D.; Barresi, A.A. Influence of Operating Conditions on BaSO<sub>4</sub> Crystal Size and Morphology in a Continuous Couette Precipitator. *J. Therm. Anal. Calorim.* **1999**, *56*, 1423-1433.
- Petres, J.J.; Deželić, G.; Težak, B. Monodisperse Sols of Barium Sulfate. III. Electron-Microscopic Study of Internal Structure of Particles. *Croatica Chem. Acta* **1969**, *41*, 183-186.
- Petrova, A. *Kombinierte Fällung und mechanische Desintegration am Beispiel von Bariumsulfat*. Ph.D. Thesis, Otto von Guericke University Magdeburg, Germany, 2008.
- Phillips, R.; Rohani, S.; Bałdyga, J. Micromixing in a Single-Feed Semi-Batch Precipitation Process. *AIChE J.* **1999**, *45* (1), 82-92.
- Piton, D.; Fox, R.O.; Marcant, B. Simulation of Fine Particle Formulation by Precipitation using Computational Fluid Dynamics. *Can. J. Chem. Eng.* **2000**, *78*, 983-993.
- Pitzer, K.S. Thermodynamics of Electrolytes. I. Theoretical Basis and General Equations. *J. Phys. Chem.* **1973**, *77* (2), 268-277.

- Pitzer, K.S. *Activity Coefficients in Electrolyte Solutions*; CRC Press, Boca Raton, 1991.
- Pitzer, K.S.; Kim, J.J. Thermodynamics of Electrolytes IV, Activity and Osmotic Coefficients for Mixed Electrolytes. *J. Am. Chem. Soc.* **1974**, *96* (18), 5701-5707.
- Pitzer, S.; Mayorga, G. Thermodynamics of Electrolytes, III. Activity and Osmotic Coefficients for 2-2 Electrolytes. *J. Solution Chem.* **1974**, *3* (7), 539-546.
- Podczec, F. A Shape Factor to Assess the Shape of Particles using Image Analysis. *Powder Technol.* **1997**, *93* (1), 47-53.
- Pons, M.-N.; Vivier, H.; Dodds, J. Particle Shape Characterization using Morphological Descriptors. *Part. Part. Syst. Charact.* **1997**, *14*, 272-277.
- Ramkrishna, D. *Population Balances: Theory and Applications to Particulate Systems in Engineering*; Academic Press, N.Y., 2000.
- Rauscher, F.; Veit, P.; Sundmacher, K. Analysis of a Technical-Grade w/o-Microemulsion and its Application for the Precipitation of Calcium Carbonate Nanoparticles. *Colloids Surf. A* **2005**, *254*, 183-191.
- Schubert, H.; Mersmann, A. Determination of Heterogeneous Nucleation Rates. *Trans. IChemE* **1996**, *74* (A), 821-827.
- Schulek, E.; Pungor, E.; Guba, F. Beiträge zur Morphologie des nach dem L.W. Winkler'schen Verfahren hergestellten BaSO<sub>4</sub>-Niederschlags. *Anal. Chim. Acta.* **1954**, *10*, 506-512.
- Schwarzer, H.-C.; Peukert, W. Experimental Investigation into the Influence of Mixing on Nanoparticle Precipitation. *Chem. Eng. Technol.* **2002**, *25* (6), 657-661.
- Schwarzer, H.-C.; Peukert, W. Combined Experimental/Numerical Study on the Precipitation of Nanoparticles. *AIChE J.* **2004**, *50* (12), 3234-3247.
- Schwarzer, H.-C.; Schwertfirm, F.; Manhart, M.; Schmid, H.-J.; Peukert, W. Predictive Simulation of Nanoparticle Precipitation Based on the Population Balance Equation. *Chem. Eng. Sci.* **2006**, *61*, 167-181.
- Shaw, J.S. *Introduction to Colloid and Surface Chemistry*; Fourth Edition, Butterworth-Heinemann, Oxford, 1999.
- Söhnel, O.; Garside, J. *Precipitation: Basic Principles and Industrial Applications*; Butterworth-Heinemann Ltd., Oxford, 1992.
- Song, X.; Sun, S.; Fan, W.; Yin, Z. Self-assemblies of the different Morphology ultrafine Barium Sulfate in situ Interface. *Materials Letters* **2003**, *57*, 3026-3030.

- Steyer, C.; Mangold, M.; Sundmacher, K. *Semi-batch Precipitation in a Stirred Tank Reactor: Influence of Feeding Strategy on Particle Size and Morphology*. (Oral), BIWIC 15th International Workshop on Industrial Crystallization, Magdeburg, Germany, September 10-12, **2008**; Lorenz, H., Kaemmerer, H., Eds.; Shaker Verlag: Aachen, 2008; 73-80.
- Steyer, C.; Sundmacher, K. Impact of Feeding Policy and Ion Excess on Particle Shape in Semi-batch Precipitation of Barium Sulfate. *J. Cryst. Growth* **2009a**, *311*, 2702-2708.
- Steyer, C.; Sundmacher, K. Morphology of Barium Sulfate Crystals from Seeded Precipitation. (Communication) *Chem. Eng. Technol.* **2009b**, *32* (7), 1127-1130.
- Steyer, C.; Mangold, M.; Sundmacher, K. Modelling of Particle Size Distribution for Semi-batch Precipitation of Barium Sulfate using Different Activity Coefficient Models. *Ind. Eng. Chem. Res.* **2010**, *49*, 2456-2468.
- Stieß, M. *Mechanische Verfahrenstechnik*; Springer Verlag Berlin, 1995.
- Taguchi, K.; Garside, J.; Tavare, N.S. Nucleation and Growth Kinetics of Barium Sulphate in Batch Precipitation. *J. Cryst. Growth* **1996**, *163*, 318-328.
- Taguchi, K.; Garside, J.; Tavare, N.S. Mixing, Reaction and Precipitation: Semibatch Barium Sulphate Precipitation. Editor: Benkreira, H. Conference: Symposium on Fluid Mixing 6, Bradford, GB, July 07-08, 1999. *Institution of Chemical Engineers Symposium Series* **1999**, *146*, 395-419.
- Takiyama, K. Formation and Aging of Precipitates. X. An Electron Micro-Diffraction Study on Crystal Habit of Barium Sulfate Precipitates. *Bull. Chem. Soc. Japan* **1958**, *32* (1), 68-72.
- van der Leeden, M.C.; Rosmalen, G.M. Adsorption Behavior of Polyelectrolytes on Barium Crystals. *J. Colloid Interface Sci.* **1995**, *171*, 142-149.
- van Leeuwen, M. *Precipitation and Mixing*. Ph.D. Thesis, Delft University of Technology, Netherlands, 1998.
- van Leeuwen, M.; Bruinsma, O.S.L.; van Rosmalen, G.M. Three-Zone Approach for Precipitation of Barium Sulfate. *J. Cryst. Growth* **1996**, *166*, 1004-1008.
- Vicum, L. *Investigation of the Influence of Turbulent Mixing on Precipitation Processes carried out in Stirred Tank Reactors*. Ph.D. Thesis, ETH Zurich, Switzerland, 2005.
- Vicum, L.; Mazzotti, M.; Baldyga, J. Applying a Thermodynamic Model to the Non-Stoichiometric Precipitation of Barium Sulfate. *Chem. Eng. Technol.* **2003**, *26* (3), 325-333.

- Vicum, L.; Mazzotti, M. Multi-Scale Modeling of a Mixing-Precipitation Process in a Semibatch Stirred Tank. *Chem. Eng. Sci.* **2007**, *62*, 3513-3527.
- Walton, A.G. *The Formation and Properties of Precipitates*. Volume 23 from "Chemical Analysis – a Series of Monographs on Analytical Chemistry and its Applications", Interscience Publishers, a division of John Wiley & Sons, New York, 1967.
- Walton, A.G.; Hlabse, T. Growth Kinetics of Barium Sulphate Suspensions. *Anual. Chim. Acta* **1963**, *29*, 249-253.
- Wang, F.; Xu, G.; Zhang, Z.; Song, S.; Dong, S. A systematic Morphosynthesis of Barium Sulfate in the Presence of Phosphonate Inhibitor. *J. Colloid Interface Sci.* **2006**, *293*, 394-400.
- Wang, F.; Xu, G.; Zhang, Z.; Xin, X. Morphology of Barium Sulfate by PEO-PPO-PEO as Crystal Growth Modifier. *J. Colloid Interface Sci.* **2005**, *259*, 151-154.
- Wei, H.; Garside, J. Application of CFD Modelling to Precipitation Systems. *Trans IChemE* **1997**, *75* (A), 219-227.
- Winn, D.; Doherty, M.F. Modeling Crystal Shapes of Organic Materials Grown from Solution. *AIChE J.* **2000**, *46* (7), 1348-1367.
- Wong, D.C.Y.; Jaworski, Z.; Nienow, A.W. Effect of Ion Excess on Particle Size and Morphology during Barium Sulphate Precipitation: an Experimental Study. *Chem. Eng. Sci.* **2001**, *56*, 727-734.
- Wong, D.C.Y.; Jaworski, Z.; Nienow, A.W. Barium Sulphate Precipitation in a Double-Feed Semi-Batch Stirred Reactor. *Trans IChemE* **2003**, *81* (A), 874-880.
- Yu, J.; Liu, S.; Cheng, B. Effects of PSMA Additive on Morphology of Barite Particles. *J. Cryst. Growth* **2005**, *275*, 572-579.

## Appendix A: Calculation of the mean activity coefficient

As an example, the mean activity coefficient for a barium sulfate solution will be calculated using the Bromley and Pitzer approaches, giving all constants used that are not already mentioned in Chapter 2.2.

The concentration values are for a mere calculation example and will be used for both methods. The concentrations listed in Table 21 are chosen with the assumption that these are the concentrations of the free ions. (Please note: The example neglects the fact that these concentrations denote the number of charges of the ions in the salts, thus in reality, barium and sulfate ion concentrations have to be lower due to complex formation (and of course precipitation) for a solution with these chloride and potassium ion concentrations. In Appendix B, real values of free ions, ion complexes, and supersaturations are listed for the different activity coefficient models. Also note that for the experimental set-up used in this work, these concentrations are twice as high as the highest possible value directly at the feed inlet point at the beginning of the experiment before the dilution effect of the semi-batch feeding policy has an impact, since the given values for the experiments denote the educt concentrations. Upon mixing the two salt solutions, the concentrations in the vessel are reduced due to the volume increase accordingly. Again, in Appendix B the valid maximum theoretical initial supersaturation values for the experiments in this work are listed.)

Please refer to Chapters 2.1 and 2.2 for the general equations. Table 21 lists the concentrations and the constants used for both methods, method-specific ones will be given in the subchapters. The calculation is done in molalities: With the assumption of density of the solution equal to the density of the solvent water, the molalities are of the same values as the concentrations.

**Table 21: Constants and concentrations (in mol/l) used**

$c_{Ba^{2+}}$	$c_{SO_4^{2-}}$	$c_{K^+}$	$c_{Cl^-}$	$K_c$	$\rho_{H_2O}$
0.1	0.01	0.2	0.02	$1 \times 10^{-9.96}$	1 kg/l

The numbers of charge of the ions are therefore:

$$|z_{Ba^{2+}}| = |z_{SO_4^{2-}}| = 2, \quad (A.1)$$

$$|z_{K^+}| = |z_{Cl^-}| = 1, \quad (A.2)$$



defining an ion strength of:

$$I_m = \frac{I_c}{\rho_{H_2O}} = \left( \frac{1}{2} \cdot (4 \cdot 0.1 + 4 \cdot 0.01 + 0.2 + 0.02) \right) / 1, \quad (\text{A.3})$$

$$= 0.33 \text{ mol / kg}.$$

### A.1 Bromley model

Values for the exchange parameters  $B_{ca}$  (in Eq. (26)) for various substances can be found in e.g. Bromley (1973, table 1):

$$B_{Ba^{2+}, Cl^-} = 0.0638 \text{ kg/mol}, \quad (\text{A.4})$$

$$B_{K^+, SO_4^{2-}} = -0.0320 \text{ kg/mol}, \quad (\text{A.5})$$

Barium sulfate is not listed in this table, thus  $B_{Ba^{2+}, SO_4^{2-}}$  has to be correlated with individual ion values  $B_{Ba^{2+}}$  and  $B_{SO_4^{2-}}$  from table 2 (in Bromley, 1973) using

$$B_{Ba^{2+}, SO_4^{2-}} = B_{Ba^{2+}} + B_{SO_4^{2-}} + \delta_{Ba^{2+}} \cdot \delta_{SO_4^{2-}} \quad (\text{A.6})$$

with  $\delta_{Ba^{2+}}$  and  $\delta_{SO_4^{2-}}$  being correction terms. The values for barium sulfate are listed in Table 22.

$$B_{Ba^{2+}, SO_4^{2-}} = 0.0022 + 0 + 0.098 \cdot (-0.4) \quad (\text{A.7})$$

$$= -0.037 \text{ kg / mol},$$

**Table 22: Individual ion values of B and  $\delta$  in aqueous solution at 25 °C (from Bromley, 1973)**

Ion i	$B_i$	$\delta_i$
Ba <sup>2+</sup>	0.0022	0.098
SO <sub>4</sub> <sup>2-</sup>	0.000	-0.40

$$B_{Ba^{2+}, SO_4^{2-}}^* = \frac{(0.06 + 0.6 \cdot (-0.037)) \cdot 2 \cdot 2}{\left(1 + \frac{1.5 \cdot 0.33}{2 \cdot 2}\right)^2} + (-0.037) \quad (\text{A.8})$$

$$= 0.0827 \text{ kg / mol},$$

$$B_{Ba^{2+},Cl^{-}}^* = \frac{(0.06 + 0.6 \cdot (-0.0638)) \cdot 2}{\left(1 + \frac{1.5 \cdot 0.33}{2}\right)^2} + 0.0638 \quad (\text{A.9})$$

$$= 0.1901 \text{ kg / mol},$$

$$B_{K^{+},SO_4^{2-}}^* = \frac{(0.06 + 0.6 \cdot (-0.0320)) \cdot 2}{\left(1 + \frac{1.5 \cdot 0.33}{2}\right)^2} + (-0.0320) \quad (\text{A.10})$$

$$= 0.0204 \text{ kg / mol},$$

$$\bar{z}_{Ba^{2+},SO_4^{2-}} = \frac{1}{2}(2 + 2) = 2, \quad (\text{A.11})$$

$$\bar{z}_{Ba^{2+},Cl^{-}} = \frac{1}{2}(2 + 1) = 1.5, \quad (\text{A.12})$$

$$\bar{z}_{K^{+},SO_4^{2-}} = \frac{1}{2}(2 + 1) = 1.5, \quad (\text{A.13})$$

$$F_{Ba^{2+}} = \frac{1}{1}(0.0827 \cdot 2^2 \cdot 0.01 + 0.1901 \cdot 1.5^2 \cdot 0.2) \quad (\text{A.14})$$

$$= 0.08886,$$

$$F_{SO_4^{2-}} = \frac{1}{1}(0.0827 \cdot 2^2 \cdot 0.1 + 0.0204 \cdot 1.5^2 \cdot 0.02) \quad (\text{A.15})$$

$$= 0.03401,$$

$$\log \gamma_{Ba^{2+}}^{m, Bromley} = -4 \cdot 0.5148 \frac{\sqrt{0.33}}{1 + \sqrt{0.33}} + 0.08886, \quad (\text{A.16})$$

$$= -0.6621,$$

$$\begin{aligned}\log \gamma_{SO_4^{2-}}^{m,Bromley} &= -4 \cdot 0.5148 \frac{\sqrt{0.33}}{1 + \sqrt{0.33}} + 0.03401, \\ &= -0.6621,\end{aligned}\tag{A.17}$$

$$\begin{aligned}\log \gamma_{\pm}^{m,Bromley} &= -4 \cdot 0.5148 \frac{\sqrt{0.33}}{1 + \sqrt{0.33}} + \frac{1}{2}(0.08886 + 0.03401), \\ &= -0.6895,\end{aligned}\tag{A.18}$$

$$\gamma_{Ba^{2+}}^{m,Bromley} = 0.2177,\tag{A.19}$$

$$\gamma_{SO_4^{2-}}^{m,Bromley} = 0.1919,\tag{A.20}$$

$$\gamma_{\pm}^{m,Bromley} = 0.2044,\tag{A.21}$$

$$\begin{aligned}S_a^{Bromley} &= \sqrt{\frac{0.1 \cdot 0.01}{1 \times 10^{-9.96}}} \cdot 0.2044 \\ &= 617.24.\end{aligned}\tag{A.22}$$

## A.2 Pitzer model

Some of the interaction parameters needed for the calculation of the example are taken out of Luckas und Krissmann (2001) (Table 24). The others are from Monnin (1999), who gave values of fitting constants to calculate the parameters  $\beta_{ij}^{(0)}$ ,  $\beta_{ij}^{(1)}$ , and  $C_{ij}^{\ominus}$  with Eq. (A.23) which are listed in Table 23. More data can be found in the literature (Felmy and Weare (1986), Felmy et al. (1990), Filippov et al. (1987), Pitzer (1973, 1991), Pitzer and Kim (1974), Pitzer and Mayorga (1974)).

$$\begin{aligned}X(T) &= a_1 + a_2 T + \frac{a_3}{T} + a_4 \ln T + \frac{a_5}{T - 263} + a_6 T^2 \\ &+ \frac{a_7}{680 - T} + \frac{a_8}{T - 227} + a_9 T^3 + a_{10} T^4\end{aligned}\tag{A.23}$$

**Table 23: Values of the fitted constants (Eq. (A.23)) for the binary interaction parameters for aqueous electrolytes (from Monnin, 1999)**

		a1	a2	a3	a4	a5
		a6	a7	a8	a9	a10
$K^+ - SO_4^{2-}$	$C^\Phi$	$-1.88 \times 10^{-2}$	0.0	0.0	0.0	0.0
		0.0	0.0	0.0	0.0	0.0
$Ba^{2+} - Cl^-$	$\beta^{(0)}$	$3.438314 \times 10^1$	$6.375 \times 10^{-4}$	$-1.33653 \times 10^3$	-5.302131	0.0
		$4.608725 \times 10^{-6}$	0.0	0.0	0.0	0.0
	$\beta^{(1)}$	$-1.042305 \times 10^2$	$3.225 \times 10^{-3}$	$4.37411 \times 10^3$	$1.587517 \times 10^1$	0.0
		$-6.77403 \times 10^6$	0.0	0.0	0.0	0.0
	$C^\Phi$	$-2.412012 \times 10^1$	$-1.537 \times 10^{-4}$	$7.871978 \times 10^2$	3.903953	0.0
		$-1.10262 \times 10^{-5}$	0.0	0.0	$8.761508 \times 10^{-9}$	0.0

**Table 24: Parameters for the Pitzer activity coefficient model. (a) from Luckas and Krissmann (2001); (b) from Monnin (1999); calculated with values of Table 23 using Eq. (A.23)**

ion pair ij	$\beta^{(0)}$	$\beta^{(1)}$	$C^\Phi$
$K^+ - Cl^-$	0.0484 <sup>(a)</sup>	0.2122 <sup>(a)</sup>	-0.00084 <sup>(a)</sup>
$K^+ - SO_4^{2-}$	0.0500 <sup>(a)</sup>	0.7793 <sup>(a)</sup>	-0.0188 <sup>(b)</sup>
$Ba^{2+} - Cl^-$	0.2906 <sup>(b)</sup>	1.2495 <sup>(b)</sup>	-0.0304 <sup>(b)</sup>

$$A_\Theta = 0.5148 \frac{\ln 10}{3} \sqrt{\text{kg/mol}} = 0.3949 \sqrt{\text{kg/mol}}, \quad (\text{A.24})$$

$$\begin{aligned} B_{K^+, SO_4^{2-}}^P &= 0.0500 + \frac{2 \cdot 0.7793}{2^2 \cdot 0.33} \left[ 1 - (1 + 2\sqrt{0.33}) \cdot \exp(-2\sqrt{0.33}) \right] \\ &= 0.42647 \text{ kg/mol}, \end{aligned} \quad (\text{A.25})$$

$$\begin{aligned} B_{Ba^{2+}, Cl^-}^P &= 0.2906 + \frac{2 \cdot 1.2495}{2^2 \cdot 0.33} \left[ 1 - (1 + 2\sqrt{0.33}) \cdot \exp(-2\sqrt{0.33}) \right] \\ &= 0.89427 \text{ kg/mol}, \end{aligned} \quad (\text{A.26})$$

$$\begin{aligned}
 B'_{K^+,Cl^-} &= \frac{2 \cdot 0.2122}{2^2 \cdot 0.33^2} \left[ -1 + \left( 1 + 2\sqrt{0.33} + 0.5 \cdot 2^2 \cdot 0.33 \right) \cdot \exp\left(-2\sqrt{0.33}\right) \right] \\
 &= -0.10681 \left( \frac{\text{kg}}{\text{mol}} \right)^2,
 \end{aligned} \tag{A.27}$$

$$\begin{aligned}
 B'_{K^+,SO_4^{2-}} &= \frac{2 \cdot 0.7793}{2^2 \cdot 0.33^2} \left[ -1 + \left( 1 + 2\sqrt{0.33} + 0.5 \cdot 2^2 \cdot 0.33 \right) \cdot \exp\left(-2\sqrt{0.33}\right) \right] \\
 &= -0.39225 \left( \frac{\text{kg}}{\text{mol}} \right)^2,
 \end{aligned} \tag{A.28}$$

$$\begin{aligned}
 B'_{Ba^{2+},Cl^-} &= \frac{2 \cdot 1.2495}{2^2 \cdot 0.33^2} \left[ -1 + \left( 1 + 2\sqrt{0.33} + 0.5 \cdot 2^2 \cdot 0.33 \right) \cdot \exp\left(-2\sqrt{0.33}\right) \right] \\
 &= -0.62894 \left( \frac{\text{kg}}{\text{mol}} \right)^2,
 \end{aligned} \tag{A.29}$$

$$C_{K^+,Cl^-} = \frac{-0.00084}{2\sqrt{|1 \cdot 1|}} = -0.00042 \left( \frac{\text{kg}}{\text{mol}} \right)^2, \tag{A.30}$$

$$C_{K^+,SO_4^{2-}} = \frac{-0.0188}{2\sqrt{|1 \cdot 1|}} = -0.006647 \left( \frac{\text{kg}}{\text{mol}} \right)^2, \tag{A.31}$$

$$C_{Ba^{2+},Cl^-} = \frac{-0.0304}{2\sqrt{|1 \cdot 1|}} = -0.01076 \left( \frac{\text{kg}}{\text{mol}} \right)^2, \tag{A.32}$$

$$f^\gamma = -0.3949 \left[ \frac{\sqrt{0.33}}{1 + 1.2\sqrt{0.33}} + \frac{2}{1.2} \ln\left(1 + 1.2\sqrt{0.33}\right) \right] = -0.47944, \tag{A.33}$$

$$Z = 0.1 \cdot 2 + 0.01 \cdot 2 + 0.02 \cdot 1 + 0.2 \cdot 1 = 0.44, \tag{A.34}$$

$$F = -0.47944 + 0.02 \cdot 0.01 \cdot (-0.39225) + 0.02 \cdot 0.2 \cdot (-0.10681) + 0.1 \cdot 0.2 \cdot (-0.62894) = -0.49253, \quad (\text{A.35})$$

$$\ln \gamma_{Ba^{2+}}^{m,Pitzer} = 2^2 \cdot (-0.49253) + 0.2 \cdot (2 \cdot 0.89427 + 0.44 \cdot (-0.01076)) + 2 \cdot [0.02 \cdot 0.01 \cdot (-0.006647) + 0.02 \cdot 0.2 \cdot (-0.00042) + 0.1 \cdot 0.2 \cdot (-0.01076)] = -1.6138, \quad (\text{A.36})$$

$$\ln \gamma_{SO_4^{2-}}^{m,Pitzer} = 2^2 \cdot (-0.49253) + 0.02 \cdot [2 \cdot 0.42647 + 0.44 \cdot (-0.006647)] + 2 \cdot [0.02 \cdot 0.01 \cdot (-0.006647) + 0.02 \cdot 0.2 \cdot (-0.00042) + 0.1 \cdot 0.2 \cdot (-0.01076)] = -1.9535, \quad (\text{A.37})$$

$$\gamma_{Ba^{2+}}^{m,Pitzer} = 0.19914, \quad (\text{A.38})$$

$$\gamma_{SO_4^{2-}}^{m,Pitzer} = 0.14177, \quad (\text{A.39})$$

$$\gamma_{\pm}^{m,Pitzer} = \sqrt{0.19914 \cdot 0.14177} = 0.16802, \quad (\text{A.40})$$

$$S_a^{Pitzer} = \sqrt{\frac{0.1 \cdot 0.01}{1 \times 10^{-9.96}}} \cdot 0.16802 = 507.42. \quad (\text{A.41})$$

## Appendix B: Values of supersaturation $S_a$

The values of the activity based supersaturation depend on the activity model used and whether ion complex formation of barium and sulfate is considered.

The simplest way of calculating  $S_a$  is by assuming ideal solution, which in Chapter 2 is already shown to be inappropriate for barium sulfate solutions in terms of describing real solution behaviour. In the next subchapters, first the calculation of the supersaturation values used for characterizing the experiments in this work (“theoretical maximum initial supersaturation  $S_a$ ”) will be explained. In the second subchapter, different values of  $S_a$  calculated with different methods will be listed as a comparison.

### B.1 Theoretical maximum initial supersaturation $S_a$ of the experiments

Throughout this work, experimental conditions are characterized by the supersaturation level  $S_a$  they were performed at. These values of  $S_a$  are calculated using the extended Debye-Hückel model to determine the activity coefficient, with no complex formation, as described in Chapter 2.2.1. The ionic strength (Eq. (6)) was calculated using barium and sulfate ion concentrations, only. With this, the calculation differs from what was used to determine all other supersaturation values in the simulation of this work, as here all four ion species were considered for the ion strength, as well as the concentration reduction by ion complex formation. In the following, it can be seen that the value of the supersaturation depends strongly on the method chosen to calculate it.

The naming was kept to ensure consistency to the author’s other publications relevant to this context (Steyer et al. 2008, 2010; Steyer and Sundmacher, 2009a,b). If to be chosen for this work only, the author would have taken  $S_a$  values calculated with the Pitzer model considering ion complex formation.

### B.2 Different values of $S_a$ calculated with different methods

Table 25 gives the concentrations of reactants as used in this work for the experiments (ref. Chapter 3). The concentrations listed for the ion species in the vessel are the resulting theoretical maximum initial ones if the reactants would be mixed completely and instantly. The row numbers given are used as indicator in Table 26 to Table 30.

Table 26 shows values for  $S_a$  calculated with different models and without the consideration of ion complex formation. It can be seen that the driving force for precipitation decreases for increasing consideration of ion species and interaction thereof. The marked column denotes the values used for characterization of experimental conditions in this work.

In Table 27, the ion complex formation was considered but all other interactions between ions neglected ( $\gamma_{\pm}^m = 1$ ).

Table 28 lists values of  $S_a$  along with the activity coefficient and the free ion concentrations calculated with the extended Debye-Hückel method as presented in Chapter 2.2.1. Ion complex formation is considered.

Table 29 lists for the same initial values the resulting free ion concentrations, activity coefficients, and supersaturations for the Bromley method (Chapter 2.2.2). For Table 30, the values were calculated using the Pitzer method (Chapter 2.2.3).

If comparing the values for  $S_a$  in Table 26 to Table 30, it can be seen that neglecting the ion complex formation gives much higher values for the supersaturation.

It can be seen that if dealing with supersaturation in weak electrolytes, it is always very important to specify the exact method of calculation for the given values.

**Table 25: Concentrations of reactants and of ion species in the vessel if mixed instantly (theoretical maximum initial concentrations) [mol/l]**

row no.	$R$	concentration of reactant $\text{BaCl}_2$	concentration of reactant $\text{K}_2\text{SO}_4$	total concentration of $\text{Ba}^{2+}$ in vessel	total concentration of $\text{SO}_4^{2-}$ in vessel	concentration of $\text{Cl}^-$ in vessel	concentration of $\text{K}^+$ in vessel
1	1	0.1	0.1	0.05	0.05	0.1	0.1
2	10	0.1	0.01	0.05	0.005	0.1	0.01
3	0.1	0.01	0.1	0.005	0.05	0.01	0.1
4	7.5	0.075	0.01	0.0375	0.005	0.075	0.01
5	0.13	0.01	0.075	0.005	0.0375	0.01	0.075
6	5	0.05	0.01	0.025	0.005	0.05	0.01
7	0.2	0.01	0.05	0.005	0.025	0.01	0.05
8	1	0.01	0.01	0.005	0.005	0.01	0.01



**Table 26:  $S_a$  values for different methods without consideration of ion complex formation. For further explanations please refer to the text.**

row no. (Table 25)	ideal solution $\gamma_{\pm}^m = 1$	ext. Debye-Hückel* method	ext. Debye-Hückel method	Bromley method	Pitzer method
1	4775	1335.6	1140.5	981.83	834.46
2	1510	526.6	454.29	417.01	375.23
3	1510	526.6	454.29	399.24	361.15
4	1307.7	498.47	432.62	400.96	369.42
5	1307.7	498.47	432.62	388.23	358.81
6	1067.7	455.71	399.2	374.52	353.55
7	1067.7	455.71	399.2	366.97	346.85
8	477.5	274.4	248.52	240.25	235.78

\* $I_c$  calculated only considering barium and sulfate ions

**Table 27: Calculated values for ideal solution (ion complex formation considered). All concentrations in  $[\text{mol}/\text{m}^3]$** 

row no. (Table 25)	free ion concentration of $\text{Ba}^{2+}$	free ion concentration of $\text{SO}_4^{2-}$	concentration of $\text{BaSO}_4$ ion complexes	$S_a$
1	8.8544	8.8544	41.146	845.59
2	45.202	0.20225	4.7978	288.75
3	0.20225	45.202	4.7978	288.75
4	32.775	0.27472	4.7253	286.56
5	0.27472	32.775	4.7253	286.56
6	20.427	0.42662	4.5734	281.92
7	0.42662	20.427	4.5734	281.92
8	2.2776	2.2776	2.7224	217.51

**Table 28: Calculated values for extended Debye-Hückel method (ion complex formation considered). All concentrations in [mol/m<sup>3</sup>]**

row no. (Table 25)	free ion concentration of Ba <sup>2+</sup>	free ion concentration of SO <sub>4</sub> <sup>2-</sup>	concentration of BaSO <sub>4</sub> ion complexes	activity coefficient $\gamma_{\pm}^m$	$S_a$
1	24.751	24.751	25.249	0.28025	662.41
2	46.488	1.4882	3.5118	0.311	247.04
3	1.4882	46.488	3.5118	0.311	247.04
4	34.101	1.6007	3.3993	0.34447	243.05
5	1.6007	34.101	3.3993	0.34447	243.05
6	21.803	1.8033	3.1967	0.39359	235.69
7	1.8033	21.803	3.1967	0.39359	235.69
8	3.2685	3.2685	1.7315	0.55572	173.46

**Table 29: Calculated values for Bromley method (ion complex formation considered). All concentrations in [mol/m<sup>3</sup>]**

row no. (Table 25)	free ion concentration of Ba <sup>2+</sup>	free ion concentration of SO <sub>4</sub> <sup>2-</sup>	concentration of BaSO <sub>4</sub> ion complexes	activity coefficient of barium ions	activity coefficient of sulfate ions	mean activity coefficient $\gamma_{\pm}^m$	$S_a$
1	26.867	26.867	23.133	0.24712	0.25904	0.23574	634.04
2	46.657	1.6565	3.3435	0.28711	0.29772	0.27687	241.05
3	1.7556	46.756	3.2444	0.27444	0.27925	0.26971	237.45
4	34.251	1.7514	3.2486	0.32123	0.33054	0.31219	237.6
5	1.8262	34.326	3.1738	0.3106	0.31498	0.30628	234.85
6	21.93	1.9301	3.0699	0.37175	0.37934	0.36432	230.97
7	1.9787	21.979	3.0213	0.36383	0.36773	0.35998	229.14
8	3.3164	3.3164	1.6836	0.54009	0.54299	0.5372	171.05

**Table 30: Calculated values for Pitzer method (ion complex formation considered). All concentrations in [mol/m<sup>3</sup>]**

row no. (Table 25)	free ion concentration of Ba <sup>2+</sup>	free ion concentration of SO <sub>4</sub> <sup>2-</sup>	concentration of BaSO <sub>4</sub> ion complexes	activity coefficient of barium ions	activity coefficient of sulfate ions	mean activity coefficient $\gamma_{\pm}^m$	$S_a$
1	28.854	28.854	21.146	0.21999	0.23126	0.20927	606.2
2	46.875	1.8745	3.1255	0.26034	0.28752	0.23573	233.05
3	1.9671	46.967	3.0329	0.2501	0.23992	0.26072	229.58
4	34.416	1.9164	3.0836	0.29848	0.32224	0.27646	231.49
5	1.9873	34.487	3.0127	0.28941	0.28074	0.29834	228.81
6	22.04	2.0403	2.9597	0.35414	0.37305	0.33619	226.79
7	2.0876	22.088	2.9124	0.34692	0.34074	0.35321	224.97
8	3.3372	3.3372	1.6628	0.53338	0.53673	0.53006	169.99

## Appendix C: Own Publications

### Peer reviewed full papers:

Steyer, C.; Sundmacher, K. Impact of Feeding Policy and Ion Excess on Particle Shape in Semi-batch Precipitation of Barium Sulfate. *J. Cryst. Growth* **2009**, *311*, 2702-2708.

Steyer, C.; Sundmacher, K. Morphology of Barium Sulfate Crystals from Seeded Precipitation. (Communication) *Chem. Eng. Technol.* **2009**, *32* (7), 1127-1130.

Steyer, C.; Mangold, M.; Sundmacher, K. Modelling of Particle Size Distribution for Semi-batch Precipitation of Barium Sulfate using Different Activity Coefficient Models. *Ind. Eng. Chem. Res.* **2010**, *49*, 2456-2468.

### Public Presentations:

Rudolph, C.; Sundmacher, K. Bestimmung von Größenverteilungen disperser Systeme durch Ultraschallspektroskopie. (Poster) International Innovation Seminar, Session on Computational Chemical Engineering, 26-27 October 2000, Magdeburg, Germany.

Steyer, C.; Mangold, M.; Sundmacher, K. Semi-batch precipitation in a stirred tank reactor: Influence of feeding strategy on particle size and morphology. (Oral), BIWIC 15th International Workshop on Industrial Crystallization, Magdeburg, Germany, September 10-12, 2008; Lorenz, H., Kaemmerer, H., Eds.; Shaker Verlag: Aachen, 2008; 73-80.

### Contributions:

Mitkova, T.; John, V.; Tobiska, L.; Steyer, C.; Voigt, A.; Sundmacher, K. Simulationsmethoden für Partikel-Populationsbilanzen zur Analyse von Fällungsprozessen in Strömungsfeldern. GVC/DECHEMA Jahrestagung, Wiesbaden, Germany, September 2005. Abstract in *CIT* **2005**, *77* (8), 1040.

Mangold, M.; Steyer, C.; Niemann, B.; Voigt, A.; Sundmacher, K. Methods of State Estimation for Particulate Processes. (Oral) ESCAPE-16, 9-13 July 2006, Garmisch-Partenkirchen, Germany.

Heineken, W.; Flockerzi, D.; Steyer, C.; Voigt, A.; Sundmacher, K. Nonlinear Dynamics of Continuous Precipitation Reactors: A Model-based Analysis. (Poster) 19th International Symposium on Chemical Reaction Engineering, 3-6 September 2006, Potsdam, Germany.

- 
- Heineken, W.; Flockerzi, D.; Steyer, C.; Voigt, A.; Sundmacher, K. Nonlinear Dynamics of Continuous Precipitation Reactors: A Model Based Analysis, *Chem. Eng. Sci.* **2007**, *62*, 4896-4902.
- Mangold, M.; Schenkendorf, R.; Steyer, C.; Voigt, A.; Sundmacher, K. Model-based Measurement of Particle Size Distributions. (Oral) 3rd International Conference on Population Balance Modeling, 19-21 September 2007, Quebec City, Canada.
- Mangold, M.; Bück, A.; Schenkendorf, R.; Steyer, C.; Voigt, A.; Sundmacher K. Two State Estimators for the Barium Sulfate Precipitation in a Semi-Batch Reactor. *Chem. Eng. Sci.* **2009**, *64* (4), 646-660.

## Appendix D: Lebenslauf

### Persönliche Angaben

Name	Christiane Steyer, geb. Rudolph
Geburtsdatum	04.12.1972
Geburtsort	Stuttgart
Familienstand	verheiratet, vier Kinder

### Ausbildung und Studium

Juni 1992	Abitur am Schadow-Gymnasium, Berlin-Zehlendorf
Okt.1992 – Mai 1999	Energie- und Verfahrenstechnik, Technische Universität Berlin; Diplom Mai 1999 (Note „sehr gut“)
Sept. 1995 – Juni 1996	Studienaufenthalt (Chemical Engineering and Process Integration), University of Manchester Institute of Science and Technology (UMIST, heute The University of Manchester), GB
Juni – Sept. 1996	Studienarbeit (Fachgebiet Energietechnik, Note „sehr gut“) an der University of Manchester (UMIST), GB
Juni – Sept. 1997	Projektbezogenes Praktikum bei der Nesté Deutschland AG, damaliges Chokoladenwerk Berlin, Technische Abteilung
Sept. 1997 – Aug. 1998	Projektbezogene studentische Hilfskraft bei der Schering AG, Berlin, Werkverwaltung Charlottenburg / Betriebsbetreuung 1 (heute Bayer HealthCare AG)
Nov. 1998 – Mai 1999	Diplomarbeit (Fachgebiet Verfahrenstechnik, Note „sehr gut“), Technische Universität Krakau, Polen
Nov. 1999 – März 2010	wissenschaftliche Mitarbeiterin am Lehrstuhl für Systemverfahrenstechnik, Fakultät für Verfahrens- und Systemtechnik, Otto-von-Guericke-Universität Magdeburg (seit Okt. 2001 in Elternzeit mit Teilzeitbeschäftigung)

### Weitere Tätigkeiten

April 2010 – Januar 2011	Elternzeit
seit Februar 2011	Projektleitung Konzentrationsmesstechnik bei der metraTec GmbH, Magdeburg